



The
University
Of
Sheffield.

*SHORT CATIONIC PEPTIDES FOR GENE
DELIVERY INTO CANCER CELLS*

By
Silvia Cirillo

**A thesis submitted in partial fulfilment of the requirements for the degree of
Doctor of Philosophy**

The University of Sheffield
Faculty of Engineering
Department of Chemical and Biological Engineering

Sheffield, January 2018

Ad Angelo e Nadia che da sempre credono in me...

Faber est suaue quisque fortunae,
Appius Claudius Caecus, *Sententiae*

ABSTRACT

In this thesis, A₆K, A₉K, G(IKK)₃I-NH₂, the fluorescently FITC-labelled A₉K and G(IKK)₃I-NH₂ amphiphilic cationic peptides have been intensively studied to evaluate their interactions with eukaryotic cell and in particular their selectivity towards cancer cells. A possible usage of these cationic peptides as delivery vectors of small nucleic acids molecules was also investigated. Results showed that A₉K and G(IKK)₃I-NH₂ could bind nucleic acids and selectively carry them in 2D and 3D cancer models. However, only G(IKK)₃I-NH₂ could, once internalised, release its cargo allowing the modulation of gene expression. The toxicity of A₉K and FITC-G(IKK)₃I-NH₂ was further investigated *in vivo* using zebrafish embryos (*Danio rerio*) as animal model. A₉K did not induce developmental changes during embryogenesis unless high concentrations were used (1 – 4 ng, corresponding to 1.25 – 5 mM). FITC-G(IKK)₃I-NH₂ resulted more toxic and induced the embryos' death also at concentration as little as 6.25 pg (corresponding 3.125 μM). However, in both cases, the concentrations needed to induce toxicity in zebrafish were several times higher than the ones used in the optimised peptide-based cellular transfection, where the peptide concentration range was between 30 and 300 nM. Moreover, the peptides uptake was investigated, revealing that one or more active endocytic pathways are responsible for their intracellular internalisation. Overall, the results presented in this thesis gave an important contribution in the field of nanotechnologies, opening the doors to a possible clinical use of these amphiphilic cationic peptides.

ACKNOWLEDGEMENTS

First of all, I would like to thank my supervisor, Dr. Xiubo Zhao, for allowing me to work on this stimulating project and who helped me getting through these four years. Another enormous thank you goes to Dr. Stephen Brown, my second supervisor and wonderful mentor who helped me every single day in this long and sometimes difficult path; he gave me strength when I needed and coped with my craziness. I could not have achieved any of this without him.

I also would like to thank everyone in the Biomedical Science Department who offered me support and guidance, especially Paul Gokhale, Chris Hill and Rob Wilkinson who were incredibly helpful and kind; Lucie N'Koy and the whole SRSF lab for the constant assistance and encouragement.

These four years have been extremely intense and full of incredible moments; I met amazing people who inspired me to become a better person. I therefore would like to thank all the friends I encountered along this tough journey, especially Ana, Steve, Tom and Dharana with whom I share precious and unforgettable moments.

I would like to give a special thank you also to Laura and Pamela who both helped me in the proofreading of several chapters of this masterpiece.

Another huge thank goes to my parents Angelo and Nadia, who never stopped faithfully supporting me and I know will always be there as my anchor.

Finally, last but not least, I would like to thank the most important person of my life; Sian, for her constant support and patience who daily dealt with my stress and desperation but always encouraged me to never give up.

TABLE OF CONTENTS

ABSTRACT	V
ACKNOWLEDGEMENTS	VI
TABLE OF CONTENTS	VII
LIST OF TABLES	XI
LIST OF FIGURES	XII
LIST OF ABBREVIATIONS AND ACRONYMS	XVII
1 INTRODUCTION	19
1.1 OLIGOPEPTIDES: HISTORY, ORIGINS AND CLASSIFICATION.....	19
1.1.2 <i>Neuropeptides</i>	22
1.1.3 <i>Peptide hormones</i>	23
1.1.4 <i>Toxins</i>	24
1.1.5 <i>Antimicrobial peptides (AMPs)</i>	25
1.2. CELL PENETRATING PEPTIDES (CPPS)	32
1.3. BACTERIAL RESISTANCE TO AMPs	33
1.4 <i>DE NOVO</i> SYNTHETIC AMPs; APPROACHES FOR THE DESIGN OF NEW MOLECULES..	35
1.5 ABILITIES OF AMPs: MORE THAN SIMPLY ANTIMICROBIAL AGENTS.....	36
1.5.1 <i>Antifungal activity</i>	36
1.5.2 <i>Antiprotozoal activity</i>	37
1.5.3 <i>Antiviral activity</i>	37
1.5.4 <i>Anticancer activity</i>	38
1.7 CURRENT STRATEGIES AND FUTURE DEVELOPMENTS	41
1.8 RESEARCH MOTIVATION	43
1.9 THESIS OUTLINE	44
2 MATERIALS AND METHODS	45
2.1 PEPTIDES SYNTHESIS AND STOCK SOLUTION PREPARATION	45
2.1.1 <i>Solution preparation</i>	46
2.2 CELL LINES AND CULTURE METHODS.....	46
2.2.1 <i>Cell lines sub-culturing</i>	47
2.2.2 <i>Freezing and thawing procedures</i>	48
2.3 AGAROSE GEL ELECTROPHORESIS	49
2.3.1 <i>Peptide/ODN complex formation</i>	49

2.3.2	<i>Gel preparation</i>	50
2.3.3	<i>Gel running</i>	51
2.4	DNA/RNA TRANSFECTION	51
2.4.1	<i>Cancer cells targeting experiment</i>	53
2.4.2	<i>Confocal microscope</i>	53
2.4.3	<i>3D spheroids</i>	54
2.4.4	<i>siRNAs transfection</i>	54
2.5	MTT ASSAY AND CELL COUNTS	56
2.6	CELL STAINING FOR IMAGING.....	57
2.7	SEM AND TEM TECHNIQUES	58
2.8	ZEBRAFISH HUSBANDRY AND INJECTIONS PROCEDURE.....	61
2.8.1	<i>Adult fish maintenance</i>	61
2.8.2	<i>E3 medium and Tricaine solution</i>	61
2.8.3	<i>Peptides and siGLO microinjections</i>	62
2.8.4	<i>Caudal injections in 4 dpf larvae</i>	63
2.9	ENDOCYTIC PATHWAYS AND RNAi GENOME-WIDE SCREEN.....	64
2.9.1	<i>Internalisation speed of FITC-G(IKK)₃I-NH₂</i>	64
2.9.2	<i>The endocytic cold assay</i>	65
2.9.3	<i>Extracellular peptide acid stripping</i>	66
2.9.4	<i>Time lapse imaging</i>	66
2.9.5	<i>HCT-116 recovery from FITC-G(IKK)₃I-NH₂ challenge</i>	67
2.9.6	<i>RNAi screen to elucidate the peptide uptake in cancer cells</i>	67
2.10	GRAPHIC AND STATISTICAL ANALYSES.....	68
3	A₆K AND A₉K PEPTIDES	69
3.1.	DNA/RNA BINDING ABILITIES <i>IN VITRO</i> AND CELL TRANSFECTION EFFICIENCY	71
3.1.1	<i>Gel electrophoresis</i>	71
3.1.2	<i>ODNs and siRNAs transfection</i>	72
3.1.3	<i>Evaluation of A₉K transfection efficiency in a 3D cancer cellular model</i>	81
3.1.4	<i>FITC- labelled A₉K confirms the transfection abilities of the peptide</i>	86
3.1.5	<i>Functional siRNA transfection</i>	87
3.2.	TOXICITY AND METABOLIC REDUCTION CAUSED BY PEPTIDES EXPOSURE	90
3.2.1	<i>MTT assay</i>	90
3.2.2	<i>Cell counts following exposure to A₆K or A₉K peptides</i>	98
3.2.3	<i>Cell counts following exposure to FITC- A₉K</i>	100

3.3. MITOCHONDRIAL MEMBRANES DRAMATICALLY CHANGE AFTER BOTH A ₆ K AND A ₉ K EXPOSURE	102
3.4. IMAGES ACQUISITION AND ANALYSIS	108
4 G(IKK)₃I-NH₂ PEPTIDE.....	109
4.1 <i>IN VITRO</i> CELL TRANSFECTION EFFICIENCY WITH DNA OR RNA	110
4.1.1 <i>ODNs and siRNAs transfection.....</i>	110
4.1.2 <i>Cell selectivity of G(IKK)₃I-NH₂ in a co-cultured system</i>	116
4.1.3 <i>A study of FITC labelled G(IKK)₃I-NH₂ to determine co-localisation.....</i>	118
4.1.4 <i>Evaluation of G(IKK)₃I-NH₂ transfection efficiency in a 3D cancer cellular model.....</i>	119
4.1.5 <i>Functional siRNAs transfection</i>	123
4.2 TOXICITY AND PHALLOIDIN STAINING	128
4.2.1 <i>Cell counting assay as evaluation of peptide toxic effect</i>	128
4.2.2 <i>Phalloidin staining to enhance the cellular boundaries</i>	131
4.3 ELECTRON MICROSCOPY EXPLORES THE EFFECTS AND INTERACTION OF FITC-G(IKK) ₃ I-NH ₂ WITH CANCER CELLS	135
4.3.1 <i>SEM technique is a reliable instrument for studying cell membranes.....</i>	136
4.3.1 <i>Cellular localisation of FITC-G(IKK)₃I-NH₂ in cancer cells using TEM..</i>	139
4.4 STUDIES TO EVALUATE THE INVOLVEMENT OF ENDOCYTOSIS IN PEPTIDE UPTAKE	143
4.4.1 <i>Internalisation speed of FITC-G(IKK)₃I-NH₂</i>	144
4.4.2 <i>Peptide internalisation using the cold assay to reduce endocytosis.....</i>	149
4.4.3 <i>Acid stripping to remove covalently bound molecules from the membranes</i>	151
4.4.4 <i>Time-lapse videos to show live internalisation of FITC-G(IKK)₃I-NH₂</i>	155
4.4.5 <i>Cancer cells can recover from peptide uptake under favourable conditions</i>	159
5 IN VIVO STUDIES ON DANIO RERIO EMBRYOS.....	162
5.1 ZEBRAFISH IS A VALUABLE ANIMAL MODEL TO STUDY HUMAN GENETICS AND DISEASES.	162
5.2 DANIO RERIO EMBRYOS AND THEIR EMPLOYMENT IN TOXICOLOGY.	163
5.3 THE FIRST 5 DAYS OF ZEBRAFISH EMBRYOGENESIS.	164
5.4 MICROINJECTIONS OF A ₉ K PEPTIDE IN ZEBRAFISH EMBRYOS	166
5.5 MICROINJECTIONS OF FITC-G(IKK) ₃ I-NH ₂ PEPTIDE IN ZEBRAFISH EMBRYOS ...	171
5.6 INJECTIONS OF siRNAs ALONE OR COMPLEXED WITH FITC-G(IKK) ₃ I-NH ₂	174

5.6.1	<i>Microinjections of siGLO to estimate the siRNA toxic threshold</i>	174
5.6.2	<i>Microinjections of FITC-G(IKK)₃I-NH₂ and siGLO complexes</i>	176
5.7	IN VIVO CAUDAL INJECTIONS OF FITC-G(IKK) ₃ I-NH ₂ PEPTIDE TO EVALUATE THE PEPTIDE DISTRIBUTION ACROSS THE ANIMAL.....	180
6	RNAI SCREENS TO IDENTIFY ENDOCYTIC PATHWAYS INVOLVED IN PEPTIDE CELLULAR UPTAKE	184
6.1	ASSAY DEVELOPMENT SCREENING FOR FITC-G(IKK) ₃ I-NH ₂	186
6.2	HIGH-CONTENT GENOME SCREEN ON FITC-G(IKK) ₃ I-NH ₂	193
6.3	RNAI MINI-SCREEN WITH FITC-A ₉ K.....	198
7	DISCUSSION AND CONCLUSIONS	205
7.1.	INTRODUCTORY BACKGROUND	205
7.2.	ACHIEVEMENTS OF THE PROJECT.....	207
7.2.1	<i>What was previously known</i>	208
7.2.2	<i>The peptides and their impact on the cells' metabolism and proliferation</i> .	210
7.2.3	<i>Could the peptides have a role as delivery vectors of nucleic acids molecules?</i>	213
7.2.4	<i>Exploiting the peptides fluorescence to explore the interactions with the cells</i>	216
7.2.5	<i>RNAi screens to elucidate the endocytic pathway involved in the peptide uptake</i>	219
7.2.6	<i>In vivo toxicity and bio distribution in Danio rerio embryos</i>	223
7.3.	DISCUSSION.....	225
7.3.1	<i>Membranolytic or mitochondrial target?</i>	225
7.3.2	<i>Endocytosis as mechanism of cellular internalisation</i>	227
7.3.3	<i>RNAi screen reveals the importance of having functional recycling and vesicle trafficking systems</i>	231
7.3.4	<i>Cancer cell selectivity is maintained</i>	234
7.3.5	<i>Antibodies binding as a possible new strategy to kill cancer cells</i>	235
7.3.6	<i>The ability of efficiently deliver nucleic acid molecules in cancer cells</i>	236
7.3.6	<i>In vivo toxicity</i>	238
7.3.7	<i>Caudal injections of FITC-G(IKK)₃I-NH₂ in 4 dpf larvae leaked out</i>	243
7.4.	CONCLUSIONS, FUTURE WORKS AND PERSPECTIVES	244
8	REFERENCES	246

LIST OF TABLES

TABLE 1. EXAMPLES OF NATURAL OLIGOPEPTIDES	21
TABLE 2. CLASSIFICATION OF AMPS ACCORDING TO THEIR SECONDARY STRUCTURES	26
TABLE 3. HCT-116 AND HDFs CELL NUMBER EVALUATED WITH HIGH-CONTENT MICROSCOPY AFTER EXPOSURE TO SODIUM CHROMATE (NA ₂ CRO ₄)	129
TABLE 4. LIST OF THE GENES FOR WHICH siRNAs WERE SELECTED IN THE ASSAY DEVELOPMENT SCREENING AS POSSIBLE “HITS” FOR FITC-G(IKK) ₃ I-NH ₂ PEPTIDE.....	187
TABLE 5. LIST OF THE GENES FOR WHICH siRNAs WERE SELECTED IN THE MINI-SCREEN FOR FITC-A ₉ K PEPTIDE	198
TABLE 6. LIST OF GENES IN ASD2 siRNA LIBRARY	202
TABLE 7. LIST OF GENES IN THE TRAFFIC-OME siRNA LIBRARY	203
TABLE 8. BACTERICIDAL EFFECT OF A ₆ K, A ₉ K AND G(IKK) ₃ I-NH ₂ EXPRESSED AS MINIMUM INHIBITORY CONCENTRATION (MIC ₅₀)	208
TABLE 9. INHIBITORY EFFECT OF A ₉ K AND G(IKK) ₃ I-NH ₂ ON DIFFERENT HUMAN CANCER CELL LINES EXPRESSED AS INHIBITORY CONCENTRATION (IC ₅₀)	209
TABLE 10. INHIBITORY EFFECT OF A ₉ K AND G(IKK) ₃ I-NH ₂ ON DIFFERENT NORMAL MAMMALIAN CELL LINES EXPRESSED AS INHIBITORY CONCENTRATION (IC ₅₀) OR ERYTHROCYTES LYSIS (EC ₅₀)	209
TABLE 11. METABOLIC INHIBITORY EFFECT OF A ₆ K AND A ₉ K EVALUATED IN A431 EPITHELIAL CANCER CELLS AND HDF ₅ HUMAN FIBROBLASTS	210
TABLE 12. EFFECTS ON CELL VIABILITY OF G(IKK) ₃ I-NH ₂ AND FITC-G(IKK) ₃ I-NH ₂ EVALUATED IN HCT-116 COLON CANCER CELLS AND HDF ₅ HUMAN FIBROBLASTS ..	212
TABLE 13. <i>IN VIVO</i> TOXICITY OF A ₉ K AND FITC-G(IKK) ₃ I-NH ₂ ON ZEBRAFISH EMBRYOS.....	223
TABLE 14. <i>IN VIVO</i> TOXICITY OF siGLO RED ON ZEBRAFISH EMBRYOS	224

LIST OF FIGURES

FIGURE 1. ODN BINDING ASSAY FOR PEPTIDES	72
FIGURE 2. A ₉ K EFFICIENCY IN DELIVERY FLUORESCENTLY LABELLED ODNs INTO EPITHELIAL CANCER CELLS	73
FIGURE 3. CONFOCAL EXAMINATION OF THE INTRACELLULAR LOCALISATION OF FLUORESCENT ODN MOLECULES AFTER TRANSFECTION WITH A ₉ K PEPTIDE.....	74
FIGURE 4. STACK ANALYSIS OF SEQUENTIAL CONFOCAL IMAGES OF FLUORESCENT ODN MOLECULES IN A431 CANCER CELLS	75
FIGURE 5. A ₉ K DELIVERY OF FLUORESCENTLY LABELLED ODNs INTO A NON-CANCER CELL LINE	76
FIGURE 6. A ₉ K DELIVERY OF FLUORESCENTLY LABELLED siRNA MOLECULES INTO EPITHELIAL CANCER CELLS	78
FIGURE 7. CONFOCAL EXAMINATION OF THE INTRACELLULAR LOCALISATION OF FLUORESCENT siRNA MOLECULES AFTER TRANSFECTION WITH A ₉ K PEPTIDE	79
FIGURE 8. STACK ANALYSIS OF SEQUENTIAL CONFOCAL IMAGES OF FLUORESCENT siRNA MOLECULES IN A431 CANCER CELLS	80
FIGURE 9. A ₉ K DELIVERY OF FLUORESCENT siRNA INTO FIBROBLASTS	81
FIGURE 10. A ₉ K TRANSFECTION OF FLUORESCENTLY LABELLED siRNA MOLECULES INTO HCT-116 CANCER CELLS	83
FIGURE 11. A ₉ K DELIVERY OF FLUORESCENTLY LABELLED siRNA MOLECULES IN TUMOUR SPHEROIDS	84
FIGURE 12. LIGHT-SHEET MICROSCOPY TO EVALUATE THE PENETRATION OF A ₉ K WHEN TRANSFECTING 3D CANCER MODELS	85
FIGURE 13. ORTHOGONAL VIEWS OF HCT-116 SPHEROIDS SHOWING THE LOCATION OF siGLO siRNAs IN XYZ SPATIAL COORDINATES	85
FIGURE 14. SUBCELLULAR CO-LOCALISATION OF INTERNALISED siRNA AND FLUORESCENTLY LABELLED A ₉ K	86
FIGURE 15. siRNA DELIVERY AND KNOCK DOWN EFFICIENCY OF A ₉ K ON A431 CELLS. .	88
FIGURE 16. siRNA DELIVERY AND KNOCK DOWN EFFICIENCY OF A ₉ K ON HCT-116 CELLS.....	89

FIGURE 17. ASSESSMENT OF A ₆ K ACTIVITY USING THE MTT ASSAY PERFORMED ON A431 AND HDFs FOR 24 HRS	92
FIGURE 18. ASSESSMENT OF A ₆ K ACTIVITY USING THE MTT ASSAY PERFORMED ON A431 AND HDFs FOR 48 HRS	93
FIGURE 19. ASSESSMENT OF A ₆ K ACTIVITY USING THE MTT ASSAY PERFORMED ON A431 AND HDFs FOR 72 HRS	94
FIGURE 20. ASSESSMENT OF A ₉ K ACTIVITY USING THE MTT ASSAY PERFORMED ON A431 AND HDFs FOR 24 HRS	95
FIGURE 21. ASSESSMENT OF A ₉ K ACTIVITY USING THE MTT ASSAY PERFORMED ON A431 AND HDFs FOR 48 HRS	96
FIGURE 22. ASSESSMENT OF A ₉ K ACTIVITY USING THE MTT ASSAY PERFORMED ON A431 AND HDFs FOR 72 HRS	97
FIGURE 23. A431 CELL NUMBER EVALUATED WITH HIGH-CONTENT MICROSCOPY AFTER EXPOSURE TO A ₆ K AND A ₉ K PEPTIDES	99
FIGURE 24. HIGH-CONTENT MICROSCOPY OF CANCER CELLS EXPOSED TO A FLUORESCENT PEPTIDE	100
FIGURE 25. HCT-116 CELL NUMBER EVALUATED WITH HIGH-CONTENT MICROSCOPY AFTER EXPOSURE TO FITC-A ₉ K PEPTIDE	101
FIGURE 26. MITOCHONDRIAL MORPHOLOGY OF CANCER CELLS FOLLOWING PEPTIDE EXPOSURE	103
FIGURE 27. MITOCHONDRIAL MORPHOLOGY OF CANCER CELLS FOLLOWING FLUORESCENT PEPTIDE EXPOSURE	104
FIGURE 28. MITOCHONDRIAL MEMBRANE POTENTIAL ($\Delta\Psi_M$) STATUS OF CANCER CELLS FOLLOWING PEPTIDE EXPOSURE	105
FIGURE 29. QUANTITATIVE ANALYSES OF $\Delta\Psi_M$ VARIATION FOLLOWING PEPTIDE EXPOSURE	106
FIGURE 30. QUANTITATIVE ANALYSES OF $\Delta\Psi_M$ VARIATION CAUSED BY A ₆ K EXPOSURE.....	107
FIGURE 31. QUANTITATIVE ANALYSES OF $\Delta\Psi_M$ VARIATION CAUSED BY A ₉ K EXPOSURE.....	108
FIGURE 32. G(IKK) ₃ I-NH ₂ EFFICIENCY IN DELIVERING FLUORESCENTLY LABELLED ODNs INTO EPITHELIAL CANCER CELLS	111
FIGURE 33. G(IKK) ₃ I-NH ₂ EFFICIENCY IN DELIVERY OF FLUORESCENTLY LABELLED ODNs INTO A NON-CANCER CELL LINE	112

FIGURE 34. G(IKK) ₃ I-NH ₂ EFFICIENCY IN DELIVERY OF FLUORESCENTLY LABELLED siRNA MOLECULES INTO EPITHELIAL CANCER CELLS	113
FIGURE 35. G(IKK) ₃ I-NH ₂ EFFICIENCY IN DELIVERY OF FLUORESCENTLY LABELLED siRNA MOLECULES INTO COLON CANCER CELLS	114
FIGURE 36. G(IKK) ₃ I-NH ₂ EFFICIENCY IN DELIVERY OF FLUORESCENTLY LABELLED siRNA MOLECULES INTO A NON-CANCER CELL LINE	115
FIGURE 37. G(IKK) ₃ I-NH ₂ DELIVERY OF FLUORESCENTLY LABELLED siRNA MOLECULES INTO A CO-CULTURED SYSTEM	117
FIGURE 38. SUBCELLULAR CO-LOCALISATION OF INTERNALISED siRNA MOLECULES AND FLUORESCENTLY LABELLED G(IKK) ₃ I-NH ₂	119
FIGURE 39. G(IKK) ₃ I-NH ₂ EFFICIENCY IN DELIVERY OF FLUORESCENTLY LABELLED siRNA MOLECULES INTO 3D CANCER MODELS	121
FIGURE 40. LIGHT-SHEET MICROSCOPY TO EVALUATE THE PENETRATION OF G(IKK) ₃ I-NH ₂ IN 3D CANCER MODELS	122
FIGURE 41. siRNA DELIVERY AND KNOCK DOWN EFFICIENCY OF G(IKK) ₃ I-NH ₂ ON A431 CELLS	124
FIGURE 42. siRNA DELIVERY AND KNOCK DOWN EFFICIENCY OF FITC-G(IKK) ₃ I-NH ₂ ON HCT-116 CELLS	126
FIGURE 43. KNOCK DOWN EFFICIENCY OF DF1 AND FITC-G(IKK) ₃ I-NH ₂ ON COLON CANCER CELLS	127
FIGURE 44. HCT-116 AND HDFs CELL NUMBER EVALUATED WITH HIGH-CONTENT MICROSCOPY AFTER EXPOSURE TO G(IKK) ₃ I-NH ₂	129
FIGURE 45. HCT-116 AND HDFs CELL NUMBER EVALUATED WITH HIGH-CONTENT MICROSCOPY AFTER EXPOSURE TO FITC-G(IKK) ₃ I-NH ₂	130
FIGURE 46. HCT-116 AND HDFs PHALLOIDIN STAINING EVALUATED WITH HIGH-CONTENT MICROSCOPY AFTER EXPOSURE TO FITC-G(IKK) ₃ I-NH ₂	133
FIGURE 47. HCT-116 AND HDFs CELLS EXPOSED TO 50 μM OF FITC-G(IKK) ₃ I-NH ₂	134
FIGURE 48. SEM IMAGES SHOWING THE MORPHOLOGY OF CANCER CELLS FOLLOWING EXPOSURE TO FITC-G(IKK) ₃ I-NH ₂	137
FIGURE 49. HIGHER MAGNIFICATION SEM IMAGES SHOWING CHANGES IN THE PLASMA MEMBRANE MORPHOLOGY OF CANCER CELLS FOLLOWING EXPOSURE TO FITC-G(IKK) ₃ I-NH ₂	138

FIGURE 50. TEM IMAGES OF CANCER CELLS FOLLOWING 3 HRS EXPOSURE TO FITC-G(IKKK) ₃ I-NH ₂ AND ANTI-FITC ANTIBODY CONJUGATED WITH 10 NM AU NANOPARTICLES	141
FIGURE 51. TEM IMAGES OF CANCER CELLS FOLLOWING 24 HRS EXPOSURE TO FITC-G(IKKK) ₃ I-NH ₂ AND ANTI-FITC ANTIBODY CONJUGATED WITH 10 NM AU NANOPARTICLES	142
FIGURE 52. TEM IMAGES OF CANCER CELLS FOLLOWING 24 HRS EXPOSURE TO FITC-G(IKKK) ₃ I-NH ₂ AND ANTI-FITC ANTIBODY CONJUGATED WITH 10 NM AU NANOPARTICLES	145
FIGURE 53. HCT-116 CELLS EXPOSED FOR 24 HRS TO FITC-G(IKKK) ₃ I-NH ₂	146
FIGURE 54. FITC-G(IKKK) ₃ I-NH ₂ INTERNALISATION EVALUATED ON FIBROBLASTS AT DIFFERENT TIME POINTS	147
FIGURE 55. HDFs EXPOSED FOR 24 HRS TO FITC-G(IKKK) ₃ I-NH ₂	148
FIGURE 56. THE PEPTIDE UPTAKE IS BLOCKED IN A COLD ENVIRONMENT	150
FIGURE 57. QUANTITATIVE ANALYSIS OF FITC AVERAGE INTENSITY PER CELL IN UNWASHED AND WASHED CELLS	153
FIGURE 58. ACID WASH REMOVAL OF NON-COVALENTLY BOUND PEPTIDE MOLECULES FROM THE CELL MEMBRANE	154
FIGURE 59. LIVE TIME-LAPSE IMAGING SHOWING PEPTIDE UPTAKE IN CANCER CELLS ...	157
FIGURE 60. DIFFERENCES IN BRIGHT FIELD AND FLUORESCENCE ACQUISITIONS	158
FIGURE 61. CANCER CELLS CAN RECOVER FROM FITC-G(IKKK) ₃ I-NH ₂ UPTAKE	160
FIGURE 62. MICROINJECTION OF A ₉ K INDUCES DOSE-DEPENDENT TOXICITY IN WILD TYPE ZEBRAFISH EMBRYOS	167
FIGURE 63. MORPHOLOGICAL CHANGES IN 1 DPF EMBRYOS INJECTED WITH A ₉ K	169
FIGURE 64. MORPHOLOGICAL CHANGES IN 3 DPF EMBRYOS INJECTED WITH A ₉ K	170
FIGURE 65. FITC-G(IKKK) ₃ I-NH ₂ MICROINJECTION INDUCES TOXICITY BY 5 HPF IN WILD TYPE ZEBRAFISH EMBRYOS	172
FIGURE 66. FITC-G(IKKK) ₃ I-NH ₂ MICROINJECTIONS INDUCE SEVERE TOXICITY IN WILD TYPE ZEBRAFISH EMBRYOS	173
FIGURE 67. MICROINJECTIONS OF FLUORESCENT siRNA IN ZEBRAFISH EMBRYOS	175
FIGURE 68. MICROINJECTION OF FLUORESCENT siRNA INDUCES DOSE-DEPENDENT TOXICITY IN WILD TYPE ZEBRAFISH EMBRYOS	176
FIGURE 69. MICROINJECTIONS OF FITC-G(IKKK) ₃ I-NH ₂ AND FLUORESCENT siRNA COMPLEXES IN ZEBRAFISH EMBRYOS	177

FIGURE 70. MICROINJECTIONS OF FITC-G(IKK) ₃ I-NH ₂ AND FLUORESCENT siRNA COMPLEXES IN ZEBRAFISH EMBRYOS	178
FIGURE 71. MICROINJECTIONS OF FITC-G(IKK) ₃ I-NH ₂ PEPTIDE COMPLEXED WITH siRNA HAVE A REDUCED TOXIC EFFECT IN WILD TYPE ZEBRAFISH EMBRYOS	179
FIGURE 72. MICROINJECTIONS OF FLUORESCENT siRNA ALONE OR COMPLEXED WITH FITC-G(IKK) ₃ I-NH ₂ PEPTIDE INDUCE TOXICITY BY 5 HPF IN WILD TYPE ZEBRAFISH EMBRYOS	180
FIGURE 73. LIGHT SHEET IMAGES OF FITC AND FITC-G(IKK) ₃ I-NH ₂ CAUDAL INJECTIONS IN 4 DPF LARVAE	182
FIGURE 74. LIGHT SHEET IMAGES OF A ZEBRAFISH HEAD, TRUNK AND DETAILED DORSAL VESSEL AFTER FITC CAUDAL INJECTIONS IN 4 DPF LARVAE	183
FIGURE 75. HCT-116 CELL NUMBER EVALUATED WITH HIGH-CONTENT MICROSCOPY AFTER RNAI AND FITC-G(IKK) ₃ I-NH ₂ EXPOSURE	190
FIGURE 76. BOTTOM 5% OF HCT-116 CELLS NUMBER COUNT EVALUATED WITH HIGH-CONTENT MICROSCOPY AFTER KINASES KNOCK DOWN VIA RNAI AND FITC-G(IKK) ₃ I-NH ₂ EXPOSURE	191
FIGURE 77. VARIATION IN THE FLUORESCENCE INTENSITY EVALUATED WITH HIGH-CONTENT MICROSCOPY IN HCT-116 CANCER CELLS AFTER RNAI AND FITC-G(IKK) ₃ I-NH ₂ EXPOSURE	192
FIGURE 78. Z-SCORES DISTRIBUTION AND STRING MAP OF PUTATIVE HITS GENES	194
FIGURE 79. SCHEMATIC REPRESENTATION INTERACTIONS BETWEEN THE HITS FOUND IN THE SCREEN	195
FIGURE 80. HCT-116 CELL NUMBER EVALUATED WITH HIGH-CONTENT MICROSCOPY AFTER RNAI AND FITC-A ₉ K EXPOSURE	200
FIGURE 81. VARIATION IN THE FLUORESCENCE INTENSITY EVALUATED WITH HIGH-CONTENT MICROSCOPY IN HCT-116 CANCER CELLS AFTER RNAI AND FITC-A ₉ K EXPOSURE	201
FIGURE 82. SCHEMATIC REPRESENTATION OF A ₉ K SELF-ASSEMBLING AND INTERACTING WITH NUCLEIC ACID MOLECULES	213
FIGURE 83. SCHEMATIC REPRESENTATION OF THE HITS' MAIN FUNCTIONS IN THE CELL ENDOCYTOSIS	222

LIST OF ABBREVIATIONS AND ACRONYMS

- $\Delta\psi_m$ – Mitochondrial membrane potential
1dpf – 1 day post fertilisation
3dpf – 3 days post fertilisation
5hpf – 5 hours post fertilisation
ACPs – Anticancer peptides
AMPs – Antimicrobial peptides
CACs – Critical aggregation concentrations
CCPs – Cell penetrating peptides
CP – Choroid plexus
DF1 – DharmaFECT1
DMEM – Dulbecco's Modified Eagle's Medium
DMSO – Dimethyl sulfoxide
ER – Endoplasmic reticulum
FAM – Carboxyfluorescein
FITC – Fluorescein isothiocyanate
MTT – 3-(4,5-Dimethylthiazol-2-yl)-2,5-diphenyltetrazolium bromide
ODNs – Oligonucleotides
P/S – Penicillin/Streptomycin
PBS – Phosphate Buffered Saline
SLPs – Surfactant-like peptides
RNAi – RNA-mediated interference
siRNA – small interference RNA
SNAREs – SNAP (Soluble NSF Attachment Protein) Receptors
TGN – Trans Golgi Network
UHQ – Ultra-High Quality

1 INTRODUCTION

This PhD project is focused on studying the interactions between small cationic amphipathic peptides and different living models (Human 2D and 3-D cell culture and *Danio rerio* embryos). The main purpose of this thesis is to highlight the biological mechanisms involved in peptide uptake and distribution, mode of action and whether there are any phenotypic changes caused by the peptides. Numerous experimental approaches are used; including imaging (wide-field, confocal, light-sheet fluorescent microscopy, SEM and TEM), high-throughput screening, in vitro and in vivo toxicity assays, RNAi, and nucleic acids transfections. The results obtained in this thesis will be helpful in determining the efficiency of peptides as therapeutic tools in a wide range of biomedical applications.

In the following sections, an overview of what has been discovered so far regarding the origin, classification and modes of action of small peptides, together with exhaustive examples of drugs and successful treatments currently used in medicine with peptides as therapeutic agents.

1.1 Oligopeptides: history, origins and classification

Peptides are molecules composed of short chains of amino acids. If the total sequence length does not exceed 50 residues they are normally called oligopeptides which differ from larger polypeptides (proteins) for both physicochemical and biological properties. Natural oligopeptides are ubiquitously expressed in prokaryotic and eukaryotic species and considered essential biochemical regulators involved in almost every vital process. Oligopeptides can be divided into several functional classes: the most abundant are neuropeptides, hormones, toxins and antimicrobials (see Table 1).

Interest in these small molecules increases every year as shown by the number of publications (>50000) listed in PubMed. Hundreds of oligopeptides have been identified and their structure fully characterised. Many online data banks are available; the EROP-Moscow database ¹ is one of the most complete, where almost 15000 oligopeptides are

classified according to their structure, function or species identification. Other databases are more specific and collect data only from one class of oligopeptides; for example, NeuroPep is the most complete database for neuropeptides ², while CAMP_{R3}, Collection of Anti-Microbial Peptides ³ and ADP, The Antimicrobial Peptide Database ⁴ focus on antimicrobial peptides. CancerPPD ⁵ instead, collects data from verified anticancer peptides (ACPs) and anticancer proteins.

In the following sections, some of the most important studied classes of oligopeptides will be presented. More attention will be given to the antimicrobial peptides and their relevance in anticancer therapies since this crucial aspect provided inspiration for this PhD thesis.

Table 1. Examples of natural oligopeptides. Legend: HM hormone; NP neuropeptide; TX toxin; AM antimicrobial

Peptide	Type	Sequence	Function	Species	Reference
α-amanitin	TX	IWGIGCNP	Inhibition of RNA polymerase II	<i>Amanita</i>	Hallen et al., ⁶
α-Defensin HNP3	AM	DCYCRIPACIAGERRYGTTCIYQG RLWAFCC	Antibiotic, anti-fungi and antiviral activity	<i>H. sapiens</i>	Hill et al., ⁷
Angiotensin I	HM	DRVYIHPFHL	Regulate volume and mineral balance of body fluids	Animalia	Basso et al., ⁸
β-endorphin	NP	YGGFMTSEKSTPLVTLFKNAII KNAYKKGE	Reduce body stress and maintain homeostasis	<i>H. sapiens</i>	Dalayeun et al., ⁹
Crotamin	TX	YKQCHKKGGHCFDKEKICLPSS DFGKMDCRWRWKCKKGS	Analgesic and myotoxic	<i>C.durissus terrificus</i>	Nicastro et al., ¹⁰
Gastrin	HM	WLEEEEEAYGWMDF	Stimulation of HCl secretion by parietal cells in gastric mucosa	<i>H. sapiens</i>	Dockray et al., ¹¹
Glucagon	HM	HSQGTFPSDYSKYLDSRRAQDF VQWLMNT	Promotion hydrolysis of glycogen and lipids; increase the blood sugar level	Animalia	Jiang et al., ¹²
LL-37	AM	LLGDFFRKSKEKIGKEFKRIVQRI KDFLRNLVPRTES	Antimicrobial activity against several Gram-positive and Gram-negative bacteria, spirochaete and yeast	<i>H. sapiens</i>	Dürr et al., ¹³
Magainin-I	AM	GIGKFLHSAGKFGKAFVGEIMKS	Growth inhibition of numerous of bacteria and fungi species and induction of osmotic lysis in protozoa	<i>X. laevis</i>	Zasloff ¹⁴
Melittin	AM	GIGAVLKVLTTGLPALISWIKRK RQQ	Strong haemolytic activity	<i>A. mellifera</i>	Raghuraman et al., ¹⁵
Oxytocin	NP	CYIQNCPLG	Cause the contraction of the uterus smooth muscles and mammary glands	Mammalia	Ross et al., ¹⁶
Substance P	NP	RPKPQQFFGLM	Respond to painful or noxious stimuli. Associated with inflammatory processes and pain transmission	Mammalia	Harrison et al., ¹⁷

1.1.2 Neuropeptides

The term “neuropeptides” refers to small molecules expressed and regulated exclusively by neurons that are involved in the neural chemical signalling mediated by receptors in the brain ¹⁸. The neuronal system is composed of an intricate cellular network that, to work efficiently, requires organised communication skills. This can be done via special chemical signals control released by neurons. The signalling molecules are very heterogeneous, starting from simple gases (such as NO) ¹⁹ and finishing with neuropeptides which are the largest and most diverse class of molecules that act like long range neurotransmitters, autocrine or paracrine regulators or hormones ¹⁸. The secretion of neuropeptides follows a strictly regulated pathway and the molecules, are controlled for release by external stimuli (for example increasing of intracellular Ca²⁺) ²⁰. So far, more than 100 genes in mammals (90 in humans) have been reported to encode for neuropeptides. These can be further divided in subfamilies, according to their precursor structure or function. Neuropeptides, but oligopeptides more in general, have a very complex biosynthesis, and they derive from larger inactive polypeptidic precursors, which need one or more post-translational processes to become functional. In some cases, one precursor can produce many different bioactive peptides, via differentiated cleavages in accordance to the tissue localisation. For instance, the processing of proopiomelanocortin (POMC) precursor gives a wide array of bioactive products in a tissue-specific manner. The encoded protein is expressed in corticotroph cells of the anterior pituitary gland, in the arcuate nucleus, in the nucleus tractus solitarius of the brainstem (NTS) and in several peripheral tissues. It can be cleaved on different sites producing adrenocorticotrophins (ACTH), melanocyte-stimulating hormones (MSHs), β -lipotropins and β -endorphins, which all have important roles in pain and energy homeostasis (appetite regulation), melanocyte stimulation, immune system modulation and sexual behaviour. Mutations in POMC gene have been associated with early onset obesity, adrenal insufficiency and red hair pigmentation ²¹.

Many neuropeptides are hormones, expressed by neurons but then transported through the bloodstream to distant targeted tissues or organs. β -endorphin, for example, is secreted by arcuate neurons and derives from a post-translational cleavage of POMC precursor. It travels via the cerebral spinal fluid in the spinal cord to the peripheral

nervous system and to other different body locations. It can also be locally released in the brain, in areas such as the amygdala and the hypothalamus. β -endorphin has a wide variety of functions; from physiological to behavioural, such as reducing body stress, modulating pain perception, regulating food intake, controlling sexual behaviour and inducing euphoria or reward effects ²². Alterations in the hormone levels can often be associated with mental disorders like depression ²³ and schizophrenia ²⁴, or in alcohol and drug addiction ^{25,26}.

1.1.3 Peptide hormones

Within an organism, cells at distant locations easily communicate with each other thanks to small signalling molecules that can travel via the circulatory system. These molecules, secreted by endocrine glands, are called hormones and are extremely important in the maintenance of the body homeostasis. Many oligopeptides have hormone function and are produced by several organs in the body; when produced by the neurons of hypothalamus and hypophysis (or pituitary gland) they are called neuropeptides (see previous paragraph), otherwise they are just defined as “peptide hormones”.

Organs that form part of the digestive system such as the stomach, liver and pancreas secrete peptide hormones in order to regulate the digestion and movements of the food through the gastrointestinal tract. Gastrin from the stomach, angiotensin-I from the liver or glucagon from the pancreas are just few examples, which will be discussed in the following paragraphs.

Gastrin is a peptide hormone produced by gastrin (G) cells: trans-epithelial transducing cells of the gastric antral mucosa. It is a stimulant of acid secretions (HCl) through paracrine mechanisms and controls the proliferation of gastric epithelial cells ¹¹. For this reason, when deregulated, gastrin could increase the risk of development of several gastrointestinal cancers, including gastric cancer ²⁷.

Angiotensin-I is secreted by the liver and derived from the precursor angiotensinogen. It is cleaved by renin; an enzyme produced by the kidneys, and together with other

hormones, is involved in the renin-angiotensin-system (RAS). The main function of RAS is to regulate the water and salt retention of the body via vasoconstriction⁸. Angiotensin-I has no direct biological activity and its only purpose is to work as substrate for the angiotensin-converter enzyme (ACE), which cleaves the molecule in angiotensin-II. Inappropriate activations of RAS provoke renal and cardiovascular diseases such as hypertension,²⁸ atherosclerosis²⁹ and abdominal aortic aneurysms³⁰.

Glucagon is a peptide hormone derived from the precursor proglucagon. It is processed and secreted in the pancreatic α -cells of the islets of Langerhans, and once released in the bloodstream it stimulates the hepatic glucose release to increase the blood glycaemic levels. Together with insulin, glucagon is responsible for the glucose homeostasis in the body¹². Elevated levels of this peptide hormone are associated with pancreatic cancer³¹, diabetes mellitus³² and glucagonoma³³, while reduced levels cause hypoglycaemia which is often linked to diabetes³⁴.

1.1.4 Toxins

An oligopeptide could be defined as a toxin if it has poisonous effects once absorbed by an organism due to its interactions with other biomolecules. Toxins are found in some species of fungi but more commonly in the venom of several species of insect, snakes, scorpions and spiders.

Amongst the fungi, the genus *Amanita* is definitely the most dangerous, accountable for more than 90% of the fatalities caused by mushroom poisoning events in humans, and in particular the Death Cap (*Amanita phalloides*) is responsible for 50% of all cases, normally because it is mistaken for an edible mushroom⁶. The *Amanita* mushrooms contain three classes of toxins: amatoxins, phallotoxins and virotoxins. The first group is composed by at least 9 bicyclic octapeptides (included α -amanitin), which are extremely toxic. Amatoxins are resistant to heat therefore remain toxic whether eaten raw or cooked. Once ingested and absorbed by the liver, they strongly inhibit RNA polymerase II causing a slow but irreversible damage of the hepatocytes³⁵. Phallotoxins instead are bicyclic heptapeptides consisting of at least 7 compounds (including phalloidin). Their main mechanism of action is the stabilization of F-actin preventing

the depolymerisation and degradation, but due to poor absorption phallotoxins are poisonous only when administered parenterally. Phalloidin, due to its great affinity for F-actin is widely used in microscopy, conjugated with various fluorophores to selectively label actin^{36, 37}. Finally, Virotoxins are a class of 5 monocyclic oligopeptides. They are very similar to phallotoxins in terms of chemical structure, toxicity and biological action suggesting that these two classes probably share common precursor pathways³⁸.

Another interesting example of toxin peptide is Crostamine, the major toxic component of venom of the South American rattlesnake *Crotalus durissus terrificus*. It induces hind limbs spastic paralysis in rodents, recognizable by a typical stretched posture with the limbs completely immobilised³⁹. For this reasons Crostamine is often considered a myotoxin. Pharmacological studies have shown that this toxin interacts with Na⁺ channels and induces membrane depolarisation in skeletal muscles cells by increasing the Na⁺ permeability¹⁰. Low doses of Crostamine have instead an analgesic activity⁴⁰. Recently, Crostamine regained interest when studies reported that this small molecule has a much wider variety of functions including antimicrobial, antifungal and anticancer activities. Therefore it is sometimes considered like an antimicrobial peptide or a cell penetrating peptide as well⁴¹.

1.1.5 Antimicrobial peptides (AMPs)

Among the several categories of oligonucleotides, the one composed by antimicrobial peptides (AMPs) is certainly the most appealing from a therapeutic point of view. These small molecules are ubiquitous in nature and can be found in almost every living organism⁴². AMPs are essential components of the host defence mechanisms against infections. They can directly kill microbes via membrane disruption or intracellular targets, and indirectly via modulation of the innate immune response⁴³⁻⁴⁵. The first AMPs were discovered in the late 80's thanks to the pioneering works of Boman, Zasloff and Lehrer, who independently discovered and purified insect Cecropins, amphibian Magainins and mammalian Defensins, respectively^{14, 46, 47}. Despite being a heterogeneous group in terms of length, amino acid composition or secondary structure, AMPs share some common fixtures, such as a significant proportion of hydrophobicity,

a net charge or a relative small size ⁴⁸. The classical way to categorise AMPs, is to follow their secondary structure, such as α -helical, β -sheet, extended or loop which are the commonly divided groups (Table 2) ⁴⁹.

Table 2. Classification of AMPs according to their secondary structures ⁴⁹.

Structure	Peptide	Tissue	Species
α-helical	Buforins, Cecropins, Dermcidin LL-37 Magainins Melittin	Stomach Haemolymph Sweat glands Leukocytes Skin Apitoxin (bee venom)	Bufo bufo gargarizans Hyalophora cecropia Homo sapiens Homo sapiens Xenopous laevis Apis mellifera
β-sheet	α -defensins β -defensins θ -defensins Lactoferricin B Tachyplesin	Neutrophils, Paneth cells Leukocytes, epithelial cells Leukocytes Mammary glands Haemolymph	Mammalia Mammalia Macaca mulata Bos taurus Tachyplesus tridentatus
Extended	Histatins Indolicidin Tritrpticin	Salivary glands Leukocytes Leukocytes	Homo sapiens Bos taurus Sus scrofa
Loop	Bactenecins Thanatin	Neutrophils Haemolymph	Bos taurus Podisus maculiventris

1.1.5.1 AMPs' secondary structures

Most of the AMPs fall in the first two groups (α -helical and β -sheet peptides). α -helical AMPs, the most abundant and broadly studied, are generally linear with charged and the hydrophobic residues positioned at opposite faces of the helix. To reduce the toxicity towards host cells, these peptides often exist in aqueous solution as unstructured monomers, folding into α -helical structures only when in contact with bacterial lipid membranes ⁵⁰.

β -sheet peptides are characterized by rigid anti-parallel β -hairpin-like structures due to the presence of disulphide bonds between conserved cysteine residues. Different from α -helical AMPs, β -sheet peptides are more ordered in aqueous solution and do not drastically change conformation upon membrane interaction ⁵¹.

A smaller proportion of natural AMPs belong to the groups of extended peptides. Extended AMPs are so called because they lack regular secondary structures and adopt instead more variable conformations. They have an unusually high proportion of amino acids such as arginine, tryptophan, proline and/or histidine residues. Many of the extended peptides are not membrane active but instead have intracellular targets ⁴⁸.

Finally, the loop peptides are characterised by a distinct loop structure given by the presence of a single (either disulfide, amide or isopeptide) bond ⁴⁹.

AMPs are usually cationic due to the presence of positively charged residues such as lysine or arginine but some of them, like the human Dermcidin ⁵², are anionic (AAMPs). The net positive charge favours the initial electrostatic interactions with the negatively charged microbial membranes, while the amphipathicity promotes the insertion into the bacterial membranes leading to cell disruption ⁵³. AAMPs mode of action is still not completely understood, but some evidence suggests that it is the cationic N-terminus that initially gets electrostatically attracted, albeit weakly, to the negatively charged bacterial membranes and initiates cell permeabilization ⁵⁴.

1.1.5.2 The problem of multidrug-resistant bacteria

The rise of multidrug-resistant bacteria called “superbugs” has placed scientists in the position of urgently needing to develop alternatives to antibiotics. The so-called superbugs are bacterial strains, which are resistant to two or more conventional antibiotics. Just a few months ago, the WHO published a list of antibiotic-resistant “priority pathogens”, considered the greatest menace to human health. At the top of the list there are the bacteria that can cause severe and often deadly infections in patients from hospitals and nursing homes, including *Acinetobacter baumannii*, *Pseudomonas aeruginosa*, and several enterobacteria. The list also includes increasingly drug-resistant bacteria that cause more common diseases such as *Staphylococcus aureus*, *Helicobacter pylori*, *Neisseria gonorrhoeae*, *Streptococcus pneumoniae* and *Haemophilus influenzae*. Alternatives to conventional antibiotics have been intensively investigated and a few approaches are currently being investigated, in both clinical and nonclinical research. Amongst the possible novel drug candidates are antibodies,

bacteriophages, vaccines and of course antimicrobial peptides (both natural and synthetic) ⁵⁵.

1.1.5.3 Modes of action of AMPs

The reason why AMPs have rapidly captured attention as substitutes to conventional antibiotics is linked to their distinctive mode of action in killing pathogens. As previously mentioned, AMPs have the unique ability to recognise and specifically target bacterial membranes thanks to electrostatic bonds between the cationic amino acidic residues and the negatively charged bacterial surfaces. This is in contrast with antibiotics, which usually target specific receptors and proteins. The cytoplasmic membranes of both Gram-positive and Gram-negative bacteria are indeed rich in phospholipids (phosphatidylglycerol, cardiolipin, and phosphatidylserine), which have negatively charged head groups. Additionally, more negative charges are also given by teichoic acids (cell wall of Gram-positives) and lipopolysaccharides (LPS) (outer membrane of Gram-negatives). In contrast, eukaryotic membranes are full of zwitterionic phospholipids asymmetrically distributed. The outer leaflet is predominantly composed of the neutral phosphatidylethanolamine, phosphatidylcholine, and sphingomyelin phospholipids, whereas the inner leaflet is composed of negatively charged phosphatidylserine. Furthermore, mammalian membranes are rich in cholesterol, which not only stabilises the phospholipid bilayer, but also drastically reduces the affinity for AMPs. These differences contribute to the AMPs' selectivity for bacterial cells ^{48, 51, 56}.

Like the bacterial, fungal membranes are negatively charged due to the presence of phosphomannans and other related constituents, such as negatively charged phosphatidylinositol, phosphatidylserine and diphosphatidylglycerol, which make them susceptible to the AMP action ⁵¹.

Many AMPs act rapidly and physically destroy the microbial membrane creating pores and causing the collapse of the transmembrane electrochemical gradients, while others, after the initial interaction, translocate across the membrane and accumulate into the cytoplasm where they target cellular functions such as DNA synthesis, cell wall

synthesis, protein synthesis and enzymatic activities^{43, 49, 53}. The amphipathic nature of AMPs is responsible for bacterial membrane permeabilization; with the hydrophobic residues interacting with the lipid constituents and the hydrophilic regions positioned in the lumen of the pore, or interacting with the phospholipid head groups⁵³.

1.1.5.4 Mechanistic models of α -helical peptides

In recent years, several mechanistic models have been proposed to explain how, after the initial electrostatic contact, AMPs provoke the permeabilization of bacterial membranes. These models are called “barrel-stave” “toroidal pore” or “carpet” and are generally associated with α -helical peptides, due to their ability to adopt to different conformations, depending on the surrounding environment.

Barrel-stave model

In the “barrel-stave model”, the peptide monomers initially aggregate on the bacterial surface and then insert perpendicularly into the lipid bilayer like staves in a barrel. The result is the formation of peptide-lined transmembrane pore in which the peptide hydrophobic residues face the acyl chains of membrane lipids while the hydrophilic regions face the pore lumen. As a consequence, cytoplasmic material starts leaking out from the pore causing cell death. This mechanism is unique, and it has been experimentally supported only for Alamethicin, a neutral α -helical peptide isolated from *Trichoderma viride* fungus^{49, 51, 56, 57}.

Toroidal pore model

The “toroidal pore model” is more common and can be associated with a great variety of peptides. Initially, the peptides accumulate parallel to the membrane surface and start accumulating. Once the critical concentration is reached, AMPs perpendicularly insert into the membrane and force the membrane phospholipids to bend continuously from one leaflet to the other. This process causes the spontaneous formation of pores composed by the peptides and membranous phospholipid head groups which are likely to cover the cationic peptide charges^{43, 56}. Recently, a version of this model called

“disordered toroidal pore” was proposed. In this model, the phospholipid bilayer is still bending inwards, but only one or two peptides are effectively inserted into the pore and interact with head groups while the majority of AMPs stay on the pore edges ⁵⁸. Mellitin, Magainins and human Cathelicidin LL-37 are all examples of peptides that form toroidal transmembrane pores ^{13, 59, 60}.

Carpet model

Finally, in the “carpet model” AMPs do not insert into the bacterial membrane but accumulate and align parallel (like carpets) to the phospholipid bilayer and ultimately disrupt the membrane in a detergent-like manner. During this process, the peptides stay in contact with the lipid head groups and, at the same time, coat the membranes. This specific orientation causes local disturbances in membrane stability, which can lead to the formation of fractures, holes and eventually micelles from where cytoplasmic component can leak out. The model has been observed *in vitro*, for example on cecropins ⁶¹, and mostly applies when high concentrations of peptides are used. It is often seen as an extreme consequence of the “toroidal pore model” ^{48, 49, 56}.

Non-membrane lytic peptides

However, not every α -helical peptide is membrane disruptive. Buforins, for example, which is a histone-derived AMP isolated from the stomach tissue of the Asian toad *Bufo bufo gargarizans*, translocates across the membrane without inducing significant membrane permeabilisation. The presence of a proline in the amino acidic sequence induces a kink in the α -helix structure and enhances the cell-penetrating properties of the peptide. Since *in vitro* studies showed that Buforins binds nucleic acids it has been hypothesised that the intracellular target of these AMPs might be indeed the DNA ⁶².

1.1.5.5 Mode of action of β -sheet peptides

The mode of action of β -sheet peptides is still poorly understood. For example, studies on the Defensins suggest that this class of AMPs are membrane lytic. However, the exact mechanism that leads to pore formation is not yet certain. Recent studies suggest

that they could be involved in several other biological functions such as chemo-attraction and consequently linked to the innate and adaptive immunity^{43,45}.

Defensins, for example, are a family of antimicrobial peptides found in many species of invertebrates and vertebrates, humans included. They possess a characteristic β -sheet structure and a framework of six disulphide-linked cysteines⁵¹. There are 3 main subfamilies, α - β - and θ -. While α - and β - defensins are widely distributed in nature, θ -defensins, the only known class of cyclic peptides in mammals, have been isolated from 3 species of primates; rhesus macaques (*Macacca mulata*), olive baboon (*Papio anubis*) and hamadryas baboon (*Papio hamadryas*). θ -defensin genes in humans are believed to exist as pseudogenes and are not functional⁶³. Defensins are normally expressed in cells and tissues involved in host defence against microbial infections, and are therefore considered as part of the innate immune system. The highest concentrations are synthesized in the bone marrow and then accumulate in leukocytes granules, i.e. neutrophils, but smaller amounts are found also in epithelial cells and in the intestinal Paneth cells⁶⁴.

Experimental evidence suggests that certain β -sheet AMPs are not only membrane active, but possess intracellular targets. Marine Tachyplesin I and bovine Lactoferricin B are two such examples⁴⁸. Tachyplesin I, derived from the Japanese horseshoe crab (*Tachypleus tridentatus*), is a cationic antimicrobial peptide with a typical cyclic antiparallel β -sheet structure. The AMP's primary target is the bacterial membrane which is destroyed by toroidal pores, however, Tachyplesin I can also translocate across the membrane and inhibit the intracellular protein synthesis⁶⁵. The difference in the Tachyplesin I interactions with the bacterial membrane is still poorly understood, however it seems that high concentrations of the peptide favour pore formation, while low concentrations promote activation of the intracellular translocation⁶⁶.

Lactoferricin B instead, is generated by gastric pepsin cleavage of bovine Lactoferrin and has several antimicrobial properties, including intracellular activities. The precise mode of action is not fully elucidated, but evidence suggests that this AMP can accumulate in the bacterial cytoplasm⁶⁷. A recent study reported that one of the possible targets is the pyruvate metabolism⁶⁸.

1.1.5.6 Mode of action of extended and loop peptides

AMPs with extended or loop structures, due to their lack of a classical secondary structure, are believed to have mainly intracellular targets. Indolicidin is probably the best characterised representative of the extended AMPs family. It was isolated from cytoplasmic granules of bovine neutrophils, and is the peptide with the highest content of tryptophan. Studies showed that it can bind DNA duplexes causing the inhibition of DNA synthesis⁶⁹. Thanatin, a loop peptide isolated from the spined soldier bug (*Podisus maculiventris*), does not permeabilise the bacterial membrane, but instead blocks the cells' motility inducing their aggregation⁷⁰.

1.2. Cell penetrating peptides (CPPs)

Peptides with the ability to transport a variety of cargos into cells and their intracellular compartments (such as cytoplasm, mitochondria and even nucleus) are referred to the term cell-penetrating peptides (CPPs). They are generally small (less than 40 aa long), often cationic and amphipathic. The importance of CPPs resides in their ability to transport into the cell cargoes such as proteins, nucleic acids, drugs and other peptides. The conjugation with the cargoes normally occurs either via covalent or non-covalent bonds^{71,72}. The mechanisms of cellular uptake are currently under investigation and the pathways involved in this process have not been fully elucidated. However, there are two main possibilities; energy-independent direct penetration, or energy-dependent endocytosis mediated. The direct translocation across the cellular membrane follows the same models described for AMPs (barrel-stave, toroidal pore, carpet), while the energy-dependent internalisation follows one of the endocytic pathways (macropinocytosis, clathrin- or caveolin-mediated endocytosis, and clathrin/caveolin- independent endocytosis). The same CPP can use both mechanisms, sometimes simultaneously, and the balance between the pathways strongly depends on the peptide sequence and extracellular concentration, cargo-conjugation, cell surface composition, temperature and exposure time^{73,74}. High concentrations of CPPs are often associated with a direct translocation, while low concentrations especially when cargo-conjugated preferably follow an active endocytic pathway^{75,76}.

The first isolated CPPs were Tat, corresponding to the basic domain of the viral HIV-1 Trans-Activator of Transcription (Tat) and Penetratin, corresponding to the third helix of the Antennapedia homeodomain, a transcription factor of the fruit fly (*Drosophila melanogaster*). HIV-1 Tat protein is internalised by cells *in vitro* and once in the nucleus it promotes viral gene expression, while Antennapedia enters nerve cells and regulates the neural morphogenesis^{77,78}.

CPPs can be classified in three big groups; peptides derived from truncated versions of full length proteins, chimeric peptides composed by combined natural sequences of different proteins, or synthetic peptides from rationally designed sequences developed using predictive programs⁷⁹.

Crotamine, the already mentioned toxin is sometimes referred as a CCP because in recent studies it has been shown that this peptide has the ability to bind plasmid DNA molecules and carry them into actively proliferating cells^{80,81}.

1.3. Bacterial resistance to AMPs

For years it has been speculated that microbes are unable to produce resistance against AMPs because it would involve deep modifications of the bacterial membrane, which in terms of genetics and physiological functions would be really difficult to achieve. Another common reason is that a host can produce many AMPs and it would be virtually impossible for a pathogen to develop resistance against all the AMPs at the same time⁵¹. Nevertheless, recent studies have showed that this is not true; host and pathogen have continued to co-evolve for thousands of years following mutual inhibition and adaption strategies⁸². Common defence mechanisms to avoid the peptides' action include, production of proteases and peptidases, alterations in net surface charges and membrane composition (lipid and proteins), secretion of specific proteins that bind AMPs, and expression of efflux pumps⁸³.

Bacteria have specific sensors that can perceive AMPs in the environment and enhance the resistance mechanisms. For example, Gram-positive *Staphylococcus aureus* can

recognise, the presence of AMPs such as human beta defensin 3. To avoid degradation, it changes the net surface charges by activating the D-alanylation of teichoic acids and by inclusion of lysylphosphatidylglycerol in the bacterial membrane. Alternatively, it expresses the *vraFG* AMP efflux pump to export the AMPs outside the cytoplasm and away from the membrane ⁸⁴. Increased expression levels of efflux systems are found also in Gram-negative *Neisseria* strains (*N. gonorrhoeae* and *N. meningitidis*) which give high resistance not only to AMPs, but also antibiotics ⁸⁵.

Gram-negative *Salmonella typhimurium* instead can remodel the bacterial envelope modifying the composition of lipid A (acidic moiety of lipopolysaccharide) via palmitoylation, hydroxylation and deacylation ⁸⁶. The most common method of AMP inactivation is mediating proteases and peptidases that can degrade the peptides. Linear and α -helical AMPs are the ones more easily targeted. Human Cathelicidin LL-37 for example, is cleaved by *Salmonella enterica* serovar Typhimurium outer-membrane protease PgtE or by the V8 and aureolysin proteases from *Staphylococcus aureus* ^{87,88}.

To circumvent enzymatic degradation, AMPs evolved in more stable structures thanks to the addition of disulphide bridges, proline residues in the amino acid sequence, amidation of the C-terminal and acetylation of the N-terminal. Normally the capture and extrusion of AMPs by bacterial proteins and efflux pumps depend on direct recognition of specific peptide sequences or structural motifs. For this reason, many related families of AMPs are produced with modifications in their sequences that will not alter the antimicrobial functions but can mislead bacterial defence systems. Finally, to maintain the affinity for bacterial membranes even when the net anionic surface charge is reduced, AMPs have progressively increased their net positive charges ⁸².

Nevertheless, most of the bacterial resistance against AMPs observed so far was related with *in vitro* experiments, where the conditions experienced by bacteria are, by default, very different compared to those in nature. Indeed, in a natural environment, pathogens are not continuously exposed, generation after generation, to the same AMP, but instead they interact with several peptides that can belong to different hosts and tissues. The exposure normally lasts for a limited amount of time and it is generally accompanied by other components of the host immunity system given that AMPs can modulate the innate immune response. These conditions drastically reduce the selection pressure that generally causes the development of resistance ⁵¹.

1.4 *De novo* synthetic AMPs; approaches for the design of new molecules

The systematic study of natural AMP sequences and secondary structures together with their biological functionalities allowed the design of *de novo* synthetic oligopeptides that could be used for targeting drugs-resistant pathogens. The main goal is to improve not only the antimicrobial activity, but also the stability and especially the safety against the host organism when compared to natural AMPs ⁸⁹. Indeed, when an AMP is selected as a therapeutic agent it should theoretically have great affinity for bacterial cells but, at the same time, not show any toxic effects on mammalian cells. In reality, the interactions between natural peptides and host membranes can vary for each particular AMP, and to a certain extent every single AMP shows some toxicity towards mammalian cells. Normally, cytotoxicity is reported as AMP erythrocytes haemolytic activity or by decreases in the cells viability (often on fibroblasts) ⁹⁰. Sometimes it is referred to as Therapeutic Index (TI), which is the ratio of the haemolytic activity and the minimal inhibitory concentration (MIC) ⁹¹.

Several methods are currently used to improve the AMP cells specificity. The optimisation of the various physicochemical parameters (net charge, amphipathicity, helicity etc..) is definitely the most important, followed by the introduction of D-amino acids (which have opposite chirality), fluorinated or unusual amino acids (peptoids such as N-substituted glycines). Constraining of the peptide conformations (cyclization of linear peptides) and modification of peptides by polymer (PEGylation) gave promising results as well ⁹².

There are many approaches to designing new synthetic AMPs. The easiest method is to choose a well-known AMP with proven good antimicrobial activity and use its amino acidic sequence as a template. Analogues of the template are then synthesised with just single or double amino acidic substitutions ⁸⁹. A good example of this methodology is revealed by Pexiganan, a synthetic analogue of the amphibian AMP Magainin-2. This peptide is currently in phase III of clinical trials as topical antimicrobial cream for the treatment of mild infections associated with diabetic foot ulcers ⁹³.

Other typical methodologies use computational and virtual screenings⁸⁹. The biophysical modelling studies are centred around understanding of the AMP activity, when in contact with the bacterial membranes, and in designing improved variants of the same AMPs using molecular dynamics simulations and thermodynamic calculations of the peptide-membrane interactions. This type of approach helped in the design of Novispirins, a less toxic AMP analogue of the synthetic Ovispirin, an AMP derived from the bovine SMAP-29. Both Ovispirin and SMAP-29 have good antimicrobial activity, but they are unsuitable for therapeutic use due to their toxicity towards human erythrocytes and epithelial cells. Novispirins, on the other hand, showed a consistent decrease in toxicity without changing its antimicrobial properties⁹⁴.

Finally, in the virtual screening methods, predictive algorithms are used to determine the peptide physicochemical properties according to the amino acidic sequence alone. Once the properties are defined, structure–activity relationship models (SAR) are used to evaluate all the possible biological activities of the peptide⁸⁹.

1.5 Abilities of AMPs: more than simply antimicrobial agents

The importance of AMPs is linked to their broad spectrum of activities against pathogens. Many peptides display not only antimicrobial properties against both Gram-positive and Gram-negative bacteria, but have also antifungal, antiprotozoal antiviral and even anticancer effects⁵³.

1.5.1 Antifungal activity

Histatins, for example, are AMPs found in the saliva of humans and other higher primates, they have not only antibacterial properties, but also exhibit strong antifungal activity. They are constitutively expressed in the parotid and sublingual salivary glands and they have a pivotal role in controlling the infections in the oral cavity. Histatin 5 is, amongst the family, the peptide with the strongest effect against *Candida albicans*.

They are small histidine-rich peptides with an extended secondary structure and intracellular targets as their main mode of action. It has been shown that histatins can translocate across the fungal membrane into the cytoplasm, and target the mitochondria causing depletion of intracellular ATP content, which leads to energy loss and generation of ROS with consequent arrest of the cell cycle and ultimately death⁹⁵. In humans, Histatins seem to have also an important role as wound-closure stimulator factors⁹⁶. A synthetic analogue of Histatin 3 and Histatin 5 called PAC-113 was in the second phase of clinical trials as a mouth-wash to treat oral candidiasis in HIV seropositive patients (ClinicalTrials.gov Identifier: NCT00659971).

1.5.2 Antiprotozoal activity

Protozoal parasites such as *Plasmodium spp*, *Trypanosoma cruzi*, *Toxoplasma gondii*, *Cryptosporidium* or *Leishmania spp* are responsible for severe diseases in humans (malaria, trypanosomiasis, toxoplasmosis, cryptosporidiosis, and leishmaniasis) which can be fatal in immunocompromised individuals. Because of their broad spectrum of activities, Amphibian AMPs such as Magainin 2 or Dermaseptins have been investigated as possible therapeutic agents against protozoa infections. A similar mode of action of AMPs towards protozoa has been discovered (membrane permeabilization or intracellular targets). Despite being eukaryotic, the cell membrane is characterised by the presence of anionic phospholipids and other sterols similar to the bacterial ones which make a perfect target for AMPs⁹⁷.

1.5.3 Antiviral activity

To date, few studies have been conducted on AMPs to explore their possible antiviral properties. Results showed that cationic host peptides can fight viral infections representing the first line of defence against viruses before the intervention of the adaptive immune response. It is still not clear if the peptide secondary structure is somehow related with the possession of antiviral activity since both classes of peptide α -helical and β -sheet have been found able to target viruses. The modes of action are complex and extremely variable and may include blocking of viral entry by the

interaction with receptors or heparan sulfate, inhibition of the virus cell-to-cell spread, and direct interactions with the viral envelope. Some peptides (α - and β -defensins) can induce cytokines and chemokines production and have chemotactic activity for T cells, monocytes and immature dendritic cells⁵³.

Defensins and Cathelicidins are the most studied classes of AMPs for their antiviral activity. Human α - and β -defensins and primates θ -defensins are able to protect against several viral infections, included herpes simplex virus (HSV), influenza A virus (IAV), human papillomavirus (HPV) and human adenovirus (HAdV)⁹⁸⁻¹⁰¹. LL-37 instead, the only human member of the Cathelicidins family, has showed *in vitro* a direct antiviral activity against the Respiratory Syncytial virus (RSV), while giving protection against infection in mice and in humans^{102, 103}. Due to the importance of Defensins and Cathelicidins in fighting viral infections, few synthetic analogues have been engineered with the aim of enhancing the peptide antiviral activity¹⁰⁴.

1.5.4 Anticancer activity

AMPs with anticancer properties are referred to as anticancer peptides (ACPs) and have the potential of being novel entities¹⁰⁵. The majority of current anticancer drugs are based on alkylating agents and antimetabolites, which have poor selectivity against normal mammalian cells. They interact with intracellular targets, penetrating through membranes inside cells, but once they reach the cytosol many of these agents are immediately deactivated by intrinsic resistance mechanisms that transport the drugs out of the cell before they can effectively interact with their intracellular targets¹⁰⁶.

Thus, the development of novel drugs and delivery systems with different modes of action and better cancer cell selectivity is crucial to battle drug resistance and reduce normal cell cytotoxicity. In this context, ACPs could be resourceful candidates and their possible usage as peptide therapeutics has been extensively explored over the years¹⁰⁶.

Peptides that display anticancer properties are usually divided into two categories; peptides that have potent effects against bacteria and cancer cells but are harmless towards normal mammalian cells (e.g. Cecropins, Magainins) or peptides which exhibit indiscriminate toxicity towards bacteria, cancer and normal cells (e.g. Mellitin, Defensins and human LL-37)¹⁰⁷.

The specificity for cancer cells that some AMPs display is currently under investigation. Despite controversial theories, the general consensus in the field is that the differences in membrane composition between cancer and non-cancer cells are the main reason for the peptide selectivity. Cancerous cell plasma membrane electrostatic charge differs from normal cells due to the presence of anionic molecules such as phospholipid phosphatidylserine (PS), O-glycosylated mucins, sialylated gangliosides and heparin sulfate. These anionic molecules confer a net negative charge compared to the mammalian cell membranes normally rich in neutral zwitterionic phospholipids and sterols. Moreover, it has been shown that cancer cell membranes often have a reduced amount of cholesterol, which would normally protect mammalian cells from the insertion of lytic peptides. Therefore, altered levels of cholesterol increase the membrane fluidity, which may facilitate the binding of cationic peptides with their destabilising action. Furthermore, tumour cells, due to their extreme motility and invasive properties have on their membranes more filopodia, which give the malignant cells a higher total surface area available for the peptides to interact with ^{105, 106, 108}.

The specific mode of action against cancer cells is not completely understood, but some evidence suggests that it follows the same rules applied for bacteria, where peptides can kill tumour cells through membrane permeabilization or by targeting intracellular pathways. Mitochondria are common intracellular targets; peptides permeabilise their membrane inducing cytochrome-c release. Membranolytic peptides normally kill cells by necrosis while peptides targeting mitochondria kill cells inducing apoptosis ¹⁰⁷.

Nevertheless, peptides are not only cell death regulators, but can also interfere with several cancer-related signal transduction pathways, especially those involved in cell adhesion, receptor interaction and metastasis; peptides have been found to target hormone receptors, cell-adhesion proteins, protein kinases and their substrates ¹⁰⁹.

Peptides can even induce an immunomodulatory effect via stimulation of natural killer cells (NK cells), peripheral blood lymphocytes and interferon (IFN) ¹¹⁰.

Among the natural AMPs with anticancer properties, Cecropins A-B and Magainin II are the most studied due to their good selectivity for cancer cells and their ability to kill them at concentrations not harmful for normal mammalian cells ¹¹¹. For example, Cecropin A and B both inhibit the cell growth of four bladder cancer cell lines (RT4,

647V, J82 and 486P) via membrane permeabilization and lysis, while sparing normal murine and human fibroblasts ¹¹².

Magainin II activity was tested as well on bladder cancer cell lines (RT4, 647V, and 486P) and on murine and human fibroblasts. Results clearly showed that the amphibian peptide had a cytotoxic and antiproliferative effect by pore formation in the bladder cancer cell lines, but it did not have this effect on the normal murine and human fibroblasts ¹¹³.

Recently, Magainin II modified polydiacetylene (PDA) micelles were synthesised to enhance the anticancer activity of the peptide. The micelles were tested on A549 lung carcinoma, KB epidermal carcinoma and MCF-7 breast adenocarcinoma cells, showing a consistent decrease in cell viability. Images showed a cytoplasmic localisation of the micelles, and studies on the uptake ratios revealed that for KB cells the particle internalisation is temperature dependent, suggesting that an active process is involved (i.e. endocytosis). Moreover, the micelles effectively suppressed tumour growth in a murine xenograft model ¹¹⁴.

Several hybrid or synthetic peptides have been designed trying to improve their selectivity and activity towards cancer cells. One of the main goals is certainly to reduce adverse side effects and resistance mechanisms which are a constant in normal chemotherapeutic drugs. Unfortunately, despite the efforts to date, very few ACPs are in clinical trials as possible anticancer drugs. This partial lack of success is due to many challenges related with the development of peptides as pharmaceutical drugs; big obstacles are the highly elevated production costs which come with the synthesis, followed by sensitivity to proteolytic degradation, a poor oral bioavailability, and reduced penetration through the intestinal membrane. To reduce the synthesis costs, the newly designed peptides tend to be shorter than the natural ones, and to increase resistance to protease activity natural amino acid can be substituted with unnatural ones, while more cell specificity and penetration could be achieved using cell penetrating peptides (CPPs) conjugated with drugs, antibodies or anticancer peptides ^{105, 108, 115}.

The synthetic A₉K and G(IKKK)₃I-NH₂, two of the peptides described in this PhD project, were tested against several cancer and non-cancer cell lines to prove their selectivity towards one specific type of cells. Both peptides inhibited the growth of human HeLa and promyelocytic leukaemia HL60 cells. A₉K remained benign to

monkey kidney Cos 7 cells, mouse fibroblast NIH3T3 and to human erythrocytes. G(IKK)₃I-NH₂ instead did not induce toxicity in human dermal primary fibroblasts HDFa, mouse embryonic fibroblasts NIH/3T3 and in human erythrocytes^{116, 117}. Moreover, G(IKK)₃I-NH₂ did not induce non-specific immunogenic responses in lymphocytes but showed noticeable inhibition of tumoral growth in nude mice following inoculation of HeLa cells¹¹⁸.

1.7 Current strategies and future developments

In the last section of this introductory chapter, some examples of cationic amphipathic peptides that are going through clinical development will be presented, with important differentiations between antimicrobial or anticancer activities. AMPs-drugs based are usually topical creams or gels which can be locally applied to fight bacterial (or fungal) infections. Some exceptions include the already mentioned PAC-113, originally designed as a mouthwash for oral candidiasis in immune depressed patients. The product is currently available in Taiwan and will be soon released in South China as well under the name of P113+; an over-the-counter ("OTC") personal care product in the format of mouth rinse solution, oral mouth spray, feminine cleansing wash, feminine soothing spray and anti-bacterial hand cream.

Surotomylin instead is a novel cyclic lipopeptide analogue of daptomycin (derived by microbial fermentation of *S. roseosporus*) designed to fight *Clostridium difficile* infections. It is orally administered and thanks to its stability, high aqueous solubility and low oral bioavailability, it accumulates in the gastrointestinal tract where it can exceed the minimum inhibitory concentration required for killing *C. difficile*¹¹⁹.

ACPs, as previously mentioned, are poorly adsorbed if orally administered, therefore all the peptides currently in clinical trials are formulated to be intravenously injected. Synthetic ACPs designed to inhibit the tumoral growth are often used as therapeutic cancer vaccines which are able to stimulate the immunity system to recognise and attack cancer cells.

ITK-1, for example, is a synthetic personalised peptide vaccine consisting of 14 different tumour-associated peptide antigens derived from conserved human proteins involved in cellular proliferation and frequently overexpressed in cancer cells. Prior to vaccination, the cellular and specific humoral immunity responses in human leukocyte antigen (HLA)-A24—were assessed and the peptides showing the strongest reactions were then selected as personalised vaccines for patients with recurrent or progressive glioblastoma multiforme (GBM) and prostate cancer. ITK-1 is currently on phase III after successfully passed the previously clinical trials ¹²⁰.

To improve cancer cell selectivity and to simultaneously reduce adverse effects on normal host cells, the development of a drug delivery system using cell penetrating peptides (CPPs) or more specifically tumour targeting peptides (TPPs) as cargo carriers has been recently proposed ¹²¹. TPPs are a class of penetrating peptides that interact with receptors which are overexpressed on cancer cells. Studies on surface receptor differences between cancer cells and normal cells allow identification of those molecules which are overexpressed in cancer cells, thus making them perfect targets for TPPs ¹²².

For example, Angiopep-2 (An2) is a 19-amino acid peptide able to cross the blood–brain barrier (BBB) by receptor-mediated transcytosis. It binds to the low-density lipoprotein-like receptor-1 (LRP-1), which is overexpressed in several brain cancers. An2 has been recently conjugated with the antineoplastic drug paclitaxel or with the Anti-HER2 monoclonal antibody (mAb) to treat several brain tumours, including brain metastasis caused by breast cancer HER2+. The two drugs are respectively called ANG1005 and ANG4043; ANG1005 successfully completed phase II and soon will start phase III, while ANG4043 is in preclinical trials ^{123, 124}.

1.8 Research motivation

The purpose of this PhD project is to explore the cancer cell selectivity of three cationic amphiphilic peptides; A₆K, A₉K and G(IKKK)₃I-NH₂. The positive preliminary results achieved against both bacteria and cancer cells inspired a more in-depth investigation in order to better elucidate the cancer cell toxic effects previously observed. The peptides' binding abilities for different negative nucleic acids' molecules have been investigated as well. Both traditional monolayer cultures and innovative 3D models have been tested. The results obtained could be crucial in identifying if any of these molecules could be used as possible carriers for drug delivery specifically targeting cancerous cells. Moreover, an *in vivo* model (zebrafish, *Danio rerio*) has been used to observe the behaviour of the cationic small peptides in a more complex biological environment. Extensive toxicity assays have been performed and the health of animal embryos monitored. Finally, a complete evaluation of possible endocytic pathways used for the peptides internalisation has been carried out using several approaches including a high-content genome screen.

With the results obtained we hope to unravel aspects of the biological activities involved in the cationic peptides and eukaryotic cells which at the moment are still unclear and create a foundation for a step forward in anti-cancer treatments.

1.9 Thesis outline

Chapter 1 gives a general introduction on natural and synthetic oligopeptides, emphasising on current medical and therapeutic applications and possible future developments of antimicrobial peptides in fields not related with microbiology.

Chapter 2 is centred on describing the methodology adopted for the experimental part of this PhD project.

Chapter 3 is focused on the synthetic β -sheet A₆K and A₉K peptides. Results of the experiments conducted on these two peptides are listed and fully explained.

Chapter 4 is based on the synthetic α -helical peptide G(IKK)₃I-NH₂. Detailed descriptions are given of the most significant and successfully performed experiments.

Chapter 5 explains the data collect using A₉K and FITC-G₃(IKK)I-NH₂ peptides on the *Danio rerio* (zebrafish). A brief introduction on the importance of zebrafish as animal model is given as well, to facilitate the reader understanding the results.

Chapter 6 treats the topic of high-throughput genome screens. Data collect from RNAi screens of cells exposed FITC-A₉K and FITC-G(IKK)₃I-NH₂ peptides are showed and explained in detail.

Chapter 7 is the conclusive chapter of this manuscript. All the results obtained with A₆K, A₉K and G(IKK)₃I-NH₂ are brought together. Ideas on future work and developmental strategies are also discussed.

2 MATERIALS AND METHODS

In the following sections, the procedures adopted in the experimental part will be discussed; unless stated otherwise, the plates used in all the described experiments were Grenier Bio One 96 well plates (Cat n° 655088) or Perkin Elmer 384 well plates (Cat n° 6007460).

2.1 Peptides synthesis and stock solution preparation

The β -sheet A₆K and A₉K peptides and the α -helical G(IKK)₃I-NH₂ were synthesized using standard Fmoc solid phase synthesis, from natural L-amino acids, on a commercial CEM Liberty microwave peptide synthesizer. In order to obtain an amidated C-terminal, a Rink-amide MBHA resin (0.83 mM/g) was used at the beginning. After deprotection of the Rink-amide resin, Fmoc-Lys (Boc)-OH was introduced and coupled with resin, followed by Fmoc deprotection and coupling with Fmoc-Ala-OH. This cycle was repeated several times, until the peptides were generated. After Fmoc deprotection of the N-terminal residue, acetic anhydride was used to cap, prior to cleavage from the resin. The whole procedure lasted 3 hrs and was executed at room temperature. These modifications are important to enhance the resistance of the peptides from the peptidases action. G(IKK)₃I-NH₂ peptide instead was capped at the N-terminus with a glycine (G), in this way, the chances of having α -helical hydrogen bonding are increased¹²⁵. The peptides were centrifuged at 10000 rpm for 20 minutes at 4 °C and followed by cold ether precipitation of the supernatant, repeated at least 8 times to get a high purity level. After purification, the solid products were dissolved in Milli-Q water, freeze-dried in a lyophilizer for 2 days and subjected to reverse-phase high performance liquid chromatography (RP-HPLC) and MALDI-TOF mass spectrometry analyses which revealed purity over 98%^{117, 126}.

The synthesis of the fluorescent versions of A₉K, and G(IKK)₃I-NH₂ peptides were also performed using the standard Fmoc based solid phase protocol. To reduce degradation during the last cleavage step of the N-terminals FITC labelling, a 6-

aminohexanoic acid (Ahx) group was introduced between the last amino acid (A or G) and the fluorescein motif ¹²⁷.

2.1.1 Solution preparation

The synthesized peptides have relatively high water solubility and were dissolved in pure water (25 °C) and at pH 6.0. Stock solutions were made at various concentrations, depending on the experiment, between 1 mM and 5 mM.

For A₆K and A₉K the critical aggregation concentrations (CACs) determined to be about 0.2 mM and 0.02 mM respectively. Stock solutions of A₆K, A₉K and FITC-A₉K were stored at 4 °C to aid the self-assembly process while G(IKK)₃I-NH₂ and FITC-G(IKK)₃I-NH₂ stocks were kept at -20 °C prior to use.

2.2 Cell lines and culture methods

A431, a human epithelial cancer cell line (obtained from Prof. Elizabeth Smythe, Professor of Molecular Cell Biology at the Department of Biomedical Science, University of Sheffield), HCT-116, another human epithelial cancer line and (obtained from Dr. Spencer Collis CRUK Senior Cancer Research Fellow at Department of Oncology & Metabolism, University of Sheffield Medical School), and HDFs human primary dermal fibroblasts (a kind gift of Dr. Zoe Hewitt, Project Manager UKRMP Pluripotent Stem Cell Platform, Centre for Stem Cell Biology, University of Sheffield) were the cells used to perform all the experiments described in this thesis. A431 and HCT-116 were selected as cancer models and the primary human dermal fibroblasts as control lines. Since both the cancer cell lines have epithelial origins the results obtained with them could be comparable.

The A431 tumour cell line was established from an epidermoid squamous carcinoma extracted from a 85 years-old patient vulva ¹²⁸. A431 cells are normally hypertriploids, they overexpress the epidermal growth factor (EGFR) due to an amplification of EGFR gene on chromosome 7, and they are mutant for p53 gene ¹²⁹.

HCT-116 epithelial cancer cells derive from a colorectal carcinoma extracted from an adult male. This line has a mutation in codon 13 of K-Ras proto-oncogene on chromosome 12 and is positive for transforming growth factor β 1 (TGF- β 1) and β 2 (TGF- β 2)¹³⁰⁻¹³².

The HDFs are primary culture derived from the dermis of normal human neonatal foreskin.

All the cell lines were cultured in DMEM (Dulbecco's Modified Eagle Medium, GIBCO®, Thermo Fisher Technologies, Cat. No. 11965092) with high glucose (4500 mg/ml), L-glutamine and without Sodium Pyruvate and HEPES, supplemented with 10% heat-inactivated foetal bovine serum, FBS (Sigma-Aldrich®, Cat. No. F9665), 100 U/ml penicillin and 100 μ g/ml streptomycin (GIBCO®, Thermo Fisher Scientific, Cat. No. 15140122).

2.2.1 Cell lines sub-culturing

All cultures were carried out in complete sterile conditions, under a laminar flow cabinet (Esco Airstream® Class II Biological Safety Cabinet). Cell lines were kept in incubator (MCO-20AIC, Sanyo), with standard parameters (37 °C; 5% CO₂; 95% air humidity) and normally sub-cultured in 75 cm² flasks (treated flask, blue filtered cap, Nunc™, Cat. No. 156499) every 2-3 days or as soon as they reached the 70-80% of confluence.

For passaging, the old complete culture medium was discarded, followed by washing with 10 ml of PBS (Phosphate Buffer Saline, 1x pH 7.2, without CaCl₂ and MgCl₂ ions, GIBCO®, Thermo Fisher Scientific, Cat. No. 10010023), pre-warmed at 37 °C. The PBS step is important, to remove Ca²⁺ ions involved in cellular adhesion. Subsequently 1-2 ml of pre-warmed (37 °C) Trypsin-EDTA (0.05% GIBCO®, Thermo Fisher Scientific, Cat. No. 25300104) were added for the necessary time to allow the detachment of the cells from the flask bottom.

The cells were counted using an automated cell counter (Countess® II Automated Cell Counter, Life Technologies, Thermo Fisher Scientific); 10 µl of cells sample were mixed with 10 µl of 0.4% Trypan Blue (Invitrogen™, Thermo Fisher Scientific) and then pipetted into a Countess® Cell Counting Chamber Slide (Invitrogen™, Thermo Fisher Scientific, Cat. No. C10313). Cell number per ml was then calculated. Otherwise without counting and depending on the cell type, ratios between 1:3 and 1:6 were directly added in a new flask, together with 10 ml of complete culture medium.

2.2.2 Freezing and thawing procedures

To ensure that all the cells used in the experiments were originated from the same starting population, a frozen cell bank has been created from an early passage.

For cryopreservation, cells at 70% of confluence were harvested and divided in aliquots to have at least 1×10^6 cells suspension in 1 ml of cryopreservation medium per cryovial (Starlab, Cat. No. E3110-6122). The freezing medium is composed of 90% of Foetal Bovine Serum, FBS and 10% of sterile DMSO (Dimethyl sulfoxide, CAS number: 67-68-5, Thermo Fisher Scientific). The cryovials were then placed in the Mr. Frosty™ Freezing Container (Thermo Fisher Scientific), previously filled with isopropanol (CAS number: 67-63-0, Acros Organics), or in a CoolCell® LXCell Freezing Container (BioCision) and transferred to the -80 °C freezer overnight. The freezing containers are designed to have a control rate temperature of -1 C°/minute to allow gradual freezing. The following day, cryovials were quickly transferred to a liquid nitrogen tank for long-term storage.

To thaw the cells from the liquid nitrogen dewar, the cryovial was warmed approximately one minute in the 37 °C bath, until nearly thawed, then wiped with 70% ethanol to sterilise the outside surface and placed into the laminar flow cabinet. Subsequently, the whole cryovial content (1×10^6 cells suspension in 1 ml) was gently transferred in a 15 ml tube (BD Falcon™, Cat. No. 352096), previously filled with 9 ml of pre-warmed complete culture medium. The 15 ml Falcon was centrifuged at 200 x g for 5 minutes, then the supernatant removed, and 10 ml of complete culture medium added. Finally, the cell suspension was transferred into a T-25 flask (treated flask, blue

vent/close cap, Nunc™, Cat. No. 156499) and placed in the incubator. To ensure that any traces of DMSO were fully removed, the following day the complete culture medium was changed again. Afterwards cells could be split as usual after 2-3 days.

2.3 Agarose gel electrophoresis

The ability of A₆K and A₉K peptides to specifically bind DNA or RNA molecules was evaluated using the agarose gel electrophoresis technique. With this assay different sized nucleic acids and complexes of peptides and single stranded antisense DNA oligonucleotides (ODNs), labelled with 5'-FAM (carboxyfluorescein-5-succinidyl ester) (Eurogentec Ltd, Cat. No. MD-FL001-05004) were separated.

2.3.1 Peptide/ODN complex formation

The complexes were made at different cationic/anionic charge ratios (5/1; 3/1; 2/1; 1/1 and 0.5/1). Briefly, ODNs solutions were prepared in UHQ water and diluted at appropriate concentrations in order to always have, after mixing with the peptides, a constant ODNs concentration of 0.1 µg/µl. Peptide solutions were instead diluted to the desired concentrations to achieve different cationic/anionic charge ratios which were based on the cationic charge on the lysine side chains and the anionic charges on the phosphate group of each nucleotide of the ODN.

Each nucleotide has a slightly different molecular weight (A = 313.21, T = 304.2, C = 289.18, G = 329.21) but for simplicity the value of 308 g/mol of anionic charges has been used as an average. The molecular weight of A₆K molecule is 613.7 g/mol, so it means that roughly 1 mol of peptide corresponds to 2 mol of ODNs; the molecular weight of A₉K is 826.89 g/mol, in this case 1 mol of peptide corresponds to 2.7 mol of ODNs. The amount of DNA has been fixed to be 1 µg per well (10 µl of a 0.1 µg/µl concentrated solution) and different calculations have been made to achieve different ratios (5/1; 3/1; 2/1; 1/1 and 0.5/1 between peptides and ODNs). For example, to achieve a charge ratio of 1/1, a same volume (10 µl) of A₆K peptide with a concentration of 0.2 µg/µl (or 0.27 µg/µl in the case of A₉K peptide) was mixed with the ODN solution. Once mixed together, peptides and DNA were left to equilibrate and

complex for at least 30 min at room temperature before use. Samples with only peptide or only DNA were included in the experimental set as controls.

A peptide will bind the DNA through the charge interaction between its positive charges and the nucleic acids' negative ones to achieve the neutralization complex formation. When an electrical field is applied if the net charge of the complexes is almost zero the complex will be observed inside the agarose well. Whilst the complexes that were not fully neutralized will instead migrate a certain length through the agarose gel. Therefore, different charge ratios of peptides-DNA complexes would result in different rates of DNA migration.

2.3.2 Gel preparation

The 1% w/v agarose gel (Agarose high resolution HS, BDH Laboratory Supplies, Cat. No. 43712 3Y) was made in 1x Tris-acetate-EDTA (TAE) buffer which was composed by 40 mM Tris-acetate and 1 mM EDTA (CAS number: 6381-92-6, Sigma-Aldrich®). Tris-acetate solution was prepared with Tris base (CAS number: 77-86-1, Thermo Fisher Scientific), glacial acetic acid (CAS number: 64-19-7, Thermo Fisher Scientific) and UHQ water. The TAE buffer pH was adjusted to about 8.0, as otherwise the EDTA powder wouldn't dissolve completely in the water. To melt the agarose/buffer mixture, the solution was heated on a hot plate, until agarose was completely dissolved. Subsequently 5 µl of ethidium bromide (EtBr, CAS number: 1239-45-8, Sigma-Aldrich®) at a concentration of 10 µg/µl was added to have a final concentration of 0.5 µg/ml, and then the solution was let cooled down for 5 minutes. Ethidium bromide was added to the agarose gel to bind the nucleic acids and visualise the retarded complexes. After the gel tray was placed into the casting apparatus (Mini Plus Submarine Gel, Thermo Fisher Scientific), a comb was inserted at a suitable position to create wells and the molten agarose was poured into the gel mold. The gel was left at room temperature for 30 minutes until it was completely solidified. Then the comb was removed, and the casting apparatus was filled with 1x TAE solution until the gel was fully covered.

2.3.3 Gel running

A gel loading buffer (Gel Loading Buffer II from the T7 MEGAscript kit, Ambion, Cat. No. AM1334) 6 times the starting volume was added to each sample. Then, the samples were carefully loaded into the wells previously created with the comb and the electrophoresis was run at 100 V for 30 minutes. Afterwards the gel was removed from the casting apparatus and visualized under a UV transilluminator. Safety goggles, gloves and lab coat were worn to protect the skin from UV light.

2.4 DNA/RNA transfection

DNA and RNA transfection experiments have been conducted on A431, HCT-116 and HDFs cell lines. Different conditions were tested to find the most suitable. For DNA transfection experiments, FAM-labelled oligonucleotides (FAM-ODNs) were used, while for RNA transfection experiments, a commercial double stranded siRNA, the red fluorescent siGLO (Red Transfection Indicator, Dharmacon, Cat. No. D-001630-02-05) was used.

A wide range of complexes peptide/nucleic acids at different cationic/anionic charge ratios were tested (0.1/1; 0.25/1; 0.5/1; 1/1; 2/1 and 3/1). Transfection experiments using the same conditions have been performed as well with FITC-A₉K, G(IKK)₃I-NH₂ and its fluorescent version, FITC-G(IKK)₃I-NH₂.

Cells were seeded initially in a 96 wells plate at a density of $2-5 \times 10^3$ cells per well, depending on the cell type, in 100 μ l of complete culture medium (DMEM, 10% FBS and 1% Penicillin and Streptomycin (P/S)) and incubated overnight. The following day media was removed and replaced with 90 μ l of fresh one.

In the DNA transfection experiments, the amount of ODNs per well was kept fixed at 0.05 μ g, while for siRNA transfection experiments, the siGLO concentration was used at 75 nM while for knock down, in the range of 30-50 nM¹³³. The procedure to make peptides/ODNs or peptides/siRNA complexes was the same used for the agarose gel

electrophoresis assay and already described in the corresponding sections. The molecular weight of G(IKKK)₃I-NH₂ is 1635.6 therefore 1 mol of peptide should correspond to 5.3 mol of ODNs, but since the peptide has 6 positive lysines so to make 1/1 cationic/anionic charge ratio, it has to be further diluted by 6 and 1 mol of peptide corresponds effectively to 0.88 mol of ODNs.

After 30 minutes incubation at room temperature 10 µl of each peptides/nucleic acid mixed solution were added to the wells. FAM-ODNs, siGLO or peptides alone were included as negative controls, while the commercial Oligofectamine™ (Invitrogen™, Life Technologies, Cat. No. 12252011) or DharmaFECT 1 (DF1) (Dharmacon, Cat. No. T-2001-02) transfection reagents have been used as positive controls to transfect ODNs and siRNA, respectively. Both Oligofectamine™ and DharmaFECT1 were diluted following the suppliers' instructions and mixed with the appropriate amount of ODNs or siRNA. Complexes of Oligofectamine™ and FAM-ODNs were left in incubation for 15-20 minutes while complexes DharmaFECT1 and siGLO were incubated for 30 minutes, then added to the correspondent wells and incubated overnight at 37 °C. According to the manufacturers protocols, DMEM only (without serum and antibiotics) was used in the case of ODNs and Oligofectamine™, while siRNA and DF1 complexes were dissolved in medium complemented with 10% FBS but without P/S.

The following day, cells were washed once with pre-warmed PBS and then fixed in 4% paraformaldehyde fixative solution (37% Formaldehyde solution, CAS number: 50-00-0, Sigma-Aldrich®, diluted in PBS) for 15 minutes. Hoechst 33342 (Thermo Fisher Scientific, Cat. No. 62249) was used and diluted in the fixative in a final working concentration of 2 µg/ml to stain nuclei. Cells were incubated and protected from light to avoid photo bleaching. Finally, the plates were washed twice with PBS to remove any aldehydes residues or excessive Hoechst 333342 stain and filled with at least 100 µl of PBS. A fluorescent automated wide field microscope (ImageXpress® Micro System) and MetaXpress® Software 5.3.01 (Molecular Devices) were used for the acquisition and segmentation analyses.

FITC-A₉K and FITC-G(IKKK)₃I-NH₂ transfection efficiencies were tested out only using the red fluorescent siGLO, because FITC and FAM have the same max excitation-emission wavelengths (490-525 nm). The two are effectively both derivatives of the same organic fluorescent compound, the fluorescein.

2.4.1 Cancer cells targeting experiment

HCT-116 and HDFs cells have been co-cultured together and transfected with 50 nM of siGLO red fluorescent siRNA, using DF1 or G(IKK)₃I-NH₂ at different ratios (0.5/1, 2/1 and 3/1) to determine if the peptide would preferably transfect the cancer cells instead of the fibroblasts. Briefly, 5x10³ HCT-116 and 2x10⁴ HDFs cells were seeded on a 96 wells plate in 90 µl of complete culture medium. Next day, in each of the positive control wells (DF1) the complete medium was removed and substituted with 75 µl of DMEM complemented with 10% FBS but without P/S. Complexes with siGLO and DF1 were made following the supplier's instructions (0.3 µl of DF1 mixed with 24.75 µl of DMEM and 0.25 µl of red siGLO 20 µM) and incubated for 30 minutes at room temperature before being added to the cells. Peptide/siRNA complexes were made as previously described in the agarose gel electrophoresis section. After 30 minutes of incubation, 10 µl of complex mixture of different charge ratios were added to the correspondent wells. Control wells with only siRNA addition were prepared as well. Next day the plate was fixed and stained following the standard fixation procedure using 4% paraformaldehyde and Hoechst 33342 (2 µg/ml) solution and the images were taken with the IN Cell Analyzer 2200 (GE Healthcare) microscope in bright field mode.

2.4.2 Confocal microscope

To determine the subcellular localisation of the peptides-DNA/RNA complexes, a confocal microscope (Nikon A1+) was used and the data were analysed with NIS Element software. Briefly, cells were seeded in 1 ml of complete culture medium in a glass bottom dish (µ-Dish 35 mm, high, Ibidi, Cat. No. 81156). The quantity of FAM-ODNs (0.3 µg) and the number of cells (25x10³) seeded were adjusted according to the different growth surface areas. The amount of siGLO was kept constant to 75 nM. This experiment has been performed only with A₉K peptide on A431 cancer cells.

2.4.3 3D spheroids

3D cultures are becoming extremely useful in cancer research, especially for *in vitro* drug screenings, where the conventional 2D cellular monolayers simply can't mimic the complex organisation and heterogeneity of solid tumours found in patients^{134, 135}.

We therefore decide to grow spheroids first with A431 and subsequently with HCT-116 cancer cells and test the transfection efficiency of both A₉K and G(IKK)₃I-NH₂ peptides. Briefly, cells were seeded in ultra-low attachment 96 well plates (round clear, Corning, Cat. No. 3474) at the density of 1×10^4 . Spheroids were allowed to grow for 48 hrs and then transfected with 75 nM of red fluorescent siGLO using the commercial reagent DharmaFECT1 (DF1) or different charge ratios of A₉K and G(IKK)₃I-NH₂ peptides (2/1 and 5/1). Complexes with the fluorescent siRNA and DF1 or peptides were made following the detailed procedure described previously in this chapter. Next day, spheroids were carefully fixed and stain in 4% paraformaldehyde solution and Hoechst 33342 (2 µg/ml final concentration). Images were acquired using the fluorescent automated wide field microscope (ImageXpress® Micro System) or a light sheet fluorescent microscope (Zeiss Lightsheet Z.1) and analysed with analysed ZEN 2014 SP1 software.

2.4.4 siRNAs transfection

Once peptides were shown to enter cells, an assay was designed to test whether they were capable of transfecting cells, ie, carrying a cargo and releasing it so as to induce a phenotypic change in the target cell. siRNAs were chosen, as they are small nucleic acids and able to induce changes in gene expression through the endogenous RNAi pathway.

ECT2 (Epithelial Cell Transforming 2) and PLK1 (Polo-Like Kinase 1) siRNAs were selected as functional molecules and experiments were performed on A431 and HCT-116 cell lines, as both target genes caused a reduction in cell viability and growth¹³⁶⁻¹³⁸. A₉K and G(IKK)₃I-NH₂ and both their fluorescent versions, FITC-A₉K and FITC-G(IKK)₃I-NH₂, were tested. The FITC-A₉K transfection experiments were performed with the help of Joanna Henry, a master student who worked, under my supervision, on this project as part of her MSc degree.

Transfection of ECT2 siRNA was performed on A431 using A₉K and G(IKK)₃I-NH₂, while transfection with PLK1 siRNA was carried out on HCT-116 using the fluorescent peptides. The siRNAs were from the On Target-Plus Dharmacon siRNA collection. 10 μM stock solutions were made according to the instructions provided by the supplier. For these experiments, the reverse transfection protocol was adopted as described in *Ivatt, et al.*,¹³⁹. Briefly, 384 wells plates were used in a reverse transfection; 5 μl of siRNA (from a stock of 150 nM) were added to the wells with 5 μl of DMEM containing 0.05 μl of DF1 (DharmaFECT1). siRNA and DharmaFECT1 were left to complex for 30 minutes at room temperature. After incubation, 15 μl of 2x10³ cells were added to each well. Cells were resuspended in culture medium with 10% FBS without the antibiotics since the combination of DF1 and antibiotics causes cell death. The plate was sealed, to minimize evaporation, left on the bench for 30 minutes and then put in the incubator overnight at 37 °C. The following day, 25 μl of DMEM (with 10% FBS and 2% P/S) were added to the plate and incubated again at 37 °C for other 2-3 days. siRNAs uptake occurs within 30 mins but RNAi knock down in the cells requires 2-3 days for gene-silencing. After the knock down, cells were fixed and stain with 4% paraformaldehyde fixative solution in PBS and Hoechst 33342 (2 μg/ml) for 15 minutes, as previously described. Fluorescent automated wide field microscope (ImageXpress® Micro System) was used for recording the high-resolution images.

Transfection using the red fluorescent siGLO was added as a control to verify that cells were healthy and transfected and more important to prove that an eventual decrease in the cells number was exclusively due to the RNAi gene silencing and not to unrelated events, such as an increased sensitivity toward the transfection conditions.

For the conjugation peptides/siRNAs the exact same procedure described above was adopted; peptides were diluted in 5 μl of DMEM in order to form complexes with the siRNAs at different cationic/anionic charge ratios from 0.5/1 to 10/1. Cells were subsequently added to the wells but in complete culture medium since the presence of antibiotics doesn't interfere with the peptides uptake and doesn't cause cell death.

Inhibition of ECT2 or PLK1 in cancer cells causes apoptosis, therefore successfully transfected cells should have an apoptotic appearance and a significant reduction in cell number compared to the controls. To count and analyse the differences in cell number in each of the experimental conditions MetaXpress® Software 5.3.01 (Molecular

Devices) was used. Data collected from the various conditions were normalised and compared to the number of survived cells after being transfected with siGLO.

2.5 MTT assay and cell counts

To investigate the cell response after exposure to the amphiphilic peptides, the MTT assay was carried out, a technique normally used to evaluate cell viability.

Yellow MTT (Sigma-Aldrich®, CAS number: 298-93-1), 3-(4,5,-Dimethylthiazol-2-yl)-2,5-diphenyltetrazolium bromide, is a tetrazole which is reduced into vivid purple formazan only in living, and therefore, metabolically active cells¹⁴⁰⁻¹⁴². The MTT assay was performed on A431 and HDF cell lines, using 5 different concentrations of A₆K and A₉K between 6.25 µM and 100 µM at 24 hrs, 48 hrs and 72 hrs. Appropriate dilutions were made so as to add only 10 µl of each peptide solution to the cells.

Briefly, cells were seeded in a 96 well plate (clear, flat bottom, Corning, Cat. No. 3596) with 90 µl of complete culture medium at a variable cell density, depending on the cell type and exposure times (5-7x10³ cells per well for 24 hrs and 48 hrs or 4-6x10³ cells for 72 hrs). The following day, 10 µl of the different peptides concentrations were added to the cells for the final volume to be 100 µl. Negative and positive controls were added to each experimental set; Na₂CrO₄ (Sodium chromate tetrahydrate, CAS number: 10034-82-91, Sigma-Aldrich®) has been used as positive control at the concentration of 200 µM, while the peptide diluent, UHQ water, as negative control. At the end of exposure to the peptide, the medium was removed and 90 µl of fresh media added with 10 µl of a MTT solution (5 mg/ml per well) and the plate incubated for 3 hrs. After that, the medium was carefully removed, and 100 µl of DMSO were added to dissolve formazan crystals. The plate was placed on a vibrating plate shaker for 15 minutes and the absorbance read at 570 nm with a spectral scanning multimode reader (Varioskan Flash™, Thermo Fisher Scientific).

A consistent discrepancy between the MTT assay results and the number of cells observed under the microscope was noticed. Therefore, it was decided to perform a cell counting experiment using High Content Analysis. Cells were seeded in a 96 well plate as described in the MTT section. After the exposure time, cells were washed once with

100 μ l of pre-warmed PBS and fixed and stained for 15 minutes, as previously described, with 4% paraformaldehyde fixative solution and Hoechst 33342 (2 μ g/ml). Images of the plates were acquired using the fluorescent automated wide field microscope (ImageXpress® Micro System) and the cells counted using MetaXpress® Software 5.3.01 (Molecular Devices).

With G(IKK)₃I-NH₂ the same range of concentrations (0-100 μ M) and exposure time (24-72 hrs) was investigated, but instead of performing the MTT assay, cell counts were made of the plates after peptide exposure. The experiments were performed on HCT-116 and HDFs cell lines. A cell count experiment using the same conditions was made using FITC-A₉K the fluorescent version of the peptide. For this part, the student Joanna Henry is responsible for the collection of the relevant data but always under my supervision. FITC-G(IKK)₃I-NH₂ toxicity was assessed instead for 24 hrs only, on both HCT-116 and HDFs cell lines.

2.6 Cell staining for imaging

In this PhD project, several fluorescent dyes have been used to stain different cellular compartments; the already cited Hoechst 33342 was used to stain nuclei, MitoTracker® Red CMXRos (Thermo Fisher Scientific, Cat. No. M7512) and JC-1 (Thermo Fisher Scientific, Cat. No. T3168) both used to stain mitochondria and Alexa Fluor® 568 Phalloidin (Thermo Fisher Scientific, Cat. No. A12380) used to stain the F-actin filaments.

A431 or HCT-116 mitochondria were stained with MitoTracker® Red CMXRos. Three different concentrations (6.25 μ M, 25 μ M and 100 μ M) of A₆K and A₉K were chosen as experimental points and 72 hrs as exposure time in A431 cells while HCT-116 cells were exposed to 6.25 μ M, 12 μ M and 25 μ M of FITC-A₉K for 48 hrs. Cells were seeded in a 96 well plate with 90 μ l of complete media and the next day 10 μ l of a peptide solution was added to the wells. After exposure, the media was removed from the wells and the cells were incubated for 30 minutes with 250 nM of MitoTracker® Red CMXRos at 37 °C. As this probe is susceptible to potential oxidation in serum, DMEM lacking FBS was used. After that, cells were washed once with pre-warmed

PBS and fixed and stained for 15 minutes at room temperature with 4% paraformaldehyde and Hoechst 3342 (2 µg/ml) solution. Cells were washed twice again with PBS to remove the excess of stain. 100 µl of PBS was added for imaging.

JC-1 dye is normally used to monitor cell health because it can fluoresce differently depending on the variations of the mitochondrial membrane potential ($\Delta\psi_m$), which is considered as a direct indicator of cells' functional status. JC-1 exists in an aqueous solution as monomer with excitation and emission peaks in the green but under specific conditions it can form aggregates shifting its emission in the red spectrum.¹⁴³ Cells were seeded in a 96 well plate and exposed to the different peptide concentrations as described earlier in this session. For JC-1 live staining, cells were washed once in pre-warmed PBS and incubated at 37 ° C for 20 minutes with JC-1 diluted in complete growth medium (final concentration 2 µg/ml). Afterwards, cells were washed once with PBS to remove the excess dye, media added and live imaged under the fluorescent microscope.

Finally, Alexa Fluor® 568 Phalloidin was used to stain F-actin filaments in cell lines after 24 hrs exposure to FITC-G(IKK)₃I-NH₂ between 6.25 and 50 µM. Cells were seeded in a 96 wells plate (white, clear flat bottom, Greiner Bio One) and exposed to peptides concentrations, then washed once in pre-warmed PBS and fixed and stained for 15 minutes using 4% paraformaldehyde and Hoechst 3342 (2 µg/ml). The fixed plate was subsequently washed twice with PBS and incubated with 150 nM of Alexa Fluor® 568 Phalloidin for 20 minutes at room temperature. To avoid photo bleaching, the whole procedure was executed away from bright light sources. Afterwards, cells were washed twice with PBS and left in of 100 µl of PBS for imaging.

2.7 SEM and TEM techniques

To better investigate the fate of FITC-G(IKK)₃I-NH₂ once internalised by the cells and evaluate its interaction with their membranes, Scanning Electron Microscopy or Transmission Electron Microscopy were performed on HCT-116 after exposure to the fluorescent peptide.

For SEM samples, HCT-116 cells were seeded in 12 well plates (clear flat, Corning, Cat. No. 3513) on glass cover-slips (13 mm diameter, thickness No. 1.5, VWR international, Cat. No. 631-0150) with 1 ml of complete culture medium at a density of 3×10^5 cells per well and incubated at 37 °C overnight. Next day cells were exposed for 24 hrs to different concentration of FITC-G(IKKK)₃I-NH₂ (0.3, 6.25 and 100 μM). An untreated control was prepared as well. Then cells were washed with pre-warmed PBS and fixed in 3% Glutaraldehyde (CAS number 111-30-8, Sigma-Aldrich®) in 0.1 M Sodium Cacodylate (CAS number 6131993, Sigma-Aldrich®) buffer (pH 7.4) overnight. Next day, the samples were rinsed in the Cacodylate buffer and post fixed using 2% aqueous Osmium tetroxide (CAS number 20816-12-0, Sigma-Aldrich®). Then, briefly washed in distilled water, dehydrated in a graded ethanol series and dried in a 50:50 mixture of 100% ethanol and Hexamethyldisilazane (HEX) (CAS number 999-97-3, Sigma-Aldrich®). Finally, samples were dried in 100% HEX and left to dry in a fume hood, overnight. Next day samples were mounted onto a pin-stub using a gold coated Leit-C sticky tab and an Edwards S150B sputter coater and examined using a Philips XL-20 Scan Electron Microscope at 15 kV.

TEM was used to visualize the internalized peptide in the cells and identify the cellular compartments in which FITC-G(IKKK)₃I-NH₂ is majorly localized. A mouse monoclonal antibody anti-FITC labelled with 10 nm gold nanoparticles was used (Aurion, Cat. No. 25583).

Colloidal gold nanoparticles, due to their electron density can be visualized on a TEM as dark spherical dots, which make them perfect for immuno-labelling using electron microscopy^{144, 145}. Briefly, HCT-116 cancer cells were seeded in a 96 well plate at the density of 2×10^4 cells per well in 90 μl of complete culture medium and incubated overnight at 37 °C. After one day attachment, the cells were treated with 6.25 μM of FITC-G(IKKK)₃I-NH₂. Despite what suggested by the antibody manufacturer and the various immunogold labelling protocols available online, it was impossible to successfully label the samples with the monoclonal antibody.

Ultimately, it was decided to mix the antibody with the peptide and then add the formed complexes to live cells. The mouse monoclonal antibody anti-FITC labelled with 10 nm gold nanoparticles was coupled with FITC-G(IKKK)₃I-NH₂ for 6 hrs in the fridge at a 1/100 dilution and then added to cells for either 3 or 24 hrs. Controls with antibody only were prepared and tested. The cells were washed with pre-warmed PBS and fixed.

The samples were originally fixed as a pellet in 4% paraformaldehyde solution for 15 minutes followed by ethanol dehydration in proportion 50:50 with the acrylic LR white resin and 100% ethanol and left overnight on a rotor to mix. Next day, fresh resin was changed twice, and the samples kept on the rotor to keep mixing for 8 hrs. The samples were embedded in fresh LR white resin and put in polyethylene capsules (TAAB, Cat. No. C094). The capsules were covered with parafilm, the lid firmly shut to avoid air and then placed in the oven to polymerise at 60 °C. Next day the resin was checked to be set and sample sections were cut.

An alternative fixation method was performed on some samples, to enhance cellular contrast and reduce image darkness. In this case, specimens were fixed overnight as a pellet using 3% Glutaraldehyde in 0.1 M Sodium Cacodylate buffer (pH 7.4) then washed in the same buffer and post fixed with 2% Osmium Tetroxide. After a brief wash in distilled water, the samples were dehydrated through a series of ethanol solutions with increasing alcohol percentage, cleared in epoxypropane (EPP) (CAS Number 16088-62-3, Sigma-Aldrich®) and infiltrated in 50:50 araldite resin and EPP mixture on a rotor and left it overnight. The samples were replaced twice, over a period of 8 hrs with fresh araldite resin mixture before being embedded and curing in an oven at 60 °C for 48-72 hrs.

For both the fixation procedures, when samples were ready, ultrathin section of approximately 85 nm thick were cut on a Leica UC 6 ultramicrotome onto 200 mesh copper grids and stained for 30 minutes with saturated aqueous Uranyl Acetate followed by Reynold's Lead Citrate for 5 minutes. Sections were examined using a FEI Tecnai Transmission Electron Microscope at an accelerating voltage of 80 kV. The electron micrographs were recorded using a Gatan Orius 1000 digital camera and the Digital Micrograph software.

Both SEM and TEM samples preparations (fixation, resin mounting and TEM sections cutting) were made by Chris Hill, from the Electron Microscopy Facility, University of Sheffield, but the remain of the procedure by me.

2.8 Zebrafish husbandry and injections procedure

2.8.1 Adult fish maintenance

Adult fish were raised in the Bateson Centre (University of Sheffield) aquaria and maintained in a recirculating system at 28.5 °C on a 14:10 hour light/dark cycle, in accordance with UK Home office regulations and under project licence 40/3708 issued to Dr. Fredericus van Eeden.

Adults were fed three times daily with *Artemia* nauplii and maintained at a maximum density of five fish per litre of aquarium water.

Embryos were collected only following natural spawning of adult wild type (WT) from the AB strain, in accordance with United Kingdom Animals (Scientific Procedures) Act 1986 and staged as described by Kimmel ¹⁴⁶.

2.8.2 Transgenic line

To investigate the fate of FITC-G(IKK)₃I-NH₂ in the fish blood stream the transgenic line TG(*kdr1:HRAS-mCherry*), which has red fluorescent blood vessels, was used.

The TG(*kdr1:HRAS-mCherry*) line was generated for the first time by Hogan *et al.*, containing a 6.8 kb fragment of the *kdr*-like promoter upstream of a *ras*-cherry fusion element into one cell-stage embryos ¹⁴⁷.

The transgenic line was kept as heterozygous carriers mediating outcrossing to healthy wild type fish. The fluorescent reporter transgene gives a dominant effect with an expected Mendelian ratio of 50% upon outcrossing heterozygous carriers.

For these experiments, the transgenic fish were in crossed resulting in expected Mendelian ratio of 75% for *mCherry* phenotype. Prior to injection, the embryos were selected for transgene fluorescence to exclude those with the WT phenotype.

2.8.2 E3 medium and Tricaine solution

For embryo growth and incubation, we used E3 medium. A 10-fold stock solution was made using 28.7 g NaCl 5 mM (CAS number: 7467-14-5, Sigma-Aldrich®), 1.27 g KCl

0.17 mM (CAS number: 7447-40-7, Sigma-Aldrich®), 4.8g CaCl₂ 0.33 mM (CAS number: 10043-52-4, Sigma-Aldrich®), 8.17 g MgSO₄ 0.33 mM (CAS number: 7487-88-9, Sigma-Aldrich®) and kept at room temperature. The working solution was made by diluting the stock in UHQ water and adding 100 µl of Methylene blue 0.05% (CAS number: 61-73-4, Sigma-Aldrich®) as fungicide. Ethyl 3-aminobenzoate methanesulfonate, commonly called Tricaine or MS-222 (CAS number: 886-86-2, Sigma-Aldrich®) was used as anaesthetic during imaging, injection procedures and as euthanasia agent. The stock solution contains 400 mg of Tricaine powder dissolved in 97.9 ml of UHQ water and 2.1 ml of Tris base 1 M (CAS number: 77-86-1, Sigma-Aldrich®) while the pH is adjusted to 7.0. The stock solution was stored in the freezer while for embryos manipulation and sedation a working dose of 40 mg/l was used and stored in the fridge.

2.8.3 Peptides and siGLO microinjections

The night prior to injections 4-5 zebrafish pairs were set up in breeding tanks with dividers in place. The dividers kept the males and females separated to avoid fish mating. The following morning the dividers were removed and the fish left undisturbed to mate for at least 20 minutes. With a strainer, eggs were collected and poured into a water filled Petri dish. Embryos were then sorted and lined up against a microscope slide in a Petri dish, forming a single long column. Embryos were injected using 1.0 mm diameter borosilicate glass capillary needles (WPI Florida, USA, Cat. No. TIP02TW1F), previously pulled using a micropipette puller (Sutter instruments California, USA) and mounted on a microinjector PV820 pneumatic Picopump (World Precision Instruments Florida, USA). The needle tip was pinched off using a pair of sharp tweezers. It was left narrow enough to be able to pierce the chorion and yolk without damaging the embryo in the process. The volume of each injection was calibrated using a 10 mm/0.1 division stage micrometer immersed in oil and a dissection microscope S6E (Leica). Since a droplet with diameter of 0.1 mm contains 500 pl of injection material, the pressure was adjusted to have drops of that size^{148, 149}. Needles were loaded using a microloader pipette and embryos were injected with volumes between 0.5 and 2 nl. Embryos were injected within the first 20 minutes after spawning, when they are still at the one-cell stage and before they start the cellular

divisions. In this way, there are higher chances to hit the cytoplasm and not the yolk together with the certainty that the injected solution will be equally distributed in all the embryo's cells.

At least 50 embryos per concentration were injected and several uninjected embryos were kept as controls. After completion of each column of eggs, they were moved into a Petri dish, filled with E3 medium. At the end of the injections procedure, all the Petri dishes were transferred in an incubator at 28 °C. Different concentration of A₉K peptide (150 - 4000 pg) and FITC-G(IKKK)₃I-NH₂ (6.25-4000 pg) per embryo were injected. 5 hours post fertilisation (hpf) the Petri dishes were checked and the unfertilised eggs removed to minimise the risk of bacterial and fungi infections. Embryos were checked after 1 and 3 days post fertilisation (dpf) and the number of survivors and dead embryos recorded. Before reaching 5.2 dpf embryos were anaesthetised using Tricaine (40 mg/l) and sacrificed in a bleach solution.

siGLO red (Dharmacon) and complexes FITC-G(IKKK)₃I-NH₂ / siGLO were injected in one-cell stage embryos following the exactly same procedure just described. The fluorescent siRNA was injected in a concentration range of 20-80 pg per embryo while complexes were made with 20 pg of siGLO and 20 or 80 pg of peptide.

A stereomicroscope, Leica MZ16, was used to check embryos at 5 hpf, 1 and 3 dpf while images of embryos were acquired using a Leica M165 FC stereomicroscope. Fluorescent images of embryos injected with siGLO and FITC-G(IKKK)₃I-NH₂ were taken using the fluorescent stereomicroscope Zeiss Axio Zoom V16.

2.8.4 Caudal injections in 4 dpf larvae

The transgenic line, TG(*kdrl:HRAS-mCherry*), was paired in breeding tanks and left to mate. Embryos were collected and transferred into a Petri dish filled with E3 medium. Unfertilised eggs were removed and embryos were left to develop for 4 days. On the 4th day, the embryos can be arbitrary referred as larvae. Larvae expressing the fluorescent transgene were selected for injection with either FITC-G(IKKK)₃I-NH₂ or just the control fluorophore FITC and were injected in the caudal vein at a concentration of 25 pg/nl. The larvae were anaesthetised with Tricaine (40 mg/l) and then mounted on a Petri

dish lid in 3% low-melting point agarose, containing Tricaine. Embryos were positioned laterally to allow access to the caudal vein before setting of the agarose ¹⁵⁰. The needle was loaded with FITC or the peptide solution, mounted on microinjector PV820 pneumatic Picopump (World Precision Instruments Florida, USA) and calibrated to dispense 0.5 nl per pulse, as described previously.

Once injected, the embryos were checked under a fluorescent stereomicroscope (Leica M165 FC) and mounted in a glass capillary tube (Transferpettor caps, DE-M, 50 µl, green) with 3% low-melting point agarose and imaged using a Zeiss Lightsheet Z.1 and analysed with ZEN 2014 SP1 software ¹⁵¹.

2.9 Endocytic pathways and RNAi genome-wide screen

The mode of entry of the peptides into the cell were investigated using the fluorescent FITC-labelled versions of A₉K and G(IKK)₃I-NH₂ peptides. The data with FITC-A₉K were collected by the MSc student Joanna Henry as part of her MSc project, but under my supervision and experimental planning.

2.9.1 Internalisation speed of FITC-G(IKK)₃I-NH₂

The presence of FITC attached on the N-terminal of G(IKK)₃I-NH₂ allowed to directly track the peptide internalisation. Different concentrations, 6.25 to 100 µM, were tested at a 24 hrs exposure time on HCT-116 and HDFs. Two concentrations of FITC-G(IKK)₃I-NH₂, 12.5 and 25 µM, were chosen and their rate of internalisation tested on both HCT-116 and HDFs cells at shorter time points (15 mins to 3 hrs). Cells were fixed and stained in the Hoechst as previously stated. The rate of the peptide complexed with a nucleic acid was also tested with 75 nM of red fluorescent siGLO (Dharmacon) complexed to FITC-G(IKK)₃I-NH₂ and transfected in both cell lines. As for the peptide only experiment, different time points were included (15 mins to 3 hrs) while DharmaFECT1 (DF1) was used as the positive control. 4/1 and 24/1 were the tested peptide/siRNA ratios. The complete peptide/siRNA complexing procedure could be found in the DNA/RNA transfection section of this chapter.

2.9.2 The endocytic cold assay

With temperatures below 37 °C, many cellular functions, such as vesicular trafficking, are slowed down. It has been reported that at a temperature of 4 °C, all the endocytic pathways are completely blocked^{152, 153}. Exploiting this information, a cold assay was performed to evaluate the uptake of FITC-G(IKK)₃I-NH₂ in a low temperature environment.

HCT-116 cancer cells were seeded in 6 well plates (clear, flat bottom, Corning, Cat. No. 3516) at the density of 8×10^5 and incubated overnight at 37 °C. The following day the medium was removed and the plate washed twice in cold PBS (4 °C) to block endocytosis. 900 µl of cold complete growth medium were added to the wells together with 100 µl of 12.5 µM FITC-G(IKK)₃I-NH₂. Plates were then left under the hood for 30 minutes in ice, keeping the temperature below 4 °C.

Expired the incubation time, the medium was removed and cells were washed in cold PBS. Afterwards they were fixed and stained in the usual 4% paraformaldehyde and Hoechst 33342 (2 µg/ml) solution. To evaluate the ability of HCT-116 in restoring the endocytic functions, some cells instead of being fixed were moved in the incubator at 37 °C for further 3 hrs. In addition to that, two different experimental conditions were set up; some cells were kept in the original medium (complete culture medium and 12.5 µM FITC-G(IKK)₃I-NH₂), while for some others the original medium was discharged and replaced with new warm one lacking the peptide solution.

Controls were prepared as well; no cold solutions were used this time, and after the peptide addition, cells were directly placed in the incubator at 37 °C for 30 minutes or 3 hrs. Expired the time, plates were normally fixed and stained with the 4% paraformaldehyde and Hoechst 33342 (2 µg/ml) solution.

Images from the plates were acquired the fluorescent microscope IN Cell Analyzer 2200 (GE Healthcare) analysed with In Cell Developer Toolbox 1.9 (GE Healthcare).

2.9.3 Extracellular peptide acid stripping

Aldehyde fixatives, such as paraformaldehyde, can produce holes in the cell surface allowing the passage of material in the cytoplasm during fixation¹⁵⁴. This might adversely affect the amount of peptide observed inside fixed cells. To evaluate whether this is the case, cells were washed with an acid solution before fixation¹⁵⁵.

First either 6.25, 12.5, 25 or 50 μM FITC-G(IKK)₃I-NH₂ was incubated with HCT-116 and HDFs cells for a 24 hrs exposure. Controls cells with no peptide were prepared. Cells were incubated with the acid wash which was, composed of 50 mM glycine-HCl (CAS number: 6000-43-7, Sigma-Aldrich®), 2 M urea (CAS number: 57-13-6, Sigma-Aldrich®) and 100 mM NaCl at a pH of 3, for 5 minutes then washed in PBS 3 times to return the pH to normal conditions. The sequence was repeated 3 times, then cells were fixed and stained with the 4% paraformaldehyde and Hoechst 33342 (2 $\mu\text{g}/\text{ml}$) solution. Following fixation, cells were stained using CellMask Orange (Thermo Fisher Scientific, Cat. No. C10045). Images were acquired using the fluorescent microscope (ImageXpress® Micro System, Molecular Devices) and segmentation of peptides analysed with the MetaXpress® Software 5.3.01 (Molecular Devices).

2.9.4 Time lapse imaging

Live cell imaging was performed on 6.25 and 100 μM FITC-G(IKK)₃I-NH₂ in HCT-116 cells for 18 to 24 hrs after peptide addition, acquiring a picture every 30 minutes using the fluorescent microscope IN Cell Analyzer 2200 (GE Healthcare) in bright field and fluorescent mode in 96 well plates at the density 2.5×10^4 in 90 μl per well. The following day, 10 μl of the appropriate peptide concentration were added to each well. Some of the wells were loaded with 10 μl of UHQ water and considered as negative control. The plate was then positioned in the microscope and the imaging recording started. At the end of the acquisitions the plates were fix and stain with 4% paraformaldehyde and Hoechst 33342 (2 $\mu\text{g}/\text{ml}$) solution and acquired again using ImageXpress® Micro System, Molecular Devices fluorescent microscope for segmentation analysis.

2.9.5 HCT-116 recovery from FITC-G(IKKK)₃I-NH₂ challenge

HCT-116 cancer cells are sensitive to FITC-G(IKKK)₃I-NH₂ and depending on the concentration, a decrease in cellular viability is observed. The cells ability to recover from high peptide concentration exposure was therefore evaluated.

Briefly, 2.5×10^4 cells were seeded in 90 μ l per well of a 96 well plate and allowed to settle and grow overnight. The following day, 10 μ l of the fluorescent peptide solution was added and the plate incubated for 30 minutes at 37 °C. The plate was then put overnight in the incubator. In some wells, the peptide solution was removed and new complete culture medium added. The following day, the plate was fixed and stained with the usual solution of 4% paraformaldehyde and Hoechst 33342 (2 μ g/ml). Live bright field images were acquired using the IN Cell Analyzer 2200 (GE Healthcare) microscope while fixed plate was instead acquired with ImageXpress® Micro System fluorescent microscope.

2.9.6 RNAi screen to elucidate the peptide uptake in cancer cells

To evaluate the genes controlling cellular uptake of fluorescently labelled FITC-A₉K a mini screen was performed while in the case of FITC-G(IKKK)₃I-NH₂ a RNAi screening assay was developed first, followed by a screen using more than 200 siRNAs targeting genes involved in endocytic pathways.

2×10^3 HCT-116 cells were seeded in 384 well plates and were reverse transfected, using DF1, with 30 nM final concentration of siRNAs for 3 days and then incubated with 6.25 μ M of FITC-A₉K or FITC-G(IKKK)₃I-NH₂ peptides for 24 hrs. Cells were fixed and stained with Hoechst 33342 (2 μ g/ml). Cell images were acquired with the ImageXpress® Micro System, Molecular Devices fluorescent microscope and the fluorescence intensity analysed using the MetaXpress® Software 5.3.01 (Molecular Devices). The data obtained were subsequently analysed to calculate the robust Z score of each silenced gene and to quality control the data.

For the mini screen on FITC-A₉K, actin related protein 2/3 complex subunit 1 B (ARPC1B), adaptor related protein complex 2 subunit alpha 2 (AP2A2), adaptor related

protein complex 2 subunit beta (AP2B1), clathrin light chain A (CLTA), clathrin light chain B (CLTB) and clathrin heavy chain (CLTC) siRNAs were chosen as positive controls, due to their function in endocytosis of bio-macromolecules¹⁵⁶⁻¹⁵⁸. Red fluorescent siGLO was selected as positive control for the transfection procedure, while 5 non-targeting siRNAs (On-TARGET*plus* non-targeting controls #1, #2, #3, #4 (each a single siRNA) and the non-targeting pooled siRNA of each of the 4 single controls were selected as negative controls.

For the development of the screen on FITC-G(IKK)₃I-NH₂, a collection of siRNAs defined in a plate (assay development plate 2 (ASD2)) specifically designed for genome-wide RNAi screens by the Sheffield RNAi Screening Facility (SRSF) (<http://www.rnai.group.shef.ac.uk/>) was used to develop the assay. The plate contained ~100 siRNAs, actin related protein 2 homolog (ACTR2), ADP-ribosylation factor 6 (ARF6), caveolin 1 (CAV1), clathrin heavy chain (CLTC), dynamin 2 (DNM2), myosin Va (MYO5A), myosin Vb (MYO5B), myosin Vc (MYO5C) and ras-related protein 7a (RAB7A) which were believed to be good positive control siRNAs¹⁵⁷⁻¹⁶⁴ and 4 non-targeting siRNAs (On-TARGET*plus* non-targeting control #2, #3, #4 #5). The plates used for the focussed larger screen on FITC-G(IKK)₃I-NH₂ fluorescent peptide were a specific library of Traffic-ome targeting siRNAs and were specially designed by Doctor Andrew Peden and Professor Elizabeth Smythe (Biomedical Science Department, Sheffield University).

2.10 Graphic and statistical analyses

All the images acquired and described in this chapter were ultimately processed with Image J to adjust brightness and contrast to the same level. Prism GraphPad was used to create graphs while the figures composition was made using Corel Draw. Where needed, Student T-test was used to test for statistical significance. The robust Z-score of RNAi high-content screen was calculated using Microsoft Excel.

3 A₆K AND A₉K PEPTIDES

Short cationic peptides have been extensively studied because of their ability to kill bacteria through the disruption of the lipid bilayer structure^{165, 166}. They are defined as antimicrobial peptides (AMPs) and are naturally part of invertebrate and vertebrate innate immunity systems. Their structure and physical properties allow them to selectively target bacterial membranes of both Gram-negative and Gram-positive microbes, due to the microbial surface containing net negative charge, caused by the lipopolysaccharides (LPS) (Gram-negative) and to the acidic polysaccharides (Gram-positive)^{48, 167}. Most of the AMPs have an amphipathic structure, which seems to be crucial for their antimicrobial activity^{61, 168, 169}. The interaction with negatively charged moieties is not only related with outer membrane lipids but also with other biomolecules such as nucleic acids and phosphorylated proteins. With the aim of creating more effective target antibiotics, the publications related to AMPs have substantially increased in recent years. Hundreds of AMPs have been isolated and characterised in order to better understand their mechanism of action, while many more have been *de novo* designed and synthetically produced⁵¹.

One class of *de novo* designed peptides are surfactant-like peptides (SLPs) having hydrophobic amino acids as tails and hydrophilic amino acid heads. Tails are generally composed of non-polar amino acid residues (G, A, V, I, L, P or F). Heads are more variable; they could contain positively (H, K or R) or negatively (D or E) charged amino acids or they could be composed of a combination of these two groups¹⁷⁰. The two amphiphilic parts can even be swapped but this rearrangement seems not to be particularly viable for functionality¹⁷¹. It is the hydrophobic tail, with its dislike for water, which drives the molecular self-assembly into different nanostructures (nanotubes, nanofibres, nanorods, nanovesicles or membrane sheets). The hydrophilic head faces the aqueous phase while the tail is buried inside the core of the molecule¹⁷². A₆K and A₉K hydrophobic tails are composed by a sequence of alanines, while the positive hydrophilic head in this case is a lysine^{173, 174}. When dissolved in aqueous solutions and under neutral pH conditions, A₆K and A₉K self-assembled into ordered structure, mainly through hydrophobic interactions¹⁷⁵. The tail length is extremely important for the self-assembly process as its hydrophobicity can be modulated

depending on the number of amino acids normally a typical tail is composed of 3 and 9 residues. An increased hydrophobicity (due to a longer tail) involves the development of different aggregates because solubility, together with the Critical Aggregation Concentration (CAC), progressively decreases^{175, 176}.

A₆K self-assembles in long nanofibers while A₉K forms short nanorods¹⁷⁴. The long and stable nanofibres formed by A₆K have lengths in excess of 1 µm and diameters around 8 nm while the nanorods formed by A₉K have much shorter lengths, normally less than 100 nm and diameter around 3 nm^{174, 177}. Both peptides have been previously tested against bacteria to evaluate their antimicrobial effects^{126, 177}. In a paper published by Chen *et al.*, A₆K and A₉K were successfully used against *E. coli* DH5α and *S. aureus*; the pair exhibited, with increasing concentrations, antibacterial effect.

However, A₉K is the peptide with highest efficacy among the two. A possible explanation of this difference can be attributed to the distinct grade of hydrophobicity that these peptides possess. With the increase of the hydrophobic alanine residues, the total molecular hydrophobicity of A₉K is of course enhanced and this enables the peptide to have stronger self-association and aggregation tendencies compared to A₆K. These characteristics, together with the cationicity given by the lysine, promote a better initial contact with the negatively charged bacterial surface via electrostatic interactions causing increased antimicrobial activity¹⁷⁸.

However, their capability of delivering DNAs/RNAs into cells has not been investigated. For this reason, part of this PhD project was focused on the use of two cationic peptides A₆K and A₉K for the delivery of ODNs and siRNAs into cancer cells.

3.1. DNA/RNA binding abilities *in vitro* and cell transfection efficiency

3.1.1 Gel electrophoresis

In the last couple of decades, amphiphilic cationic peptides have been extensively studied as possible new vectors for gene delivery and gene silencing, especially using plasmid DNA¹⁷⁹⁻¹⁸⁴. One of the main purposes of this PhD project is to use amphiphilic peptides as transfection vectors for DNA or RNA molecules. In order to do that, the peptide efficiency in binding nucleic acids was initially tested using the agarose gel retardation technique. Because of A₆K and A₉K abilities to interact with anionic moieties, it was hypothesised that each peptide would bind nucleic acid. Agarose gel electrophoresis was used to separate DNA by size (e.g. smaller nucleic acids migrate faster than larger molecules), based upon the electrical field moving the negatively charged DNA toward the positive electrode. Peptide binding to the nucleic acids would prevent migration towards the cathode, since the negative charges would be nullified by the peptides positive ones. As consequence, when the gel is visualized under UV light, the DNA will be immobilised in the wells and bound to the peptide.

Complexes at different cationic/anionic charge ratios (0.5/1; 1/1; 2/1; 3/1 and 5/1) were made with FAM-labelled oligonucleotides (ODNs) according to the calculations explained in the Materials and Methods section “2.3.1 Peptide/ODN complex formation”. Figure 1 shows the wells with only peptides or ODNs, included as negative and positive controls (lanes 1 and 7). The concentration of only peptide was the same of the highest charge ratio complex; 1 µg/µl concentrated solution for A₆K and 1.35 µg/µl concentrated solution for A₉K, both corresponding to 1.63 mM. The amount of DNA in the positive control was 1 µg/well, as for the other samples. Surprisingly A₆K did not bind the DNA at any of the tested concentrations and all the nucleic materials migrated to the positive electrode (Figure 1 a). Contrary to this, A₉K inhibited ODN migration through the agarose gel matrix. An appreciable different DNA intensity is observed inside the wells with an increase of charge ratios, followed by a weaker migration

through the positive electrode, as seen by the lack of lower bands in lanes 5 and 6 (Figure 1b).

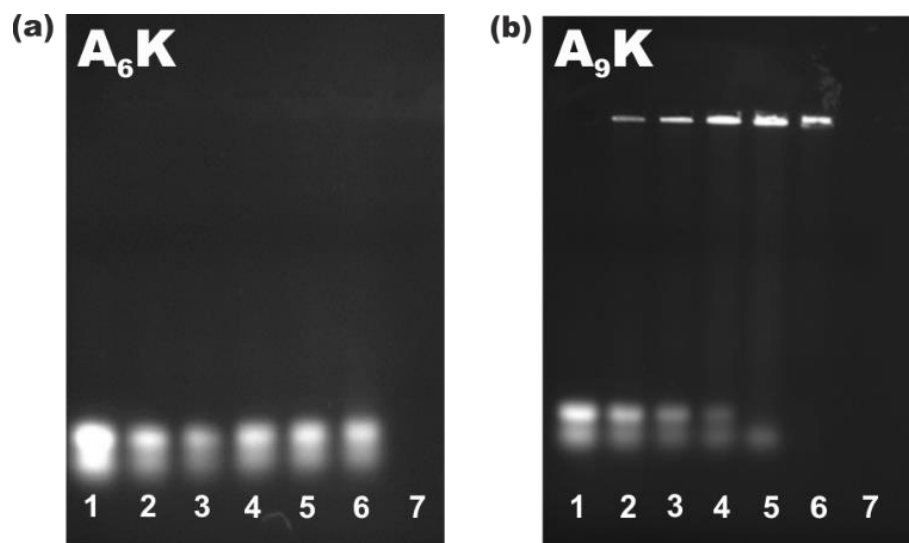


Figure 1. ODN binding assay for peptides. Agarose gel electrophoresis with A₆K (a) and A₉K (b) complexed with FAM-ODNs. The first line on the left was loaded with ODNs and represents the positive control. Complexes were made at 0.5/1; 1/1; 2/1; 3/1 and 5/1 charge ratios (from line 2 to 6 respectively). The last lane (7) of each group was loaded with peptides only and it is not visible with the EtBr staining. Unbound nucleic acids travelled unimpaired through the gel, close to the bottom of each image. Upper bands represent binding of peptide with nucleic acid.

3.1.2 ODNs and siRNAs transfection

After the preliminary results achieved with the gel retardation assay, cell transfection was carried out using the same ODNs, but with A₉K, since A₆K showed no ability to bind to DNA. A cancer and non-cancer cell lines were selected for study. A431, a human epithelial cell and HDFs, primary human dermal fibroblasts cells were transfected with complexes of 0.05 μ g of ODNs (1.6 μ M) and an increasing amount of peptide (0.1; 0.25; 0.5/1; 1/1; 2/1 and 3/1) ratios compared to the DNA. Transfection with Oligofectamine was used as positive control, while the negative control is represented by free ODNs mixed to culture medium and shows that, without a carrier, the DNA molecules cannot cross the plasma membrane.

Figure 2 shows an experiment to test whether A₉K, in a complex with an ODN, can bind and translocate into cells using wide-field microscopy. Most ODNs work by acting in the nuclear compartment, so this experiment was designed to test whether A₉K can locate there with its cargo. The positive control, using the commercial transfection reagent, Oligofectamine, reveals that when complexed with FAM-labelled ODNs is capable of entering the cell and locating in the nucleus. A₉K can enter cells, together with its cargo, and the process is concentration dependent, as an increase in A₉K is commensurate with green FAM-ODN/A₉K presence. However, the complexes do not locate to the nucleus of the A431 cells, as compared to the transfection control using Oligofectamine, suggesting that A₉K is not able to cross the nuclear membrane.

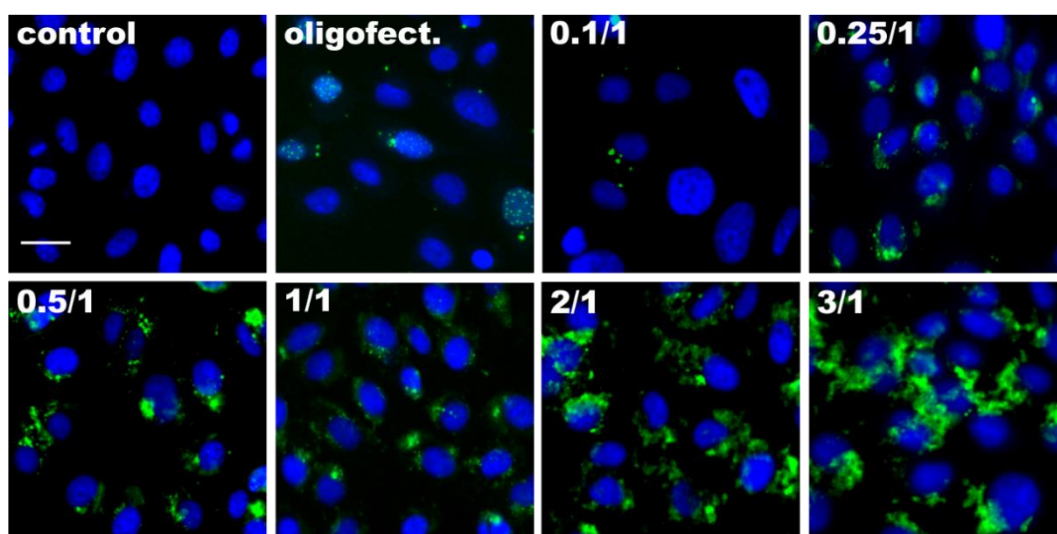


Figure 2. A₉K efficiency in delivery fluorescently labelled ODNs into epithelial cancer cells. A431 cancer cells were transfected for 24 hrs with 0.05 μ g of FAM-labelled ODN (corresponding to 1.6 μ M) and an increasing charge ratio of A₉K. Oligofectamine (oligofect) has been used as positive control and transfection has been made according to the manufacturer's protocol, while un-complexed ODNs mixed to the culture medium represented the negative control (control). The images show the progressively higher amount of ODNs transfected into cancer cells directly proportionate to the A₉K/FAM-ODN charge ratio changes. Hoechst 33342 (2 μ g/ml) (blue) was used as nuclear staining, FAM-labelled ODN in green. Bar = 25 μ m. All images are scaled to the same size.

To confirm the presence of the fluorescent ODNs inside the cells, confocal microscopy was used, as thin section stacks could be used to determine a more precise location of the particles inside cells. A₉K/nucleic acid complexes between 0.1/1 and 1/1 charge ratios were assessed. The images at higher resolution showed that, at the charge ratios considered, all the fluorescent DNA was present inside the cells, while with 1/1 some of the DNA material was visible also outside the cells (Figure 3). When internalised, the fluorescently labelled ODNs appeared like small distinctive puncta but when attached on the cell membranes they tended to clump together forming big aggregates.

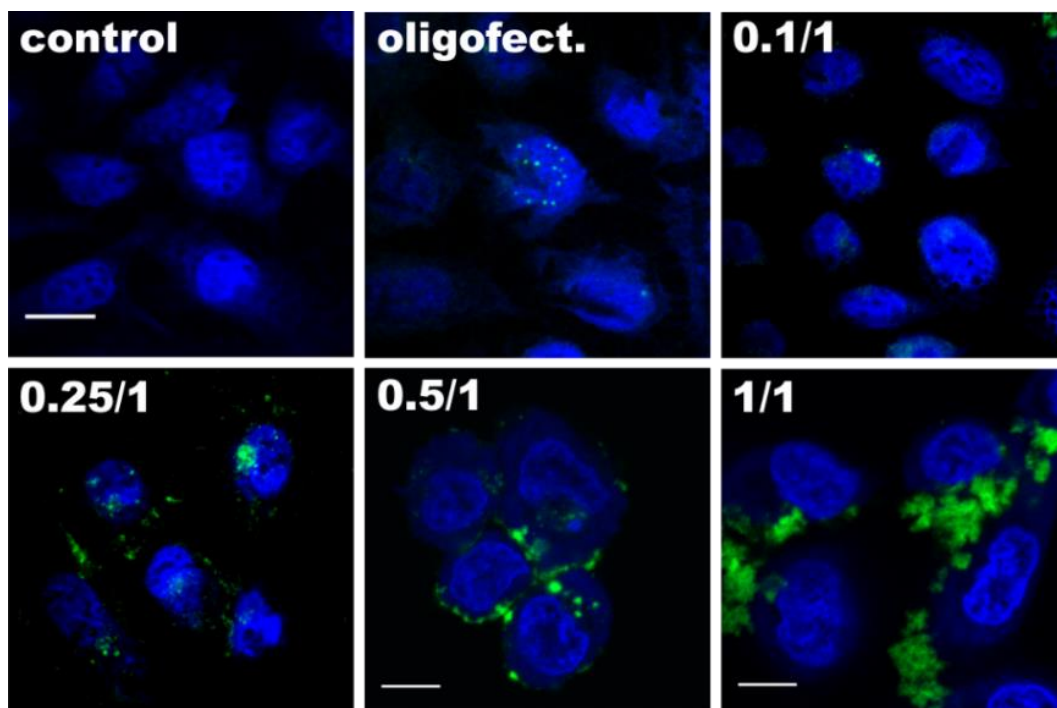


Figure 3. Confocal examination of the intracellular localisation of fluorescent ODN molecules after transfection with A₉K peptide. Confocal images of A431 cancer cells transfected for 24 hrs with of 0.3 µg FAM-labelled (corresponding to 1 µM) and increased charge/ratios of A₉K. Oligofectamine™ (oligofect) has been used as positive control and transfection has been made according to the manufacturer protocol, while un-complexed ODNs mixed to the culture medium represented the negative control (control). The images show the localisation of the fluorescent ODNs within the cellular boundaries according to the peptide ratio used for transfection. Hoechst 33342 (2 µg/ml) (blue) was used as nuclear staining. FAM-labelled ODNs in green. Bar 25 = µm. All the images are scaled at the same size except for 0.5/1 and 1/1 ratios where the scale bar measures 10 µm and the magnification is 100X.

The Z stacks were composed by several sections taken a few microns apart from each other. In this way, multiple focus planes of the cells were imaged and the exact location of the green fluorescent DNA could be easily determined. In Figure 4 there are some stacks taken from the previous figure's 0.5/1 peptide/ODN ratio showing the appearance of the green puncta according to the focal plane. This proved that the DNA was correctly internalised into the cytoplasm.

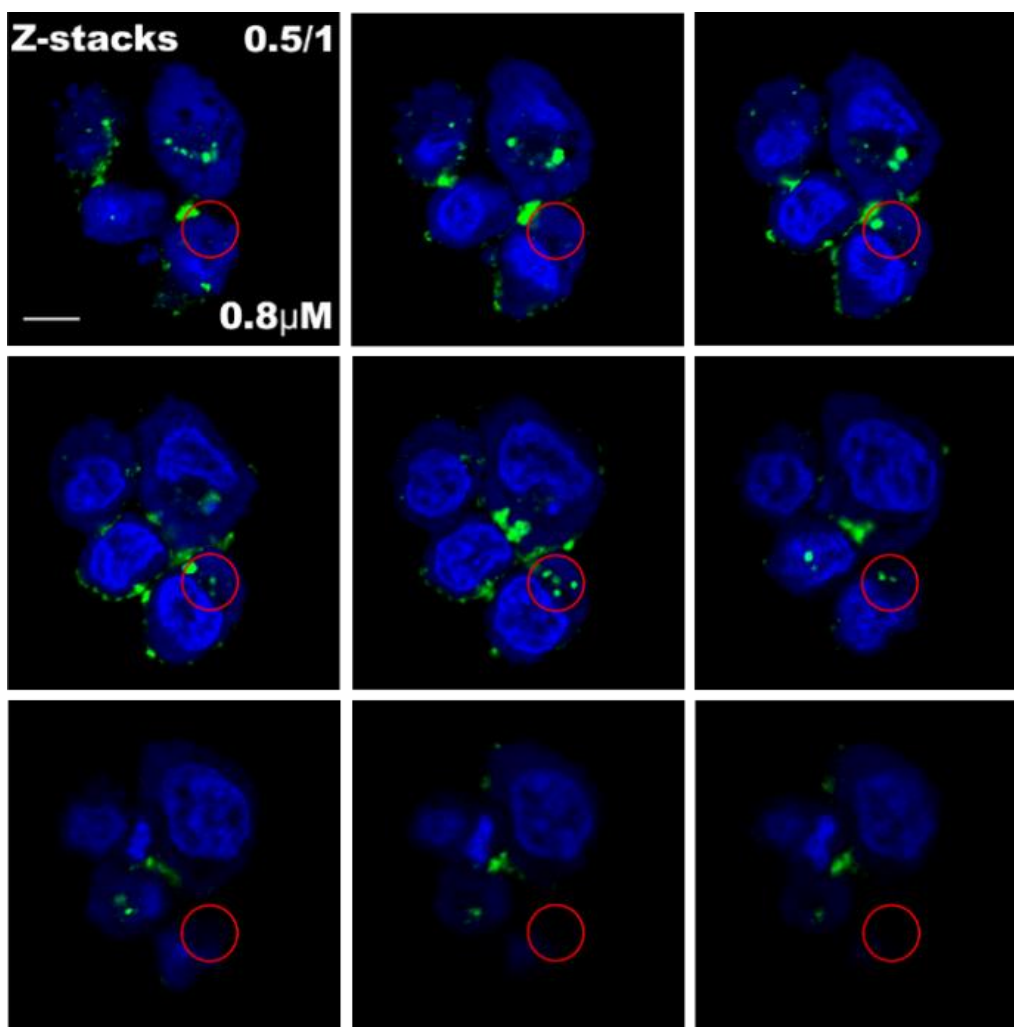


Figure 4. Stack analysis of sequential confocal images of fluorescent ODN molecules in A431 cancer cells. A431 cancer cells transfected for 24 hrs with of 0.3 μg FAM-labelled (corresponding to 1 μM) and 0.5/1 charge/ratio of A₉K. The images show Z-stacks of the same group of cells acquired using confocal microscopy. The pictures were taken in 0.8 μm sections and display the ODNs positioned in the middle sections of the stack highlighted with red circles. Hoechst 33342 (2 $\mu\text{g}/\text{ml}$) (blue) was used as nuclear staining. FAM-labelled ODNs in green. Bar 10 = μm . All the other images are scaled at the same size.

The literature has a few examples of peptides, similar to A₉K, used to penetrate cells, but most have chosen cancer cells to test out their effectiveness in cell transformation^{105, 122}. In this study, it was also important to determine whether A₉K, can enter and deliver a cargo of nucleic acids to a non-cancer cell type, such as fibroblasts, so that this could be used as a reference experiment for future use. Similar to the previous experiments, A₉K was complexed with FAM-labelled ODNs and incubated with Human dermal neonatal foreskin fibroblasts at different charge ratios. Figure 5 shows representative images acquired using the high throughput, wide-field microscope. The control positive transfection reagent, Oligofectamine, shows large amounts of green fluorescence in cytoplasm of each cell. At lower charge ratios (0.1/1 to 0.5/1) little green can be seen in each of these images and it is only with higher charge ratios that the FAM-ODNs complexed with A₉K can be observed and is mainly surrounding cells, forming clumps.

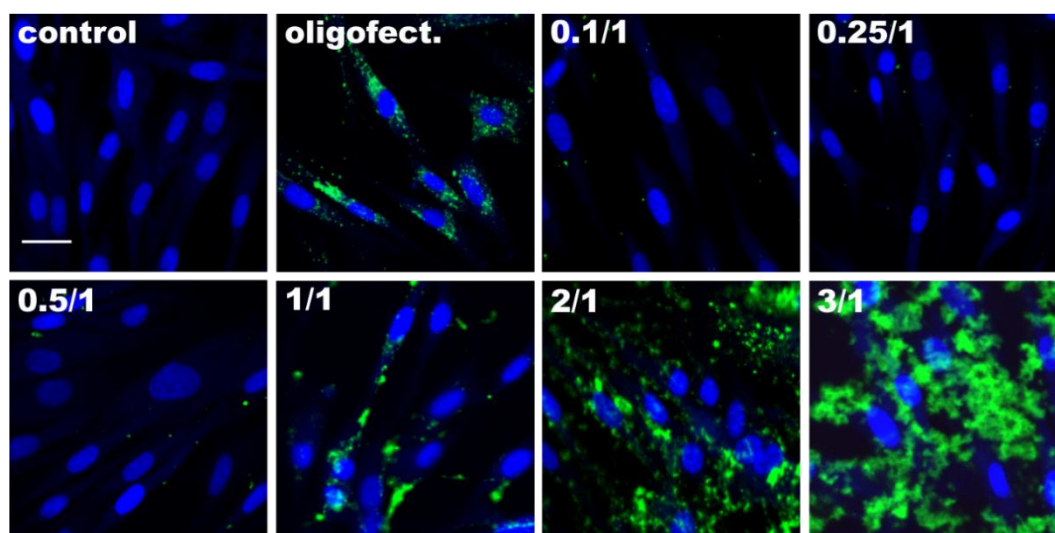


Figure 5. A₉K delivery of fluorescently labelled ODNs into a non-cancer cell line. HDFs primary cells were transfected for 24 hrs with 0.05 μ g of FAM-labelled ODNs (corresponding to 1.6 μ M) and increased charge/ratios of A₉K. Oligofectamine has been used as positive control and transfection has been made according to the manufacturer protocol, while un-complexed ODNs mixed to the culture medium represented the negative control (control). At low ratios, the peptide has poor transfection efficiency and fewer green puncta can be seen, while at high ratios many fluorescent puncta are visible, in the form of big clumps and mainly externally localised. Hoechst 33342 (2 μ g/ml) (blue) was used as nuclear staining. FAM-labelled ODNs in green. Bar 25 = μ m. All the images are scaled at the same size.

In addition to antisense oligonucleotides, gene expression can be modulated using RNAi, a form of posttranscriptional RNA silencing that causes the reduction or loss of gene activity due to degradation by nucleases of mRNAs transcripts ¹⁸⁵. Synthetic double-stranded RNA molecules (siRNAs) of 21-23 nucleotides can be used to trigger the RNAi pathway and selectively silence the gene expression of targeted proteins. For this reason, siRNA-based therapies are rising as novel approach to treat several human conditions, cancer included ¹⁸⁶. Unfortunately, there are still many barriers that preclude the widespread of siRNA as effective therapeutics; these include toxicity towards host cells, activation of the immune response and off-targets effects ^{187, 188}. Because the toxicity is often caused by the vectors used to deliver siRNAs into the system, many studies are performed to try reducing, as much as possible, their adverse effect. Liposomes, polymers and nanoparticles showed promising potential, but are still a long way off before the development of effective siRNA delivery ¹⁸⁷.

For this purpose, A₉K was tested as a possible carrier and complexed with siRNA molecules. Transfection experiments were conducted in both cancer and non-cancer cell lines and A₉K was tested for the delivery of siRNAs into cells. Red fluorescent non-targeting siGLO (Dharmacon) was selected as the molecule to be transfected in the cells at the concentration of 75 nM. Transfection using DharmaFECT1 (DF1) was added as positive control while free siGLO dissolved in the culture medium was considered the negative control. A431 human epithelial cancer cells and HDFs, human primary fibroblasts were selected as the model cell lines for the experiment., Figure 6, shows internalisation by A₉K of siGLO in the A431 cancer cells. The amount of red fluorescent siGLO found inside the cells correlates with the increase in A₉K used for transfection, and for some ratios (2/1 and 3/1), the level of transfection is improved compared to DF1 reagent. Surprisingly, high charge/ratios did not produce big clumps visible outside the cells as it was noticed previously with the ODN transfection.

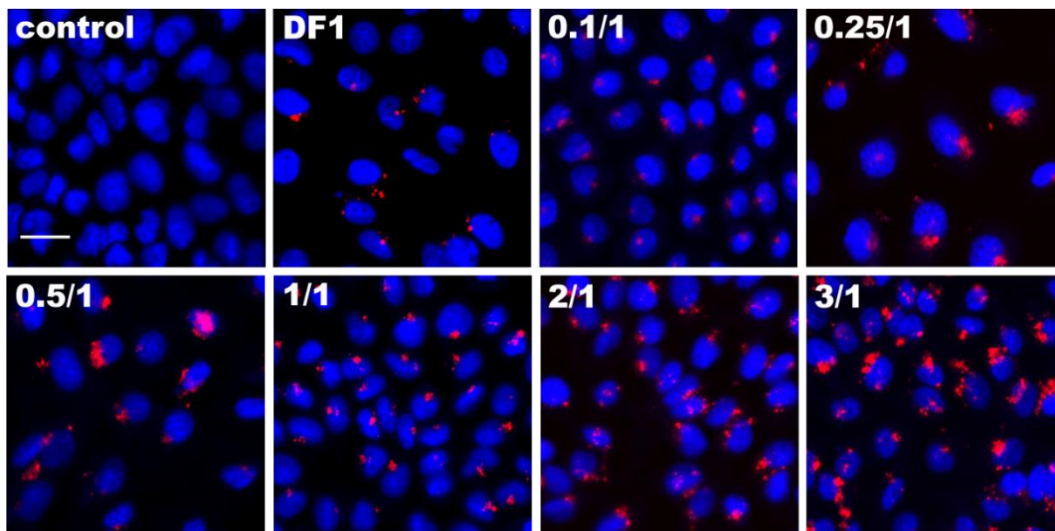


Figure 6. A₉K delivery of fluorescently labelled siRNA molecules into epithelial cancer cells. A431 cancer cells were transfected for 24 hrs with 75 nM of siGLO, (red) with increasing charge/ratios of A₉K. DharmaFECT1 (DF1) was used as a positive control, while un-complexed siGLO mixed to the culture medium represented the negative control (control). Images show the transfection efficiency of A₉K in delivery siRNA molecules in cancer cells with increased ratio producing more red (siRNA) inside cells. Hoechst 33342 (blue) was used as nuclear staining. Bar = 25 μm. All the images are scaled to the same size.

To confirm the presence of fluorescent siGLO located in the cell cytoplasm, confocal microscopy was used. Figure 7 shows high-resolution images of A431 following transfection with either DF1 or peptide with different ratios.

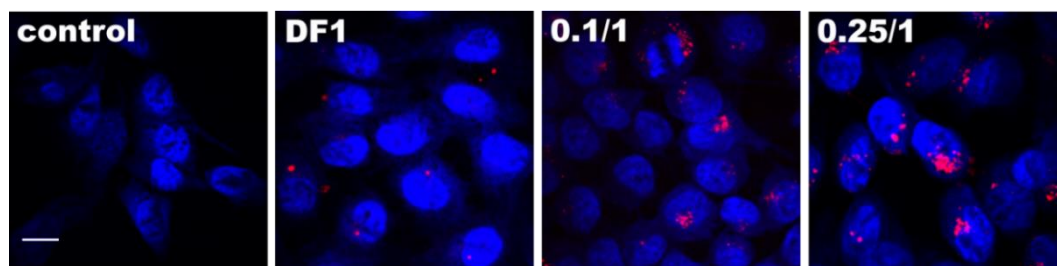


Figure 7. Confocal examination of the intracellular localisation of fluorescent siRNA molecules after transfection with A₉K peptide. Single sections of confocal images of A431 cancer cells transfected for 24 hrs with 75 nM of siGLO, red fluorescent indicator and increased charge/ratios of A₉K. DharmaFECT1 has been used as positive control. Un-complexed siGLO mixed to the culture medium represented the negative control (control). Images show complexes of peptide and siGLO localised in the cytoplasm acquired using confocal microscopy. Hoechst 33342 (2 µg/ml) (blue) was used as nuclear staining. Bar 25 = µm. All the images are scaled to the same size.

The confocal images were taken as z stacks at 0.3 µm slices. Several multiple focal planes of the same group of cells could be observed in detail. Figure 8 shows the stacks taken for the 0.1/1 ratio with progressively appearing and disappearing of the red siRNA puncta according to the focal plane.

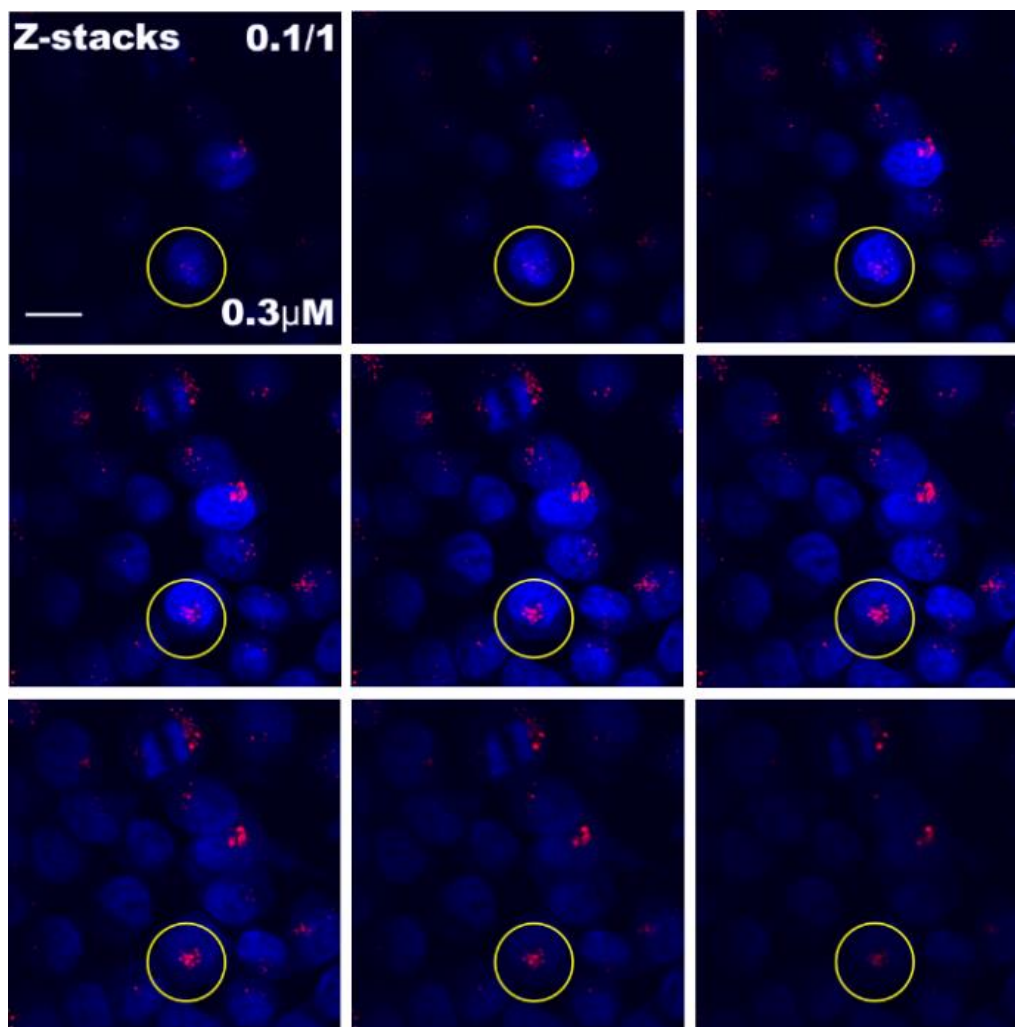


Figure 8. Stack analysis of sequential confocal images of fluorescent siRNA molecules in A431 cancer cells. Cells were transfected for 24 hrs with of 75 nM siGLO, (red) at 0.1/1 charge/ratio of A₉K. Each image shows a 0.3 μm slice from a Z-stacks series of the same cells acquired using the confocal microscope. The images display the siRNAs positioned in the centre section within the stack, confirming an intracellular localisation (yellow circles). Hoechst 33342 (2 μg/ml) (blue) was used as nuclear staining. Bar 25 = μm. All the images are scaled to the same size.

When A₉K was used to transfect the fibroblasts, a contrary result showed poor siGLO internalisation (Figure 9). The positive control DF1 showed efficient uptake, however, in the peptide transfection conditions, even at the highest ratio (3/1), the transfection of red siGLO puncta inside the cells was limited.

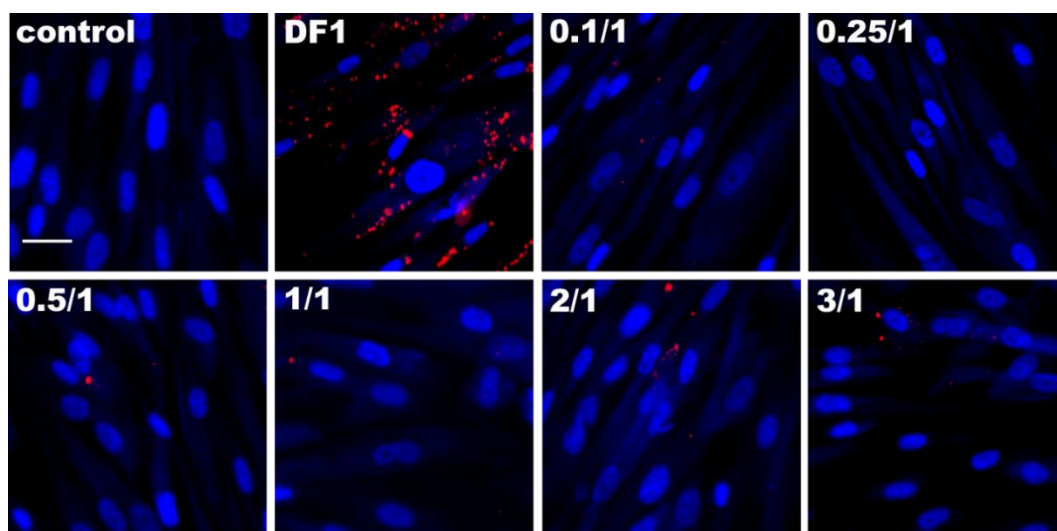


Figure 9. A₉K delivery of fluorescent siRNA into fibroblasts. HDFs primary cells were transfected for 24 hrs with 75 nM of siGLO, (red) at increasing charge/ratios of A₉K. DharmaFECT1 was used as positive control. Un-complexed siGLO mixed with medium represent the negative control (control). Images show poor efficiency of A₉K transfection in fibroblasts with siRNA molecules. Hoechst 33342 (2 µg/ml) (blue) was used as nuclear staining. Bar 25 = µm. All the images are scaled at the same size.

3.1.3 Evaluation of A₉K transfection efficiency in a 3D cancer cellular model

Many treatments used to induce regression in tumours fail to penetrate the centre of the mass and therefore are excluded during the treatment process¹⁸⁹. For this reason, *in vitro* models of cancers have been widely used in research to provide a more relevant bridge between cell lines grown in 2D and *in vivo* tumours¹³⁵. There are many types of spheroid models described over the past four decades, some of which are widely used in cancer research¹⁹⁰.

To evaluate the ability of A₉K to infiltrate tumours and its potential use as a vector for a drug or a biologic delivery, a spheroid cancer model was used. Initially the cell line A431, which had been reported as a good model for tumour spheroid, was tested¹⁹¹. A431 cells were allowed to form spheroids and were transfected with the peptide complexed with siRNA molecules (Figure 11). However, under inspection using wide-

field microscopy, the agglomerate did not form a single cohesive mass. In fact, the resultant spheroids appeared quite irregular and extremely fragile (Figure 11). Still, the peptide/siRNA complex did penetrate into the centre of the spheroids and appeared much more efficient than DF1 in doing this. A₉K showed promise compared to the control experiment. Due to the uncertainties of the A431 spheroid morphology, another model was sought.

There are many examples in the literature of groups using HCT-116 colon cancer cells to form tumour spheroids which display more compactness^{192, 193}. However, HCT-116 cells have never been tested with A₉K, so, prior to continuing with 3D models, the cells were tested in 2D for transfection with the peptide. 75 nM of siGLO red fluorescent siRNA were transfected in HCT-116 monolayers using both A₉K and DF1. Figure 10 shows that, for all the tested peptide concentrations, siRNA transfection is detectable. In particular, at higher ratios (2/1 or 3/1), siRNA transfection is superior to the positive control (DF1). After this initial transfection experiment, 3D spheroids were cultured according to the detailed procedure explained in the “2.4.3 3D spheroids” section of the Materials and Methods chapter.

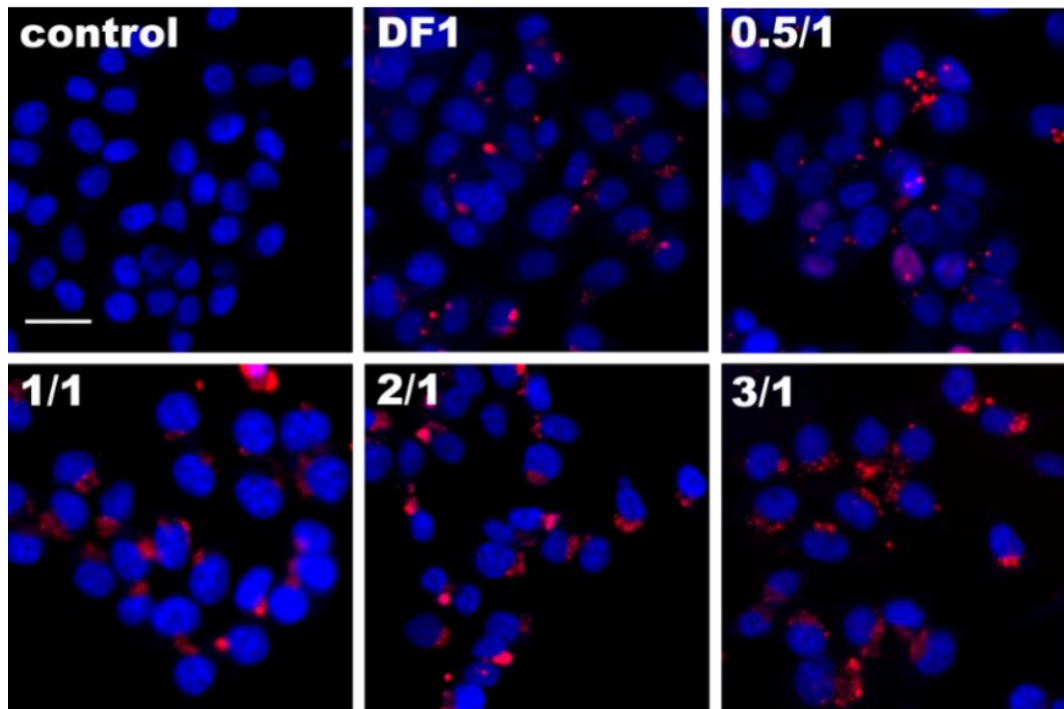


Figure 10. A₉K transfection of fluorescently labelled siRNA molecules into HCT-116 cancer cells. Cells were transfected for 24 hrs with of 75 nM of siGLO, (red) at increasing charge/ratios of A₉K. DharmaFECT1 (DF1) was used as positive control. Untreated siGLO was mixed to the culture medium to represent the negative control (control). Hoechst 33342 (2 µg/ml) (blue) was used as nuclear staining. Bar 25 = µm. All the images are scaled at the same size.

Figure 11 shows images of A431 and HCT-116 3D spheroids transfected with red fluorescent siGLO using DF1 as positive control or A₉K peptide at different charge ratios (2/1 or 5/1). The shape of the spheroids reveals a difference between A431 and HCT-116. HCT-116 shows a compact spherical mass with an average diameter of 600-800 µM. With DF1, especially in HCT-116 spheroids, most of the red signal seemed to be on the surface of the spheroid. A₉K, on the contrary, appeared to enter the spheroids' core. Due to the nature of the microscope used to acquire these images, it was not possible to determine the exact location of the red puncta within the spheroids and more importantly, how deep the peptide effectively transfected the spheroids.

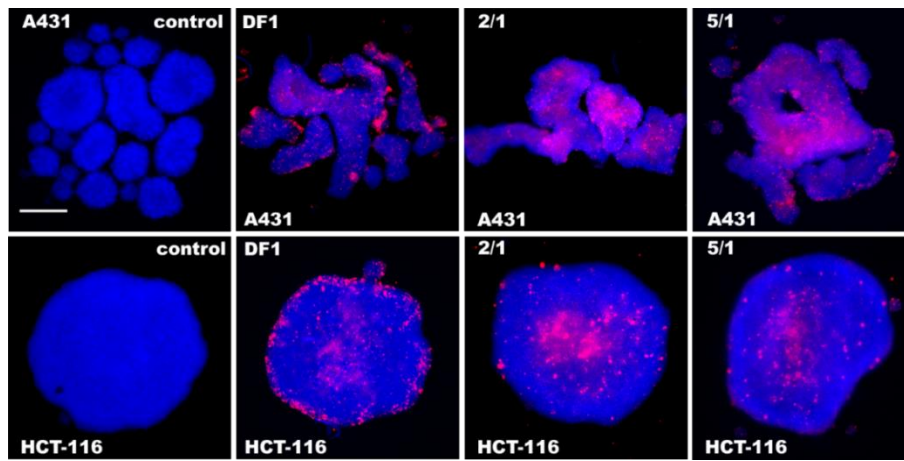


Figure 11. A₉K delivery of fluorescently labelled siRNA molecules in tumour spheroids. A431 or HCT-116 3D spheroids were transfected for 24 hrs with 75 nM of siGLO, (red) using the A₉K peptide at different ratios. DharmaFECT1 (DF1) was used as positive control, while un-complexed siGLO mixed to the culture medium represented the negative control (control). Hoechst 33342 (2 µg/ml) (blue) was used as nuclear staining. Bar 250 = µm. All the images are scaled at the same size.

For this reason, images with a light-sheet fluorescence microscope were acquired. This type of microscopy is ideal for larger samples, such as 3D models like spheroids, and allows the collection of multiple stacks with the opportunity for the production of 3D pictures¹⁹⁴. In Figure 12 it is possible to appreciate 3D sagittal view images (top left corners) of HCT-116 spheroids transfected with DF1 (left panel) or A₉K (right panel). To examine the penetration of siRNA molecules when transfected with DF1 or A₉K, middle section planes were chosen from the Z-stacks as a representation of the spheroidal sagittal views. Moreover, the two fluorescent channels used to acquire the images, DAPI for the blue nuclei staining and CY3 for the red siRNAs, were further divided in two separate pictures in order to visualise the distribution of siGLO. When A₉K was used as transfection agent, the red fluorescence was predominantly concentrated in the centre of the spheroid while when DF1 was used the siRNA appeared more superficially distributed (Figure 13).

Figure 12 and Figure 13 show the different transfection abilities of DF1 and A₉K peptide, suggesting that, while the commercial reagent is only able to transfect the surface of 3D objects, such as spheroids, the amphiphilic peptide instead gets to the core of the spheroid.

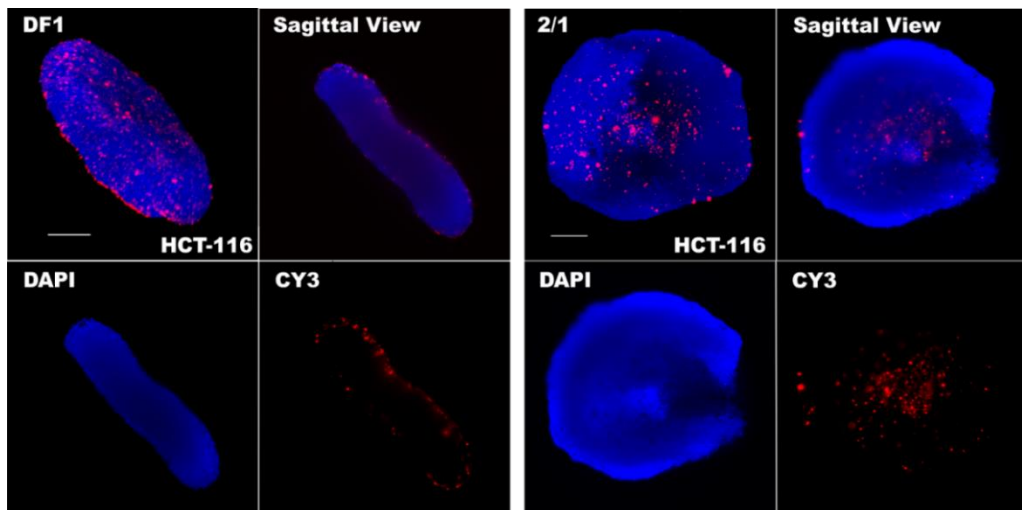


Figure 12. Light-sheet microscopy to evaluate the penetration of A₉K when transfecting 3D cancer models. Light-sheet imaging of 3D reconstructions of HCT-116 spheroids testing transfection ability of A₉K complexed with siGLO. The left four panels are control HCT-116 tumour spheroids transfected with DharmaFECT1 (DF1) and right are the experimental A₉K complexed with the siRNA (red) at 2/1 ratio. Hoechst 33342 (2 µg/ml) (blue) was used as nuclear staining. Bar 250 = µm. All the images are scaled at the same size.

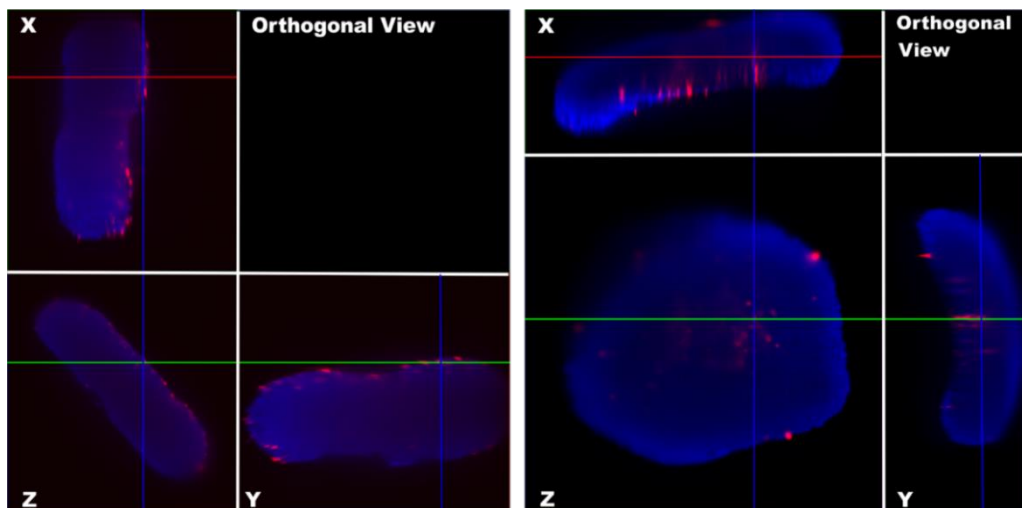


Figure 13. Orthogonal views of HCT-116 spheroids showing the location of siGLO siRNAs in xyz spatial coordinates. Images are the same ones used in Figure 12, DF1 (left panel) or the A₉K (right panel), and further analysed using the ZEN 2014 SP1 (Zeiss) software. The red, green and blue lines correspond to the xyz spatial coordinates of a single red punctum confirming the different distribution of siGLO siRNAs when transfected. Hoechst 33342 (2 µg/ml) (blue). Fluorescent siGLO in red.

3.1.4 FITC- labelled A₉K confirms the transfection abilities of the peptide

Previous experiments evaluated the transfection ability observing the localisation of fluorescent DNA or RNA molecules. However, direct visualisation of the peptide once complexed with nucleic acid inside the cell was not achieved. Therefore, a version of A₉K labelled with the fluorophore Fluorescein isothiocyanate (FITC) was introduced in the experimental plan with the aim of identifying peptide location with the nucleic acid once inside the cells.

Cancer cells HCT-116 were transfected with different charge/ratios of FITC-A₉K and 30 nM of red fluorescent siGLO and imaged using a fluorescent microscope. Both negative and positive controls were as before. Figure 14 shows the yellow puncta of colocalising peptide/siRNA complexes in the cytoplasm in all the tested peptide ratios. Note, there are both separate green and red puncta in images.

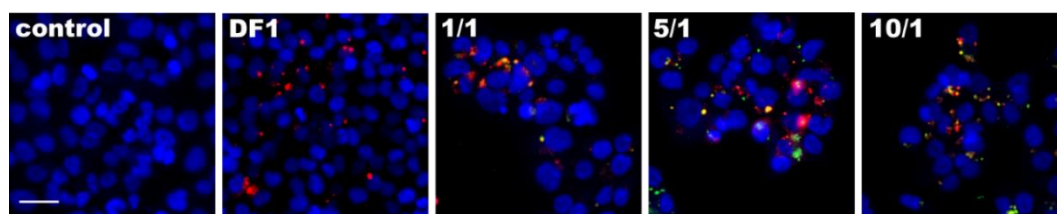


Figure 14. Subcellular co-localisation of internalised siRNA and fluorescently labelled A₉K. HCT-116 colon cancer cells were transfected for 24 hrs with 30 nM of siGLO, (red) and increasing charge ratios of FITC-A₉K (green). The presence of yellow puncta within the same subcellular compartments is an indication that green fluorescent peptide and red siGLO are located close together, if not directly complexed. DharmaFECT1 (DF1) has been used as positive control while un-complexed siGLO mixed to the culture medium represented the negative control (control). Hoechst 33342 (2 µg/ml) (blue) was used as nuclear staining. Bar 25 = µm. All the images are scaled at the same size.

3.1.5 Functional siRNA transfection

After trying different transfection experiments using a non-targeting siRNA (siGLO), which has been useful for visualisation, the efficiency of A₉K release of the siRNA inside cells was tested experimentally. Both individual red and green puncta were seen from Figure 14, showing that A₉K has the potential for release of the siRNAs, but there are other factors which could control siRNA efficiency, such as release from endocytic vesicles and the ability of the siRNA to be taken into the RISC machinery. This experiment was crucial to evaluate the effectiveness of A₉K in modulating the gene expression. For this reason, two functional siRNAs (ECT2 and PLK1) were selected for transfection in A431 or HCT-116 cancer cells. If the cargo of siRNA is released, then the cells should undergo either apoptosis or an arrest of the cell cycle and therefore a substantial decrease in the cell number would be detected.

The protein encoded by ECT2 (Epithelial Cell Transforming 2 Oncogene) is a Rho guanine nucleotide exchange factor predominantly localized in the nucleus of interphase cells. Rho family GTPases control many cellular functions; such as cell polarity, gene expression, and cell cycle progression ¹⁹⁵. The gene is expressed very high during the DNA synthesis and it stays elevated during G2 and M phases, moreover ECT2 seems to play an important role in the DNA damage response ¹⁹⁶. PLK1 (or Polo-Like Kinase 1) is a serine/threonine-protein kinase that regulates many important processes during the M phase, such as centrosome maturation, spindle assembly, mitotic exit and cytokinesis and is highly expressed during mitosis ¹⁹⁷. Because of their roles in cell cycle regulation, elevated levels of these proteins are often associated with different types of cancer and considered validated markers for poor prognosis ¹⁹⁸⁻²⁰². Their depletion in cancer cells dramatically inhibits cell proliferation and induces cell apoptosis, especially with PLK1, which is also considered a target for anticancer drugs ¹³⁶⁻¹³⁸.

Transfection of ECT2 siRNA was done on A431 cells using A₉K while HCT-116 cells were transfected with PLK1 siRNA using FITC-A₉K. PLK1 is overexpressed in colorectal cancers and has been validated in the SRSF as a good positive control for HCT-116 ^{203, 204}. A431 and HCT-116 cancer cells were transfected with 30 nM of siRNA and peptides at different ratios. Cells were imaged and counted using the Meta

Xpress® software and the graphs in Figure 15 and Figure 16 show none of the peptide ratios induced either ECT2 or PLK1 siRNA knock down. In the first case, when A431 cells were treated with ECT2 siRNA (Figure 15) no significant decrease in number was observed.

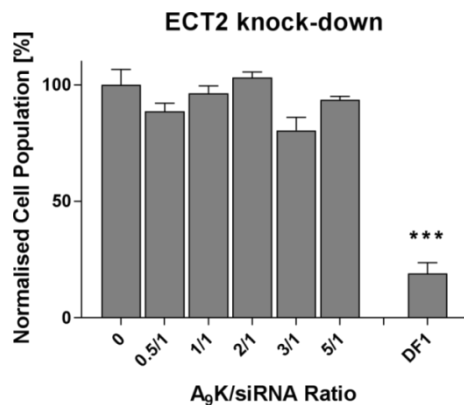


Figure 15. siRNA delivery and knock down efficiency of A₉K on A431 cells. 30 nM of ECT2 siRNA were complexed with A₉K and then transfected in A431 cells. Different ratios of peptide to ECT2 siRNA are shown on the bar-chart. The transfection reagent DharmaFECT1 (DF1) was used as positive control, showing a reasonable degree of knock down. Cells were incubated for three days with the transfection reagent or peptide, fixed, stained to reveal their nuclei with Hoechst 3342 (2 µg/ml) and counted (using nuclei as a proxy). Cell number was counted using the Meta Xpress® with the Multi Wavelength Scoring algorithm and the 2x objective. The results are expressed as a percentage normalised to the negative control (exposure to the naked ECT2 siRNA). The values obtained are average of different experiments ± standard error mean (±SEM). Statistically significant difference from the negative control was determined by Student's t-test (***)p<0.001).

A similar outcome for PLK1 siRNA transfection on HCT-116 cells was observed (Figure 16), with no significant change in cell number compared to the negative control.

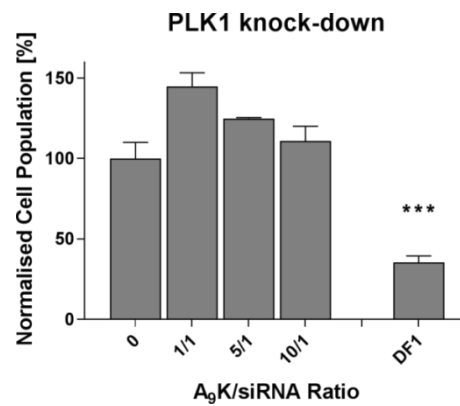


Figure 16. siRNA delivery and knock down efficiency of A₉K on HCT-116 cells. 30nM of PLK1 siRNA was complexed with A₉K and then transfected in HCT-116. Three increasing ratios of peptide to PLK1 siRNA are showed on the graph. The transfection reagent DharmaFECT1 (DF1) was used as positive control, showing a reasonable degree of knock down. Cells were incubated for three days with the DF1 or peptide, fixed, stained with Hoechst 3342 (2 µg/ml) and counted (using nuclei as a proxy). Cell population was counted using the MetaXpress® the Multi Wavelength Scoring algorithm and the 2x objective. The results are expressed as a percentage normalised to the negative control (transfection with siGLO). The values obtained are the average of different experiments ± standard error mean (±SEM). Statistically significant difference from the negative control was determined by Student's t-test (**p<0.001).

The positive control experiment, using DF1, gave 20% or 35% of cell survival with ECT2 and PLK1 siRNA respectively. This suggested that the overall experiment worked but did not yield a positive result for A₉K as a transfection reagent for siRNA functional knock down in both A431 and HCT-116 cancer cell types.

3.2. Toxicity and metabolic reduction caused by peptides exposure

3.2.1 MTT assay

Both A₆K and A₉K have been reported to have the ability to inhibit the growth of HeLa and human promyelocytic leukaemia HL60 cancer cells ^{116,177} and it is not unusual that an AMP shows some anti-cancer properties ²⁰⁵⁻²⁰⁷. To better understand the mechanism of action towards cancer cells, the processes with which these peptides can induce either a reduction in cell proliferation or an increase in cell death were analysed. To evaluate the cell viability, the first assay that was performed was MTT. A cancer and a non-cancer cell line (A431 and HDFs) were exposed to a wide range of peptides concentrations at different time points.

The MTT assay is a rapid and easy technique, generally used to evaluate cellular viability. MTT is a tetrazole and is reduced into purple formazan only in living cells. The absorbance of this coloured solution can be quantified using a spectrophotometer and measuring it at a certain wavelength (normally between 500 and 600 nm). The reduction takes place only when NAD(P)H-dependent oxidoreductase enzymes (dehydrogenases) are active and therefore conversion can be directly related to the number of viable (living) cells, although caution has to be exercised when using direct biochemical assays. The resulting purple solution is spectrophotometrically quantified and the increase in the cell number is normally directly related to the amount of MTT formazan crystals formed and with a subsequent increase in the absorbance measure ¹⁴⁰⁻¹⁴². Tetrazolium dye reduction normally involves oxidoreductases of the mitochondrial electron transport chain, but numerous other cellular dehydrogenases, oxidases or peroxidases have been shown to reduce tetrazolium dyes as well ²⁰⁸. As discussed, MTT assay was performed on A431 cancer cell line and HDFs human fibroblasts after exposure to A₆K and A₉K peptides in order to investigate their possible toxicity effects on cells. The concentrations of used peptides in this assay were in a range between 6.25 μ M (corresponding to 3.83 mg/ml of A₆K or 5.17mg/ml of A₉K) and 100 μ M (corresponding to 61.5 mg/ml of A₆K or 82.72 mg/ml of A₉K). The exposure time

varied between 24 hrs and 72 hrs. The absorbance was measured with a spectrophotometer at 570 nm wavelength. The results obtained from the treated cells were normalized to the negative control (cells treated with the UHQ water used to prepare the peptide solutions) and converted to a percentage, which gave a value of mitochondrial activity of treated samples compared to negative controls. As positive control, 200 μ M of Na_2CrO_4 was used, a well-known toxic and carcinogenic compound^{209, 210}. One set of wells with MTT and peptides but without cells was included to evaluate if A_6K and A_9K could interfere during the absorbance reading (data not shown, as the peptides did not effectively exhibit any effects alone on the assay).

The complete experimental procedure is explained in the corresponding section in the Material Method Chapter (“2.5 MTT assay and cell counts”), but briefly, cells were seeded on a plate at a variable cell density, depending on the cell type and exposure times, and next day treated with different peptide concentrations or UHQ water and Na_2CrO_4 for the negative and positive controls, respectively. At end of the exposure time, the medium was removed and a fresh one containing the MTT solution (5 mg/ml per well) was added for 3 hrs. After that, the medium was carefully removed and DMSO added instead to dissolve the formazan crystals. The plate was then placed on a vibrating plate shaker for 15 minutes and the absorbance read at 570 nm with a spectral scanning multimode reader.

The results obtained from the MTT assay are shown in the graphs below and revealed a propensity for both A_6K and A_9K peptides to selectively interact with the cancer cells and significantly inhibit their growth. The cell viability is expressed as a decrease in the mitochondrial activity and quantified using the MTT assay data.

A_6K displayed great effect against the cancer cells A431 and little reaction towards the human fibroblasts but not in a time dependent manner.

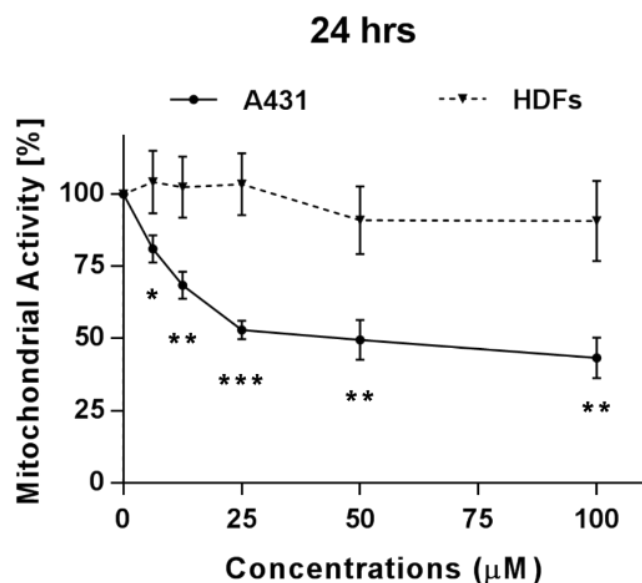


Figure 17. Assessment of A₆K activity using the MTT assay performed on A431 and HDFs for 24 hrs. The graph shows cancer cells and fibroblasts exposed to A₆K peptide for 24 hrs followed by evaluation of the mitochondrial activity via MTT assay. The absorbance of formazan crystals was quantified with a spectrophotometer and read at 570 nm wavelength. The results are normalized to the negative control and expressed as a percentage. The values obtained are averages of three independent experiments ± standard error mean (±SEM). Na₂CrO₄, 200 µM has been used as positive control (data not showed) while water has been used as negative control (0). A statistically significant difference from the negative control was determined by Student's t-test (*p<0.05; **p<0.01; ***p<0.001).

After 24 hrs of peptide exposure (Figure 17), a significant decrease in mitochondrial activity correlated with the peptide concentration for A431 cells. Cell viability progressively dropped compared to the negative control, from the 81% of 6.25 µM to 43% of 100 µM A₆K exposure. The fibroblasts were not affected by A₆K and after 24 hrs of peptide exposure none of the tested concentration caused significant diminution in the cellular mitochondrial activity.

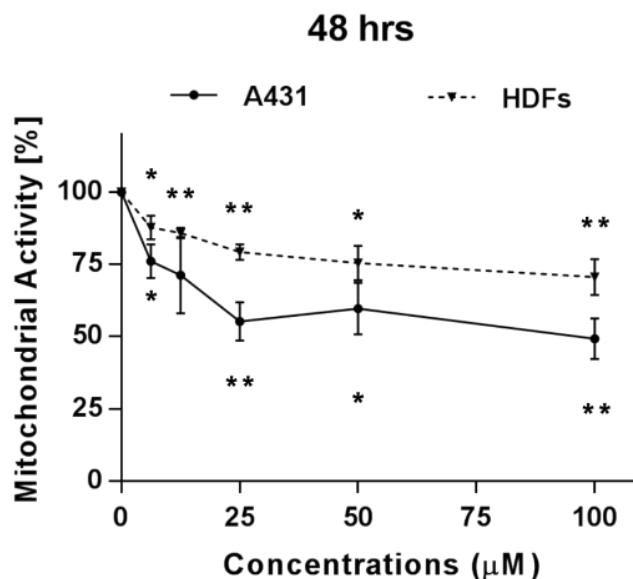


Figure 18. Assessment of A₆K activity using the MTT assay performed on A431 and HDFs for 48 hrs. The graph shows cancer cells and fibroblasts exposed to A₆K peptide for 48 hrs followed by evaluation of the mitochondrial activity via MTT assay. The absorbance of formazan crystals was quantified with a spectrophotometer and read at 570 nm wavelength. The results are normalized to the negative control and expressed as a percentage. The values obtained are averages of three independent experiments ± standard error mean (±SEM). Na₂CrO₄, 200 µM has been used as positive control (data not showed) while water has been used as negative control (0). A statistically significant difference from the negative control was determined by Student's t-test (*p<0.05; **p<0.01; ***p<0.001).

After 48 hrs of peptide exposure (Figure 18) a decrease in cell viability was observed in a dose-dependent manner in both cell lines, but more drastically in the cancer cells.

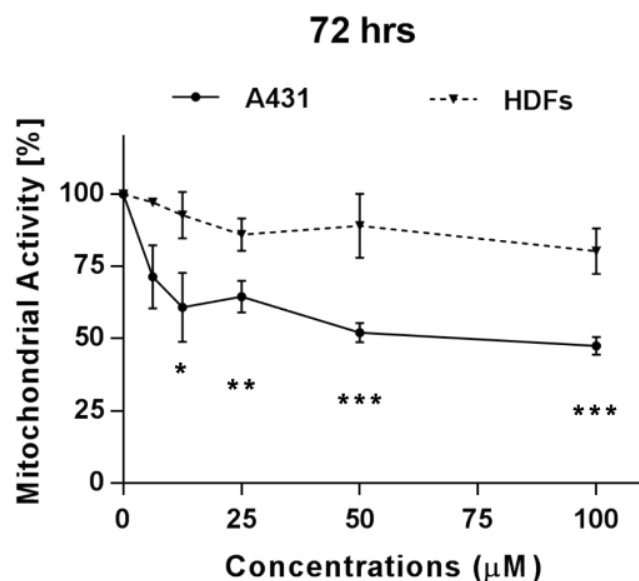


Figure 19. Assessment of A₆K activity using the MTT assay performed on A431 and HDFs for 72 hrs. The graph shows cancer cells and fibroblasts exposed to A₆K peptide for 72 hrs followed by evaluation of the mitochondrial activity via MTT assay. The absorbance of formazan crystals was quantified with a spectrophotometer and read at 570 nm wavelength. The results are normalized to the negative control and expressed as a percentage. The values obtained are averages of three independent experiments ± standard error mean (±SEM). Na₂CrO₄, 200 µM has been used as positive control (data not shown) while water has been used as negative control (0). A statistically significant difference from the negative control was determined by Student's t-test (*p<0.05; **p<0.01; ***p<0.001).

Finally, following 72 hrs exposure (Figure 19), fibroblasts did not vary in activity, despite a slight, non-statistical trend towards a decrease in their mitochondrial activity. In contrast, A431 had a reduction in mitochondrial activity of 47% compared to the negative control at 100 µM.

Overall, the decrease in mitochondrial activity of the cancer cells, due to peptide, was not time dependent, an exception being for A₆K at 6.25 µM. In summary, for most selected concentrations, on average, the mitochondrial activity dropped about 50-60% compared to the control.

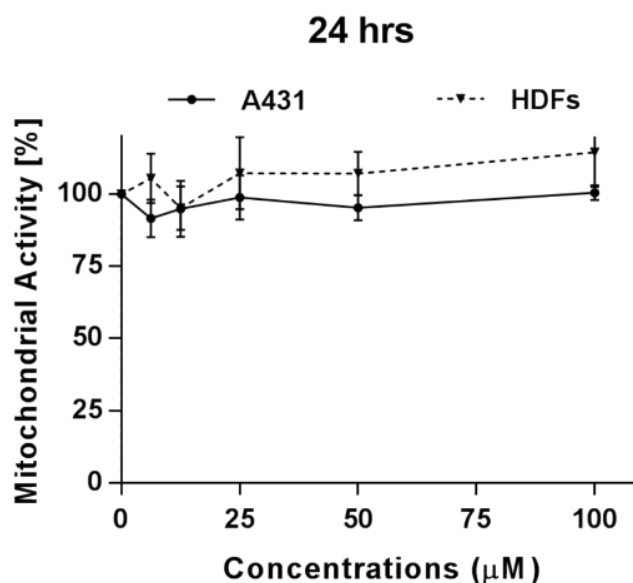


Figure 20. Assessment of A₉K activity using the MTT assay performed on A431 and HDFs for 24 hrs. The graph shows cancer cells and fibroblasts exposed to A₉K peptide for 24 hrs followed by evaluation of the mitochondrial activity via MTT assay. The absorbance of formazan crystals was quantified with a spectrophotometer and read at 570 nm wavelength. The results are normalized to the negative control and expressed as a percentage. The values obtained are averages of three independent experiments ± standard error mean (±SEM). Na₂CrO₄, 200 µM has been used as positive control (data not showed) while water has been used as negative control. Statistically significant difference from the negative control was determined by Student's t-test (*p<0.05; **p<0.01; ***p<0.001).

Replicating these experiments for A₉K, after 24 hrs (Figure 20) of exposure to the peptide, the mitochondrial activity did not decrease in either cell lines and the values were always comparable with the respective negative controls.

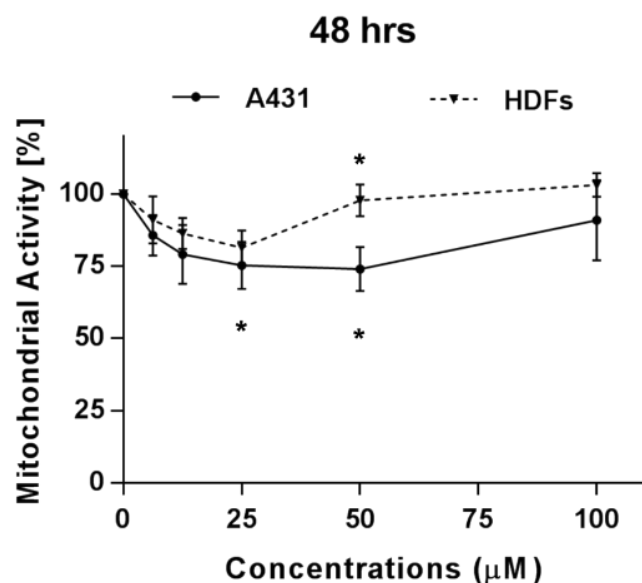


Figure 21. Assessment of A₉K activity using the MTT assay performed on A431 and HDFs for 48 hrs. The graph shows cancer cells and fibroblasts exposed to A₉K peptide for 48 hrs followed by evaluation of the mitochondrial activity via MTT assay. The absorbance of formazan crystals was quantified with a spectrophotometer and read at 570 nm wavelength. The results are normalized to the negative control and expressed as a percentage. The values obtained are averages of three independent experiments ± standard error mean (±SEM). Na₂CrO₄, 200 µM has been used as positive control (data not showed) while water has been used as negative control (0). A statistically significant difference from the negative control was determined by Student's t-test (*p<0.05; **p<0.01; ***p<0.001).

At 48 hrs exposure (Figure 22) a slightly diminution in the cell viability of A431 was observed, especially at intermediate concentrations (25-50 µM) where only 75% of mitochondrial activity was registered. Mostly ineffective, the peptide showed a statistically significant decrease in the fibroblast metabolic activity only at one experimental point: 25 µM where the mitochondrial activity decreased to 80%.

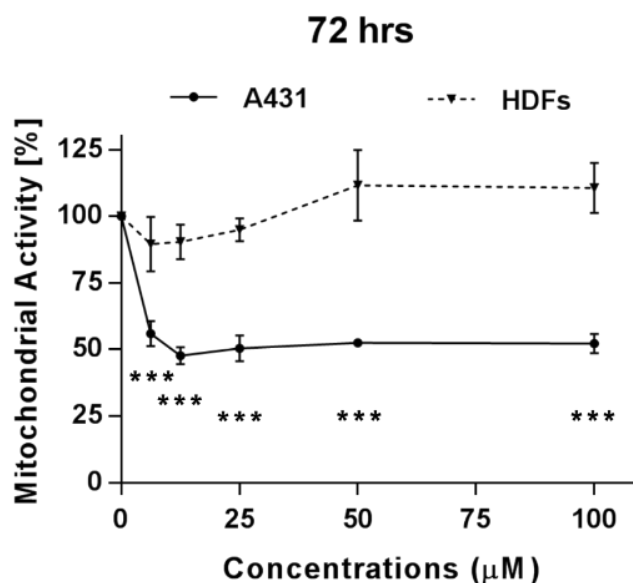


Figure 22. Assessment of A₉K activity using the MTT assay performed on A431 and HDFs for 72 hrs. The graph shows cancer cells and fibroblasts exposed to A₉K peptide for 72 hrs followed by evaluation of the mitochondrial activity via MTT assay. The absorbance of formazan crystals was quantified with a spectrophotometer and read at 570 nm wavelength. The results are normalized to the negative control and expressed as a percentage. The values obtained are averages of three independent experiments ± standard error mean (±SEM). Na₂CrO₄, 200 µM has been used as positive control (data not showed) while water has been used as negative control (0). A statistically significant difference from the negative control was determined by Student's t-test (*p<0.05; **p<0.01; ***p<0.001).

The results became significant after 72 hrs exposure (Figure 22), where the mitochondrial activity dropped down to <50% for most peptide concentrations used (with the exception of the lowest dose (6.25 µM)). Fibroblasts, once again, did not show sensitivity towards this peptide. In all the above experiments, a positive control of cells treated with Na₂CrO₄, was used and the data is not displayed. However, as expected they died and the mitochondrial activity was consequently really low; 5%, 3% and 2% for A431 and 6.5%, 1.5% and 1% for HDFs at 24, 48 or 72 hrs, respectively.

Using GraphPad, the inhibitory concentration (IC₅₀), corresponding to the concentration of peptide needed to induce a mitochondrial activity inhibition of 50%, was calculated.

Against A431 cancer cells, A₆K had an IC₅₀ of 40, 52 and 45 μM after 24, 48 and 72 hrs exposures, respectively. For A₉K instead the IC₅₀ (28 μM) was calculated only for the 72 hrs time point since in the previous ones, little variation in the mitochondria activity was observed. Both peptides were ineffective towards HDFs, therefore no IC₅₀ could be extrapolated.

3.2.2 Cell counts following exposure to A₆K or A₉K peptides

As previously mentioned, the MTT assay is often used as an estimate of the cellular viability and is easy to perform with absorbance measurements and a plate spectrophotometer. However, monitoring, using the cell microscope, it was noticed that there was little variation between the experimental conditions, with the exclusion of the wells treated with Na₂CrO₄, where it was obvious all the cells were dead. This was observed for both peptides, A₆K and A₉K, so it was decided to quantify the observations and repeat the experiment and perform a cell count using high content microscopy and counting the cells based upon a nuclear stain and an algorithm to count the nuclei (Figure 23).

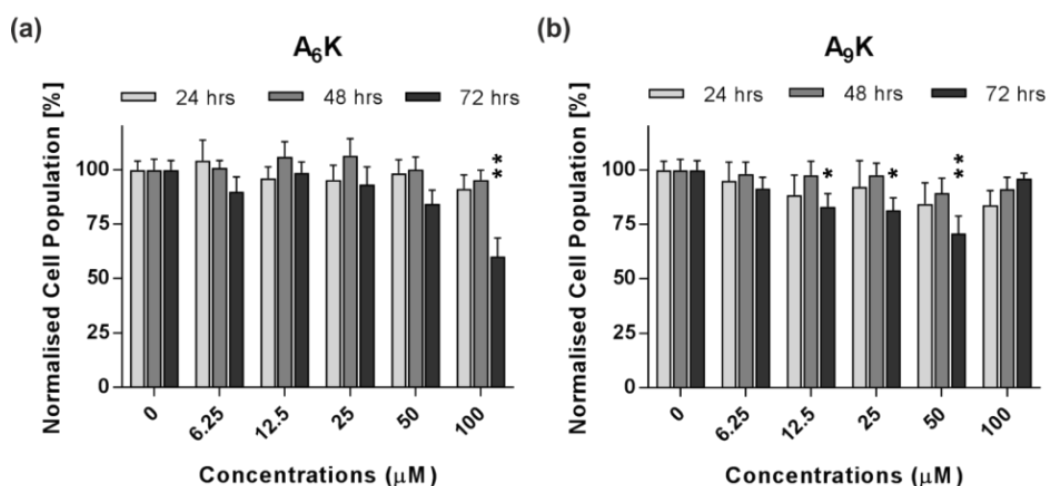


Figure 23. A431 cell number evaluated with high-content microscopy after exposure to A₆K and A₉K peptides. Cells were incubated with A₆K (a) or A₉K (b) peptides for one, two or three days, fixed in formaldehyde and stained with Hoechst 3342 (2 µg/ml) to reveal the nuclei. Images were acquired using an ImageXpress® Micro microscope (x2 objective) and cell number was counted using the Multi Wavelength Scoring algorithm within the MetaXpress® software. The results are expressed as a percentage of the number of cells and normalized to the negative control at that relative time point. The values obtained are averages of different experiments ± standard error mean (±SEM). Na₂CrO₄, 200 µM has been used as positive control (data not showed) while water has been used as negative control (0). A statistically significant difference from the negative control was determined by Student's t-test (*p<0.05; **p<0.01).

The results from Figure 23 shows a slight, but significant change in cell number at longer exposures at higher doses, but the decrease did not correspond to the MTT assay. The remarkable differences between MTT assay and the cell counting experiments, both of which have been invaluable in assessing cell toxicity in other studies, shows that the interaction between peptides and the cancer cell lines is complex. From these experiments, the cells were not directly dying but the decrease in MTT activity suggests a possible interaction between the peptides and the cellular mitochondria, or a metabolic suppression in the cell.

3.2.3 Cell counts following exposure to FITC- A₉K

As already mentioned in the transfection efficiency paragraph, a fluorescent version of A₉K, conjugated with FITC was used. This new peptide was tested to see if it had a similar effect on the cells compared to the non-fluorescent labelled one. Because of the fluorescence of the peptide, it was possible to use high-content microscopy to acquire images of the cancer cells when exposed to increasing concentrations of FITC-A₉K. In Figure 24 there are images of HCT-116 cells exposed to FITC-A₉K for 72 hrs. It is possible to observe that the amount of fluorescence associated with the cells is proportionally related with the peptide concentrations used in the experiment.

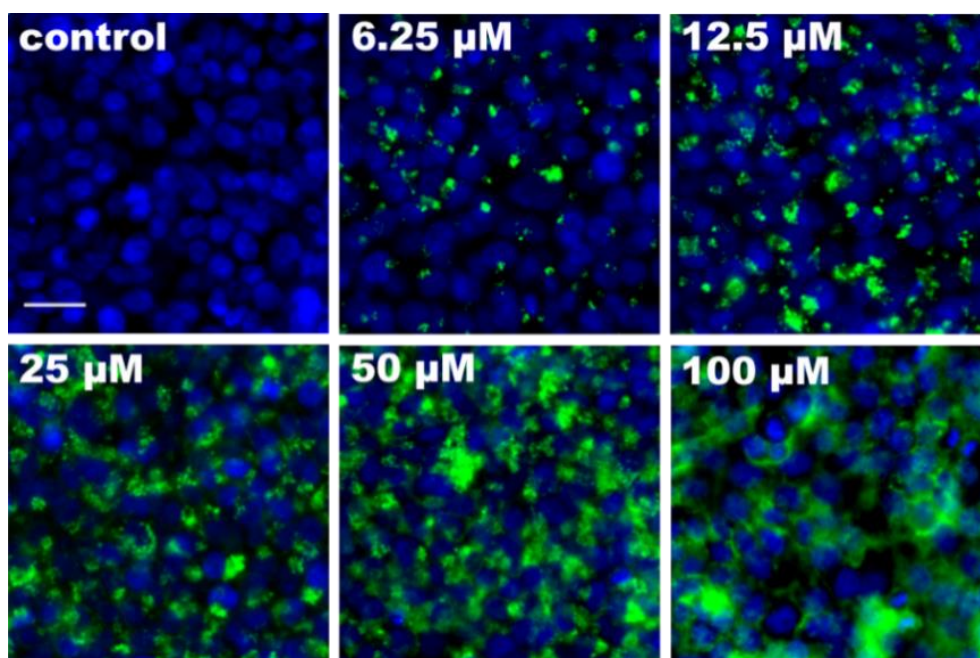


Figure 24. High-content microscopy of cancer cells exposed to a fluorescent peptide. Images show HCT-116 cancer cells exposed for 72 hrs to FITC-A₉K. The amount of fluorescence associated within the cells is proportional to the concentration of peptide used. Cells were stained with Hoechst 33342 (2 μg/ml). FITC-A₉K in green. Bar 25 = μm. All the images are scaled at the same size. Images provided by courtesy of Joanna Henry, MSc in Biomedical Science, who was involved in this project for a period of 10 months as a part of her master degree.

To evaluate if the FITC labelled A₉K behaved the same as its non-fluorescent version, cell viability was measured by counting the cells. This time HCT-116 cancer cells were selected, and the results are shown in Figure 25. The same range of concentrations (6.25-100 μM) and exposure times (24-72 hrs) were chosen. There was very little difference between the two peptides.

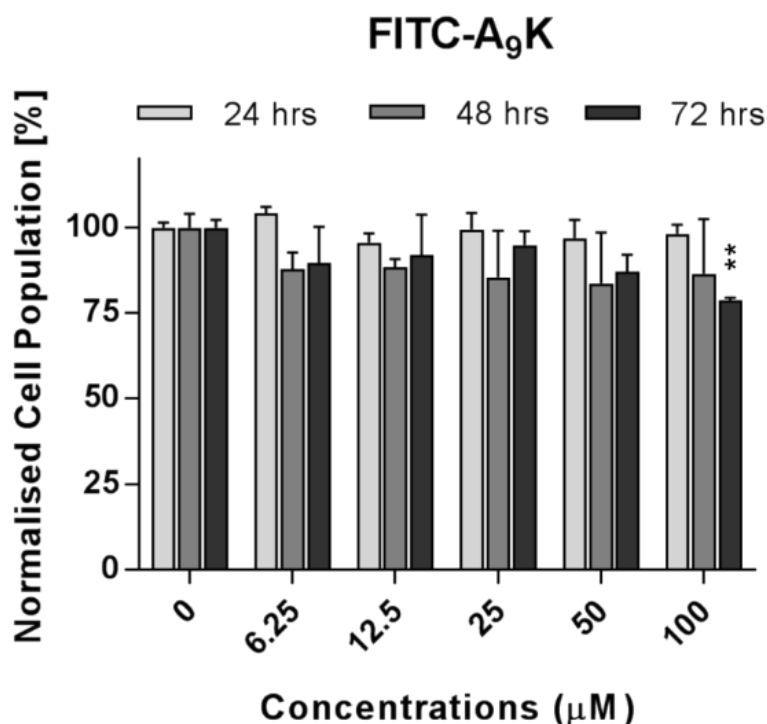


Figure 25. HCT-116 cell number evaluated with high-content microscopy after exposure to FITC-A₉K peptide. Cells were incubated with FITC-A₉K for one, two or three days, fixed in formaldehyde and stained with Hoechst 33342 (2 μg/ml) to reveal nuclei. Cell number was counted using the MetaXpress® with the Multi Wavelength Scoring algorithm and 2x objective. The results are expressed as percentage of the number of cells and normalized to the negative control at that relative time point. The values obtained are averages of three replicates for each experimental point ± standard error mean (±SEM). Na₂CrO₄, 200 μM has been used as positive control (data not showed) while water has been used as negative control (0). A statistically significant difference from the negative control was determined by Student's t-test (**p<0.01). Data provided by courtesy of Joanna Henry, MSc in Biomedical Science involved in this project for a period of 10 months as a part of her master degree.

3.3. Mitochondrial membranes dramatically change after both A₆K and A₉K exposure

Results obtained with the cell counting experiments, especially with the MTT assay, showed how these two amphiphilic peptides, although clearly interacting with the cells, do not directly cause cell death but rather interfere with the cellular metabolism, possibly via a mitochondrial route. A hypothesis was tested that the peptides caused a dramatic effect on the mitochondrial morphology.

MTT reduction mainly occurs in the mitochondria by oxidoreductases. It has also been reported to be used for endosomal and lysosomal vesicles ^{140, 141, 208, 211}. To better elucidate the effect of peptides on mitochondria, two different dyes were used; MitoTracker® Red CMXRos (Thermo Fisher Scientific), a specific cell-permeant probe containing a mildly thiol-reactive chloromethyl moiety for labelling active mitochondria ²¹², and JC-1 (Thermo Fisher Scientific), a carbocyanine with a delocalized positive charge. JC-1 normally exists in aqueous solution as monomers with the excitation and emission peak in the green. Under favourable conditions it forms J-aggregates shifting its emissions in the red peak ¹⁴³.

A431 and HCT-116 cells were exposed to A₆K, A₉K or FITC-A₉K. Cells were incubated at 37 C° for 30 minutes together with 250 nM of MitoTracker® Red CMXRos diluted in DMEM then fixed with 4% formaldehyde and the nuclei stained using Hoechst 3342 (2 µg/ml).

From the images in Figure 26 it is possible to observe how at normal conditions (0 µM) the mitochondria staining shows a network of highly interconnected long filaments. However, with increasing concentrations of A₆K and A₉K peptides, the mitochondria morphology starts changing and perinuclear, spherical, stained clumps are noticeable. This has previously been reported as an indicator of cellular stress, associated with a consequent reduction in metabolic activity ^{213, 214}.

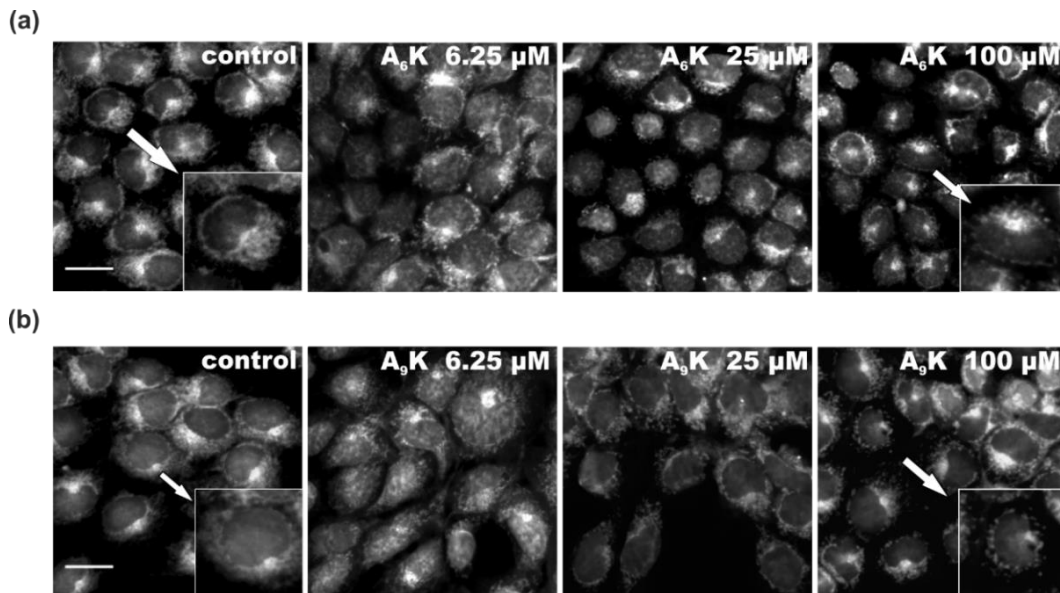


Figure 26. Mitochondrial morphology of cancer cells following peptide exposure. A431 cancer cells exposed for 72 hrs to A₆K (a) and A₉K (b) peptides and then live stained with MitoTracker® Red CMXRos 250 nM for 30 minutes followed by standard formaldehyde fixation. Images show the different morphology of mitochondria associated with A₆K and A₉K exposure. The images are presented in black and white to enhance mitochondrial morphology. Note, the controls contain filamentous stained mitochondria and as the peptide concentration increases spheroidal objects are more common. Hoechst 33342 (2 μg/ml) was used as nuclear staining. Bar 25 = μm. All the images are scaled at the same size.

Figure 27 shows the resulting images of the mitochondria from HCT-116 cells challenged with the FITC-A₉K peptide. It is possible to observe a similar pattern compared to A431 cells treated with either A₆K or A₉K peptides.

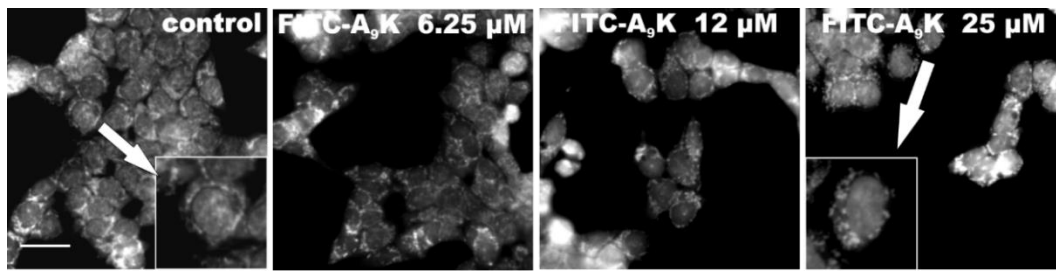


Figure 27. Mitochondrial morphology of cancer cells following fluorescent peptide exposure. HCT-116 cancer cells exposed for 48 hrs to FITC-A₉K peptide and then live stained with MitoTracker® Red CMXRos 250 nM for 30 minutes followed by standard formaldehyde fixation. Images show the different morphology of mitochondria associated with FITC-A₉K exposure. The images are presented in black and white to enhance the mitochondrial morphology. Hoechst 33342 (2 μg/ml) was used as nuclear staining. Bar 25 = μm. All the images are scaled at the same size. Data provided by courtesy of Joanna Henry, MSc in Biomedical Science involved in this project for a period of 10 months as a part of her master's degree.

The second dye we used on mitochondria is JC-1. As previously mentioned, this specific dye could fluoresce differently according to the variations of the mitochondrial membrane potential ($\Delta\psi_m$) shifting from green to red green²¹⁵. The different spectrum of excitation and emission is based on its aggregation status inside the mitochondria. Due to its cationicity, JC-1 easily interacts with the highly negative mitochondrial membranes (-140 mV). When the membranes are polarised (high $\Delta\psi_m$), it accumulates in the organelles yielding a red coloured emission (~590 nm), and vice versa, with membranes depolarisation, normally associated with unhealthy mitochondria (low $\Delta\psi_m$), JC-1 stays in low concentrations and in monomers yielding to a green fluorescent emission (~529 nm).

A431 cancer cells were exposed to A₆K or A₉K (6.25 – 100 μM) for 24 or 48 hrs. Following peptide exposure, the cells were incubated at 37 °C for 20 minutes together with 2.0 μg/ml of JC-1 diluted in growth medium, then washed and live imaged under the fluorescent microscope.

An increased number of green depolarized mitochondria, compared to the respective controls, was observed for each peptide and was dose and time dependent.

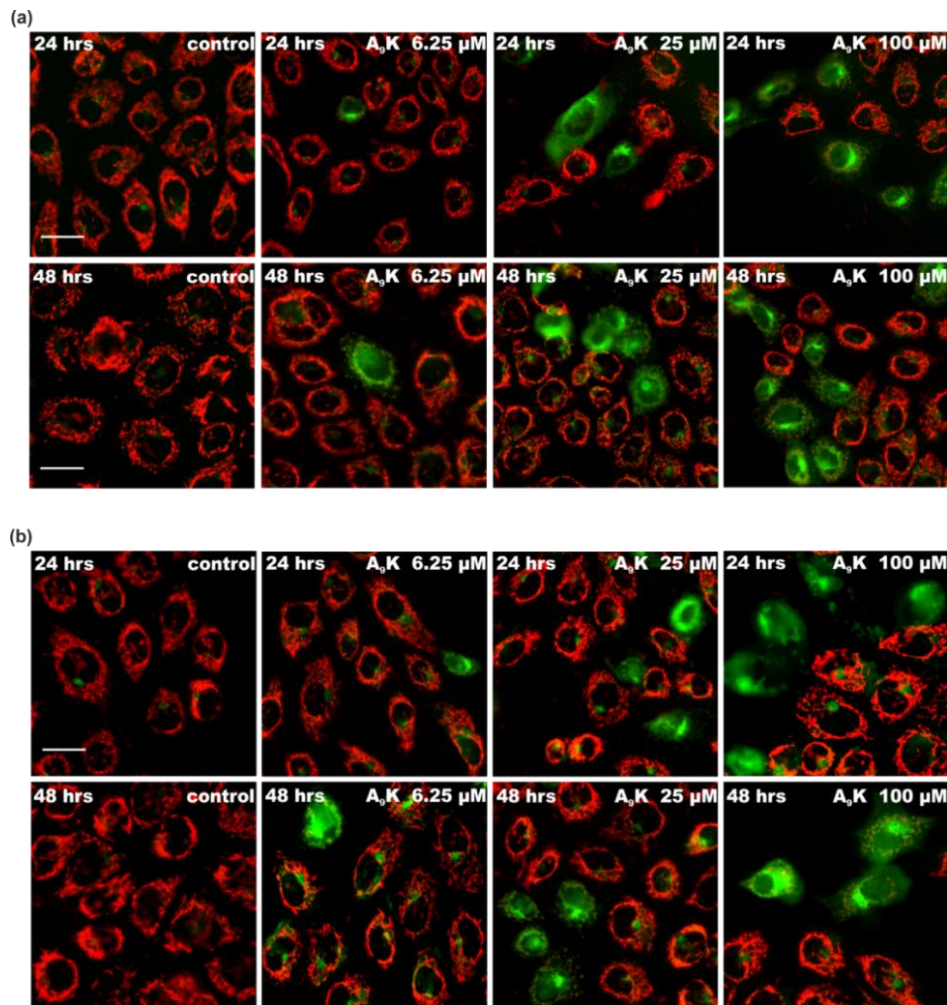


Figure 28. Mitochondrial membrane potential ($\Delta\psi_m$) status of cancer cells following peptide exposure. JC-1 staining on A431 cells exposed to different concentrations of A₆K peptide (a) for 24 hrs (top) or 48 hrs (bottom) or A₉K peptide (b) for 24 hrs (top) or 48 hrs (bottom). Cells were incubated with 2.0 μg/mL of JC-1 diluted in growth medium for 20 minutes and then live imaged. Images show the effect of A₆K and A₉K peptides on mitochondrial polarisation status. Due to the dual-colour properties of the dye JC-1, healthy mitochondria appear red, while unhealthy depolarised ones appeared green. Bar 25 = μm. All the images are scaled at the same size.

The amount of green and red mitochondria in each experimental condition was quantified using the MetaXpress® and an algorithm specifically customised to count the different coloured mitochondria was used. The results from the A₆K experiments are presented in Figure 29a and Figure 30, while the results for A₉K peptide are shown in Figure 29b and Figure 31.

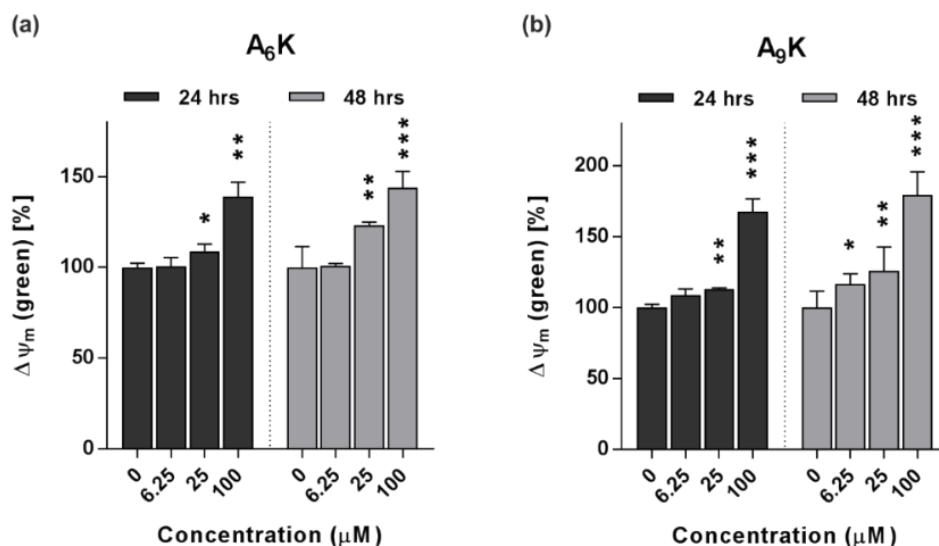


Figure 29. Quantitative analyses of $\Delta\Psi_m$ variation following peptide exposure.

The graphs show the dose response of the peptide over time and reveal the number of green mitochondria after exposure to different concentrations of A₆K (a) or A₉K (b). The results are expressed as a percentage of the number of green mitochondria normalized to the negative control at that relative time point. The values obtained are averages of independent experiments \pm standard error mean (\pm SEM). A statistically significant difference from the negative control was determined by Student's t-test (*p<0.05; **p<0.01; ***p<0.001).

For A₆K the number of green stained mitochondria increased according to the concentration of peptide. In standard conditions, the number of green mitochondria present within cells is about 20% of the total. At 6.25 μM the population of green mitochondria did not vary significantly, when compared to the control, but at 25 μM and especially at 100 μM the difference was significant. An increase of the green reporter, was not only dose, but time dependent and, after 48 hrs exposure to 25 and 100 μM of A₆K peptide, the percentage of green mitochondria rose to 23% and 43%, respectively (Figure 29 a).

A₉K exposure followed the same pattern as A₆K, showing an increase in membrane depolarisation directly related to the amount of peptide dispensed. From the quantitative analysis on the number of green mitochondria (Figure 29 b), it emerged that the A431 cells were sensitive to the A₉K peptide in a dose and time dependent manner. After 24 hrs exposure, the only peptide concentration that did not cause a substantial change in

mitochondrial number was 6.25 μM . After 48 hrs of peptide exposure at all the concentrations tested the cells showed a significant augmentation in green mitochondria

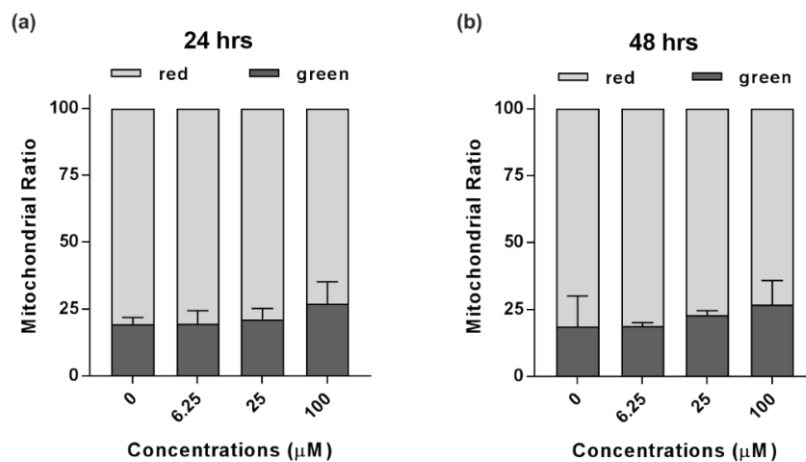


Figure 30. Quantitative analyses of $\Delta\Psi\text{m}$ variation caused by A_6K exposure.

The graphs show the total number of mitochondria counted in A431 cells after exposure to different concentrations of A_6K at 24 (a) or 48 hrs (b) time points. Mitochondria were counted using MetaXpress® and a specifically designed algorithm that was able to count and separate green mitochondria from red ones. The results are expressed as a percentage ratio of mitochondria separated by colour. The values obtained are averages of independent experiments \pm standard error mean ($\pm\text{SEM}$).

A green/red mitochondrial ratio was also calculated (Figure 30 and Figure 31) in order to evaluate the real impact of both peptides on the JC-1 colour shift, according to the mitochondrial membrane potential status ($\Delta\Psi\text{m}$). Figure 30 shows the green/red mitochondrial ratios after 24 or 48 hrs A_6K exposure. In the 24 hrs control cells, 80% of mitochondria were red and 20% were green. When the peptide was added this ratio changed slightly. With 6.25 μM no variation was observed. Almost identical results were obtained after 48 hrs exposure.

With A_9K , equivalent results were obtained at 6.25 and 25 μM for both time points, but at 100 μM the ratio of green/red mitochondria changed more than the A_6K experiment (Figure 31).

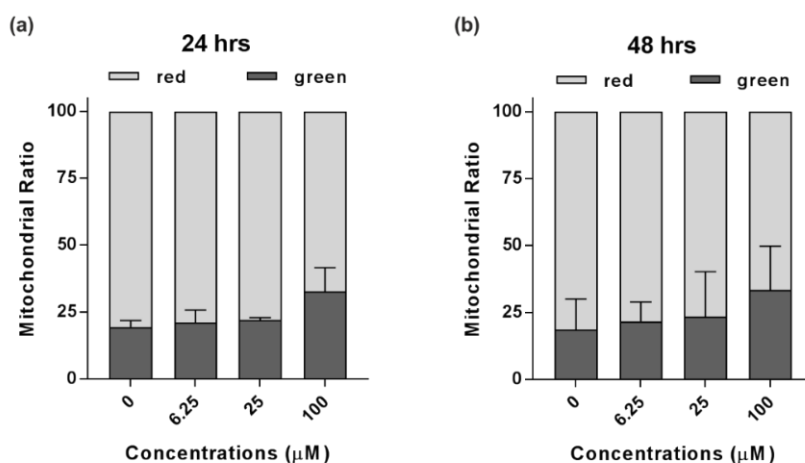


Figure 31. Quantitative analyses of $\Delta\Psi_m$ variation caused by A₉K exposure.

The graphs show the total number of mitochondria counted in A431 cells after exposure to different concentrations of A₉K at 24 (a) or 48 hrs (b) time points. Mitochondria were counted using MetaXpress® and a specifically designed algorithm that was able to count and separate green mitochondria from red ones. The results are expressed as a percentage ratio of mitochondria separated by colour. The values obtained are averages of independent experiments \pm standard error mean (\pm SEM).

3.4. Images acquisition and analysis

The images presented in this chapter were collected using the ImageXpress® Micro System wide-field fluorescent microscope with 20x objective lenses and further analysed using the MetaXpress® 5.0.0.20 software. Confocal images presented in the section “3.1.2 ODNs and siRNAs transfection” were acquired using the Nikon A1+, confocal microscope with 60 and 100x objectives lenses and analysed using the NIS Element software. Light-sheet imaging of 3D spheroids and their orthogonal views showed in the “3.1.3 Evaluation of A₉K transfection efficiency in a 3D cancer cellular model” section was made with the Zeiss Lightsheet Z.1 microscope with 2x objectives lenses and further analysed with the ZEN 2014 SP1 (Zeiss) software. Brightness and contrast were ultimately adjusted for all the images to the same level by using Image J.

4 G(IKKK)₃I-NH₂ PEPTIDE

Antimicrobial peptides (AMPs) have a wide spectrum of activity including pathogens such as bacteria, fungi, some viruses and even cancer cells ^{105, 216}. Amongst the AMPs, the alpha-helical ones are certainly the most studied; the amphibian Magainin ⁶⁰, the bee venom component Mellitin ⁵⁹ and the human LL-37 ¹³ are just few examples of this large class. Like for the β -sheet peptides, the α -helical ones share the same very important features; a net positive charge (+2 to +9), a considerable quantity of hydrophobic residues ($\geq 30\%$), a well-defined amphipathicity and a general small size (normally 6-50 aa long) ^{43, 45}. The analysis of natural α -helical AMP amino acidic sequences revealed that there is little positional conservation of individual residues but some exceptions are observed: position 1, for example is occupied by a Glycine in 70% of the cases and a lysine in position 8 is seen in 50% of cases ¹⁶⁸. Most of the α -helical AMPs do not have a defined structure in aqueous solutions but assume proper folding once in contact with a membranous environment ⁵⁰. This structure propensity is critical for antimicrobial activity and lowers the cytotoxicity towards mammalian host cells ⁴⁸.

G(IKKK)₃I-NH₂ is an alpha helical molecule, part of the novel class of synthetic short cationic peptides G(IKKK)_nI-NH₂ (n = 1-4) containing the simple repeated sequence IKKK, enabling the ratio of hydrophobic isoleucines (I) to cationic lysines (K) remaining equal. Like other α -helical peptides, it remains unfolded in aqueous solution due to significant intermolecular hydrogen bonding between the peptide backbone and the solvent, but can adopt the typical α -helical folding structure in appropriate conditions. Previous works revealed how, amongst the series, G(IKKK)_nI-NH₂, G(IKKK)₃I-NH₂ was the peptide showing the most promising results; great antibacterial activity against both Gram-positive (*B. subtilis* 168) and Gram-negative (*E. coli* DH5 α) but at the same time low cytotoxicity towards mammalian host ¹¹⁷. A recent publication showed G(IKKK)₃I-NH₂ cancer cell selectivity with a possible cytostatic effect against HeLa and promyelocytic leukaemia HL60 ¹¹⁸. Therefore, G(IKKK)₃I-NH₂ was selected as the object of study in this PhD project in order to further evaluate its efficiency in targeting cancer cells and investigate the possibility for its use as a vector for gene delivery.

4.1 *In vitro* cell transfection efficiency with DNA or RNA

The first set of experiments with G(IKK)₃I-NH₂ and its fluorescent version FITC-G(IKK)₃I-NH₂ were planned to evaluate the binding ability towards negatively charged DNA or RNA molecules and, more importantly, their transfection efficiency in different cellular models. All the images were collected using the ImageXpress® Micro System wide-field fluorescent microscope with 20x objective lenses. Following acquisition, the images were further analysed using the MetaXpress® 5.0.0.20. Brightness and contrast were ultimately adjusted for all the images to the same level by using Image J.

4.1.1 ODNs and siRNAs transfection

DNA transfection efficiency was evaluated on A431 and HDFs. Complexes made with 0.05 µg (1.6 µM) of FAM labelled oligonucleotides (ODNs) and increasing ratios of G(IKK)₃I-NH₂ (0.1; 0.25; 0.5/1; 1/1; 2/1 and 3/1) were transfected into cell monolayers according to the procedure explained in the Materials and Methods section. Transfection with Oligofectamine was used as positive control, while the addition to the cells of un-complexed ODNs, used as negative control. Without an adequate transfection reagent, the DNA molecules were not able to cross the plasma membrane.

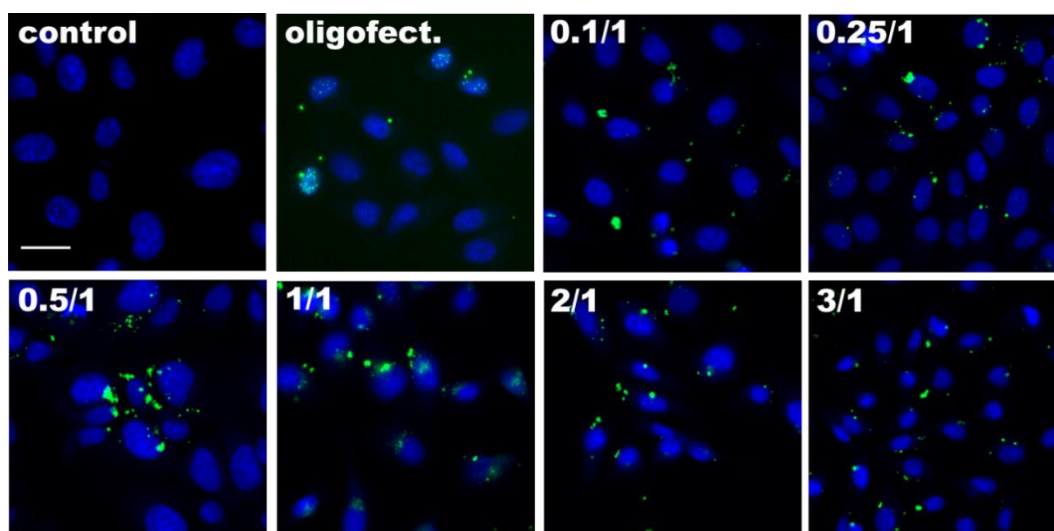


Figure 32. G(IKK)₃I-NH₂ efficiency in delivering fluorescently labelled ODNs into epithelial cancer cells. A431 cancer cells were transfected for 24 hrs with 0.05 µg of FAM-labelled ODNs (corresponding to 1.6 µM) and increased charge/ratios of G(IKK)₃I-NH₂. Oligofectamine (oligofect) was used as positive control and transfection was performed according to the manufacturer’s protocol. Un-complexed ODNs mixed to the culture medium represented the negative control (control). The images show fluorescent ODN molecules transfected into cancer cells proportionated to the G(IKK)₃I-NH₂ / FAM-ODN charge ratio changes. Hoechst 33342 (2 µg/ml) (blue) was used as nuclear staining. FAM-labelled ODN in green. Bar = 25 µm. All images are scaled to the same size.

Figure 32 shows a similar result to A₉K, as G(IKK)₃I-NH₂ can bind DNA molecules and carry them inside cells. Most cells contain several green puncta in each image and the amount of fluorescent DNA seemed to be consistent with increasing peptide ratios, especially at the 3/1 ratio. Unlike A₉K (Figure 2 in Chapter 3) where high ratios had the tendency in producing clumps, with G(IKK)₃I-NH₂ this phenomenon was not observed. Nevertheless, when G(IKK)₃I-NH₂ transfection efficiency is compared with the Oligofectamine transfection control, it is possible to observe that none of the peptide/ODN complexes are located in the nuclei. This suggests that this peptide, like A₉K, is not able to efficiently cross the nuclear membrane.

As previously assessed with A₉K, (Figure 5 in Chapter 3), it was important to determine the peptide efficiency in transfecting different cell lines, including non-cancer cell types

in order to evaluate possible selectivity toward a specific cellular type, G(IKK)₃I-NH₂ was complexed with FAM-labelled ODNs and transfected in primary cultures of HDFs. In Figure 33 only few green puncta can be observed, even at the highest peptide ratio, suggesting that almost none of the FAM-ODN complexed with G(IKK)₃I-NH₂ crossed the fibroblasts' plasma membrane. Contrary to this, the positive control showed highly transfected cells with green fluorescence mainly visible in the cytoplasmic environment.

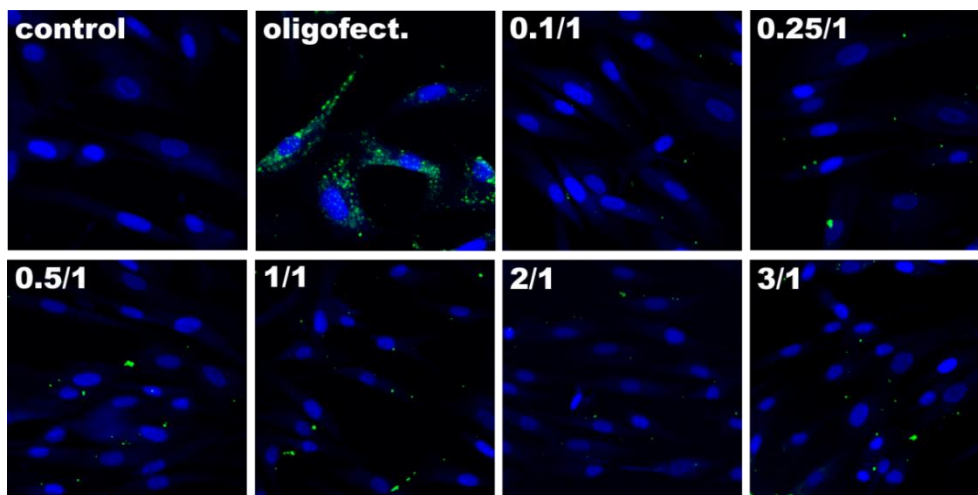


Figure 33. G(IKK)₃I-NH₂ efficiency in delivery of fluorescently labelled ODNs into a non-cancer cell line. HDFs were transfected for 24 hrs with 0.05 μg of FAM-ODNs (corresponding to 1.6 μM) and increasing charge/ratios of G(IKK)₃I-NH₂. Oligofectamine was used as positive control (oligofect), while un-complexed ODNs mixed to the culture medium represented the negative control (control). The images show the transfection rate of G(IKK)₃I-NH₂ in a normal (not-cancer) cell line: the peptide showed poor transfection efficiency at every tested ratio and very few green puncta can be seen in the cells. Hoechst 33342 (2 μg/ml) (blue) was used as nuclear staining. FAM-labelled ODNs in green. Bar = 25 μm. All the images are scaled at the same size.

ODNs mainly work in the nucleus, and so to test if a cytoplasmic functioning molecule could be used in conjunction with G(IKK)₃I-NH₂, siRNAs were tested. The ability of G(IKK)₃I-NH₂ transfection in both cancer and non-cancer cell lines was evaluated. siGLO red fluorescent indicator (Dharmacon) was chosen as siRNA molecule to be transfected into cells. Experiments were conducted on A431 and HCT-116, both cancer cell lines and HDFs as normal, not cancerous cells. Transfection using DharmaFECT1

(DF1), commercial reagent, was considered as positive control while the addition of un-complexed siGLO molecules to the cells was considered as negative control.

In Figure 34 there are representative images of A431 cells transfected with 75 nM of siGLO with progressively higher ratios of G(IKK)₃I-NH₂. The amount of red fluorescent siRNA molecules localised in the cells showed that the alpha helical peptide can transfect cells well, when compared to the positive control. Moreover, the internalisation of peptide/siRNA complexes does not depend on the charge ratios and all the tested concentrations show compatible levels of transfection.

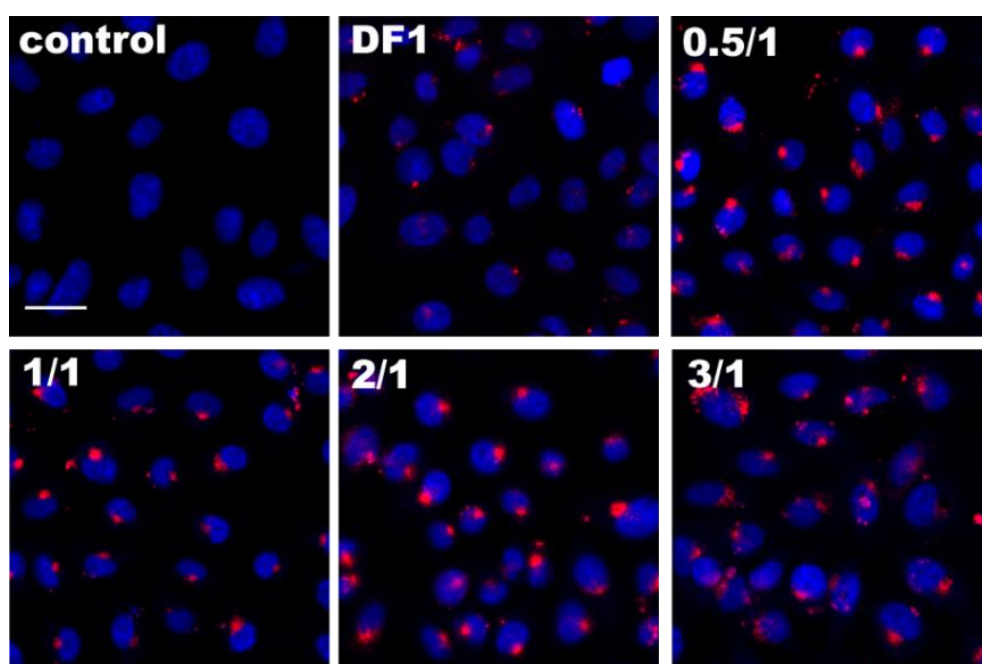


Figure 34. G(IKK)₃I-NH₂ efficiency in delivery of fluorescently labelled siRNA molecules into epithelial cancer cells. A431 cancer cells were transfected for 24 hrs with 75 nM of siGLO, red fluorescent indicator (Dharmacon) and increased charge/ratios of G(IKK)₃I-NH₂. DharmaFECT1 was used as positive control (DF1), while un-complexed siGLO mixed to the culture medium represented the negative control (control). The amount of fluorescent siRNA (red) is consistent in all the peptide / siGLO ratios and when compared to DF1, the transfection efficiency of G(IKK)₃I-NH₂ appears greater. Hoechst 33342 (2 µg/ml) (blue) was used as nuclear staining. Bar = 25 µm. All the images are scaled at the same size.

A similar outcome to the A431 experiment is observed for the experiment conducted on HCT-116 colon cancer cells (Figure 35), with the vast majority of cells showing many red puncta, indicating that a reasonable amount of siRNA had been internalised. Again, the siRNA transfection ability does not seem to be related to the peptide ratios. Moreover, for this cell line the transfection efficiencies of peptide and DF1 could be comparable. This result was also important in determining the peptide ability in transfecting colon cancer cells prior use to for 3D cancer models (see the section 4.1.4 *Evaluation of G(IKK)_{3I-NH₂} transfection efficiency in a 3D cancer cellular model* of this chapter).

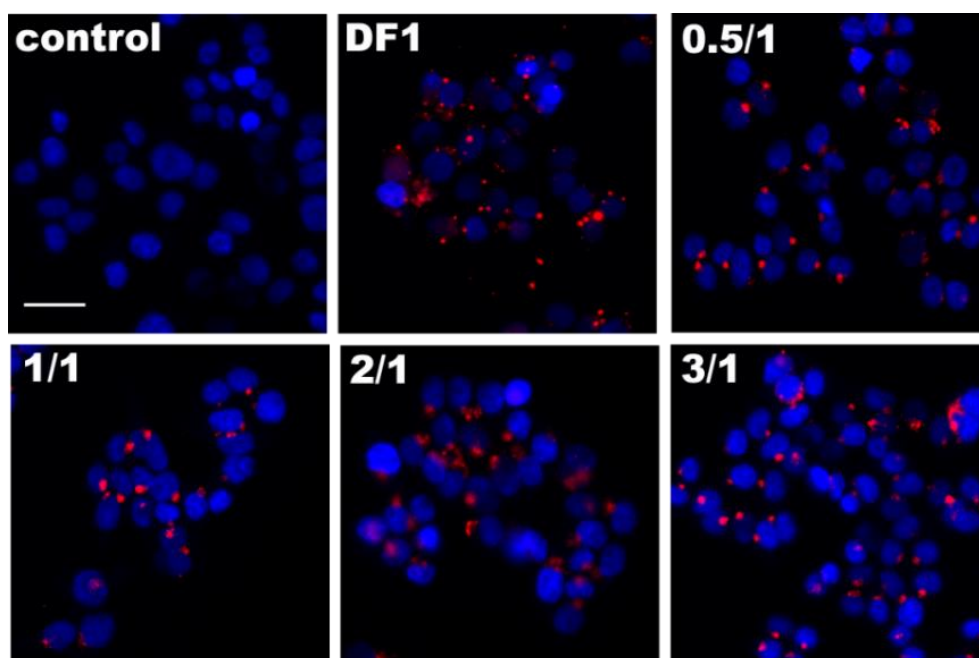


Figure 35. G(IKK)_{3I-NH₂} efficiency in delivery of fluorescently labelled siRNA molecules into colon cancer cells. HCT-116 cells were transfected for 24 hrs with 75 nM of siGLO, (red) and increased charge/ratios of G(IKK)_{3I-NH₂}. DharmaFECT1 was used as positive control (DF1), while un-complexed siGLO mixed to the culture medium represented the negative control (control). The amount of fluorescent siRNA (red) is consistent in all the peptide and DF1 experiments. Hoechst 33342 (2 µg/ml) (blue) was used as the nuclear staining. Bar = 25 µm. All the images are scaled at the same size.

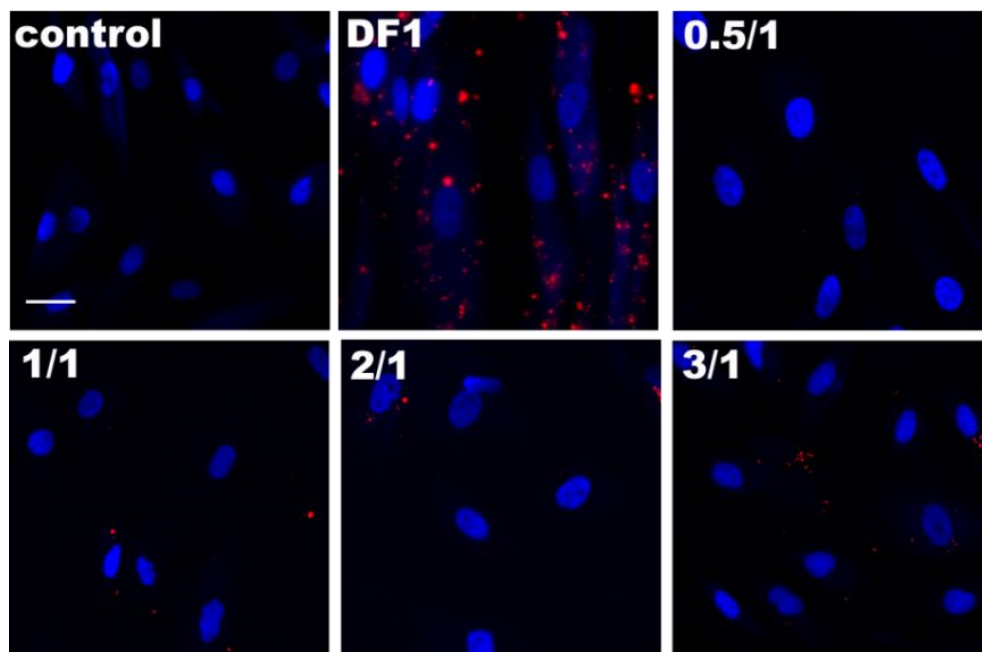


Figure 36. G(IKK)₃I-NH₂ efficiency in delivery of fluorescently labelled siRNA molecules into a non-cancer cell line. HDFs primary cells were transfected for 24 hrs with of 75 nM of siGLO (red) with increasing charge/ratios of G(IKK)₃I-NH₂. DharmaFECT1 was used as positive control (DF1) and un-complexed siGLO mixed to the culture medium represented the negative control (control). Images show the poor efficiency of G(IKK)₃I-NH₂ in transfecting fibroblasts with siRNA molecules, especially when compared to the commercial transfection reagent DF1. Hoechst 33342 (2 µg/ml) (blue) was used as nuclear staining. Bar = 25 µm. All the images are scaled at the same size.

When testing normal, non-cancerous cells, with G(IKK)₃I-NH₂ used to transfect the fibroblasts the results showed a poor siRNA internalisation, with red staining probably in between cells (Figure 36). For every tested peptide ratio, there were few, if any, red puncta, compared to the positive control, where there was an efficient rate of transfection.

4.1.2 Cell selectivity of G(IKK)₃I-NH₂ in a co-cultured system

The experiments described in the previous sections showed how G(IKK)₃I-NH₂ has a preference in transfecting cancer cells, compared to normal ones. To further evaluate the peptide ability in targeting and transfecting cancer cells, a co-culture system was prepared, in which HCT-116 colon cancer cells and HDFs primary fibroblasts were seeded together in a 96 well plate. The two cell lines were simultaneously transfected with 50 nM of siGLO using the commercial DF1 or 3 different ratios of peptide. Un-complexed siRNA molecules were added to the cell medium to represent the negative control. Images were acquired using the IN Cell Analyzer 2200 microscope with 40x objective. The results are shown in Figure 37, in which images were acquired using the bright field mode to better visualise the cell boundaries and consequently discriminate the cell types (HCT-116 or HDFs). DAPI (blue) and CY3 (red) channels were used instead to image the cell nuclei and the siGLO puncta, respectively. Fibroblasts could be easily identified due to their elongated shape, their larger nuclei and the presence of more cytoplasm. The colon cancer cells instead appeared clustered in colonies with small amount of cytoplasm and generally with a rounder morphology. Because this experiment was performed with the intent of evaluate the transfection efficiency of the alpha-helical peptide when compared to DF1, the distribution of the red fluorescent siGLO was carefully estimated. The merged images of bright field and fluorescent filters enabled the distinguishing of the siRNA molecules localisation within the two cell lines. When the transfection was made using DF1, an even distribution of red siGLO among both cells types (HCT-116 and HDFs) was observed while, when the G(IKK)₃I-NH₂ was used as complexing agent, the fluorescent siRNA was mainly associated with HCT-116 cells. The outcome of this experiment confirmed that G(IKK)₃I-NH₂ has a peculiar selectivity for cancer cells even when cultured together with other cell types.

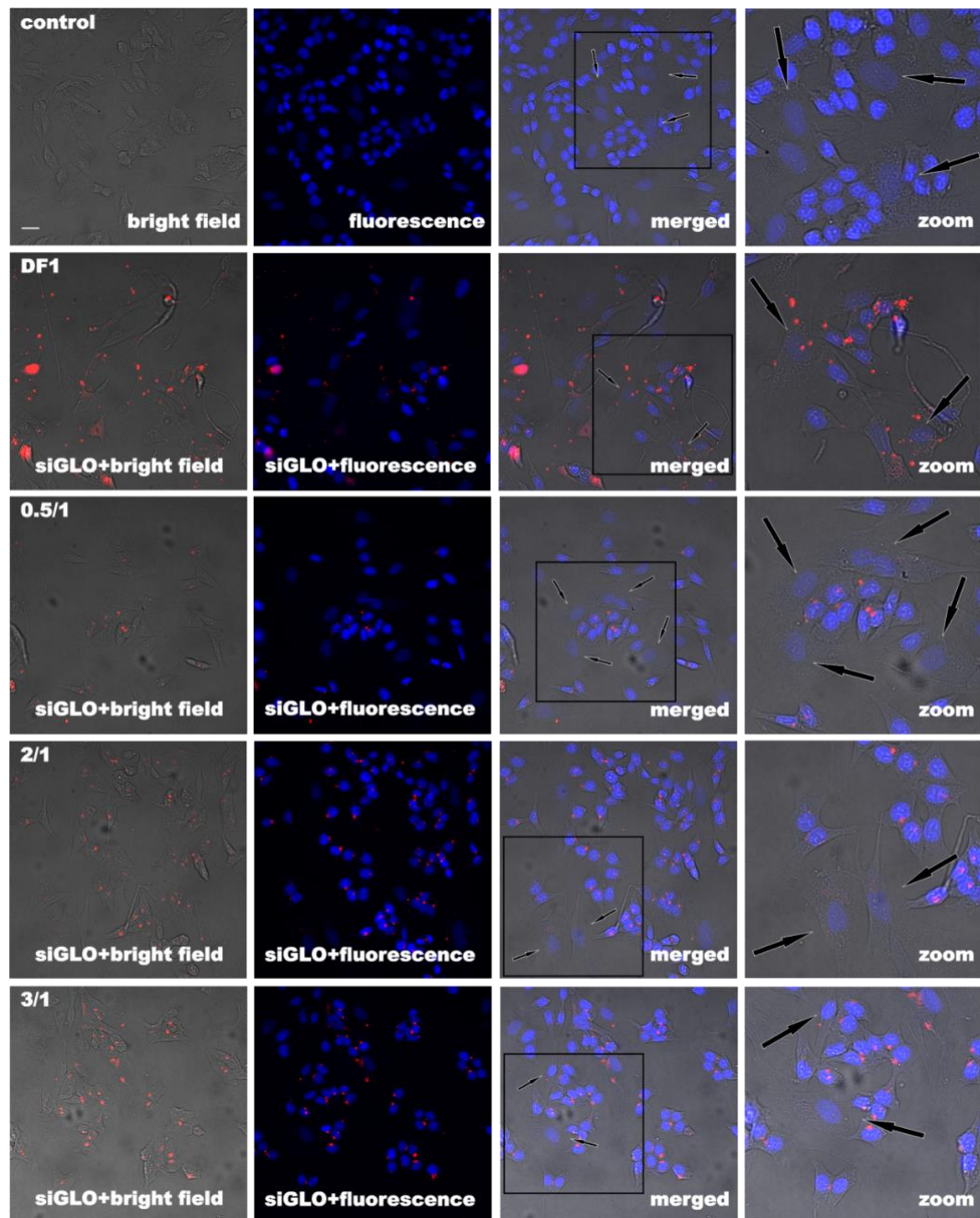


Figure 37. G(IIKK)₃I-NH₂ delivery of fluorescently labelled siRNA molecules into a co-cultured system. HCT-116 cancer cells and HDFs primary were cells co-cultured together and simultaneously transfected for 24 hrs with 50 nM of siGLO (red) and increasing charge/ratios of G(IIKK)₃I-NH₂. DharmaFECT1 was used as positive control (DF1), while un-complexed siGLO (red) mixed to the culture medium represented the negative control (control). Images were acquired in bright field or fluorescent modes. The black arrows indicate the fibroblasts while the last column of images represents a magnification of the cells in the black squares. Hoechst 33342 (2 µg/ml) (blue) was used as nuclear staining. Bar = 25 µm. All the images are scaled at the same size.

4.1.3 A study of FITC labelled G(IKK)₃I-NH₂ to determine co-localisation

A version of G(IKK)₃I-NH₂, labelled with the FITC was synthesised with the aim of visualising the peptide with siRNA once internalised by the cells.

Both HCT-116 and HDFs cells were transfected independently with 50 nM of red siGLO using the fluorescent FITC-G(IKK)₃I-NH₂ and following the same procedure applied to the other transfection experiments. Figure 38 shows the results achieved; similarly to the non-labelled version of the peptide, FITC-G(IKK)₃I-NH₂ preferably targeted and transfected mainly HCT-116 cells, while DF1 was not so selective and equally amounts of red fluorescent puncta (siGLO) were observed in both cell types. Because of FITC-G(IKK)₃I-NH₂ fluorescence, it was finally possible to observe the presence of both peptide and siRNA molecules in the transfected cells. This remarkable feature unequivocally confirmed the peptide ability in binding and transfecting siRNA molecules into cells. Moreover, the peptide/siRNA complexes, when co-localised in the same cellular compartment, appeared as yellow puncta, as consequence of the fluorescent green and red signals overlapping. The presence of few red puncta also suggested that, once the complexes are internalised, the peptide can release its cargoes allowing the modulation of gene expression mediated by the RNAi pathway. To better visualise fluorescence of the peptide in the co-localised complexes, a higher ratio (24/1) was used. At this ratio, even in some HDFs few yellow puncta could be observed.

It is important to underline that the cells, following the transfection procedure, did not show any toxicity signs, even at the highest used ratio 24/1 (1.2 µM of peptide complexed with 50 nM of siRNA). This because the concentrations of peptide employed for transfection were always below the toxic range identified with the cell counting assay and showed in Figure 45 (IC₅₀ 60 µM).

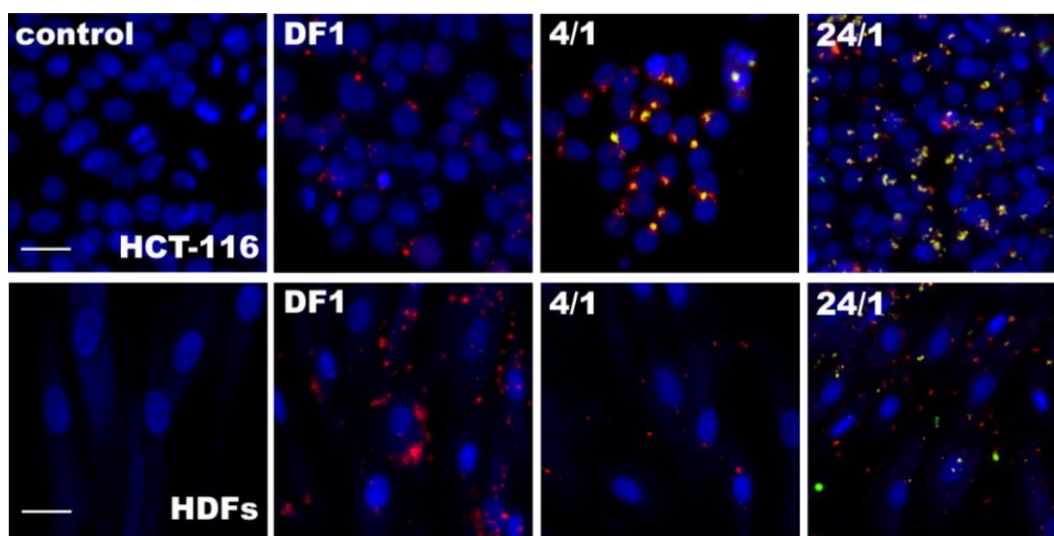


Figure 38. Subcellular co-localisation of internalised siRNA molecules and fluorescently labelled G(IKK)₃I-NH₂. HCT-116 colon cancer cells and HDFs primary cells were transfected for 24 hrs with 50 nM of siGLO (red) and two different charge/ratios of FITC-G(IKK)₃I-NH₂ (green). In the images it is noticeable that there is an overlap of the red and green fluorescent signals, indicating co-localisation. DharmaFECT1 was used as positive control (DF1), while un-complexed siGLO mixed to the culture medium represented the negative control (control). Hoechst 33342 (2 µg/ml) (blue) was used as nuclear stain. Bar = 25 µm. All the images are scaled at the same size.

4.1.4 Evaluation of G(IKK)₃I-NH₂ transfection efficiency in a 3D cancer cellular model

The siRNA transfection efficiency of G(IKK)₃I-NH₂ was evaluated in a 3D culture system, making it more relevant than 2D¹³⁴. Generally, one of the most important qualities that a cancer treatment should have is a good level of tumour penetration. Cells situated in the centre of solid tumours are normally hypoxic and, as evidence suggests, not only are they resistant to radiation treatment, but they possess regenerative properties, even after intense chemotherapy²¹⁷. Therefore, if a cancer therapy is unable to reach all the cells in a solid tumour, treatment efficacy is jeopardised¹⁸⁹.

To evaluate the ability of G(IKK)₃I-NH₂ to penetrate solid tumours, and its possible role as a carrier for drug or gene delivery, 3D spheroids of A431 were initially tested. Previously the cell line had been transfected with siRNA molecules (Figure 34). 3D spheroids were generated using ultra-low attachment well plates. Unfortunately, despite reports that A431 were a good spheroid model, the preliminary observation under the wide-field microscope revealed that these spheroids were extremely fragile, with irregular shapes¹⁹¹. HCT-116 cells were selected for experimentation and 3D spheroids were created^{192, 193}.

Images of spheroids were acquired using the ImageXpress® Micro System wide-field fluorescent microscope and the Zeiss Lightsheet Z.1 microscope with 2x objective lenses. Following acquisition, wide-field and light-sheet images were further analysed using the MetaXpress® 5.0.0.20 and the ZEN 2014 SP1 (Zeiss) software, respectively. Brightness and contrast were ultimately adjusted for all images to the same level using Image J. In Figure 39 it is possible to observe images of several spheroids from both cell lines transfected with 75 nM of red siGLO using DharmaFECT1 or different peptide ratios (2/1 or 5/1). Un-complexed siGLO was mixed with the culture medium and directly exposed to the cells representing the negative control. A431 spheroids were asymmetrical and differently sized, while HCT-116 spheroids were compact, spherical and with an average size of 600-800 µM.

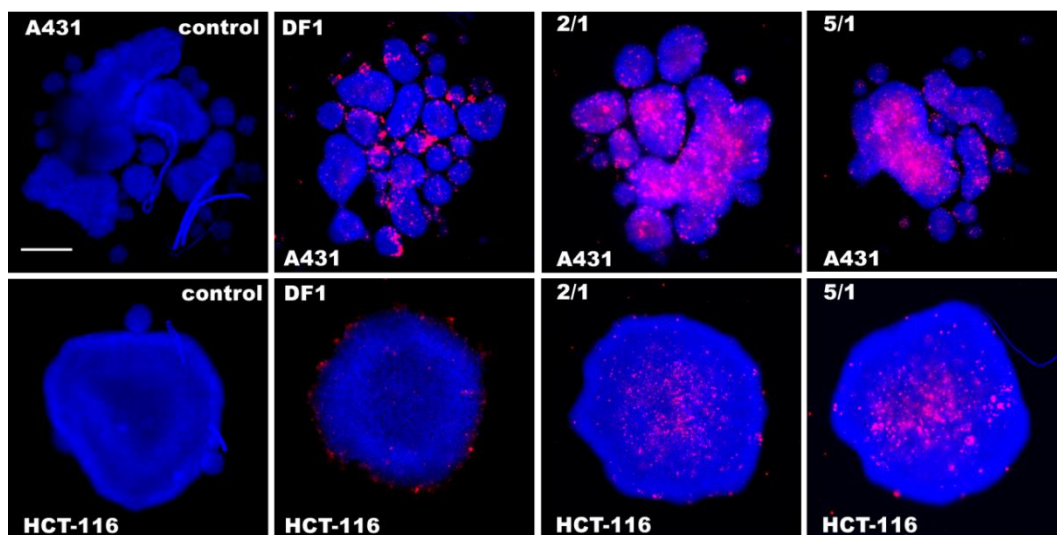


Figure 39. G(IKK)₃I-NH₂ efficiency in delivery of fluorescently labelled siRNA molecules into 3D cancer models. A431 or HCT-116 3D spheroids transfected for 24 hrs with 75 nM of siGLO, red fluorescent indicator (Dharmacon) using G(IKK)₃I-NH₂ peptide at different ratios. DharmFECT1 transfection was used as positive control (DF1), while un-complexed siGLO (red) mixed to the culture medium represented the negative control (control). Transfection performed using the G(IKK)₃I-NH₂ appears more successful in deeply penetrating the central cores of the spheroids. Hoechst 33342 (2 µg/ml) (blue) was used as nuclear staining. Bar = 250 µm. All the images are scaled at the same size.

The main visible difference between transfections made with DF1 or with G(IKK)₃I-NH₂ was the distribution of the red fluorescent siRNA molecules. When DF1 was used, the vast majority of red signal was located on the outer layer of the spheroidal mass and very little could be detected in the middle part. When the peptide was used, most of the fluorescent siRNAs were concentrated in the centre of the spheroids. Unfortunately, these images do not clarify the exact location of the red puncta due to the lack three-dimensionality.

To obtain better quality images in 3D, light-sheet-based fluorescence microscopy (LSFM) was used. This innovative technique allows not only to penetrate deep into the specimen with high imaging speed and ultra-low intensity light excitation, but also to acquire multiple stacks of the same sample, creating, with a dedicated software, exhaustive three-dimensional reconstructions ¹⁹⁴.

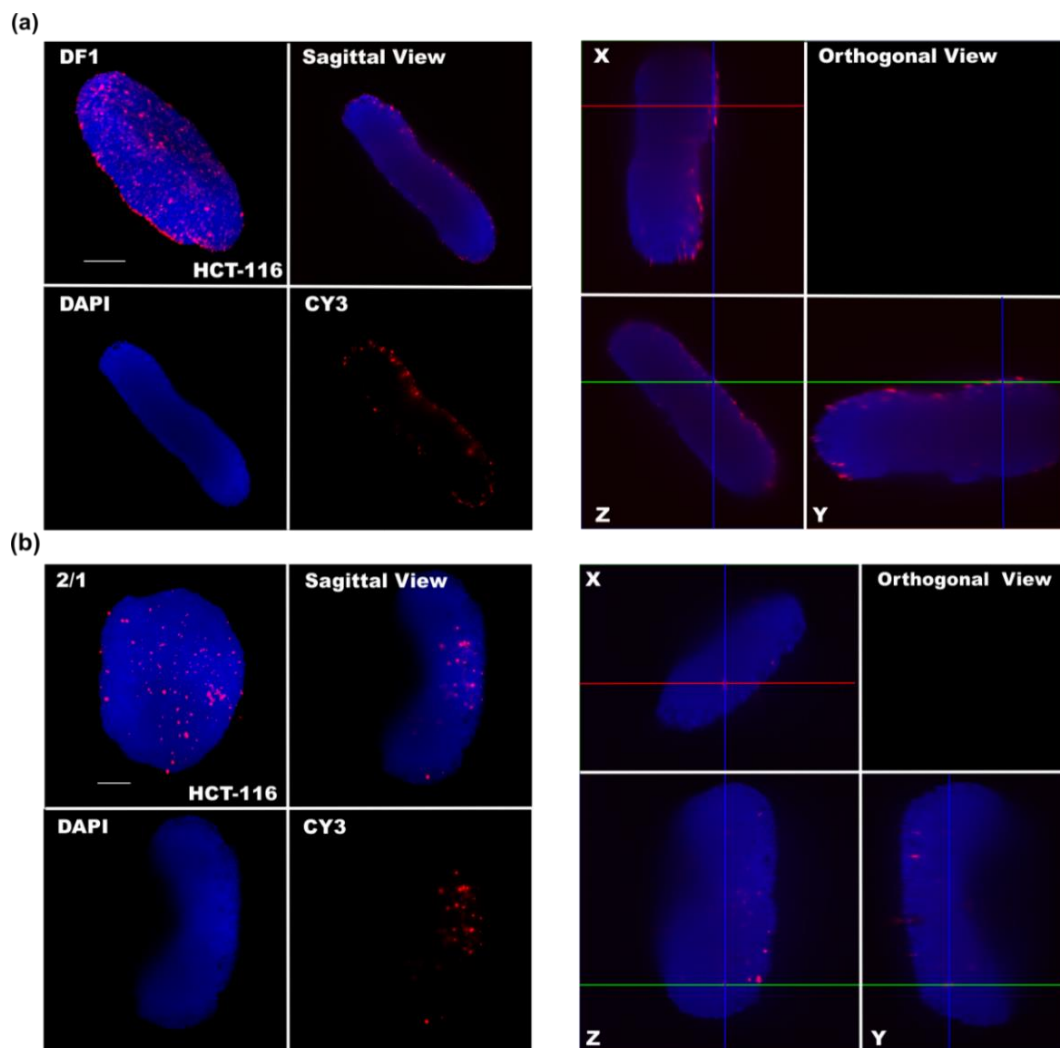


Figure 40. Light-sheet microscopy to evaluate the penetration of G(IKK)₃I-NH₂ in 3D cancer models. Light-sheet images of HCT-116 spheroids transfected for 24 hrs with 75 nM of siGLO using DharmaFECT1 (DF1) (a) or G(IKK)₃I-NH₂ at 2/1 ratio (b). The first image on top left corners in the left panels are 3D reconstructions showing the complete spheroids shape, while the others, in the same panel, represent sagittal views with combined or separated DAPI (blue nuclei) and CY3 (red siRNA) channels showing the difference distribution of the red fluorescent siRNA within the spheroid body. In the right panels, orthogonal views of the same spheroids show the location of the red siGLO in xyz planes. Hoechst 33342 (2 µg/ml) (blue) was used as nuclear staining. Bar = 250 µm. All the images are scaled at the same size.

Figure 40 shows, not only the 3D reconstruction of HCT-116 spheroids (top left corner, left side panels), but the distribution of the fluorescent siRNA molecules. The ZEN 2014 SP1 (Zeiss) software was used to create the 3D reconstructions and the spheroid orthogonal views with distinct xyz planes where the blue, red and green lines display the localisation of single red spots in the xyz spatial distribution. In the sagittal and orthogonal planes it is possible to observe the localisation of the fluorescent siRNA molecules. These image sets clearly show DF1 was unable to deeply transfect the spheroid, with the siGLO exclusively concentrated on the outer surface, while the peptide was able to reach deep into the spheroid where many red puncta are centrally located.

4.1.5 Functional siRNAs transfection

All the transfection experiments described in the previous sections used a non-targeting siRNA (siGLO), which has been really useful for visualisation purposes, but does not tell us anything about the efficiency of G(IKK)₃I-NH₂ in releasing siRNA molecules to functionally knock down gene expression once internalized into the cellular environment. Therefore, to evaluate the effectiveness of the peptide in modulating gene expression through RNAi, two functional siRNAs were selected as cargoes. ECT2 (Epithelial Cell Transforming 2 oncogene) and PLK1 (Polo-Like Kinase 1), which both can decrease cellular growth, were selected for transfection in A431 and HCT-116 cancer cells. If the cargo of siRNA is correctly released and incorporated into the RISC machinery, then the cells should undergo either apoptosis or an arrest of the cell cycle and therefore a substantial decrease in the cell number would be detected.

ECT2 siRNA was transfected in A431 cells using G(IKK)₃I-NH₂ while PLK1 was used on HCT-116 using the fluorescently labelled peptide FITC-G(IKK)₃I-NH₂. ECT2 is a protein largely localised in the nucleus of interphasic cells and it is responsible, among many things, for cell cycle progression and cytokinesis. Over-expression of ECT2 is believed to potentiate tumorigenesis via activating small GTPases such as Rho, Rac and Ras and elevated levels are often found in several types of human tumours^{218, 219}. Moreover, the knock down of ECT2 via RNAi should provoke a decrease of the cellular population²²⁰.

30 nM of siRNA together with peptides at different ratios were added to a plate and left to complex for 30 minutes. Afterwards, cells diluted in media lacking antibiotics were added and left incubate to for three days. Transfection using DharmaFECT1 (DF1) was used as positive control while un-complexed siRNAs diluted in the culture medium or transfection using the non-targeting red fluorescent siGLO were considered the negative control. MetaXpress® software was used to count the number of cells in each well and data normalised to the relative negative controls.

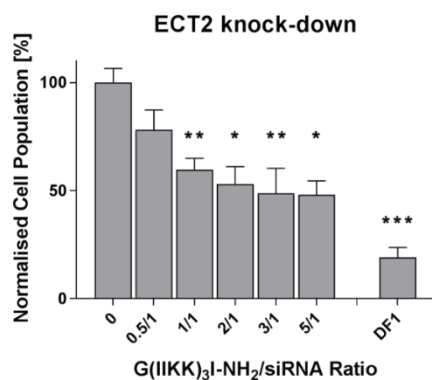


Figure 41. siRNA delivery and knock down efficiency of G(IKK)₃I-NH₂ on A431 cells. 30 nM of ECT2 siRNA were complexed with G(IKK)₃I-NH₂ and then transfected in A431 cells. To allow a complete knock down of ECT2 via RNAi the cells were left in the transfection medium (DF1 or peptide) for a total of 72 hrs, then fixed in formaldehyde and stained with Hoechst 3342 (2 µg/ml) to visualise the nuclei. Cell number was evaluated through nuclei counting using MetaXpress with the Multi Wavelength Scoring algorithm and the 2x objective. The results are expressed as a percentage and normalised to the negative control (exposure to the naked ECT2 siRNA). Different ratios of peptide to ECT2 siRNA are shown on the bar-chart. The transfection reagent DharmaFECT1 (DF1) was used as positive control, showing a reasonable degree of knock down. With the exception of 0.5/1, the other peptide ratios showed a significant decrease in cell number consistent with a successful gene knock down. The values obtained are the average of different experiments ± standard error mean (±SEM). Statistically significant difference from the negative control was determined by Student's t-test (*p<0.05; **p<0.01; ***p<0.001).

The number of A431 cells in each experimental condition were imaged and counted. The data were then normalised to the negative control (cells exposed to un-complexed ECT2 siRNA) and represented as a percentage. Transfection using DF1 was considered as the positive control. From Figure 41, DF1 was effective in transfecting the siRNA and a significant reduction in cell number was observed (75% less cells counted than the negative control). Furthermore, G(IKKK)₃I-NH₂ could reduce the cell number in the assay and successfully deliver the siRNA molecules in ratios from 1/1 to 5/1 and could transfect and release enough siRNA inside the cells to significantly reduce the cell number to ~50%. There was an exception to this, where for the lowest ratio (0.5/1) only a 10% reduction was observed.

To test if this effect could be seen on other cells, HCT-116 were tested. The graph in Figure 42 shows the data collected from the transfection of PLK1 siRNA using DF1 or FITC-G(IKKK)₃-NH₂ on HCT-116 colon cancer cells. The Polo-like kinase proteins family are critically essential for the cell cycle homeostasis, controlling centriole duplication, mitosis, cytokinesis and the DNA damage response ²²¹, and any variations occurring in their expression could lead to tumorigenic events. PLK1, as part of this family, is crucial to maintaining the normal mitosis and when overexpressed is often used as a prognostic marker for several human cancers ²²². For this reason, PLK1 inhibition is sometimes a target for cancer therapies and new drugs have been developed showing encouraging results in early-phase clinical trials, such as volasertib (BI 6727) in patients with acute myeloid leukaemia (AML) ²²³. When PLK1 is knocked-down in cancer cells using RNAi a significant reduction in the cell number population is observed, with an increasing rate of cells arrested in G2/M phase and evidence of many apoptotic nuclei ¹³⁷.

The data obtained with the transfection experiment is expressed in graphic form in Figure 42. The negative control, from which all the data was normalised, was represented with the non-functional red fluorescent siGLO. DF1 was used as positive control as per usual and it significantly decreased the cell population by 65%. FITC-G(IKKK)₃-NH₂ transfection efficiency was even more successful, and at every ratio tested the number of cells dramatically dropped down to more than 80% of the control.

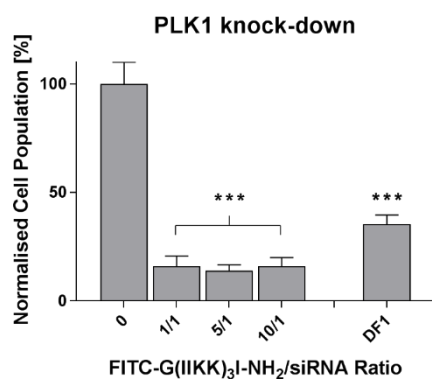


Figure 42. siRNA delivery and knock down efficiency of FITC-G(IKK)₃I-NH₂ on HCT-116 cells. 30 nM of PLK1 siRNA were complexed with FITC-G(IKK)₃I-NH₂ and then transfected in HCT-116 cells. To allow a complete knock-down of PLK1 via RNAi, the cells were left in the transfection medium (DF1 or peptide) for a total of 72 hrs, then fixed in formaldehyde and stained with Hoechst 3342 (2 µg/ml) to visualise the nuclei. Cell number was evaluated with nuclei counting using MetaXpress with Multi Wavelength Scoring algorithm and 2x objective. The results are expressed as percentage normalised to the negative control (transfection with siGLO). Different ratios of peptide to PLK1 siRNA are shown on the bar chart. All the tested peptide ratios showed a significant variation in cell population consistent with a successful gene knock-down. The transfection using DharmaFECT1 (DF1) was considered as a positive control and showed a reasonable degree of knock-down. The values obtained are the average of different experiments ± standard error mean (±SEM). Statistically significant difference from the negative control was determined by Student's t-test (***)p<0.001).

To visually compare the differences between the peptide and DF1 transfections, images of each tested condition were acquired with the wide-field microscope and the 20x objective (Figure 43). Some cells were exposed to the highest FITC-G(IKK)₃I-NH₂ concentration used to form complexes with siRNA (300 nM in the 10/1 ratio). This was important to ensure that this amount of peptide did not compromise the cell viability but could be safely used for transfection purposes. Cells following peptide exposure were counted and compared to the negative control. The results confirmed the absence of toxicity (103%) of cells counted compared to the negative control, data not showed). Transfection of PLK1 siRNA causes apoptosis in cancer cells ¹³⁷ and the cellular phenotypes observed after both DF1 and FITC-G(IKK)₃I-NH₂ transfections were compatible with apoptotic events. Interestingly, the presence of the fluorescent peptide

is visible when the highest ratio (10/1 ratio) was used. This is noticeable not only with siGLO (yellow puncta) but also in PLK1 siRNA transfection.

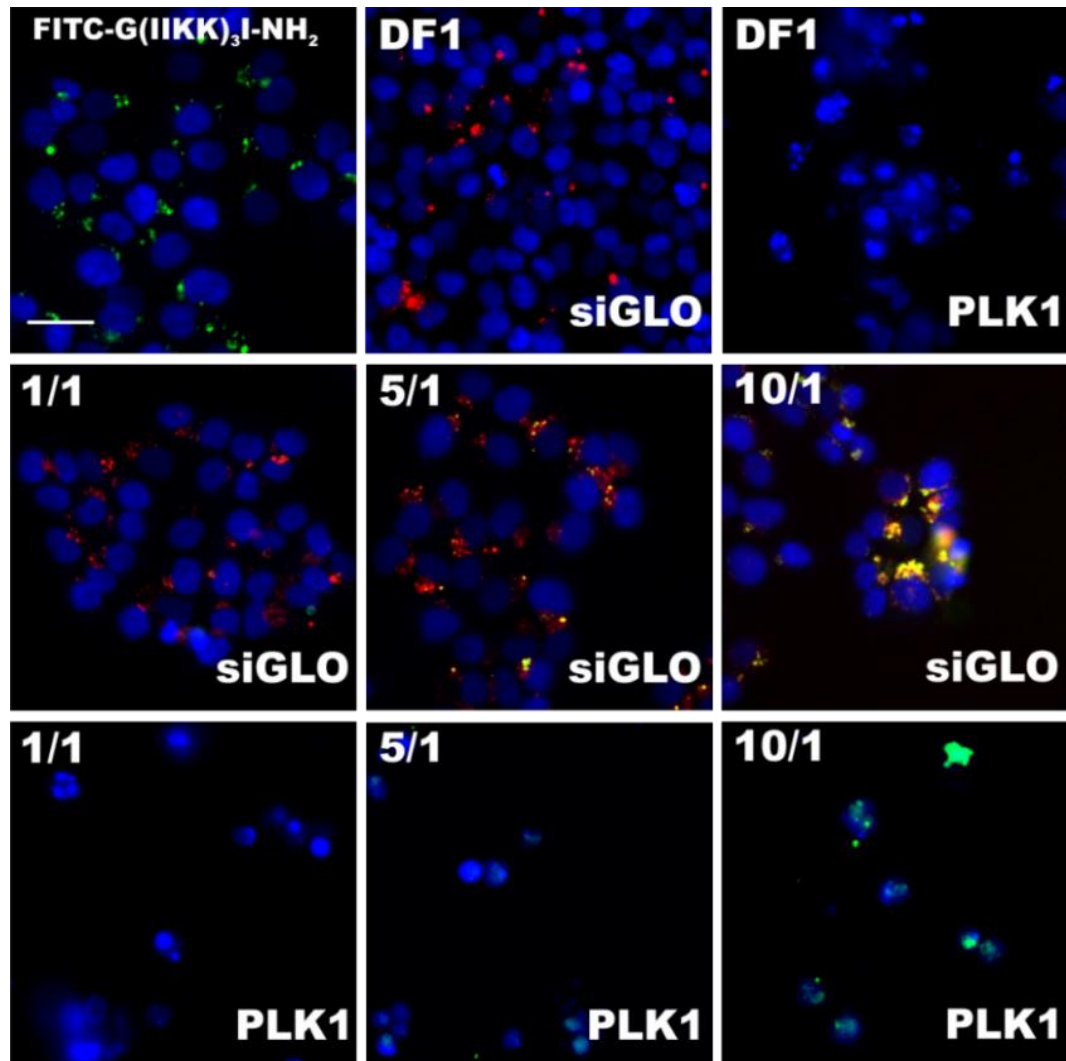


Figure 43. Knock down efficiency of DF1 and FITC-G(IKK)₃I-NH₂ on colon cancer cells. 30 nM of PLK1 or red fluorescent siGLO were complexed with three different ratios of FITC-G(IKK)₃I-NH₂ (green) and then transfected in HCT-116 cells. DharmaFECT1 (DF1) was used as positive control. In the first image in the top left corner are cells exposed to 300 nM of peptide (maximum peptide concentration used in the experiment). PLK1 knock down using RNAi causes apoptotic events in cells whose phenotype can be recognised in the images of PLK1 transfection using both DF1 and the peptide, confirming the data of the decrease in cell number shown in the graph in Figure 42. Hoechst 33342 (2 µg/ml) (blue) was used as nuclear staining. Bar = 25 µm. All the images are scaled at the same size.

These preliminary results suggest that G(IKK)₃I-NH₂ could be used as possible vector for transfection, especially after the promising data obtained with functional siRNAs experiments.

4.2 Toxicity and phalloidin staining

Previous published works showed that G(IKK)₃I-NH₂ is quite effective in inhibiting cancer cell growth (IC₅₀ values for HeLa and HL 60 being respectively 15 and 25 μM) but at the same time well tolerated by normal mammalian cells (fibroblasts were only slightly affected by the peptide exposure for concentrations up to 100 μM) ^{117, 118}.

The inhibitory effects of G(IKK)₃I-NH₂ and FITC-G(IKK)₃I-NH₂ were analysed on HCT-116 and HDFs cell lines. A range of concentrations was used (from 6.25 to 100 μM) for 24, 48 or 72 hrs of exposure time. Both peptides were compared, as it was important to establish if the relation between peptide and cells was somehow changing due to the presence of the fluorophore FITC. Moreover, the location of FITC-G(IKK)₃I-NH₂, could be tracked in both HCT-116 and HDFs using Alexa Fluor® 568 Phalloidin, a dye that binds actin filaments in the cytoplasm, allowing cellular shape to be defined ³⁷.

4.2.1 Cell counting assay as evaluation of peptide toxic effect

Cells were seeded and treated with peptides and fixed in formaldehyde, stained with Hoechst 3342 (2 μg/ml) and the nuclei of each experimental point counted and normalised to the relative negative control (untreated cells). The assessment of possible cellular toxicity was evaluated using MetaXpress software and the dedicated algorithm able to recognize cellular nuclei when stained with Dapi (or Hoechst). Na₂CrO₄, a potent toxic and carcinogenic compound ^{209, 210} was used as positive control and caused a significant decrease in cell number on both cell lines and at every time point (Table 3).

Table 3. HCT-116 and HDFs cell number evaluated with high-content microscopy after exposure to sodium chromate (Na₂CrO₄). The results are expressed as a percentage and normalized to the negative control at that relative time point.

Cell counting after 200 μ M of Na ₂ CrO ₄ exposure (%)		
	HCT-116	HDFs
24 hrs	20	26
48 hrs	2	21
72hrs	2	15

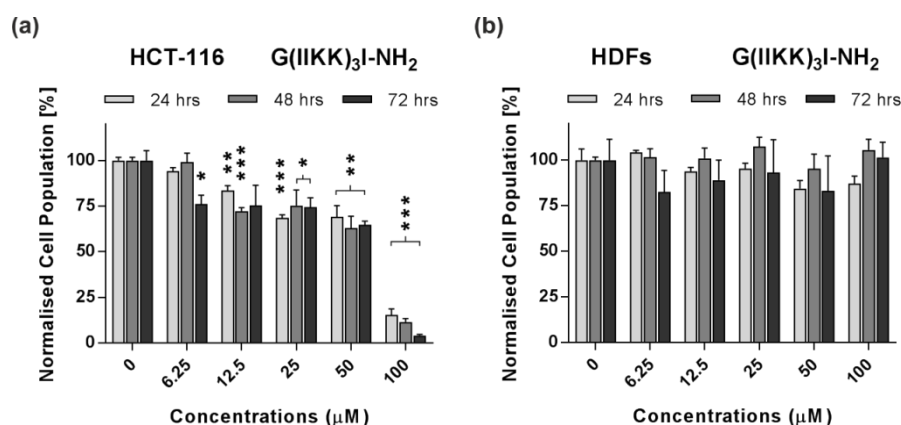


Figure 44. HCT-116 and HDFs cell number evaluated with high-content microscopy after exposure to G(IKK)₃I-NH₂. HCT-116 (a) or HDFs (b) cells were incubated for one, two or three days with increasing concentrations of G(IKK)₃I-NH₂, fixed in formaldehyde and stain with Hoechst 3342 (2 μ g/ml) to reveal the nuclei. Cell number was evaluated with nuclei staining analysis using the MetaXpress with the Multi Wavelength Scoring algorithm and 2x objective. The results are expressed as a percentage of number of cells and normalized to the negative control at that relative time point. The values obtained are averages of three independent experiments \pm standard error mean (\pm SEM). Na₂CrO₄, 200 μ M has been used as positive control (data showed in Table 3) while water has been used as negative control (0). Statistically significant difference from the negative control was determined by Student's t-test (* p <0.05; ** p <0.01; *** p <0.001).

Figure 44 represents the relative cell numbers for HCT-116 (a) and HDFs (b) to untreated samples. For the fibroblasts G(IKK)₃I-NH₂ did not have an inhibitory effect

on the cellular growth at any of the tested concentrations and exposure times, while the colon cancer cells showed sensitivity towards the peptide.

The exposure to FITC-G(IKKK)₃I-NH₂ gave slightly different results; while the cancer cells responded in a comparable way to the unlabelled one, the fibroblasts appeared to be more sensitive to this new peptide, especially at the highest concentration (100 μM). Figure 45 shows the results obtained after the cell counting. The overall toxicity observed for HCT-116 is perfectly comparable with the data of Figure 44. For example, 100 μM of FITC-G(IKKK)₃I-NH₂ caused a decrease in cell number of 84%, which is the same as the non-fluorescent peptide. On fibroblasts the same concentration caused a reduction of 63% while with the G(IKKK)₃I-NH₂ it was only 13%.

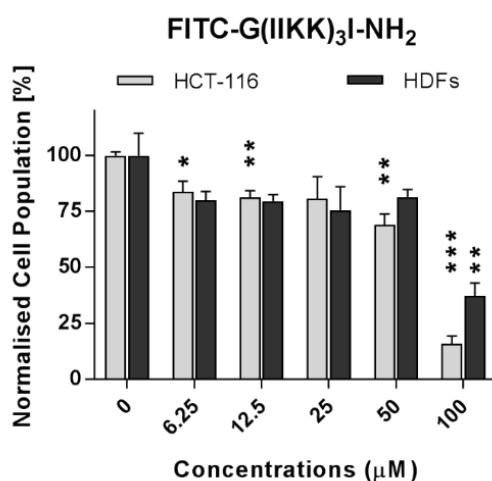


Figure 45. HCT-116 and HDFs cell number evaluated with high-content microscopy after exposure to FITC-G(IKKK)₃I-NH₂. HCT-116 or HDFs cells were incubated for one day with increasing concentrations of FITC-G(IKKK)₃I-NH₂, fixed in formaldehyde and stained with Hoechst 3342 (2 μg/ml) to reveal the nuclei. Cell number was evaluated with nuclei staining analysis using the MetaXpress with the Multi Wavelength Scoring algorithm and 2x objective. The results are expressed as a percentage of number of cells and normalized to the negative control at that relative time point. The values obtained are averages of three independent experiments ± standard error mean (±SEM). Na₂CrO₄, 200 μM has been used as positive control (data not showed) while water has been used as negative control (0). Statistically significant difference from the negative control was determined by Student's t-test (*p<0.05; **p<0.01; ***p<0.001).

Using GraphPad, the inhibitory concentration (IC_{50}), corresponding to the concentration of peptide needed to induce cellular growth inhibition of 50%, was calculated. Against HCT-116 colon cancer cells, G(IKK)₃I-NH₂ had an IC_{50} of 56, 50 and 43 μ M after 24, 48 and 72 hrs exposure, respectively. The peptide proved ineffective towards HDFs in the range of tested concentrations and no IC_{50} could be extrapolated. The IC_{50} of FITC-G(IKK)₃I-NH₂ after 24 hrs exposure was 60 μ M for the colon cancer cells and therefore perfectly comparable with the non-fluorescent peptide at the same conditions. FITC-G(IKK)₃I-NH₂ induced toxicity also in fibroblasts and the correspondent IC_{50} was 86 μ M.

It is important to underline that despite showing a certain level of toxicity, both G(IKK)₃I-NH₂ and FITC-G(IKK)₃I-NH₂ were perfectly safe to use in gene delivery experiments. This is because the highest concentrations used for transfection of either ODN and siRNA were always several folds below the peptides IC_{50} values. For example, the range of G(IKK)₃I-NH₂ used in ODNs transfection experiments varied between 160 nM and 4.8 μ M while for siRNA transfection the range was even lower; between 25 nM to 375 nM. For siRNA transfection using FITC-G(IKK)₃I-NH₂ the concentration range was between 30 nM and 1.2 μ M. Moreover, when functional siRNAs were transfected into cells only small amounts of peptides were employed and the maximum concentrations used were 150 and 300 nM for G(IKK)₃I-NH₂ and FITC-G(IKK)₃I-NH₂, respectively.

4.2.2 Phalloidin staining to enhance the cellular boundaries

To have a more precise subcellular localisation of the peptide within the cells, Alexa Fluor® 568 Phalloidin was used; a fluorescent dye which allows one to distinguish the cell shape and enhances its morphology. Phalloidin is a natural toxin that belongs to the class of phallotoxins, found in the death cap mushroom species *Amanita phalloides*. It naturally binds filamentous-actin (F-actin) and prevents its depolymerisation, ultimately causing cell death. Because of its affinity for F-actin, phalloidin, conjugated with various fluorophores, is widely used in imaging applications to selectively fluorescently label actin^{36, 37, 224, 225}.

Both HCT-116 and HDFs were exposed for 24 hrs to various concentrations of FITC-G(IKK)₃I-NH₂. Once fixed in formaldehyde they were stained with Hoechst 3342 (2 µg/ml) to enhance the nuclei and with 150 nM of Alexa Fluor® 568 Phalloidin, which gave a bright red fluorescence to the actin filaments. Images were acquired using the ImageXpress® Micro System wide-field fluorescent microscope with 20x objective lenses. Following acquisition, the images were further analysed using MetaXpress® 5.0.0.20 software. Brightness and contrast were ultimately adjusted for all the images to the same level by using Image J. To avoid confluency, which would have decreased the imaging quality of the cellular boundaries and structures, cells were seeded at low density. In this way, it was possible to capture only one or a few single cells per field with well-defined borders.

Figure 46 shows images of HCT-116 or HDFs after Alexa Fluor® 568 Phalloidin staining. Interestingly, it was observed with mitotic cells that most of the FITC fluorescence was outside, surrounding the plasma membrane and the peptide was not internalised (yellow circled cells in 12.5 and 25 µM pictures). It has been shown that during the early mitotic phases, endocytosis is inhibited²²⁶. Therefore, this evidence may suggest the possibility of an active mechanism being involved in peptide uptake. Current understanding suggests the mechanism of internalisation is through rapid binding to cancer cell membranes and the subsequent membrane permeabilization¹¹⁸. The fibroblasts, in contrast, showed localised FITC-G(IKK)₃I-NH₂ sometimes on the plasma membrane and occasionally internalised. This is true especially at higher concentrations of peptide (25-50 µM).

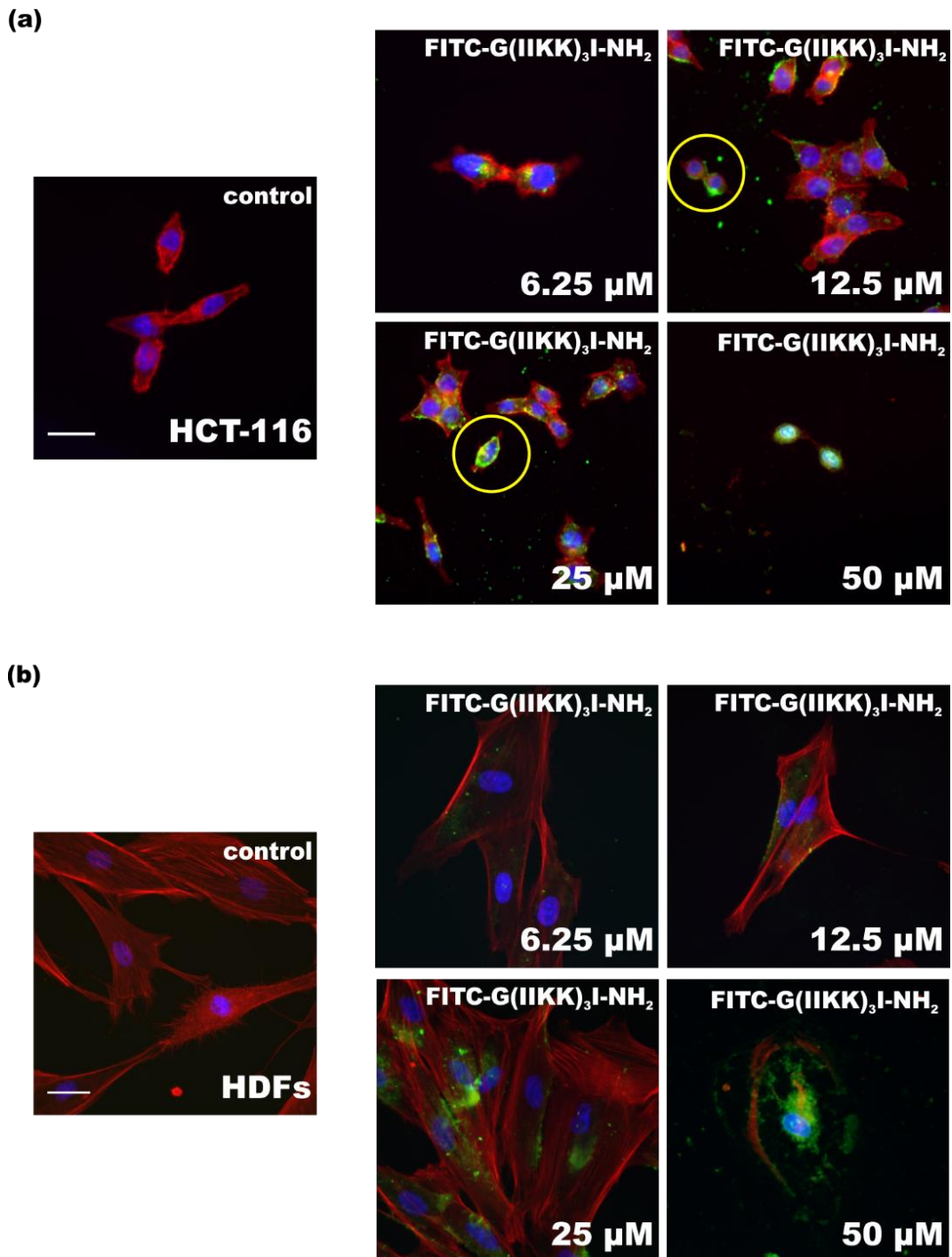


Figure 46. HCT-116 and HDFs phalloidin staining evaluated with high-content microscopy after exposure to FITC-G(IKKK)₃I-NH₂. HCT-116 (a) or HDFs (b) cells were incubated for one day with increasing concentrations of FITC-G(IKKK)₃I-NH₂ (green) and stained with Hoechst 3342 (2 μg/ml) (blue) and 150 nM of Alexa Fluor® 568 Phalloidin (red). The yellow circles show cells in mitosis with peptide molecules surrounding the plasma membranes. The control is represented by untreated cells. Bar = 25 μm. All the images are scaled at the same size.

50 μ M of FITC-G(IKK)₃I-NH₂ changed both cell shape and nuclear morphology in both cell lines (Figure 47). The peptide concentrated to the nuclear area and the F-actin filaments appeared condensed and damaged. The nuclear Hoechst stain was intense and nuclei were smaller, suggesting the cells were possibly dying via apoptosis²²⁷. The toxic effect caused by 50 μ M of peptide could be related to the reduced seeded cell number used to perform the experiment and the consequent higher peptide/cell ratio²²⁸.

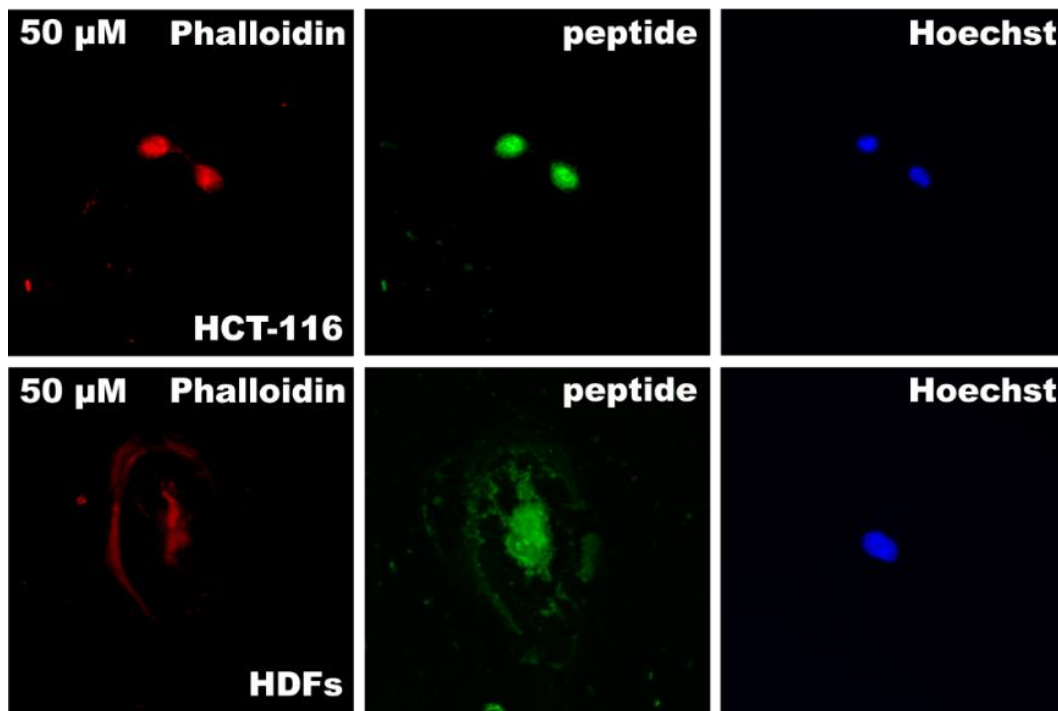


Figure 47. HCT-116 and HDFs cells exposed to 50 μ M of FITC-G(IKK)₃I-NH₂. HCT-116 or HDFs cells were incubated for one day with 50 μ M of FITC-G(IKK)₃I-NH₂ (green) and stained with Hoechst 3342 (2 μ g/ml) (blue) and 150 nM of Alexa Fluor® 568 Phalloidin (red). In these images, the three fluorescent channels were separated to show the destruction of cellular structures and the peptide distribution. Bar = 25 μ m. All the images are scaled at the same size.

4.3 Electron microscopy explores the effects and interaction of FITC-G(IKKK)₃I-NH₂ with cancer cells

To understand in more detail what is happening at the subcellular level higher resolution of imaging of HCT-116 cancer cells exposed to FITC-G(IKKK)₃I-NH₂ would be better. A scanning electron microscope (SEM) and a transmission electron microscope (TEM) were used to understand more about membrane morphology and localisation of the peptide. With these two techniques it is possible to acquire images using a focused electron beam as “light source” which, having lower wavelength, allows one to get resolutions a thousand times better than a standard light microscope.

SEM provides information regarding the surface morphology and composition of a specimen, normally scanning the top 1 µm and without destroying the sample in the process, with a resolution in the order of nanometres ^{229, 230}. TEM works with an electron beam at high energy, which travels across a column where a vacuum is created and hits an ultra-thin specimen section (usually less than 100 nm). When they hit the sample, the electrons can be scattered and consequently disappear from the beam, or stay un-scattered. At the end of the microscope there is a fluorescent screen able to capture the un-scattered electrons. From the screen, images of the various areas of the sample can be created, and depending on their density they will appear as different shades of darkness ²³¹. With this microscope it is possible to acquire extremely detailed structures, even in the order of few ångström.

4.3.1 SEM technique is a reliable instrument for studying cell membranes

HCT-116 were exposed for 24 hrs to 0, 0.3, 6.25 or 100 μM of FITC-G(IKK)₃I-NH₂ then fixed in glutaraldehyde and dried in ethanol according to the protocol described in the Materials and Methods chapter. Once ready, the samples were mounted onto a pin-stub and examined using the Philips XL-20 Scanning Electron Microscope at 15 kV. With this type of microscope, it was possible to observe any changes to the morphology of the membranes due to the peptide exposure.

Figure 48 shows lower magnification images of untreated HCT-116 cells or exposed to FITC-G(IKK)₃I-NH₂, to get a feeling for obvious differences between the concentrations. In normal healthy cells, the membranes are covered in thin actin plasma membrane protrusive structures called filopodia which are essential for the cells to sense the nearby environment and have a crucial role in cell migration, adhesion, morphogenesis, endocytosis and phagocytosis. Cells were treated with different peptide concentrations: 0.3 μM (300 nM) the highest concentration used in the functional siRNA transfection experiments (Figure 43); 6.25 μM which gave only little toxicity to the cells (Figure 45) and 100 μM which drastically decreased the cell population (Figure 45). Phenotypic changes of treated cells compared to the untreated sample were recorded. Figure 48 (a) shows images at 500X while (b) shows images at much higher magnification (2000X). Modifications were observed in cells treated with 0.3 or 6.25 μM , while with 100 μM cells, not only were they reduced in number but also were completely modified in their membrane structure. In the control or 0.3, 6.25 μM sample cells appeared healthy and with their membranes enriched with many filopodia but cells exposed to 100 μM had their filamentous protrusions completely damaged and the membranes showed signs of deterioration.

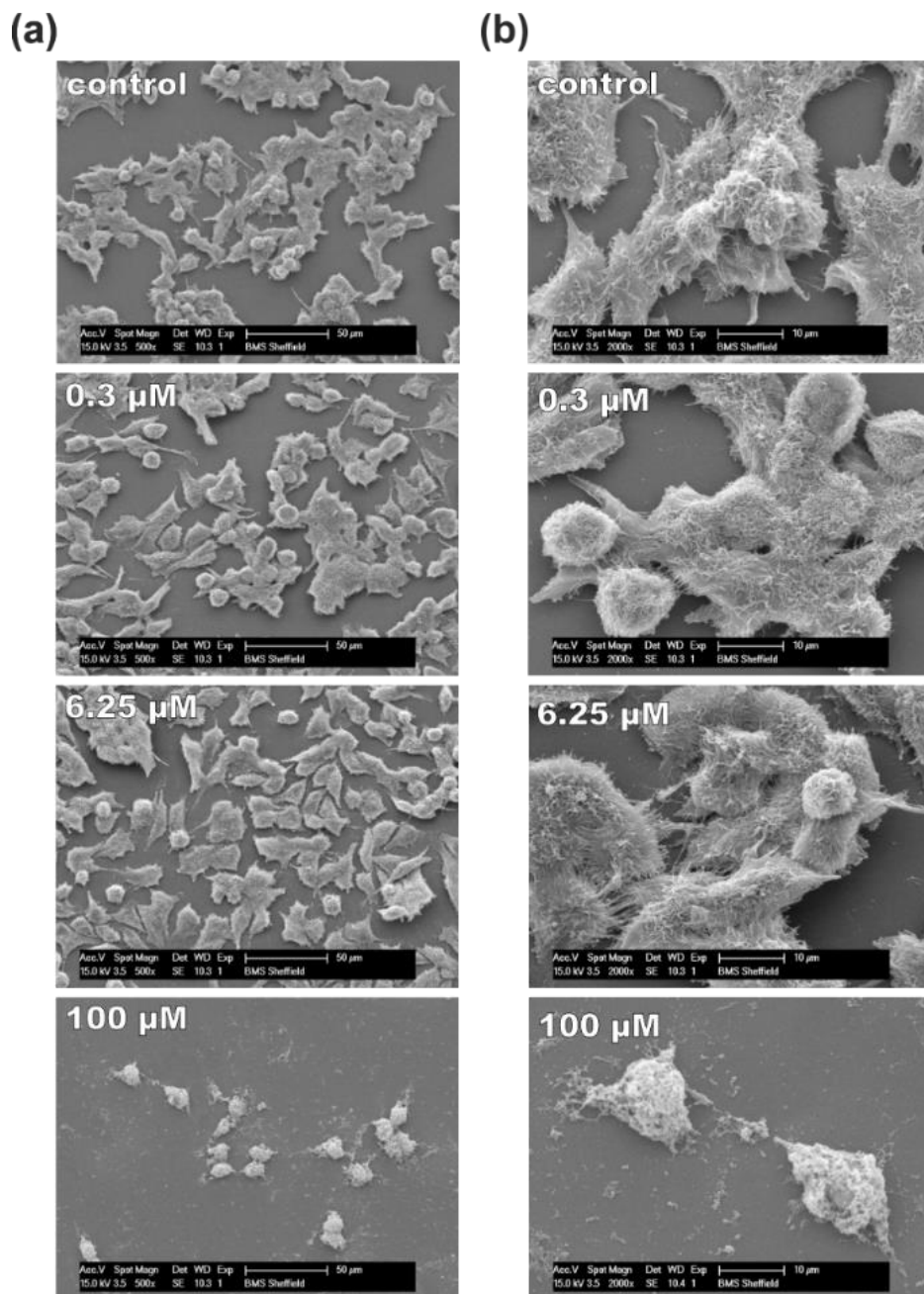


Figure 48. SEM images showing the morphology of cancer cells following exposure to FITC-G(IKK)₃I-NH₂. HCT-116 cancer were cells exposed for 24 hrs to different concentrations of FITC-G(IKK)₃I-NH₂ and imaged using the SEM microscopy with 500X (a) or 2000X (b) of magnification. Untreated cells are the control. At 0.3 μ M (highest concentration used for transfection experiments) and 6.25 μ M cells kept their typical morphological structure and the membranes stayed covered in filopodia, protruding structures containing actin filaments essential for cellular adhesion and motility. At 100 μ M, cell number is dramatically decreased and the morphology of the cells radically changed with a complete loss of filopodia and the cells had a sponge-like or porous phenotype. Bars = 50 μ m for (a) and 10 μ m for (b).

Progressively higher magnification images (Figure 49) of untreated control (a) and 100 μM treated (b) cells were taken at 5000X, 10000X and 20000X. The difference between treated and untreated cells is impressive: the plasma membrane projections which usually cover the cells' surface as numerous hair-like structures in (a) images are completely disappeared in (b) images, where the cells present an obvious “spongy” looking phenotype. It is unclear if the destruction of filopodia is a direct effect of the peptide interaction with the cell membranes or if it is an indirect consequence of the internalisation mechanism.

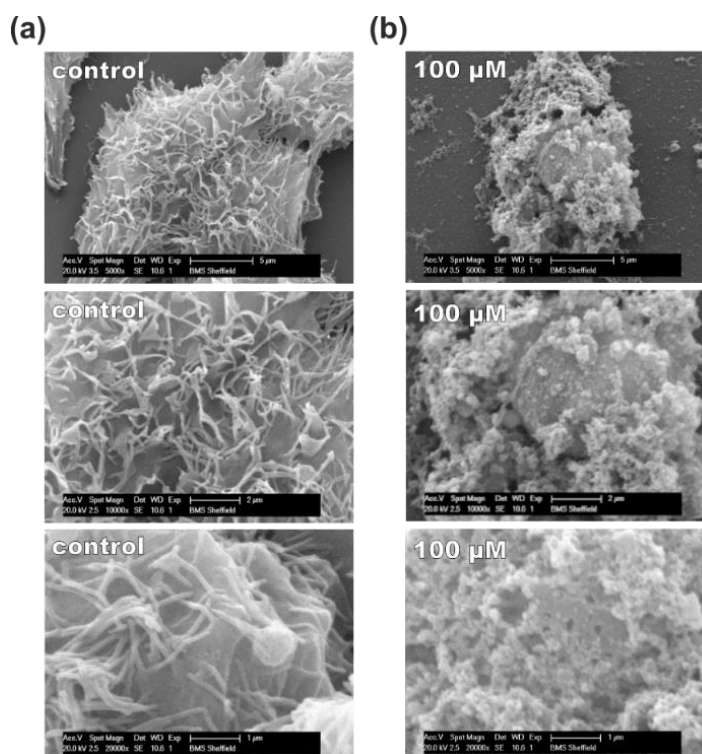


Figure 49. Higher magnification SEM images showing changes in the plasma membrane morphology of cancer cells following exposure to FITC-G(IKK)₃I-NH₂. HCT-116 cancer cells were exposed for 24 hrs to 0 μM (a) or 100 μM (b) of FITC-G(IKK)₃I-NH₂ peptide and imaged using the SEM microscopy at progressively higher magnifications (5000X, 10000X, 20000X, top to bottom). Untreated cells were considered as control. Images show the differences in the membranes' morphology of HCT-116 when treated with high concentration of peptide. Compared to normal healthy cells, the membranes of cells exposed to FITC-G(IKK)₃I-NH₂ lost all their filamentous protrusion and with the 20000X magnification it is even possible to observe in the cellular membrane structures similar to pores. Bars = 5 μm 2 μm and 1 μm , top to bottom.

4.3.1 Cellular localisation of FITC-G(IKK)₃I-NH₂ in cancer cells using TEM

Transmission Electron Microscopy (TEM) can be used to obtain high resolution images of biological internal structures such as mitochondria, endosomes or nuclei. TEM is several orders of magnitude better than from an optical or fluorescent microscope²³¹.

To investigate the fate of internalised peptide molecules in cancer cells, TEM was used on cellular samples previously exposed to the peptide. HCT-116 cancer cells were therefore exposed to 6.25 μ M of FITC-G(IKK)₃-NH₂ peptide for 3 or 24 hrs, then fixed and embedded in resin. Ultra-thin sections of 85 nm thickness were cut using an ultramicrotome and mounted on an FEI Tecnai Transmission Electron Microscope at an accelerating voltage of 80 kV. To be able to localise the peptide in the samples with the transmission electron microscope, an antibody anti-FITC conjugated with 10 nm gold nanoparticles was used. Gold nanoparticles, due to their high electron density, can indeed be easily detected using TEM and visualised as dark spherical dots inside the cells. Gold nanoparticles are used in molecular cell imaging techniques and more recently in several cancer nanotechnology disciplines (molecular diagnosis and targeted therapy)²³²⁻²³⁴.

Despite my efforts, it was impossible to immunolabel the samples using the technique suggested by the manufacturer. The pre-and post-embedding protocols (pre-embedding protocol; post-embedding protocol), which describe how to incubate the samples with the antibody before or after the resin embedding, were both tested but the results yielded nothing, always with images without gold nanoparticles.

For this reason, it was decided to directly combine the antibody with FITC-G(IKK)₃I-NH₂ and then administer to living cells. The rationale was that, if the peptide acted as a carrier for siRNA molecules then it could transport the antibody inside the cells. The antibody could be visualised using gold nanoparticles with TEM. Samples incubated with only the antibody were considered as negative controls.

The images in Figure 50 show the result of 3 hrs incubation with the peptide. Panel (a) is for reference, where the cells were fixed and stained with Hoechst. The peptide location is represented with a green fluorescent signal, visible around the nuclei (A). In

B, there is an image of an untreated control cell (both antibody and peptide absent) and in C details of the plasma membrane where several filopodia are visible. Figure 50 (b) shows a cell exposed to a solution of anti-FITC antibodies labelled with gold nanoparticles (D-E). The absence of spherical black dots in the image suggests that the antibody was unable to cross the plasma membrane. Finally, (c) displays a series of images of a cell exposed to a solution of peptide and antibody (F-I). The yellow circles show gold nanoparticles visible as dark, electron dense spheres. These are found in large vesicles (red panel) or on the cell membranes (blue and green panels).

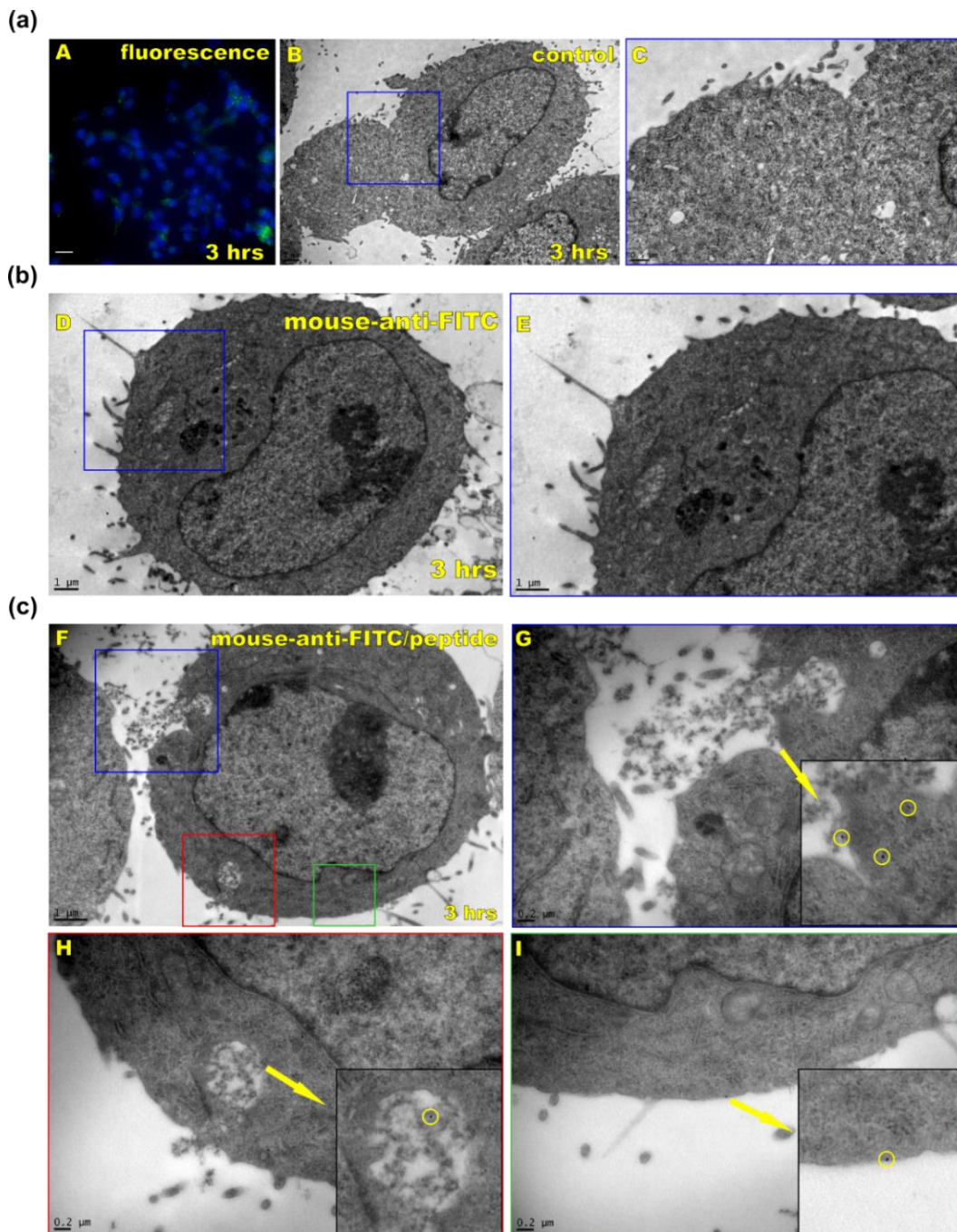


Figure 50. TEM images of cancer cells following 3 hrs exposure to FITC-G(IKKK)₃I-NH₂ and anti-FITC antibody conjugated with 10 nm Au nanoparticles. HCT-116 cancer cells were exposed for 3 hours to 6.25 μ M of FITC-G(IKKK)₃I-NH₂ complexed with a mouse monoclonal antibody anti-FITC conjugated with 10 nm Au nanoparticles (1/100 dilution) and then imaged using TEM. The antibody was used to label the peptide and localise it inside the cells. (a, A) Fluorescent image showing the presence of few peptide molecules internalised into the cells after 3 hours of peptide exposure (bar 25 μ m). (a, B-C) TEM images of a control cell (not exposed to peptide or antibody) and a detail of its membrane. (b, D-E) TEM images of a cell exposed to the mouse antibody, showing no Au nanoparticles. (c, F-I) TEM sections showing cells exposed to FITC-G(IKKK)₃I-NH₂ and anti-FITC antibody conjugated with 10 nm Au nanoparticles. Several Au nanoparticles (yellow circles) are visible in vesicles or in proximity to the plasma membrane. In the fluorescent image: Hoechst 33342 (2 μ g/ml) (blue) was used as nuclear staining. FITC-G(IKKK)₃I-NH₂ in green. Bars = 0.2, 0.5, 1 or 2 μ m.

To determine if a longer exposure could reveal more particles, a 24-hour peptide incubation was applied (Figure 51). In panel (a) a series of control images can be observed; a live bright field image taken with the IN Cell Analyzer 2200 microscope and 10x objective with many cells displaying green fluorescence, as indication of correct peptide uptake, an untreated cell with a detailed zoom on its membrane and a picture showing a control cell membrane with 2 endocytic budding vesicles. In (b) the other control samples consist of a cell treated with antibody only. In the blue and red panel are detailed images of the cell membrane full of actin protrusion (filopodia), and an exosome (blue panel). In (c), a cell exposed to the peptide/antibody complexes shows several endocytic compartments full of gold nanoparticles (yellow circles). Some are more superficial (blue panel) and possibly represent early endosomes, some more are internally localised (red panel) which might be late endosomes. Finally, in (d) there is another cell exposed to peptide/antibody complexes, but in this case the cellular health is compromised and the membrane structures are falling apart. Many gold nanoparticles could be detected (yellow circles) in really big vesicles and it is possible that due to the massive peptide/antibody uptake, the cell is irreversibly damaged and it is dying.

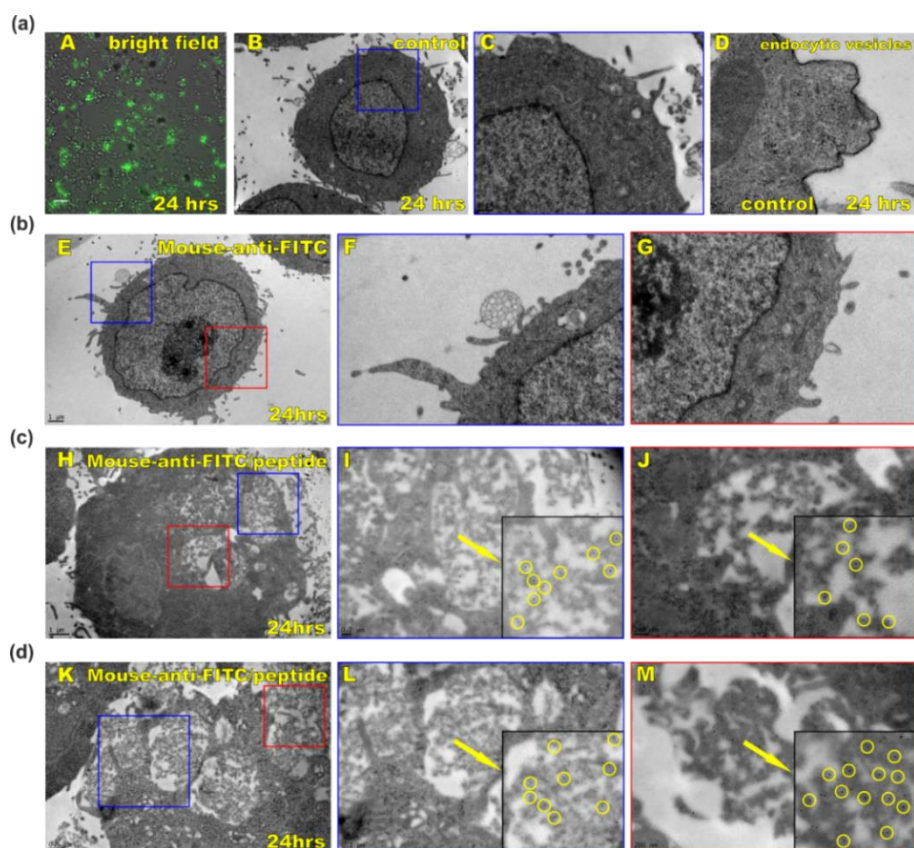


Figure 51. TEM images of cancer cells following 24 hrs exposure to FITC-G(IKK)₃I-NH₂ and anti-FITC antibody conjugated with 10 nm Au nanoparticles. HCT-116 cancer cells were exposed for 24 hours to 6.25 μ M of FITC-G(IKK)₃I-NH₂ complexed with a mouse monoclonal antibody anti-FITC conjugated with 10 nm Au nanoparticles (1/100 dilution) and then imaged using TEM. The antibody was used to label the peptide and localise it inside the cells. (a, A) Live fluorescent bright field image showing the presence of many peptide molecules (green) internalised into the cells after 24 hours of peptide exposure (bar 100 μ m). (a, B-C) TEM images of a control cell (not exposed to peptide or antibody), and details of its membrane. (a, D) a cell membrane of an untreated cell showing the invaginations typical of an endocytic process. (b E) TEM images of a cell exposed to the mouse antibody, which doesn't have Au nanoparticles; (b, F) details of an exosome; (b, G) cell membrane full of actin protrusions (filopodia). (c, H-J) TEM sections of a cell exposed to FITC-G(IKK)₃I-NH₂ and anti-FITC antibody conjugated with 10 nm Au nanoparticles showing several Au nanoparticles (yellow circles) included in a big endocytic compartment, possibly endosomes. (d, K-M) Another cell exposed to peptide/antibody complexes with many internalised Au nanoparticles (yellow circles); the cell is severely damaged and the membrane is falling apart. Bars = 0.2, 0.5, or 1 μ m.

4.4 Studies to evaluate the involvement of endocytosis in peptide uptake

Endocytosis involves a portion of the membrane being invaginated, encapsulating integral proteins, plasma membrane lipids and extracellular fluid. During this process, a membrane-bounded vesicle called an endosome is formed. The engulfment of material is not energy free and to work requires ATP and is considered an active process. Recent evidence suggests that endocytosis not only is involved in the internalisation of extracellular molecules but also plays a key role in mitosis, antigen presentation and cell migration processes ^{235, 236}. The specific mechanisms through which cargoes are recruited and internalised by the cell membranes are still partially unclear. The endocytic uptake can follow different routes depending on the nature of the internalised molecules; phagocytosis or macropinocytosis (which involve the engulfment of big particles or large volume fractions and extracellular fluid, respectively) and receptor-mediated endocytosis. Of this latter category, the most studied is certainly the clathrin mediated endocytosis (CME). Other types of clathrin-independent endocytosis include the caveolin-1 mediated endocytosis and a few others which can all go under the main group of clathrin and caveolin independent endocytosis ²³⁷.

Experiments described in the previous sections revealed evidence regarding the possibility of an active mechanism being involved in the internalisation of the peptides. This includes mitotic cells that did not uptake FITC-G(IKKK)₃-NH₂ (Figure 46) and TEM images showing gold nanoparticles (conjugated to an antibody specific against FITC (Figure 50 and Figure 51) encapsulated in vesicular compartments. To better investigate this phenomenon, several new experiments were performed: internalisation speed of peptide molecules, cold assay analysis, acid stripping to remove molecules not covalently bound from the surface of the cellular plasma membrane and time-lapse videos. The results are presented in the sections below.

4.4.1 Internalisation speed of FITC-G(IKKK)₃I-NH₂

An evaluation of the internalisation time of FITC-G(IKKK)₃I-NH₂ was conducted on both HCT-116 cancer cells and HDFs primary fibroblasts in order to obtain an estimate of how much time was needed by FITC-G(IKKK)₃I-NH₂ to be sufficiently concentrated inside the cells to give a visible fluorescent signal. Two concentrations of peptide (12.5 and 25 µM) were added to the cells, which were then fixed in formaldehyde and stained with Hoechst at various time points (from 15 minutes up to 3 hours). The speed with which siRNA molecules were transfected and internalised was also evaluated. 50 nM of red fluorescent siGLO was transfected using two peptide ratios (4/1 and 24/1, corresponding to 200 or 1200 nM of peptide, respectively) and DharmaFECT1 (DF1) used as the positive control.

Figure 52 presents images of HCT-116 cells showing FITC labelled peptide appearing after 30 minutes at both concentrations tested. With time the amount of peptide increases. The cells exposed to 25 µM peptide concentration after 3 hrs all showed some fluorescence. When complexed with siRNA, the peptide required more time to be detected; for the 4/1 ratio, no complexes were visible after 30 minutes and even after one hour only a few red fluorescent siRNAs could be localised inside the cells. With a 6-fold increase in ratio, (24/1) fluorescence could be detected after 30 minutes, and the agglomerates appeared yellow, due to the co-localisation of green peptide and red siRNA. Compared to FITC-G(IKKK)₃I-NH₂, DF1 has a higher internalisation speed and some red molecules appeared already after 15 minutes.

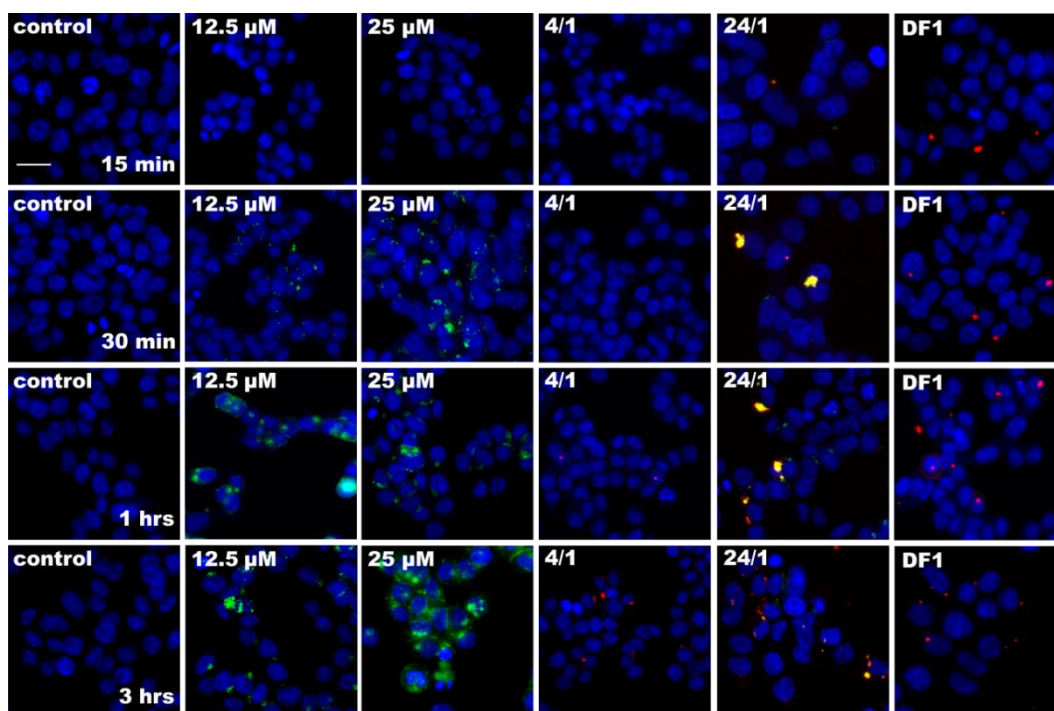


Figure 52. FITC-G(IKK)₃I-NH₂ internalisation evaluated on cancer cells at different time points. HCT-116 were exposed to two concentrations FITC-G(IKK)₃I-NH₂ (12 and 25 μM) and fixed after specific time points to evaluate uptake by the cells. 50 nM of siGLO red fluorescent indicator (Dharmacon) was transfected using 2 peptide ratios for the same purpose. DharmaFECT1 (DF1) was used instead as positive control and transfection was performed according to the manufacturer's protocol. The presence of peptide localised inside the cells is first detectable after 30 minutes while for peptide/siRNA complexes, unless a really high peptide ratio is used (24/1) a minimum of an hour is required. DF1 internalisation is faster and red puncta are visible already after 15 minutes. Hoechst 33342 (2 μg/ml) (blue) was used as nuclear staining. Fluorescent siGLO in red. FITC-G(IKK)₃I-NH₂ in green Bar = 25 μm. All the images are scaled at the same size.

Figure 53 shows images of HCT-116 exposed for 24 hrs to FITC-G(IKK)₃I-NH₂ at concentrations of 6.25-100 μM. The quantity of peptide internalised by the cells is concentration dependent: at 100 μM the signal from the fluorophore inside the cells is so high, that, at the same exposure time used to acquire all images, all the cells are completely saturated in the green channel. A reduction in cell population was also observed at this concentration. Noticeable in the 12.5 and 50 μM pictures are cells in mitosis with the peptide surrounding the plasma membrane (yellow circles).

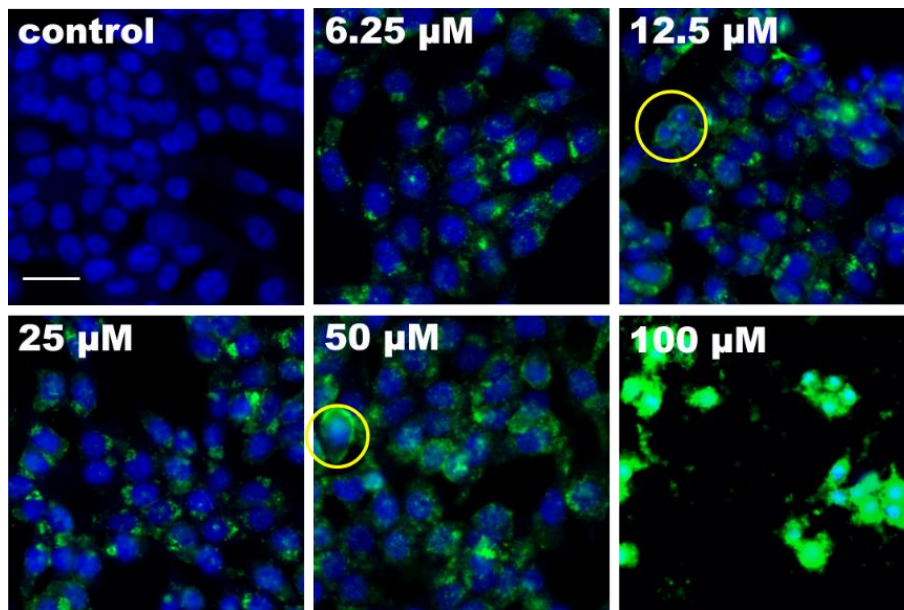


Figure 53. HCT-116 cells exposed for 24 hrs to FITC-G(IKKK)₃I-NH₂. The cells were exposed to progressively higher concentrations of the fluorescent peptide. Images show a clear correlation between the concentration used and the amount of fluorescence detected in the cells. At 100 μM, the amount of peptide internalised is so high that the green channel is saturated. In the yellow circles cells are in mitosis. Hoechst 33342 (2 μg/ml) (blue) was used as nuclear staining. FITC-G(IKKK)₃I-NH₂ in green Bar = 25 μm. All the images are scaled at the same size.

Figure 54 shows the internalisation performed of FITC-G(IKKK)₃I-NH₂ on HDFs. No fluorescence is visible in the cells, even after 3 hours of exposure. With the higher peptide ratio (24/1), a few puncta are visible after 30 minutes as yellow puncta. With DF1 internalisation was comparable to the one experienced in HCT-116 cells and red fluorescence starts to be visible even after 15 minutes.

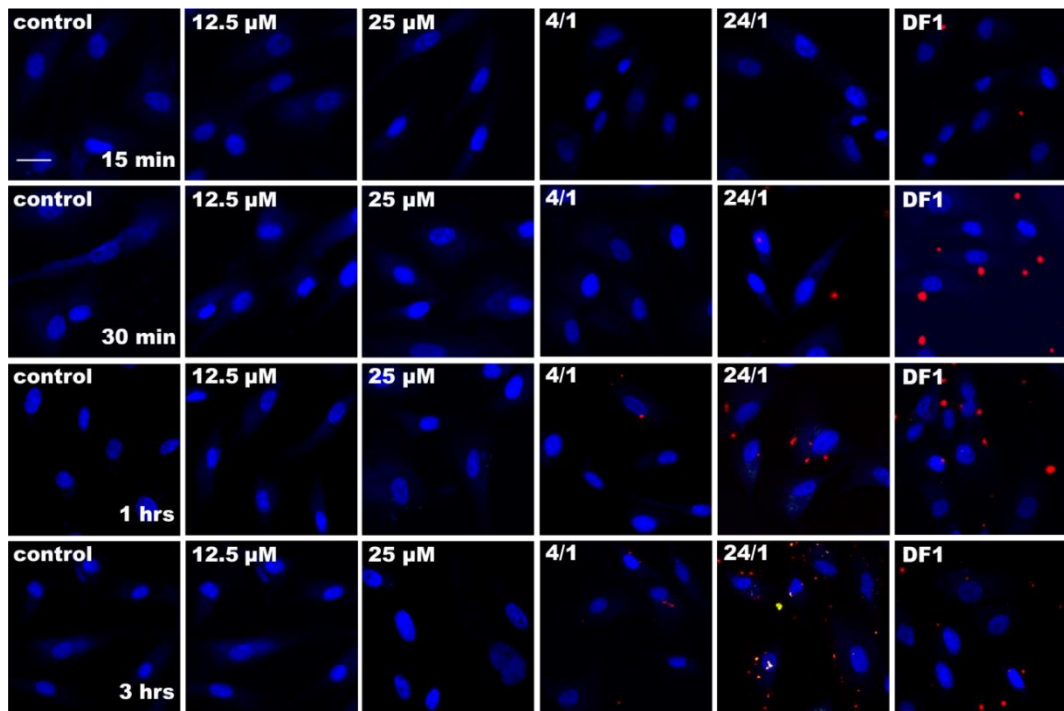


Figure 54. FITC-G(IKK)₃I-NH₂ internalisation evaluated on fibroblasts at different time points. HDFs primary cells were exposed to two concentrations of FITC-G(IKK)₃I-NH₂ (12 and 25 μM) and fixed after specific time points to evaluate uptake by the cells. 50 nM of siGLO red fluorescent indicator (Dharmacon) was transfected using 2 peptide ratios. DharmaFECT1 (DF1) was used as a positive control and transfection was performed according to the manufacturer's protocol. The presence of peptide localised inside the cells cannot be detected at any of the time points selected. For the peptide/siRNA complexes unless a really high peptide ratio is used, a minimum of an hour is required to observe red fluorescent puncta. With the 24/1 ratio, the presence of yellow puncta as an indication of peptide and siRNA molecule co-localisation is noticeable after 3 hours. DF1 internalisation can be observed after 15 minutes. Hoechst 33342 (2 μg/ml) (blue) was used as nuclear staining. Fluorescent siGLO in red. FITC-G(IKK)₃I-NH₂ in green Bar = 25 μm. All the images are scaled at the same size.

Lastly, in Figure 55, fibroblasts were exposed for 24 hrs to the fluorescent peptide. The peptide localised to the cells in a dose-dependent fashion. 100 μM of peptide had an inhibitory effect on the cellular growth. The morphology of the HDF cells in Figure 55 changed with an increase in diameter and the fibroblasts were saturated with the peptide which was located within the nuclei.

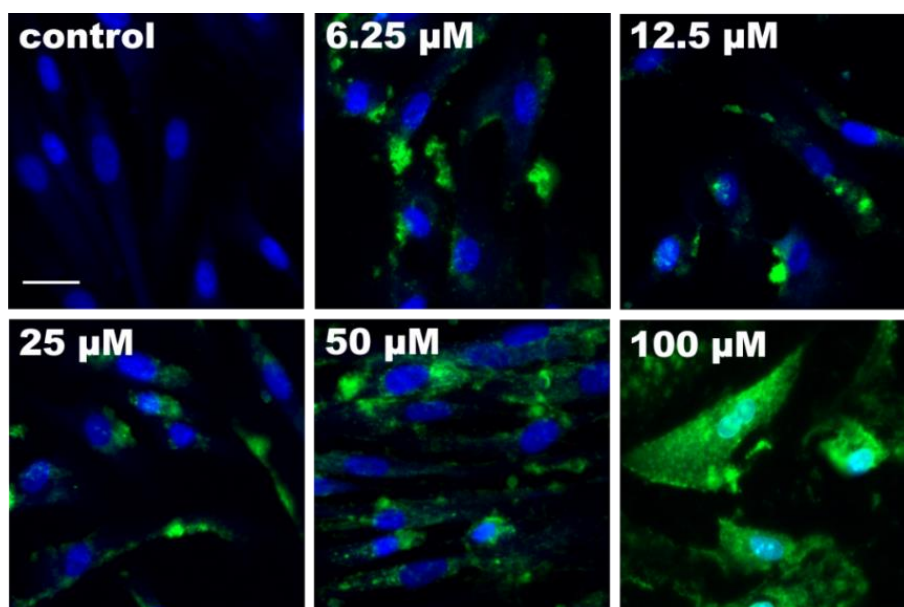


Figure 55. HDFs exposed for 24 hrs to FITC-G(IKK)₃I-NH₂. HDFs were exposed to progressively higher concentrations of the fluorescent peptide. Images show a clear correlation between the concentration used and the amount of fluorescence detected in the cells. At the concentration of 100 μM , the amount of peptide internalised caused the saturation of the cells in the green channel. Moreover, at this concentration a reduction in cell number was observed as well. Hoechst 33342 (2 $\mu\text{g/ml}$) (blue) was used as nuclear staining. FITC-G(IKK)₃I-NH₂ in green Bar = 25 μm . All the images are scaled at the same size.

Overall, the results obtained on both cancer cells and fibroblasts showed different internalisation between the two cell lines. With the cancer cells, the uptake is quick and the peptide is visible inside cells in a time window between 15 and 30 minutes, whilst at the same range of concentrations in fibroblasts, none of the fluorescent FITC-G(IKK)₃-NH₂, could be detected, even after 3 hours of incubation (Figure 52 and Figure 54). If the incubation time is prolonged to at least 24 hrs, HCT-116 and HDFs equally showed internalised molecules and 100 μM induced almost the same level of toxicity in both cell lines (Figure 53 and Figure 55).

4.4.2 Peptide internalisation using the cold assay to reduce endocytosis

Endocytosis is a dynamic and energy-dependent process which is strictly influenced by the cell temperature: several studies have shown how, by decreasing temperature, the internalisation of molecules via endocytic pathways is strongly inhibited^{152, 153, 238}.

To strengthen the hypothesis of endocytosis being involved in peptide uptake, the cold assay was performed on HCT-116 cells. Cells were initially washed with cold PBS and subsequently exposed to a solution composed by 12.5 μM of FITC-G(IKK)₃I-NH₂ and cold medium. Three different plates were prepared and each of them was kept at 4 °C for 30 minutes. At 4 °C all the endocytic pathways are blocked. If endocytosis was involved in the FITC-G(IKK)₃I-NH₂ uptake, no peptide would be detectable inside the cells. After 30 minutes, one of the plates was rapidly fixed in formaldehyde, while the other two were first moved to 37 °C for 3 hours and then fixed. In one of the two remaining plates, the original medium was discharged and substituted with new warm media prior to being moved to 37 °C, while in the other the same medium was kept till the end. Control plates, where cells were directly exposed to 12.5 μM of FITC-G(IKK)₃I-NH₂ for 30 minutes or 3 hours and at 37 °C were also prepared. All the plates were then imaged using the wide field fluorescent microscope and quantitative analysis of the internalised peptide performed. Figure 56 (a) shows images of cells acquired after fixation, while (b) shows the graph obtained from the quantitative analysis of FITC green fluorescence intensity. Images were acquired using the IN CELL Analyzer microscope with 20x objective. Brightness and contrast were ultimately adjusted for all the images to the same level by using Image J. The quantitative analysis was performed using the In Cell Developer Toolbox 1.9 software.

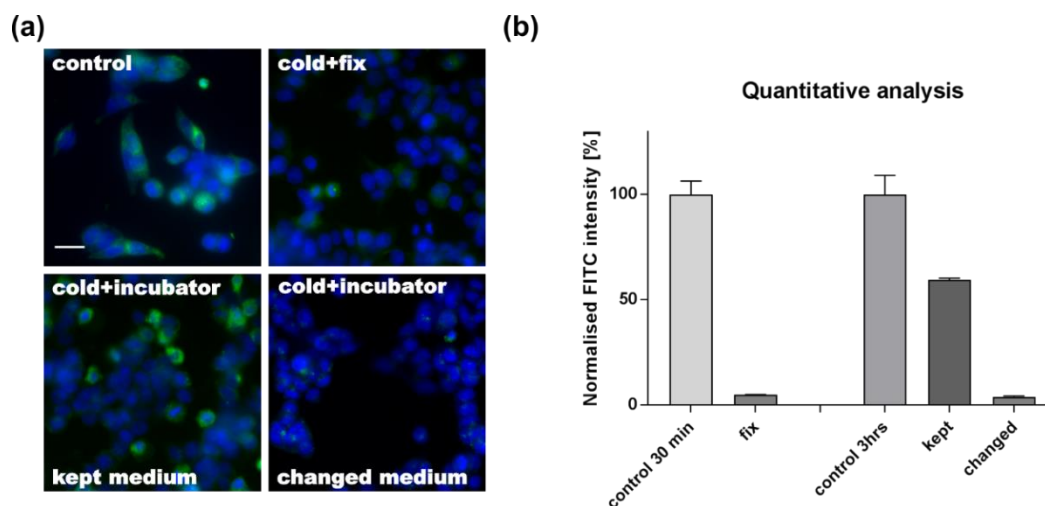


Figure 56. The peptide uptake is blocked in a cold environment. A cold assay was performed to evaluate the peptide uptake efficiency in cancer cells under cold conditions; (a) HCT-116 cancer cells were exposed to 12.5 μM of FITC-G(IKKK)₃I-NH₂ for 3 hours (control), or for 30 minutes in a cold environment directly following fixation (cold+fix). Some cells were subsequently incubated for 3 hours at 37 °C keeping the same medium (kept medium) or replacing the medium with a fresh one but lacking peptide (changed medium). The graph in (b) shows the quantitative analysis performed to evaluate the level of FITC intensity observed in the experimental conditions and normalised by the controls (cells incubated for 30 minutes or 3 hrs at 37°C). Because cells can auto-fluoresce in the green, cells without peptide were included (data not showed) in the experimental set-up and their values were subtracted from each experimental condition in order to have only the effective value of FITC intensity. The values obtained are averages of independent experiments \pm standard error mean ($\pm\text{SEM}$). The images complemented by the graph show that the peptide is not internalised by the cells unless a warm environment is provided, suggesting that the internalisation occurs mainly via an active process that requires energy to function. Bar = 25 μm . All the images are scaled at the same size.

With both images and quantitative analysis, it was found that, depending on the experimental conditions, the amount of green fluorescent intensity of FITC-G(IKKK)₃-NH₂ detected inside the cells was quite different. Cells kept in cold conditions and then immediately fixed showed very little peptide internalisation, but if the temperature was restored to normal conditions at 37 °C for 3 hrs, cells were again able to uptake the

peptide. However, if before moving the cells in the 37 °C incubator the medium was replaced with a new one lacking peptide, the level of fluorescence detected inside the cells was low. This proved not only that cells require a warm environment (and therefore energy) to uptake FITC-G(IKKK)₃-NH₂, but also that in cold conditions and in the absence of internalisation, the peptide probably does not stick onto the cellular membranes. If the medium is replaced, most of FITC-G(IKKK)₃-NH₂ is also washed away. Due to the auto-fluorescence that cells have in the green channel an extra experimental condition was created: untreated cells were seeded in a few wells and kept in an incubator (37°C) for 30 minutes or 3 hours then fixed and stained as usual. Their green fluorescence intensity was measured and used as background level to be subtracted from all the other data.

4.4.3 Acid stripping to remove covalently bound molecules from the membranes

It was important to estimate the effective amount of peptide internalised in cells to evaluate any crucial differences between cancer and not cancer cell lines. Some of the peptide could have been attached to the cell membranes without being internalised. Moreover, the fixation used formaldehyde, which can permeabilize cell membranes, meaning that the translocation inside the cells of materials attached on the outer surface may be a source for misinterpreting our observations ¹⁵⁴.

To discard both problems and evaluate if any of FITC-G(IKKK)₃I-NH₂ was attached on the membranes of both HCT-116 and HDFs cell lines, a series of washes with an acidic solution was performed prior to fixation. This potent acid stripping, with a pH of 3, allows the removal of any molecules, not covalently bound, from the plasma membrane reducing the chances of misinterpreted results ¹⁵⁵. Cells were initially incubated for 24 hrs with increasing concentrations of peptide followed by acid stripping, fixation with formaldehyde and staining with Hoechst and Cell Mask Orange to stain nuclei and plasma membranes, respectively. Images were then acquired with the ImageXpress® Micro System wide-field fluorescent microscope with a 20x objective. Following acquisition, the images were further analysed using the MetaXpress® 5.0.0.20. Brightness and contrast were ultimately adjusted for all the images to the same level by

using Image J. Quantitative analyses of the total peptide fluorescence intensity were performed to evaluate any differences between washed and unwashed cells.

Cells were exposed for 24 hrs to a range of peptide concentrations (6.25 – 50 μM). The concentration 100 μM was excluded, due to its severe toxic effect (Figure 45). The quantitative analysis showed in Figure 57 represents the total FITC intensity detected in HCT-116 or HDFs after peptide exposure. As it is possible to observe there is a difference in the amount of green fluorescence between unwashed cells and cells washed with the acidic solution. This was particularly evident for the fibroblasts, where the FITC average intensity drastically dropped at all the tested concentrations after acid wash, especially at 50 μM . In HCT-116, there was generally little or no variation. The total green fluorescence intensity observed in HDFs was smaller compared to HCT-116, but because fibroblasts are much bigger cells when compared to HCT-116, in an equal surface area they occupy more space. As a consequence, the number of cells counted in a well is much lower compared to the cancer cells. Therefore, when the data are represented as average intensity per cell, the values appeared to be higher for the fibroblasts than the colon cancer cells.

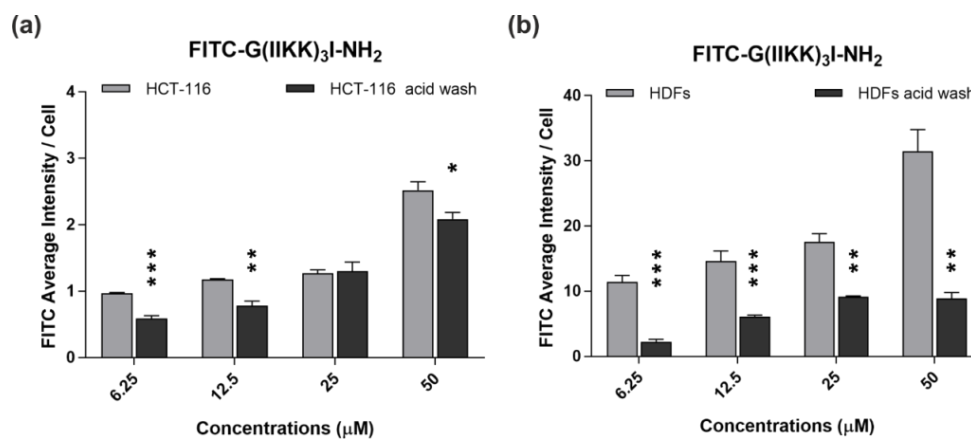


Figure 57. Quantitative analysis of FITC average intensity per cell in unwashed and washed cells. HCT-116 cancer cells (a) or fibroblasts (b) were exposed to different concentrations of FITC-G(IKK)₃I-NH₂ for 24 hours with or without an acid wash prior fixation (pH 3). The values obtained were divided by the total amount of cells counted in each experimental condition. Cells washed with this acidic buffer showed a significant decrease in the FITC intensity compared to the unwashed cells. This is particularly true for fibroblasts, where in all the tested concentrations (and especially at 50 μM) a drastic reduction in green fluorescence was observed. This data suggests that some of the peptide is located on the cellular membranes and gets internalised only after fixation. This is true especially for HDFs where the effective internalisation of FITC-G(IKK)₃I-NH₂ is quite limited. The values obtained are averages of independent experiments ± standard error mean (±SEM). Statistically significant differences between normal cells and cells treated with the acid buffer were determined by Student's t-test (*p<0.05; **p<0.01; ***p<0.001).

The images in Figure 58 show the results obtained with acid washes and cellular staining. The peptide distribution inside varied between cancer cells and fibroblasts; in the first case the vast majority of fluorescence was centrally located in the same cellular area near the nucleus (Figure 58 a) while in the second (Figure 58 b) the distribution was more randomised and did not follow a precise pattern. In Figure 58 (c) there are zoomed in images of HCT-116 cells exposed to 50 μM of FITC-G(IKK)₃I-NH₂. The white circles highlight two cells in mitosis where the vast majority of the fluorescent peptide is located on the membranes. To facilitate the observation of the peptide's distribution, the red and blue channels, representing the plasma membranes and nuclei staining, were removed from the second and third images respectively.

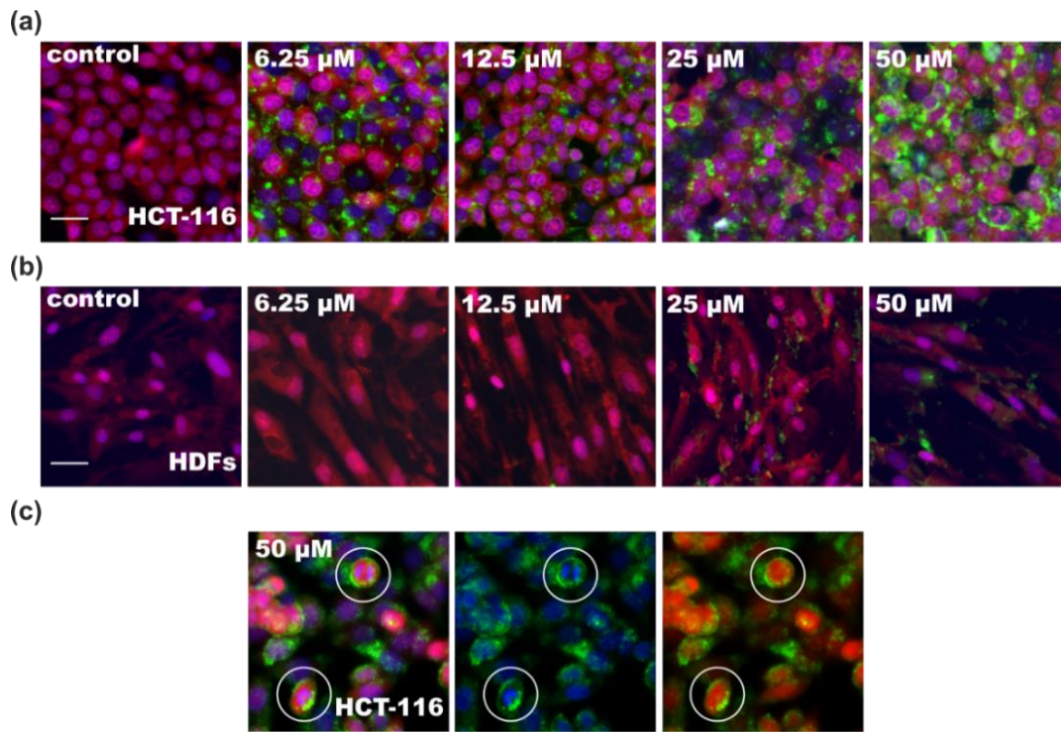


Figure 58. Acid wash removal of non-covalently bound peptide molecules from the cell membrane. HCT-116 cancer cells (a) and HDFs primary cells (b) were exposed to several concentrations of FITC-G(IKK)₃I-NH₂ for 24 hours and washed prior fixation with an acid buffer (pH 3). The acid stripping removes non-covalently bound material from the cellular membranes, and in this instance, could be used to evaluate the effective amount of peptide internalised prior to fixation. (c) HCT-116 cells exposed to 50 μM of fluorescent peptide. The white circles show cells in mitotic phase with the peptide (green) mostly externally surrounding the membrane. The plasma membrane (red) or the nuclei (blue) channels are removed in the second and third images respectively, showing peptide distribution external to the cells. Endocytosis is normally suppressed under mitotic events, therefore the presence of peptide outside these cells suggests that an active mechanism could be involved in its uptake. Hoechst 33342 (2 μg/ml) and Cell Mask Orange (0.1X of working solution) were used as nuclear and plasma membranes staining, respectively. Bar = 25 μm. All the images are scaled at the same size.

4.4.4 Time-lapse videos to show live internalisation of FITC-G(IKK)₃I-NH₂

To observe the peptide directly being taken up by living cells, time-lapse videos of HCT-116 were recorded using the IN Cell Analyzer microscope in both fluorescence and bright field mode with a 40x objective. Brightness and contrast were ultimately adjusted for all the images to the same level by using Image J. HCT-116 cells were exposed to a toxic (100 μ M) and a non-toxic (6.25 μ M) concentration of FITC-G(IKK)₃I-NH₂ and imaged every 30 minutes, for a total time of 24 hrs. Two separate movies were produced; the first one between 0 and 18 hrs of peptide exposure and the second one between 18 and 24 hrs. Cells with no peptide were filmed, as a control of normal cellular behaviour. In Figure 59 it is possible to observe cell movements and their morphological changes in response to the peptide internalisation. Control cells had heterogenous shape and morphology, showing lamellipodia, motility, migrating through the well plate surface and interacting with each other. Some underwent mitosis while some others died via apoptosis. In contrast, cells exposed to 6.25 μ M of FITC-G(IKK)₃I-NH₂ dramatically changed their morphology due to peptide internalisation. From the images in Figure 59 (a), it is possible to observe that as soon as the cells increased their peptide cargo, they suddenly stopped moving, adopting a round morphology and staying still for hours in the same area of the well. However, this behaviour was not homogenous and only some cells seemed to be affected in this drastic way. It appeared that the cells, which were still behaving normally, were lacking green fluorescence, however it is not clear whether those cells internalised any peptide. The cells exposed to 100 μ M on the other side, were completely filled by FITC-G(IKK)₃I-NH₂ in the space of only a few minutes and completely stopped moving. The amount of peptide internalised was so high that the green fluorescence signal became saturated. Due to the saturation issues, a second set of images (Figure 59 b) were acquired in bright field mode. In this way, it was possible to improve imaging of cell movements and morphologies. A similar scenario to the first movie was observed, where cells with no peptide moved freely, dividing and increasing in number, while cells exposed to 6.25 μ M of FITC-G(IKK)₃I-NH₂ had mostly changed their morphology, adopting a more circular shape and reducing their migration speed. Cells treated with the highest peptide concentration were completely stationary. The images

shown in Figure 59 a-b revealed that the peptide had mostly a cytostatic effect, inhibiting the cell proliferation. This was particularly evident in the cells exposed to 100 μ M, where the cell number did not vary between the first and the last image of each movie. The results obtained with these live videos are extremely important because they added valuable information about the cell physiology and morphology in presence of FITC-G(IKK)₃I-NH₂, which was not possible to acquire with the standard fixed fluorescent pictures.

Interestingly, the peptide distribution pattern appeared different from live and fixed images. Figure 60 shows cells prior and after fixation at the end of the movies' periods (18th or 24th hour). In live images it is possible to observe some cells showing green fluorescence, while when the cells were fixed all of them appeared with a certain amount of internalised peptide. This effect could be caused by the membranes permeabilization by formaldehyde, already discussed in the previous paragraph, or a different sensitivity between the microscope modes.

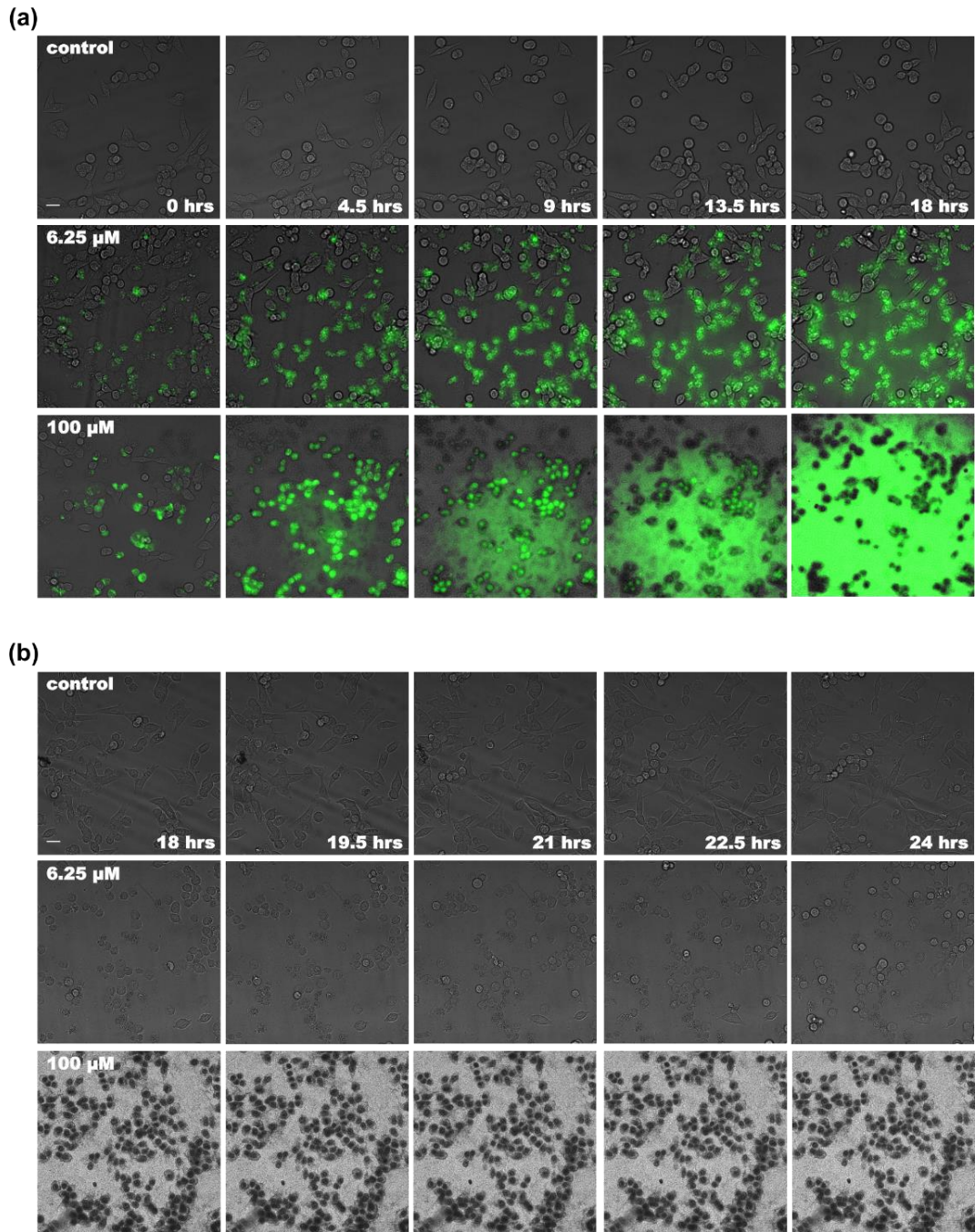


Figure 59. Live time-lapse imaging showing peptide uptake in cancer cells. HCT-116 cancer cells were exposed for 24 hrs to 0, 6.25 and 100 μM of FITC-G(IKK)₃I-NH₂ and recorded continuously for 18 hours (a) or between the 18th and 24th hours (b). The presence of peptide changed the morphology of the cells and altered their motility, especially at the 100 μM where cells were completely immobile. In (a) the 100 μM of peptide caused the saturation in the GFP channel, therefore in (b) only bright field mode was use. Bar = 25 μm . All the images are scaled at the same size.

Interestingly, the peptide distribution pattern appeared different from live and fixed images. Figure 60 shows cells prior and after fixation at the end of the movies periods (18th or 24th hour). In live images it possible to observe some cells showing green fluorescence, while when the cells were fixed all of them appeared with a certain amount of internalised peptide. This effect could be caused by the membranes permeabilization by formaldehyde, already discussed in the previous paragraph, or a different sensitivity between the microscope modes.

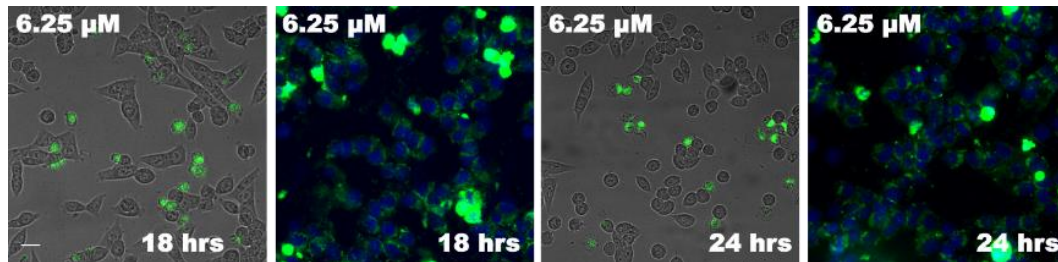


Figure 60. Differences in bright field and fluorescence acquisitions. Images of HCT-116 cells at the 18th and 24th hours before (bright field) and after formaldehyde fixation (fluorescence) showing the distribution pattern of the peptide. In the bright field images, only the cells with alterations in the cellular shape (enhanced circularity) have green fluorescent peptide, while in the fluorescent images all the cells have some of it. Bar = 25 μ m. All the images are scaled at the same size.

4.4.5 Cancer cells can recover from peptide uptake under favourable conditions

From the cell counting results and images of cells exposed to FITC-G(IKKK)₃-NH₂ it clearly appeared that 100 μM of peptide had a strong cytostatic effect on cells, especially HCT-116 (Figure 45 and Figure 53) causing a drastic decrease in the cell population growth. Even the time-lapse video showed how in very little time all the cells were completely saturated by the peptide and unable to move (Figure 59).

It is still unclear if the cells could pump out the peptide once internalised, but studies conducted on nanoparticles, for example, proved that it is not uncommon that cells use exocytosis as a mechanism to remove nanoparticles from the cytoplasm. When this happens, it is normally via vesicles or non-vesicle secretions²³⁹⁻²⁴¹.

In the experiment illustrated below, HCT-116 cancer cells were exposed to 100 μM of FITC-G(IKKK)₃I-NH₂ for 30 minutes and then left overnight in the incubator at 37 °C with or without media changes. In this way, it was possible to evaluate the cellular efficiency to recover from the peptide retention and investigate if the cancer cells were able to excrete the peptide. Unexposed cells were added as negative control. Afterwards cells were fixed with formaldehyde and stained with Hoechst. Images were acquired with the ImageXpress® Micro System wide-field fluorescent microscope or IN CELL Analyzer (bright field mode) with 2x or 20x objective lenses. Brightness and contrast of all the images were ultimately adjusted to the same level by using Image J. The cell counting analyses were performed with MetaXpress and the dedicated algorithm able to recognize cellular nuclei stained with Hoechst.

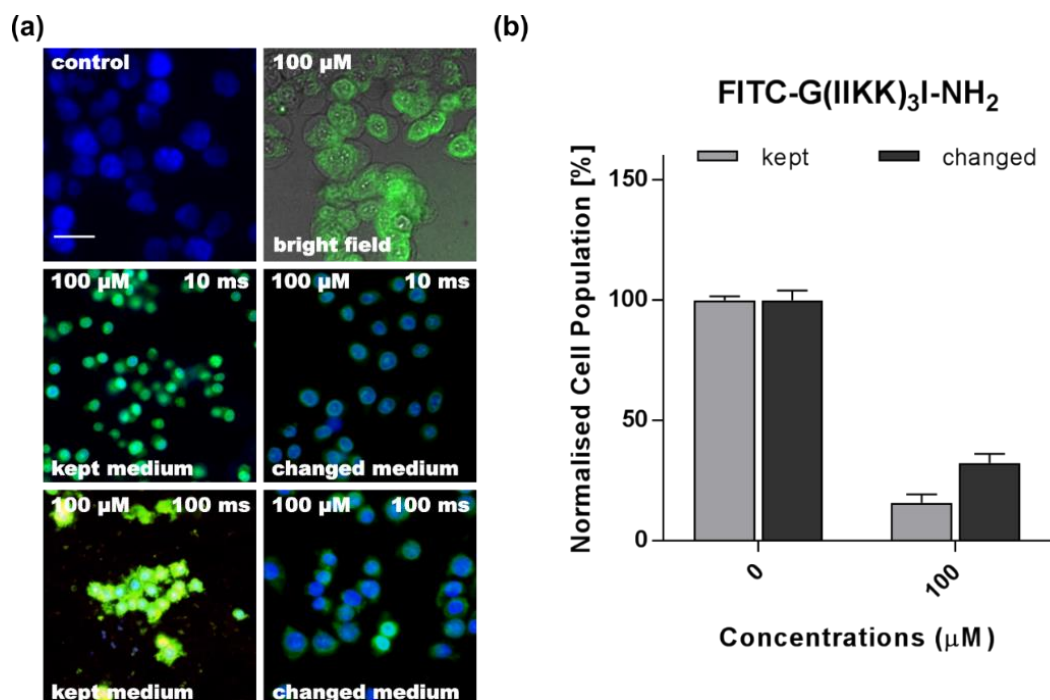


Figure 61. Cancer cells can recover from FITC-G(IKK)₃I-NH₂ uptake.

(a) HCT-116 cancer cells were exposed to 100 μM of fluorescent peptide for 30 minutes (bright field) and then incubated overnight keeping the same medium (kept medium) or changing the medium with to a fresh one but lacking peptide (changed medium). The next day, cells were fixed and stained and images acquired at 10 or 100 ms exposure time for GFP (green) channel. Cells that had the medium changed contained less peptide and could be imaged at high exposure time (100 ms) without saturating the signal. The cell number was evaluated (b) with nuclei staining analysis using the MetaXpress with the Multi Wavelength Scoring algorithm and 2x objective. According to the results obtained, cells could recover from the peptide exposure and increased in number in the space of a few hours. The results are expressed as a percentage of number of cells and normalized to the negative controls at that relative time point. The values obtained are averages of independent experiments ± standard error mean (±SEM). Water has been used as negative control (0). Bar = 25 μm. All the images are scaled at the same size.

Figure 61 (a) shows images of live cells (top panels) after 30 minutes of peptide exposure (bright field mode) or fixed cells (second and third panels) after overnight incubation with or without changing the medium (kept and changed medium). It is possible to observe from the bright field/FITC channel merged image that there is a

substantial FITC fluorescence inside the cells after 30 minutes and their morphology has already started to change. After an overnight treatment with the peptide, a low exposure time was necessary (10 ms). Nuclei appeared small and brightly stained. However, cells which had the peptide removed through washing could be imaged with a longer exposure time, with the total amount of peptide localised in the cells reduced compared to the cells where the medium was retained.

This data suggests that cells were able to secrete the peptide and when the peptide was removed from the media this became apparent. To evaluate any differences between the two experiments, cells were counted (Figure 61 b). Interestingly, a difference was observed and the cells with lower concentration of peptide in the media doubled their population compared to the ones which were exposed overnight.

5 *IN VIVO* STUDIES ON *DANIO RERIO*

EMBRYOS

5.1 Zebrafish is a valuable animal model to study human genetics and diseases.

In vivo studies are necessary to fully understand the mechanism of action of drugs, the onset of diseases or the spread of cancer. A model organism should present important features such as short generation time, high fecundity, complete sequenced genome, metabolism comparable with humans or disease models similar to humans. *Danio rerio* (or zebrafish), a tropical cyprinid fish native to the floodplains of North Eastern India and Bangladesh, is extensively used in biomedical research. It is especially useful for genetic and developmental studies, particularly after 2013 when its genome was completely sequenced. Comparisons between human and zebrafish sequences showed that 71% of human genes have at least one obvious zebrafish orthologue and that in total we share up to 82% of disease-associated targets, together with a large number of drug metabolism pathways ²⁴².

It is George Streisinger with his pioneering work started in the late 1960s, who transformed this little tropical fish into a leading model organism. Streisinger has certainly a place amongst the principal creators of the modern era of molecular genetics especially for his pivotal study published in 1981 where for the first time he produced clones of homozygous diploid zebrafish ²⁴³. Since then, the number of studies involving zebrafish exponentially increased, counting >20,000 publications ²⁴⁴. There are many advantages of using zebrafish in research laboratories. First, zebrafish are small, robust, cheap to maintain (compared to mice) and capable of producing hundreds of offspring in short periods of time. Female spawning is influenced by photoperiod and takes place within approximately an hour of exposure to light after darkness, while for many other fish species this happens only during the night ²⁴⁵. Its growth rate is fast, (blood circulation begins after only 24 hrs) and since fertilization occurs outside the mother's

body, it is easy to study early embryonic development. Moreover, the optical clarity during embryogenesis allows us to observe the internal structures during development with light microscopes¹⁴⁶. For example, haematopoiesis, cardiac and vasculature diseases are among the most studied subjects in zebrafish embryos. Haematopoiesis is conserved through vertebrate evolution and there are 80 homologues of mammalian genes involved in this process isolated so far in zebrafish²⁴⁶⁻²⁴⁹. As vertebrates, zebrafish have similar physiology, organs and tissues as humans, apart from differences due to adaptation to aquatic life. Recently, zebrafish embryos have been used for toxicology screening and as part of the drug discovery process^{242, 250, 251}.

The behaviour of A₉K and FITC-G(IKKK)₃I-NH₂ peptides was evaluated in zebrafish embryos and the results regarding their toxicity will be detailed in the following sections of this chapter. This represents the first study where zebrafish embryos have been injected to test the toxicity of cationic amphiphilic peptides.

5.2 *Danio rerio* embryos and their employment in toxicology.

Zebrafish embryos have been often used as model to evaluate the toxicity of chemical compounds and biocides released in the aquatic environment. Initially, the acute fish toxicity test (AFT)²⁵², following the Organisation for Economic Co-operation and Development (OECD) guidelines was the chosen assay for aquatic vertebrate toxicity. The assessed endpoint was fish death, so as to reduce the distress and suffering of the animals OECD decided to develop an alternative test called Fish Embryo Acute Toxicity (FET), where embryos are used instead of juvenile or adult animals²⁵³. The usage of embryos is preferred because, according to the EU Directive 2016/63/EU, in the earliest life-stages (0-5 days post fertilisation), until the beginning of independent feeding, embryos aren't considered as protected and do not fall under animal experimentation regulations. Usually in the FET the chemical compounds which needs to be tested are directly dissolved in the medium. The embryos are monitored for 96 hours and any changes from the standard embryonic development are carefully recorded²⁵⁴. Due to the high concentration of peptide needed in the fish tank for oral administration, and the route of administration of peptide, if it were to be used as a

cancer treatment for Humans, the peptides were directly microinjected into the single cell egg stage. Microinjection also avoided the chorion, a natural barrier of 1.5-2.5 μm thickness, which can potentially restrict the uptake of compounds especially if carrying a charge ^{255, 256}.

5.3 The first 5 days of zebrafish embryogenesis.

During the monitoring phase of microinjected embryos three distinct checkpoints were established. The first checkpoint was at 5 hours post fertilisation. At this developmental stage, embryos are normally at late blastula stage and approaching gastrulation (5.25 hrs post fertilization). During this check point unfertilised eggs were removed to reduce the risk of infection and to minimize the chance of other embryos dying overnight.

Following blastula stage, gastrulation begins with epiboly. During epiboly, complex co-ordination of cell movements establishes three different layers: the enveloping layer (EVL), an epithelial monolayer which will exclusively contribute to form the periderm, a protective outer surface; the yolk syncytial layer (YSL) an associated layer of cytoplasm and nuclei on top of the yolk which are critical for mesoderm and endoderm induction and the deep cell layer (DEL), a multilayer of cells of fairly uniform thickness. DEL will eventually give rise to epiblast and hypoblast which will consecutively form the 3 germ layers (ectoderm, mesoderm, and endoderm) ^{146, 257, 258}.

Gastrulation normally lasts for 5 hours and is one of the most important phases of embryogenesis; during this stage, epiboly completes and in addition other important morphogenetic cellular movements called involution, convergence and extension occur defining the primary germ layers and the embryonic axis (anterior-posterior and dorsal-ventral) ²⁵⁹. By this stage, an organ-and tissue-level fate map is available giving lineage tracing of undifferentiated precursor cells which are crucial for determining how haematopoietic, and blood vessel lineages arise in developing embryos ^{247, 260}. If the peptides induce toxicity in the embryos, signs of cellular degeneration were could be recorded at this stage, during the first planned check-point.

If an embryo manages to complete gastrulation, then the segmentation stage will commence. Somites, together with a wonderful variety of morphogenetic movements occur; rudimental organs are becoming visible, the tail is budding, the notochord develops in an apical-posterior sequence and the embryo begins to elongate. During this phase, the neural tube closes and a rudimental brain starts to develop together with primordial eyes. Segmentation lasts from 10.30 to 24 hrs post fertilization (hpf) and by completion, most cell lineages are morphologically differentiated and first body movements are observed ^{146, 258}. The end of the first day post fertilisation (1 dpf) is another critical point for the embryos' development, therefore the survival rate following the peptides microinjection was once again recorded (second checkpoint); the number of alive and dead embryos were counted and coagulated eggs discharged from the Petri dishes.

The following phase is called pharyngula and it lasts for the whole second day of post fertilisation (24 to 48 hrs). At this stage, the neuronal system becomes more complex with formation of primordial nerves. The fins begin to form and pigment cells to differentiate. By 24 hpf, the heart begins to beat and the blood can circulate through a closed set of channels by 26 hpf. Aortic arches appear together with the carotid and caudal arteries, the anterior cardinal and caudal veins. First signs of marked behavioural development appear together with tactile sensitivity and rhythmic bouts of swimming ¹⁴⁶.

The third day there is the hatching phase. At this stage embryos, emerge from the protective chorion. This process can happen anytime up to 5 dpf and does not inhibit embryonic development by this stage. After the end of the third day, zebrafish embryos can be arbitrarily called "larvae", whether they have hatched or not. During this stage, embryos keep growing and the morphogenesis of many organs is complete and slows down considerably, with the exception of the gut and its associated organs which will complete development by the fifth day ²⁶⁰⁻²⁶².

Quite noticeable is the rapid development of the pectoral fins, the jaws, and the gills. At the end of the hatching phase the mouth is wide open and it protrudes anteriorly just beyond the eye. The pectoral fins continue to expand and extending posteriorly over most of the length of yolk which is, vice versa, decreasing in size. At the third day,

since the majority of the organs have completed their morphogenesis, the survival rate of the injected larvae was checked (third checkpoint), highlighting any abnormalities and defects from normal development.

The most important changes happening in the next days (4 and 5 dpf) are the inflation of the swim bladder and the continued anterior-dorsal protrusion of the mouth. The yolk sac is reduced and the gut tube drops more ventrally. Early larvae begin to swim actively, followed by jaw, fins and eye movements. By day five these physiological changes produce rapid cascade of responses such as respiration and exogenous feeding¹⁴⁶. Before the end of the fifth day, due to legal requirements, embryos were sacrificed in bleach following prior anaesthetization with Tricaine (40 mg/l).

5.4 Microinjections of A₉K peptide in zebrafish embryos

Zebrafish were raised in the Bateson Centre aquaria and fed *Artemia* nauplii. Zebrafish adult animals were kept on a constant 14 hours on 10 hours off light cycle at 28 °C. Embryos were obtained only by natural spawning of adult wild type animals as described in the zebrafish book²⁵⁸. All the experiments performed on animals were approved by the local ethical review committee and performed under the Home Office project license 40/3708. At least 50 embryos per concentration were injected and several un-injected embryos were kept as controls. One-cell stage embryos were injected with 150 – 4000 pg (0.15 – 4 ng) of A₉K peptide (corresponding to 180 µM – 5 mM) within 20 minutes after they were laid and according to the procedure described in “2.8.3 Peptides and siGLO microinjections” section of the Materials and Method chapter. Briefly, the embryos were lined up against a microscope slide in a petri dish and injected using a needle mounted on a microinjector. The needle was broken with a pair of sharp tweezers and the injection volume calibrated, using a stage micrometer, to deliver 0.5 nl of liquid per drop (diameter 0.1 mm)^{148, 149}. After completing a line of injections, eggs were moved in a clean Petri dish filled with E3 medium and kept in an incubator at 28 °C. At the established check-points the number of embryos was recorded using a Leica MZ16 stereomicroscope.

Figure 62 graphically represents the ratio of dead and surviving embryos at one or three day post-fertilisation (1 or 3 dpf) The ratio was calculated considering as 100% the total number of injected embryos per each concentration (or un-injected for the control) and then divided between dead and survived embryos at each time point. According to the literature, for studies involving zebrafish embryos and microinjections in one cell-stage eggs to allow identification of variability, the recommend number of embryos per treatment is 40-60 ²⁵⁶. Therefore at least a full microscope slide line of embryos, which roughly corresponds to 50 eggs, was injected per concentration.

5 hpf embryos were checked but no differences were observed when compared to the initial microinjected eggs number (0 hpf) (data not represented).

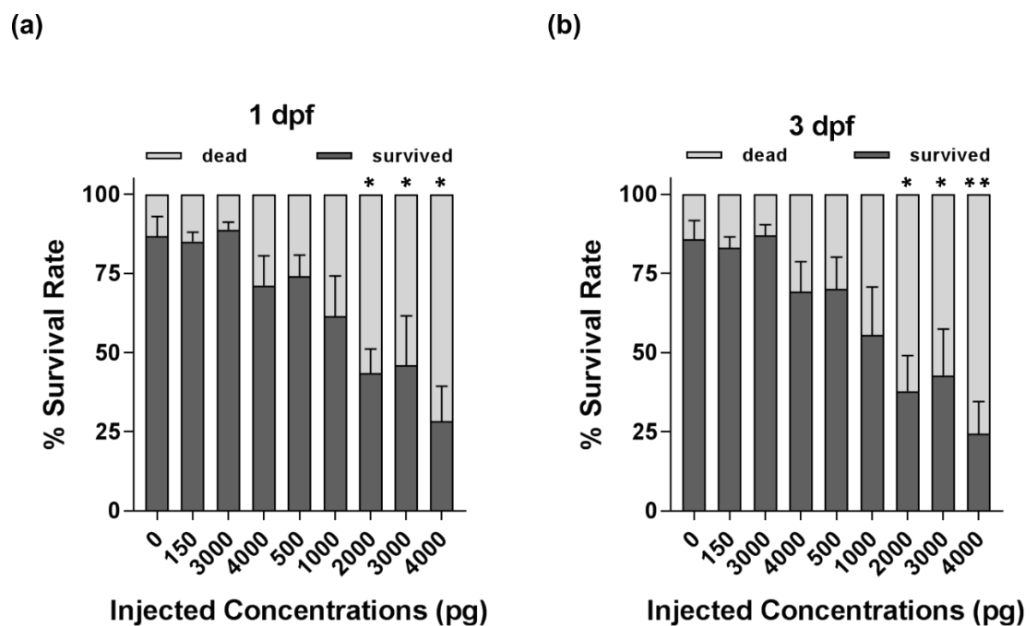


Figure 62. Microinjection of A₉K induces dose-dependent toxicity in wild type zebrafish embryos. Zebrafish embryos at one-cell stage were injected with increasing amounts of A₉K peptide and the number of surviving embryos recorded at 1 day post fertilisation (a) or 3 days post fertilisation (b). The graphs show a decrease in embryo viability consistent with the increasing volume of peptide injected with the most severe effects found with 4000 pg of peptide injected. No major differences can be observed between the two check-points. Several batches were used for the injections and for each of them, few embryos were kept as un-injected controls. An average of 50 eggs per concentration were injected in order to ensure sufficient sample size to detect variability. Statistically significant difference from the negative control was determined by Student's t-test (*p<0.05; **p<0.01).

A visible decrease in the survival rate could be observed at higher peptide concentrations (1000 – 4000 pg) while at the lower doses (150, 300 ng) the survival rate is comparable to control levels. The trend is peptide dose-dependent. Embryos were scored as dead either if the tissues were no longer transparent and had become opaque, suggesting embryonic death, or if they were no longer moving and the heart had stopped beating. The survival rate of un-injected control embryos was constant around 90% between the checkpoints.

At 1 dpf the survival rate of embryos injected with the lowest doses (150, 300 pg) matched the control and were recorded at 85-88%, respectively; at intermediate doses (400, 500 pg) the survival rate was instead at 71-74% respectively, while at high doses (1000 – 4000 pg) it drastically dropped from the 61% of 1000 pg to 28% of 4000 pg.

The number of surviving embryos counted at 3 dpf did not significantly change from previous observations. Again, the lower doses (150, 300 pg) matched the control with 83% and 87% respectively; with intermediate doses (400, 500 pg) the surviving rate was 70% while at higher doses (1000 – 4000 pg) the surviving rate was stationary from 56% for 1000 pg to 24% for 4000 pg.

Using GraphPad, the lethal concentration (LC_{50}), equivalent to the concentration of peptide needed to kill 50% of the embryos, was calculated. In 1 or 3 dpf embryos the LC_{50} were respectively 1700 and 1400 ng corresponding to 2 and 1.7 mM.

Images were acquired using a Leica M165 FC stereomicroscope to evaluate changes in the embryos phenotypes at the 1 and 3 dpf check-points. In Figure 63 it is possible to observe embryos at 1 dpf, during the pharyngula stage. At this phase, a normal embryo should have already several somites, rudimental organs, budded tail, primordial neuronal system and eye primordia (image A). From the images, it is possible to correlate the increased level of A₉K toxicity with an increment of developmental abnormalities detected in embryos exposed to high level of peptide (1000 – 4000 pg, images F-I). The embryos showed different levels of tissue degradation, defects in the notochord formation, lack of tail budding, yolk sack oedemas and a general reduced development of both head and somites.

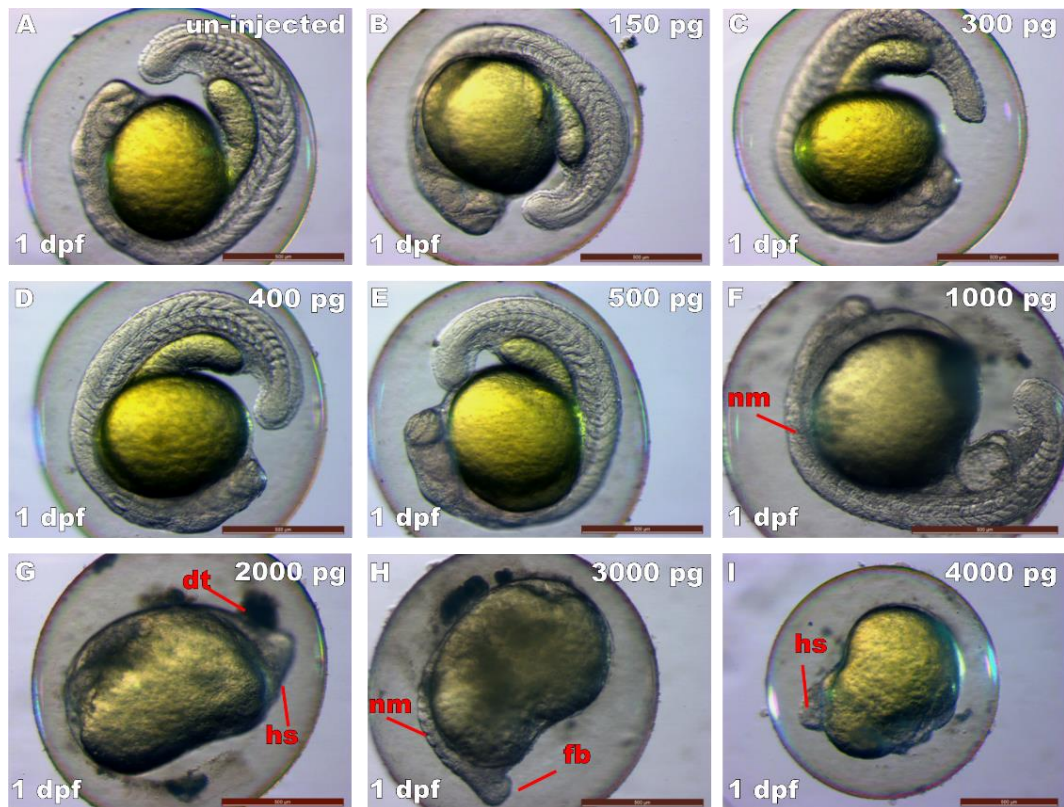


Figure 63. Morphological changes in 1 dpf embryos injected with A₉K. Embryos following microinjections with A₉K were imaged at 1 dpf and their phenotypes compared to an un-injected wild-type embryo (image A). At 150 – 500 pg of injected concentrations (images B-E), embryos did not present abnormalities and their development could be considered as normal. On the other side, embryos microinjected with higher doses of peptide (1000 – 4000 pg; images F-I), not only experience a reduced survival rate but showed several abnormalities as well, included notochord malformations (nm), general darkening tissue coagulation (dt), head suppression (hs) and failed tail budding (fb) (red acronyms and arrows). Bars = 500 μm.

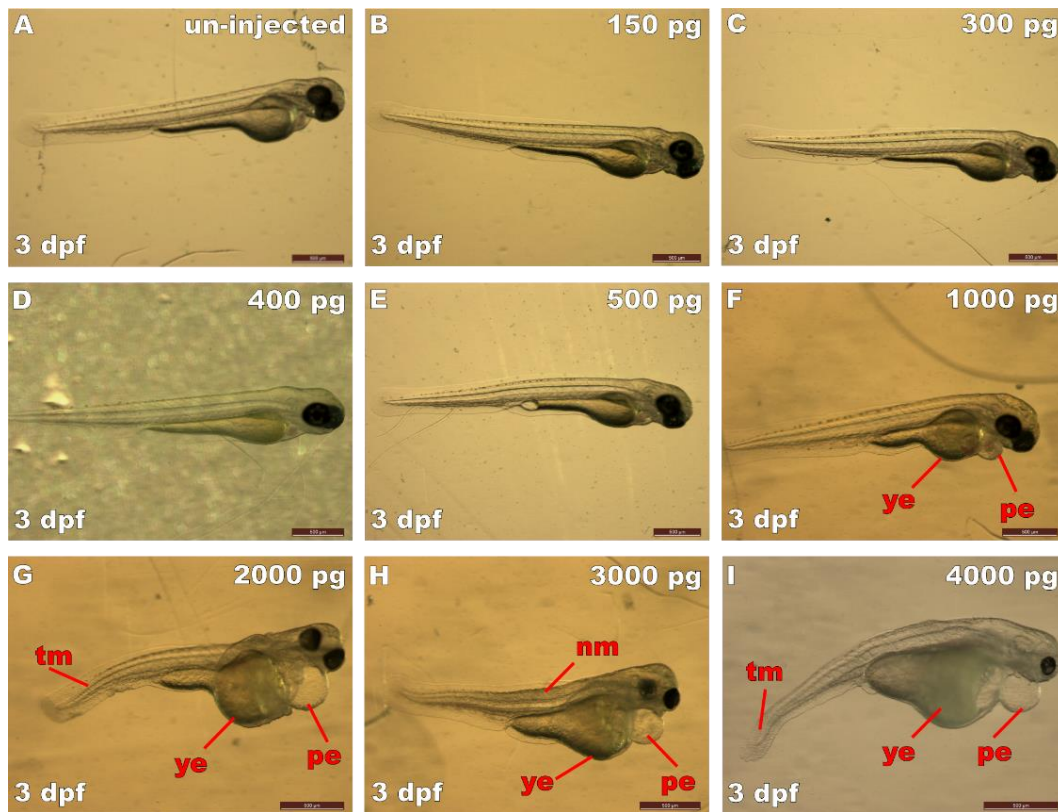


Figure 64. Morphological changes in 3 dpf embryos injected with A₉K. Embryos following microinjections with A₉K were imaged at 3 dpf and their phenotypes compared to un-injected wild-type embryo (image A). At 150 – 500 pg of injected concentrations (images B-E), embryos did not show morphological changes abnormalities and their development could be considered as normal. Embryos microinjected with higher doses of peptide (1000 – 4000 pg; images F-I), experienced a significant decreased in the survival rate and showed severe abnormalities: notochord malformations (nm), yolk sack oedemas (ye), pericardial oedemas (pe), tail malformation (tm) (red acronyms and arrows). Embryos were kept still during image acquisition using, Tricaine (40 mg/l) in E3 medium. Bars = 500 μm.

Embryos at 3 dpf are in the hatching phase and it is normal to observe at this stage some embryos swimming around the Petri dish while others still enclosed in their chorions. During this step, the embryos have complete blood circulation and a more complex nervous system, most of the organs morphologically defined and noticeable eyes ²⁶⁰⁻²⁶². From the images in Figure 64 it is possible to observe, at low and intermediate concentrations (150 – 500 pg), embryo development appears normal but at higher concentrations (1000 – 4000 pg) major defects are again visible. Pericardial and yolk

sack oedemas are the most prominent, followed by notochord or tail malformations and a general reduced brain development. With such severe abnormalities, it is unlikely that these embryos would complete embryogenesis and embryos were sacrificed.

5.5 Microinjections of FITC-G(IKKK)₃I-NH₂ peptide in zebrafish embryos

Using the same procedure described for A₉K peptide, the toxicity of FITC-G(IKKK)₃I-NH₂ was evaluated by performing microinjections in zebrafish embryos at one cell-stage. The number of embryos was recorded using a Leica MZ16 stereomicroscope.

Due to the high level of toxicity, the range of concentrations was extended to a larger interval, starting from 6.25 pg (10x higher than in cell transfection experiments) to 4 ng, corresponding to 3 μM – 2 mM. Indeed, all the concentrations with the exclusion of 6.25 pg, significantly reduced the number of embryos counted already after the 5 hours post fertilisation (hpf) check-point. Many embryos showed embryonic death and were therefore removed from the Petri dishes and scored as dead. The lowest (6.25 – 50 pg) and the highest (2000 – 4000 pg) concentrations, from the 5 hpf observations, are graphically represented in Figure 65. It is possible to notice the viability is decreased by 50% for all the concentrations, with the exclusion of the control, 6.25 pg and 2 ng.

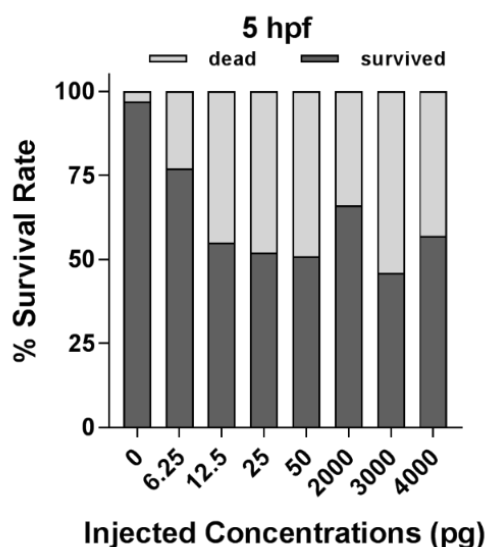


Figure 65. FITC-G(IKK)₃I-NH₂ microinjection induces toxicity by 5 hpf in wild type zebrafish embryos. Zebrafish embryos at one-cell stage were injected with increasing amounts of FITC-G(IKK)₃I-NH₂ peptide and the number of surviving embryos recorded after counted 5 hours post fertilisation. The graph shows a decrease in the embryo viability consistent with the increasing volume of peptide injected. Several batches were used for the injections and for each of them, few embryos were kept as un-injected controls. An average of 80-100 eggs per concentration were injected to ensure sufficient sample size to detect variability.

FITC-G(IKK)₃I-NH₂ showed, in both check-points (1 and 3 dpf), severe levels of toxicity at every tested concentration (Figure 66). For instance, at the 1 dpf check-point, between 1000 and 4000 pg, almost every embryo was scored as dead and at lower concentrations (12.5 pg to 500 pg) the survival rate was always found below 40%. The only recorded data above 50% was 6.25 pg, where 59% of the embryos were counted as still alive. At the 3 dpf check-point the survival rate of the injected embryos decreased even more, and the recorded viability was always below 50%. Even at 6.25 pg, the lowest injected concentration, the final count of alive embryos was only 44%.

These results showed a progressively decrease in the number of embryos scored as alive. This trend had already started at the very first check-point (5 hpf), where the survival rate per each tested concentration drastically dropped to 50% compared to the initial number of injected embryos. However, the decrease in the embryos' viability was

found to be more drastic between the first and the second check-points (5 hpf and 1 dpf) than later on, suggesting that the toxicity induced by the peptide is more severe in the first phases of embryogenesis (from gastrulation to the segmentation stage).

On the contrary, the survival rates observed in the un-injected embryos (controls) were always high (84% and 83% at 1 or 3 dpf, respectively). These percentages are in the range of what considered a standard value of viability for healthy wild type zebrafish embryos during their developmental stage and could confirm that the decreased in viability observed in the injected embryos was exclusively induced by FITC-G(IKK)₃I-NH₂

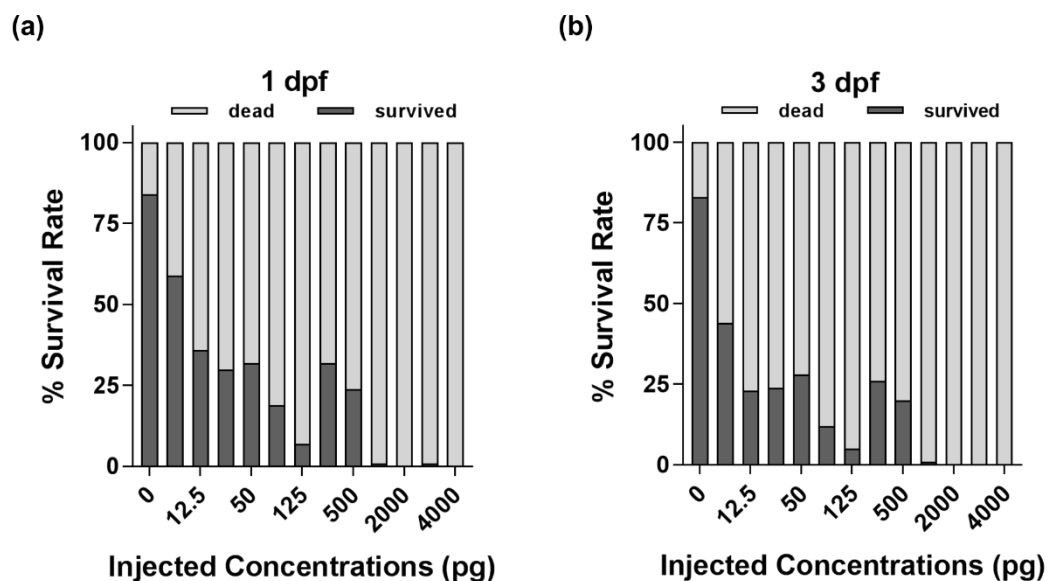


Figure 66. FITC-G(IKK)₃I-NH₂ microinjections induce severe toxicity in wild type zebrafish embryos. Zebrafish embryos at one-cell stage were injected with increasing amounts of FITC-G(IKK)₃I-NH₂ peptide and the number of survived embryos was recorded at 1 day post fertilisation (a) or 3 days post fertilisation (b). Both graphs show a drastic decrease in embryo viability at every concentration tested. No major differences can be observed between the two check-points. Several batches have been used for the experiment and for each of them, few embryos were kept as un-injected controls. An average of 80-100 eggs per concentration were injected to ensure sufficient sample size to detect variability.

Using GraphPad, the lethal concentration (LC₅₀), equivalent to the concentration of peptide needed to kill 50% of the embryos, was calculated. In 1 or 3 dpf embryos the LC₅₀ were respectively 7 and 2 pg corresponding to 3,5 and 1 μM.

5.6 Injections of siRNAs alone or complexed with FITC-G(IKK)₃I-NH₂

Complexes of FITC-G(IKK)₃I-NH₂ and red fluorescent non-targeting siRNA molecules (siGLO from Dharmacon) at different ratios were also injected into the zebrafish oocytes. The purpose was to observe if there was a reduction in peptide toxicity, due to the complexation with the siRNA molecules. The hypothesis tested would be if FITC-G(IKK)₃I-NH₂ could bind to the siRNA it might be less prone to interact with any of negatively charged cellular material found in the embryo. As consequence, the harmful effect caused by the peptide could potentially decrease.

5.6.1 Microinjections of siGLO to estimate the siRNA toxic threshold

Initially, prior to complexation with FITC-G(IKK)₃I-NH₂ peptide, siGLO on its own was tested, to evaluate any eventual toxicity towards zebrafish embryos.

In the literature, there are several studies showing the effect of siRNAs to modulate gene expression on fish, however the results are controversial. Although in some published reports there are successful results about the effectiveness of siRNAs in gene silencing, the general outcome indicates that the current methodology of RNA interference is not a useful technique for investigating gene function, especially during the early stages of zebrafish development, where the effects observed might be entirely nonspecific ²⁶³⁻²⁶⁷. To modulate gene silencing and expression in early stage development embryos, synthetic morpholino antisense oligonucleotides (MOs), are normally used ^{268, 269}. MOs are often injected at the concentration of 3 ng/embryo and more in general never above the concentration of 5 ng/embryo, since it would have an adverse effect on embryonic development. In contrast, injections of 100 pg or more of siRNA or DNA would kill most of the embryos ^{265, 269}.

For this reason, a range of siRNA concentrations between 20 pg and 80 pg per embryo was tested. siGLO red fluorescent siRNA is a non-functional siRNA and designed to be passive when transfected into the cells, and is normally used as positive control in transfection experiments. Since this siRNA has no targeting function, in these experiments its main purpose is to make complexes with the peptide and possibly reduce its negative effect on the embryos viability.

In Figure 67 it is possible to observe zebrafish embryos at 3 dpf microinjected with increasing amounts of siGLO red fluorescent siRNA. Images were acquired using a Zeiss Axio Zoom.V16 fluorescence stereomicroscope. Brightness and contrast were ultimately adjusted to the same level using Image J. The intensity in red fluorescence is directly related to the increased concentrations of siGLO injected in the embryos. The fluorescent siGLO was mainly localised in the yolk and partially in the brain and neural tube, but very little in the rest of the embryo (see arrows in Figure 67).

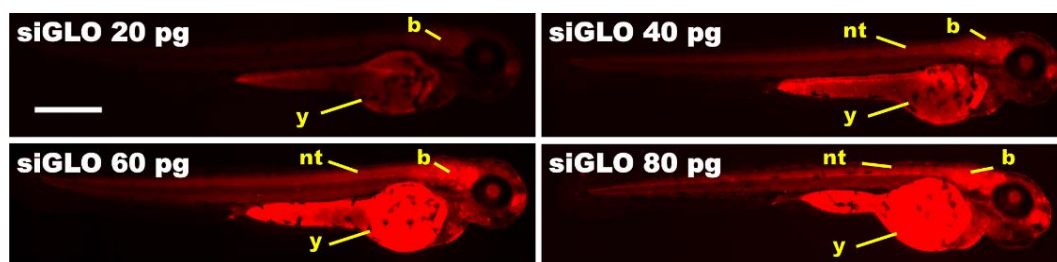


Figure 67. Microinjections of fluorescent siRNA in zebrafish embryos. One cell stage zebrafish embryos were injected with siGLO red fluorescent siRNA (Dharmacon) and imaged at 3 dpf. The images, acquired using the same exposure time, show progressively higher red fluorescence intensity comparable with the increased concentrations of fluorescent siRNA injected. The siGLO is predominantly located in the yolk sac, (y) brain (b) and neuronal tube (nt); see yellow acronyms and arrows. Bar = 500 μ m. All the images are scaled at the same size.

At 1 or 3 dpf the viability was recorded using a Leica MZ16 stereomicroscope and the results can be observed in the graph in Figure 68. High concentrations of siGLO (60, 80 pg) caused acute toxicity in zebrafish embryos with a reduction of at least 50% of the survival rate, when compared to the un-injected controls. On the contrary, 40 and 20 pg caused very little toxicity comparable to the controls. For this reason, 20 pg was the

concentration chosen for the subsequent experiments of microinjections using siRNA and peptide complexes.

Using GraphPad, the lethal concentration (LC₅₀), equivalent to the concentration of peptide needed to kill 50% of the embryos, was calculated. In 1 or 3 dpf embryos the LC₅₀ were respectively 73 and 56 pg.

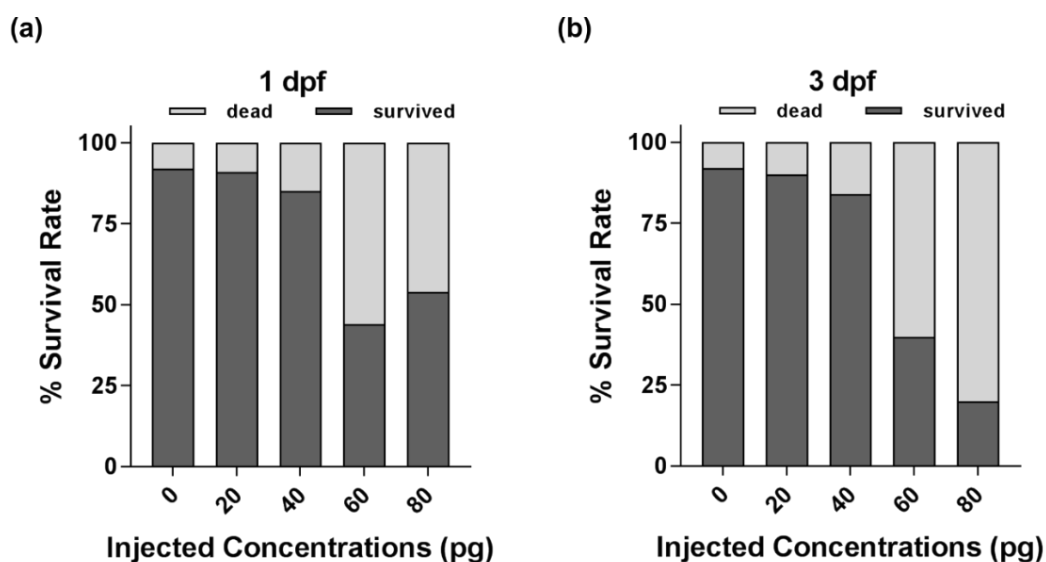


Figure 68. Microinjection of fluorescent siRNA induces dose-dependent toxicity in wild type zebrafish embryos. Zebrafish embryos at one-cell stage were injected with increasing amount of siGLO, red fluorescent indicator (Dharmacon) and the number of surviving embryos recorded at 1 day post fertilisation (a) or 3 days post fertilisation (b). The graphs show a decrease in embryo viability compatible with the increased injected volume. Several batches have been used for each experiment and some embryos were kept as un-injected controls. An average of 80-100 eggs per concentration were injected in order to ensure sufficient sample size to detect variability.

5.6.2 Microinjections of FITC-G(IKK)₃I-NH₂ and siGLO complexes

Complexes at two different ratios (1/1 or 4/1) were made according to the complexation method described in the Materials and Method Chapter for transfection experiments. 20 or 80 pg of fluorescent peptide were therefore mixed with 20 pg of siGLO in order to

have 1/1 or 4/1 ratios per embryo, respectively. Figure 69 and Figure 70 show images of embryos injected with the complex and imaged at 1 or 3 days post fertilisation. The images were acquired using a Zeiss Axio Zoom.V16 fluorescence stereomicroscope. Brightness and contrast were ultimately adjusted to the same level by using Image J. In embryos at 1dpf the distribution of both siGLO and peptide is uniform in the whole organism and no real difference in terms of fluorescent intensity can be observed between the two ratios (Figure 69).

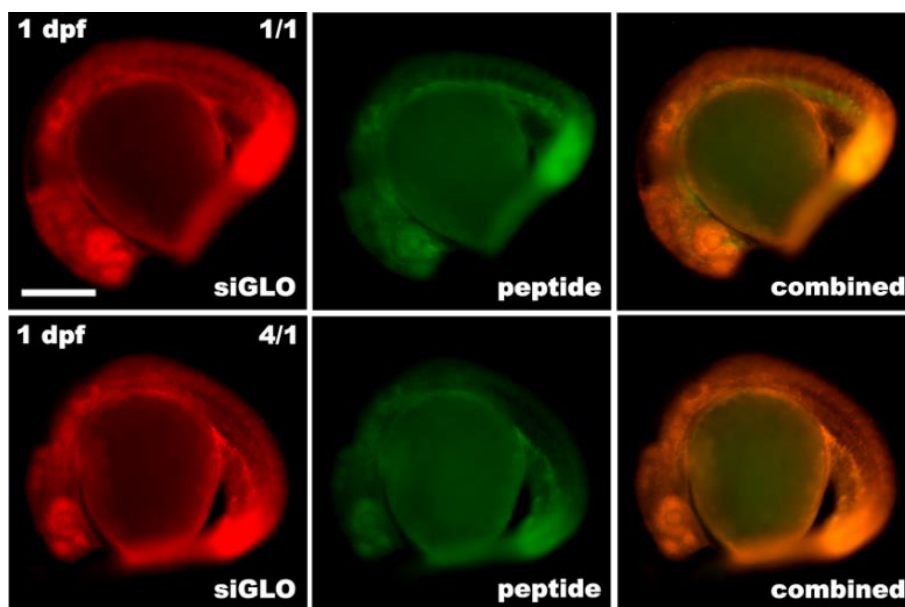


Figure 69. Microinjections of FITC-G(IKK)₃I-NH₂ and fluorescent siRNA complexes in zebrafish embryos. One cell stage zebrafish embryos were injected with FITC-G(IKK)₃I-NH₂ and siGLO red fluorescent siRNA (Dharmacon) complexes and imaged at 1 dpf. Red and green channels were separated to better visualize the distribution of peptide and siRNA in the organisms. No differences in fluorescent intensity can be observed between the ratios. Bar = 75 μ m. All the images are scaled at the same size.

In 3 dpf embryos (Figure 70), both siGLO and peptide mostly accumulated in the yolk sack and a significant difference in green fluorescence intensity is appreciable between the two ratios. The presence of both red and green fluorescence confirms successful injections of peptide/siRNA complexes.

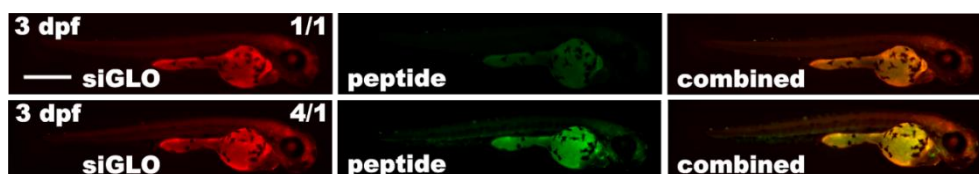


Figure 70. Microinjections of FITC-G(IKK)₃I-NH₂ and fluorescent siRNA complexes in zebrafish embryos. One-cell stage zebrafish embryos were injected with FITC-G(IKK)₃I-NH₂ and siGLO red fluorescent siRNA (Dharmacon) complexes and imaged at 3 dpf. Red and green channels were separated to better visualize the distribution of peptide and siRNA in the organisms. A difference in fluorescent intensity can be observed between the ratios. Bar = 500 μ m. All the images are scaled at the same size.

The toxicity of the complexes injected into the embryos was carefully evaluated and any variations between these data and the ones regarding the un-complexed peptide microinjections (Figure 66) recorded. Since 20 pg of siRNA do not have a toxic effect on zebrafish embryos (Figure 68), any significant decrease observed in the survival rate could be related to the peptide. Graphs in Figure 71 show the toxicity results obtained after scoring the rate of dead and alive embryos at 1 or 3 dpf check-points. In both ratios, the overall toxicity does not reach 50% and it is stable between 1 and 3 days. These results, when compared to Figure 66, show a substantial difference and the complexes of peptide/siRNA appear less toxic than peptide only. For example, 20 pg of FITC-G(IKK)₃I-NH₂ when complexed to siGLO, caused a decrease in embryo viability of 40% in both, day 1 and day 3, while a similar concentration of un-complexed peptide (25 pg) caused the death of 70% of embryos at 1 dpf and 76% by the third day. With the higher amount used in the 4/1 ratio, the difference between the complexed and un-complexed peptides was even more significant; 80 pg of FITC-G(IKK)₃I-NH₂ complexed with siGLO gave a decrease in the survival rate of 34 and 35% in 1 dpf and 3 dpf embryos, respectively. The closest concentration of un-complexed peptide instead (62.5 pg) had a severe impact on the embryos' surviving rate; 1 dpf embryos showed a mortality of 81% which, by day 3, increased to 88%.

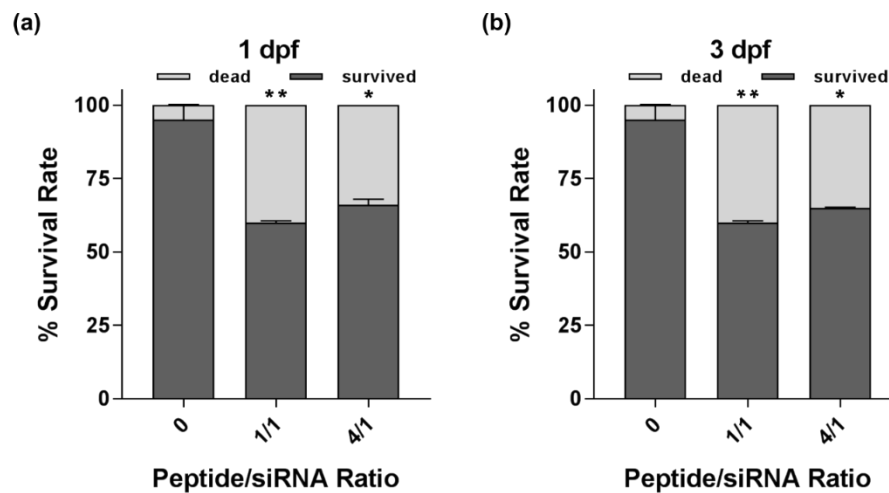


Figure 71. Microinjections of FITC-G(IKK)₃I-NH₂ peptide complexed with siRNA have a reduced toxic effect in wild type zebrafish embryos. Zebrafish embryos at one-cell stage were injected with peptide and siGLO, red fluorescent indicator (Dharmacon) complexes. The amount of siRNA chosen was 20 pg per embryo while peptide ratios were made at 1/1 or 4/1 corresponding to 20 or 80 pg of the fluorescent peptide. The number of surviving embryos was recorded at 1 day post fertilisation (a) or 3 days post fertilisation (b). The graphs show a stable decrease in embryo viability of 40% compared to the un-injected controls. Several batches have been used for the experiment and for each of them, few embryos were kept as un-injected controls. An average of 50 embryos were injected per concentration to ensure sufficient sample size to detect variability. Statistically significant difference from the negative control was determined by Student's t-test (*p<0.05; **p<0.01).

In Figure 72, the graphs show data collected after the first check-point (5 hpf) for both experiments (siGLO and peptide/siRNA complexes). A small reduction in survival rate is observed for siGLO microinjections when compared to the graphs in Figure 68; at high concentrations (60, 80 pg) the survival rate is already down to 60 and 50%, respectively, while at 40 pg is 93% and with 20 pg all the embryos were all still alive. Complexes peptide/siRNA showed lower toxicity compared to the data represented in Figure 65. For example, while 25 pg of peptide decreased the survival rate of 48%, 20 pg of the same peptide when complexed with siGLO gave a reduction of only 24%.

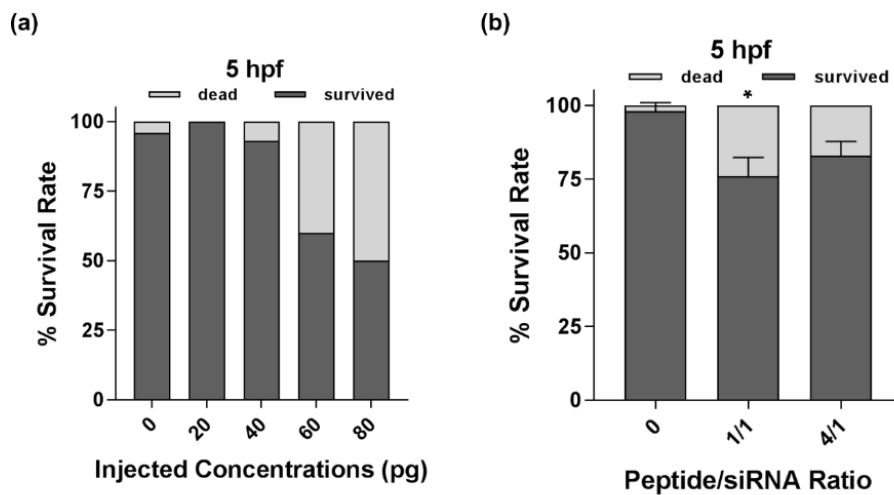


Figure 72. Microinjections of fluorescent siRNA alone or complexed with FITC-G(IKK)₃I-NH₂ peptide induce toxicity by 5 hpf in wild type zebrafish embryos. Zebrafish embryos at one-cell stage were injected with siGLO, red fluorescent indicator (Dharmacon) only (a) or complexed with FITC-G(IKK)₃I-NH₂ peptide at 1/1 or 4/1 ratios (b). The number of surviving embryos was recorded at 5 hpf. The graphs show little variation in the survival rate of embryos injected with 20 or 40 pg of siRNA when compared to the control. A more severe effect is caused by 60 and especially 80 pg where a mortality rate near 50% is observed. The peptide complexed with the siRNA had a small effect with the mortality rate around 20-25%. Several batches have been used for the experiment and for each of them, few embryos were kept as un-injected controls. An average of 50-100 eggs per concentration were injected to ensure sufficient sample size to detect variability. Statistically significant difference from the negative control was determined by Student's t-test (*p<0.05).

5.7 In vivo caudal injections of FITC-G(IKK)₃I-NH₂ peptide to evaluate the peptide distribution across the animal

The last section of this chapter explains the results obtained after injecting 4 days post fertilisation (4 dpf) larvae in their caudal vein with the peptide FITC-G(IKK)₃I-NH₂ or just the fluorophore FITC, as control. The purpose of this experiment is to observe the behaviour and localisation of the peptide once injected directly in the bloodstream of an

animal. It is important to understand how the peptide behaves in the circulation in vivo since the peptide could be potentially used to target tumours inside a living organism, therefore, it is crucial to have good understanding of its fate in a complex animal environment. Caudal injections allow the rapid delivery of soluble compounds directly in the bloodstream of the fish and are used as a standard procedure in bacteriological studies, where embryos are inoculated with bacteria strains to induce a systemic infection^{150, 270}.

The complete procedure is explained in the correspondent section in Material & Method chapter (“2.8.3 Peptides and siGLO microinjections”) but briefly, zebrafish embryos at 4 dpf were anaesthetized with Tricaine (40 mg/l) and mounted on a Petri dish in 3% low-melting point agarose. The agarose solution was made using E3 media, heated until dissolved and kept at 37 °C to avoid solidification. Tricaine (40 mg/l) was also added to the solution to guarantee continued embryos anaesthetisation during the injections procedure. Once mounted, and before the complete solidification of the agarose, embryos were positioned laterally to allow a complete view and access to the caudal vein with their tail pointing towards the needle tip. The TG(*kdrl:HRAS-mCherry*) transgenic zebrafish line was used to visualize the blood vessels under a fluorescent microscope¹⁴⁷. Both FITC and FITC-G(IKK)₃I-NH₂ were injected in the embryos at the concentration of 25 pg/nl. Once injected, the embryos were quickly checked under a Leica M165 FC fluorescent stereo microscope to evaluate injection efficiency.

Two of the correctly injected embryos per compound were taken from the Petri dish and mounted in a glass capillary tube (Transferpettor caps, DE-M, 50 µl, green) with 3% low-melting point agarose specific for Light Sheet Fluorescence Microscopy (LSFM)¹⁵¹. Images were acquired with the Zeiss Lightsheet Z.1 and further analysed with ZEN 2014 SP1 software. LSFM is becoming more and more popular as a method to image early embryonic development especially for species like *Danio rerio*, *Drosophila melanogaster* and *Caenorhabditis elegans*, because allows live imaging at low light exposures, reducing photo-bleaching and photo-toxicity^{271, 272}.

The vascular network in zebrafish embryos can be easily studied to understand pathways that are potentially important for pathological conditions, such as vascular permeability for instance, which is a major cause of morbidity and mortality in humans^{247, 273, 274}. There are a few studies showing how large molecules (>10 KDa) are

normally retained in the vasculature once injected while small molecules, on the contrary, may rapidly leak out^{275, 276}. Both, FITC with a weight of 389 Da and FITC-G(IKKK)₃I-NH₂ with a weight of 2024 Da were not retained in the vasculature system, but instead of leaking out directly from the injection point (caudal vein) they travelled in the bloodstream, to the head vasculature and leaked out at the aortic arches which will provide circulation to the future gills or at the choroid plexus, a polarised epithelial-based structure localized in the brain ventricle (Figure 73 and Figure 74)²⁷⁷.

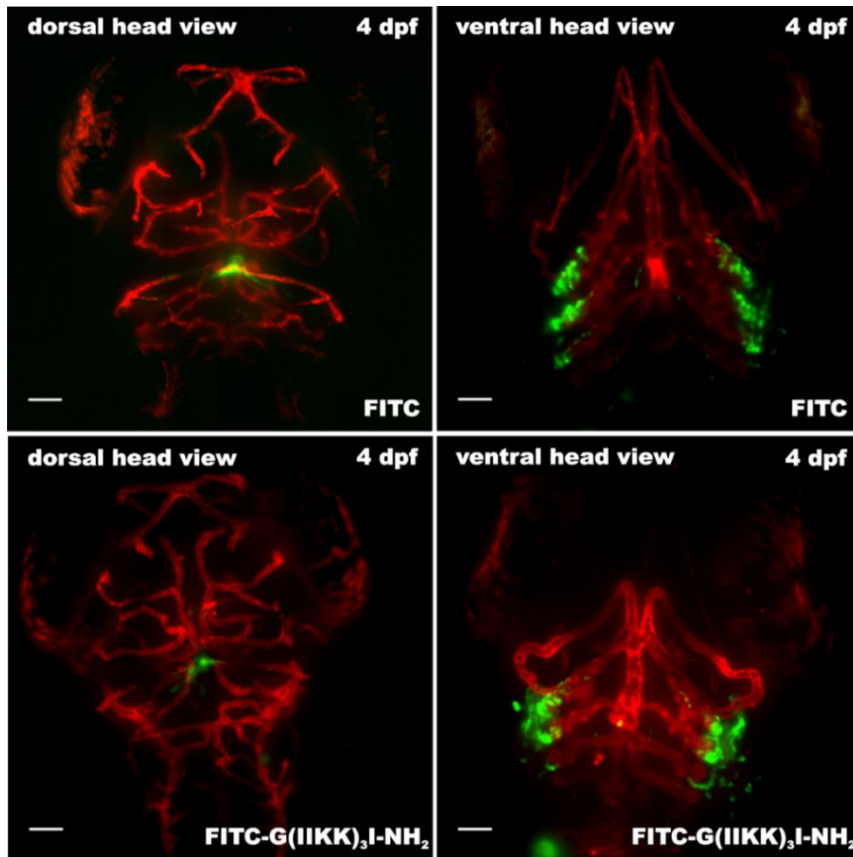


Figure 73. Light sheet images of FITC and FITC-G(IKKK)₃I-NH₂ caudal injections in 4 dpf larvae. 4 dpf larvae were anesthetized with Tricaine (40 mg/l), mounted in 3% low-melting point agarose and injected with 25 pg/nl of FITC fluorophore or FITC-G(IKKK)₃I-NH₂ peptide. Injections were made in a caudal vein and the distribution of the FITC and peptide in the bloodstream immediately observed using Light Sheet Fluorescence Microscopy (LSFM). Due to their small size, the two molecules were not retained by the vasculature and leaked from the circulation through the aortic arches connected with the gills and at the choroid plexus. The transgenic fish strain used for this experiment is TG(*kdrl:HRAS-mCherry*) with membrane localised red fluorescent blood vessels. Bar = 50 μM. All the images are scaled at the same size.

The rest of the larval bodies were clear from FITC fluorescence, as it is possible to observe from the trunk view in Figure 74. In Figure 74 it is possible to observe also a magnification of the dorsal vessel showing FITC fluorophore leaking out from the choroid plexus endothelium.

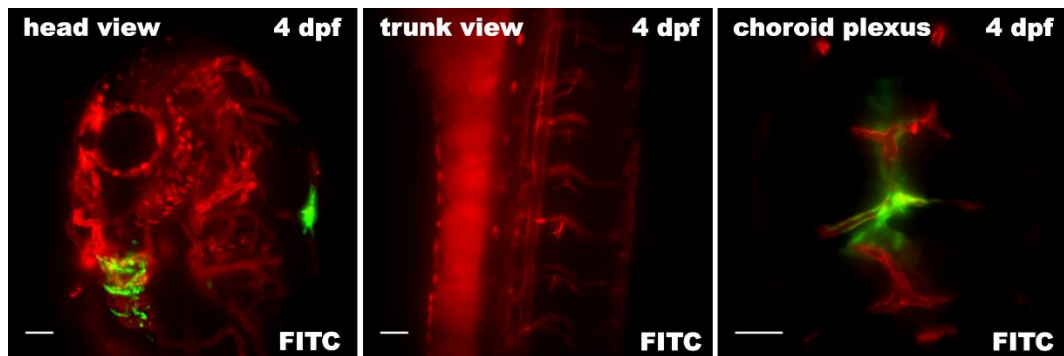


Figure 74. Light sheet images of a zebrafish head, trunk and detailed dorsal vessel after FITC caudal injections in 4 dpf larvae. 4dpf larvae were anesthetized with Tricaine (40 mg/l), mounted in 3% low-melting point agarose and injected with 25 pg/nl of FITC fluorophore. Injections were made in a caudal vein and the distribution of the FITC in the bloodstream observed using Light Sheet Fluorescence Microscopy (LSFM). Due to its small size, the fluorophore is not retained by the vasculature but instead leaked out from the fish system. There are only two leakage points; the aortic arches and a big vessel located on the dorsal side of the head, possibly the choroid plexus (CP). The rest of the body (trunk view) is clear. The fish strain used for this experiment is TG(*kdr1:HRAS-mCherry*) with red fluorescent blood vessels. Bar = 50 μ M. All the images are scaled at the same size.

6 RNAI SCREENS TO IDENTIFY ENDOCYTTIC PATHWAYS INVOLVED IN PEPTIDE CELLULAR UPTAKE

RNA-mediated interference (RNAi) is an important cellular process found in almost every eukaryotic organism, which post transcriptionally regulates gene expression. Endogenously expressed or transfected small RNA molecules target and degrade endogenous mRNA transcripts and, as result, a reduction of gene activity is observed¹⁸⁵. In animals, the phenomenon was firstly discovered in 1993 by Ambros and co-workers in the nematode *Caenorhabditis elegans* with lin-4 miRNA, an endogenous regulator of genes that control developmental timing²⁷⁸.

Many types of small RNAs (between 20-30 nt) have been discovered and can be all generally divided into three main categories; short interfering RNAs (siRNAs), which are completely synthetic, microRNA (miRNAs) and piwi interacting RNAs (piRNAs), the latter two which are found endogenous^{279, 280}. siRNAs and miRNAs derive from double stranded precursors, while piRNAs are mainly found in the germline and originate from single stranded precursors. Moreover both miRNAs and siRNAs are recognized by Argonaute (Ago) proteins while piRNAs bind to members of the Piwi family²⁷⁹. siRNAs are recognized by the protein Dicer (Dicer-2 in *Drosophila*) and are ~ 21 nt duplexes²⁸¹. The RNAs duplex is then incorporated in the RISC complex bound to Ago2, a protein member of the Argonaute family. The passenger strand is discharged while the RISC complex becomes functional. Target mRNA decay is activity dependent upon Ago2, which has a slicer function^{279, 282}. siRNAs (~ 21 nt length) duplexes are mainly synthetically produced and use to directly transfect cells^{133, 185}.

Since the discovery of RNAi, the technology moved forward on a more global scale and today many siRNA libraries are commercially available on the market. With nearly complete genome coverage for several species, human included, it is possible to pursue large-scale functional genomic screens and identify therapeutic targets or elucidate specific biomolecular pathways using a different approach compared to classical genetic screens^{283, 284}. The main advantages are that the sequences of identified genes are easily

retrieved, and can be knocked down. Unfortunately, there are some disadvantages, such as the possibility of off targets effects (OTEs) which would produce false negative/positive results and more importantly proteins with long half-lives that hardly would be affected by the knocking down activity of RNAi^{285, 286}. However, with new algorithms for rules of target design and additional chemistries to improve siRNA efficacy, recent research has abated some of the worries regarding OTEs.

High-content screening (HCS) is a recent technique developed in the late 90's that combine automated fluorescent microscopy with image analysis. With this technology, it is possible to collect quantitative data from complex biological systems. The pairing of HCS with RNAi allowed to perform either genome-scaled or focussed library cell-based screens to a wide variety of cell types, mammalian included²⁸⁷. High-content genome-wide screens are successfully applied in preclinical drug discovery or in cell biology to identify molecular targets involved in signal transduction, cell cycle, organelles morphology, protein localisation and/or function and responses to pathogens²⁸⁸. Thanks to the major progress achieved in microscopy it is now possible to finely image structures and identify molecular compartments of cells. HCS is based on the microscope's ability to acquire multiple high-quality functional and morphometric images of individual cells and contemporary analyse all the phenotypic variations in accordance to the administration of specific compounds²⁸⁹.

Using a siRNA library for endocytosis-related genes, one high-content genome screen and a mini-validation screen were performed on HCT-116 cancer cells as an approach to identify the pathway(s) involved in FITC-G(IKK)₃I-NH₂ and FITC-A₉K cellular uptake. The complete methodology is explained in section "2.9.6 RNAi screen to elucidate the peptide uptake in cancer cells" of Chapter 2, Materials and methods but briefly, HCT-116 cancer cells were transfected with 30 nM of siRNAs using the reverse transfection method¹³⁹ and after 3 days of incubation, 6.25 μM of fluorescent peptide was added for other 24 hrs. Cells were then fixed and stained with the standard solution of 4% formaldehyde and Hoechst (2 μg/ml) and imaged using the ImageXpress® Micro System fluorescent microscope. Quantitative analyses of the variations in fluorescence intensity between transfected cells were performed using MetaXpress® 5.0.0.20 software. Brightness and contrast were adjusted for all images to the same level by

using Image J. The FITC-A₉K mini-screen was performed by the student Joanna Henry, as part of her MSc final project.

6.1 Assay development screening for FITC-G(IKK)₃I-NH₂

Prior to conducting the high-content screen, assay development screening was performed. The parameters of the assay were identified from this approach, establishing the correct experimental conditions for a successful screen. The primary parameters that needed to be established were, seeded cell number, the amount of DharmaFECT1 (DF1, Dharmacon) used for reverse transfection, the assay window and in this specific case the correct peptide concentration to be added to the cells. More importantly relevant genes have to be identified as possible “hits” if knocked down using RNAi²⁸⁵.

Few experiments were conducted to evaluate the suitable initial seeding cell number for HCT-116, which was then established to be 2×10^3 cells per well (384 well plate format). A reduced cell number could in fact not only increase the cells sensitivity towards DF1 but also give misleading results such as increased sensitivity to either DF1 or peptide exposure. On the other side, an elevated cell number could equally compromise the screen outcome; if the cells reach confluence, and in the case of cancer cells, start to overgrow, it is more difficult to perform a correct analysis afterwards. Cells on the plate need to be individually identified by using pre-defined algorithms, but when over-confluent, the software would struggle to recognise individual boundaries between cells and would end up producing ambiguous results, i.e. undercounting cells or peptide.

In the same way, the amount of DF1 is critical, too much of it and cells would die but too little and the transfection efficiency would decrease. For HCT-116 the chosen volume was 0.05 μ l per well (total medium volume in each well was set at 25 μ l). Cells were left with the transfection medium for the duration of 3 days. In this way, plenty of time was given for the gene-silencing process. Finally, the selected concentration of peptides was 6.25 μ M, enough to give a good fluorescent signal but without inducing extreme toxicity (see Figure 45, Chapter 4).

For this assay, a siRNA library called assay development plate 2 (ASD2), specifically designed for genome-wide RNAi screens was used. See Table 6 at the end of this chapter for the complete list of genes. The library created by the Sheffield RNAi Screening Facility, SRSF (<http://www.rnai.group.shef.ac.uk/>) was predominantly composed of a selection of siRNAs which knock down kinases involved in many cellular functions. Few other siRNAs were specific for genes related with endocytic pathways and therefore chosen as possible “hits”. Literature was scanned and the selected siRNAs were Actin related protein 2 homolog (ACTR2), ADP-ribosylation factor 6 (ARF6), caveolin 1 (CAV1), clathrin heavy chain (CLTC), dynamin 2 (DNM2), myosin Va (MYO5A), myosin Vb (MYO5B), myosin Vc (MYO5C) and ras-related protein 7a (RAB7A) (see Table 4 for genes IDs and functions). Cells were transfected with four non-targeting siRNAs and then exposed to the peptide. They represented the negative controls and the standard phenotype to be compared with. The images collected from the possible “hits” were confronted with the negative controls in search of variations in the phenotypes and quantitatively analysed according on the amount and distribution of the fluorescent peptide across the cells compartments.

Table 4. List of the genes for which siRNAs were selected in the assay development screening as possible “hits” for FITC-G(IKK)₃I-NH₂ peptide. Gene name, NCBI's database gene ID and gene function are provided.

Gene	ID	Function
ACTR2	10097	ATP-binding component of the Arp2/3 complex which is involved in regulation of actin polymerization ¹⁵⁷
ARF6	382	GTP-binding protein involved in protein trafficking that regulates endocytic recycling and cytoskeleton remodelling ¹⁵⁹
CAV1	857	Scaffolding protein within caveolar membranes ¹⁶⁰
CLTC	1213	Clathrin heavy chain protein is one of the components of a polyhedral structure of coated pits and vesicles which entrap specific macromolecules during receptor-mediated endocytosis ¹⁵⁸
DNM2	1785	GTP-binding protein associated with microtubules and implicated in endocytosis and cell motility ¹⁶¹
MYO5A MYO5B MYO5C	4644 4645 55930	Class of actin-based motor proteins involved in cargoes transport endocytic vesicular trafficking and endosomes recycling in neuronal and epithelial cells ^{162, 163}
RAB7A	7879	Key regulator in endo-lysosomal trafficking and in the early-to-late endosomal maturation ¹⁶⁴

ACTR2 gene encodes for Actin Related Protein 2 Homolog, a component of the Arp2/3 complex¹⁵⁷. Arf 6 (ADP-ribosylation factor 6) is a GTP-binding protein with a variety of cellular functions including membrane trafficking, modulation of actin cytoskeleton, endosomal recycling, cell migration and cell polarity. Arf 6 may also contribute to the membrane recruitment of AP-2¹⁵⁹.

Caveolin 1 (Cav 1), together with Caveolin 2 and 3 (Cav 2- 3) are structural proteins required for the formation of caveolae, flask-shaped plasma membrane invaginations implicated in endocytosis, cholesterol and lipid metabolism and cellular signalling. Cav 1 and Cav 2 are expressed in many tissues but especially in endothelial cells, adipocytes, fibroblasts and smooth-muscle cells while Cav 3 is uniquely expressed in skeletal and cardiac muscle¹⁶⁰. Moreover, there have been controversial evidence implying that Cav 1 can be both a tumour suppressor and an oncogene, depending on the tissue where it is expressed. However, few studies proved that the overexpression of Cav 1 is associated with several cancers and it is responsible for tumour invasion, drug resistance and a general indicator of poor prognosis²⁹⁰. Specifically, colorectal tumours and human colon cancer cell lines, HCT-116 included, have been shown to frequently abnormally express Cav 1^{291, 292}.

Dynamin 2 (DNM2) is a large GTP-ase involved in the endocytosis. In mammals, there are three dynamin genes (DNM 1-2-3) which share 80% of homology but are expressed in different tissue; Dynamin 1 is highly expressed in neurons, Dynamin 2 is ubiquitously expressed while Dynamin 3 is found in brain (in low levels), testis and in some other tissues. Dynamins are localised at sites of endocytosis on the plasma membrane. Their principal role is the membrane fission, mainly associated with clathrin-mediated endocytosis events; dynamins self-assemble into helical polymers at the bottom of budding vesicles and via GTP hydrolysis-dependent activity promote the membrane detachment to generate a free endocytic vesicle¹⁶¹.

Myosin Vs (myo V) is a family of cytoskeletal motor proteins that transport cargoes (secretory and endocytic vesicles, mRNA, lipids and proteins) along actin filaments. In humans, there are three classes of myosin Vs (Va, Vb and Vc) which are associated to specific sets of membrane trafficking events and share about 50% of amino acidic sequence. They are organised in different domains: a globular head containing a highly conserved motor domain responsible for generating movement via an actin-activated

ATPase; an extended α -helical neck region adjacent to the head which regulates the activity of the head domain and a tail which contains the binding sites that link myosin Vs to their cargoes. Myo Va is most abundant in brain tissue and melanocytes, while myo Vb and myo Vc are mainly expressed in epithelial cells ¹⁶². Moreover, myo Vb is associated with the endosomes recycling ¹⁶³.

Ras-related protein 7a is a protein encoded by RAB7A gene. It has been called Rab 7a to distinguish it from Rab 7b, a protein involved in the regulation of membrane trafficking from late endosomes to the trans-Golgi network (TGN) ²⁹³. Rab 7a is a small GTPase of the Rab family ubiquitously expressed and mainly associated with late endosomal structures and lysosomal compartments. It controls vesicle trafficking from late endosomes to degradative compartments. Rab 7a is also required in growth-factors transport or in specialised endosomal membrane trafficking such as melanosomes, pathogen-induced phagosomes and autophagosomes ¹⁶⁴.

Four non-targeting siRNAs (On-TARGET^{plus} non-targeting control #2, #3, #4 #5) were chosen instead as negative controls.

To establish whether the negative controls did not cause any adverse effects, or the siRNAs selected to target the endocytic pathway, a series of experiments were performed. Cell counting analyses presented in Figure 75 shows that the transfections made with the non-targeting siRNAs did not interfere with the cell viability (Figure 75 a), while depending on the functional siRNA, a variation in cell number could be observed (Figure 75 b). A decrease in the cellular growth was encountered with ACTR2, CAV1 and MYO5B genes knock down where the number of cells counted were 25%, 47% and 36% compared to the negative controls average, respectively. Knock down of ARF6 and MYO5A, MYO5C and RAB7A decreased the cell number to 63%, 60%, 78% and 70%, respectively. Knock downs of CLTC and DNM2 instead did not affect the cell population.

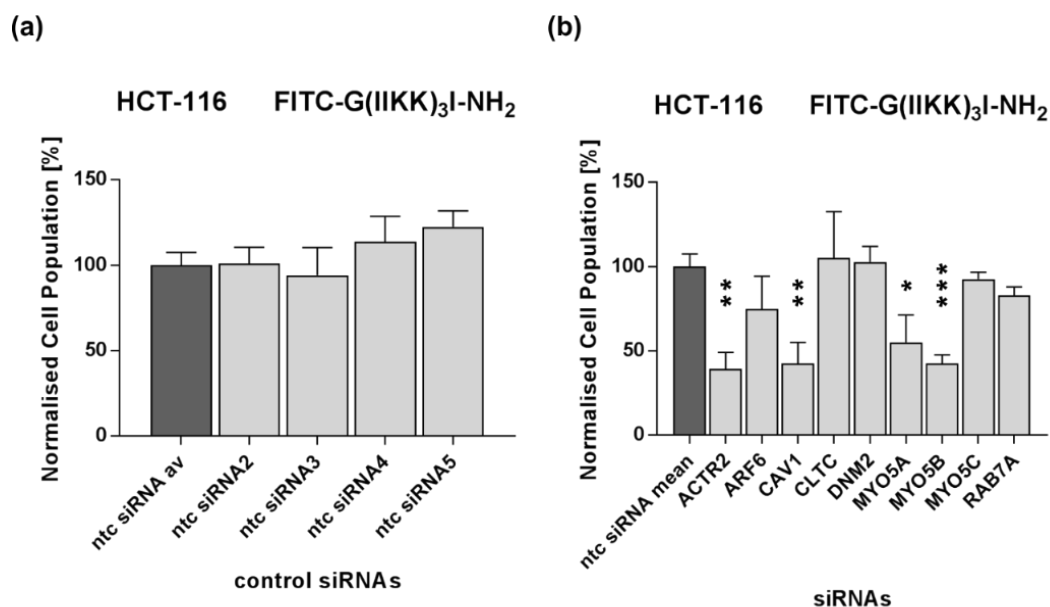


Figure 75. HCT-116 cell number evaluated with high-content microscopy after RNAi and FITC-G(IKK)₃I-NH₂ exposure. Cells were transfected with (a) non-targeting siRNAs; (b) endocytosis-related siRNAs for three days, exposed to the peptide for another day then fixed in formaldehyde and stained with Hoechst 3342 (2 µg/ml) to reveal the nuclei. Images were acquired using ImageXpress® Micro microscope and the cell number was counted using the Multi Wavelength Scoring algorithm within the MetaXpress® software. The results are expressed as a percentage of number of cells normalized to the negative control (mean of the 4 non-targeting siRNAs). The values obtained are averages of independent experiments ± standard error mean (±SEM). Statistically significant differences from the negative control were determined by Student's t-test (*p<0.05; **p<0.01; ***p<0.001).

Knock down effects and correlation with variation in the cell population were made with the rest of the plate; the siRNAs that caused a reduction in cell number of 95% or more were plotted in the graph showed in Figure 76. All the knock down genes were kinases involved in biological functions linked to metabolism, cell signalling, proliferation, inflammatory response, differentiation and apoptosis. Therefore, their cellular depletion should generally induce a significant decrease of the cell number. Moreover, upregulation of these kinases has been observed also in numerous types of cancer.

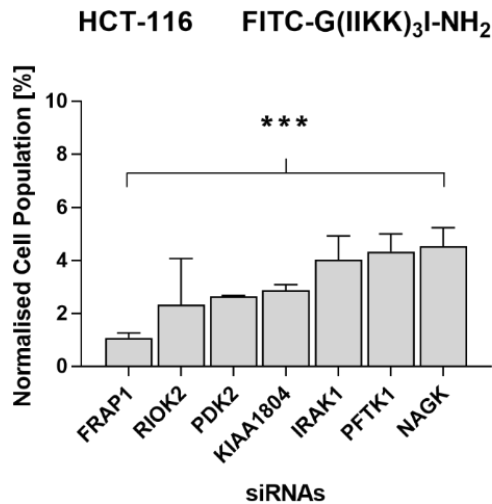
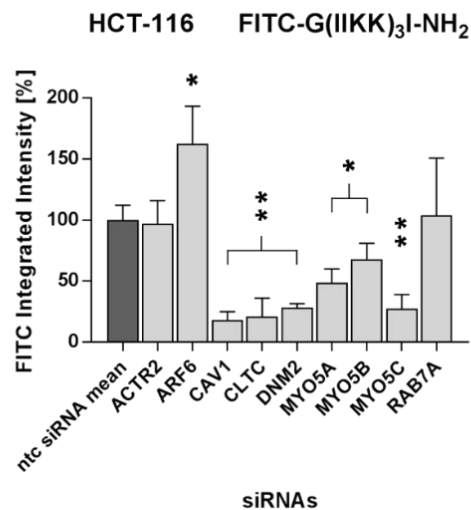


Figure 76. Bottom 5% of HCT-116 cells number count evaluated with high-content microscopy after kinases knock down via RNAi and FITC-G(IKK)₃I-NH₂ exposure. Cells were transfected with siRNAs for three days, exposed to the peptide for another extra day, then fixed in formaldehyde and stain with Hoechst 3342 (2 µg/ml) to reveal the nuclei. Images were acquired using ImageXpress® Micro microscope and cell number was counted using the Multi Wavelength Scoring algorithm within the MetaXpress® software. The results are expressed as a percentage of number of cells normalized to the negative control (mean of the 4 non-targeting siRNAs). The values obtained are averages of independent experiments ± standard error mean (±SEM). Statistically significant differences from the negative control were determined by Student's t-test (***)p<0.001).

The evaluation of the amount of internalised peptide per cell revealed interesting results; the knock down of ARF6 significantly increased the peptide concentrations while with the exclusion of ACTR2 and RAB7A which were not significant, for all the others an important decrease in peptide uptake was observed (Figure 77). ARF6 regulates the endosomal-membrane traffic and it is essential for the endosomal recycling to the plasma membrane in both clathrin-dependent and -independent pathways 159. The important observation of increased peptide concentration when Arf 6 is knock down could suggest that not only the peptide is internalised via endocytosis but also that, in normal conditions, it is recycled back to the cell surface.

(a)



(b)

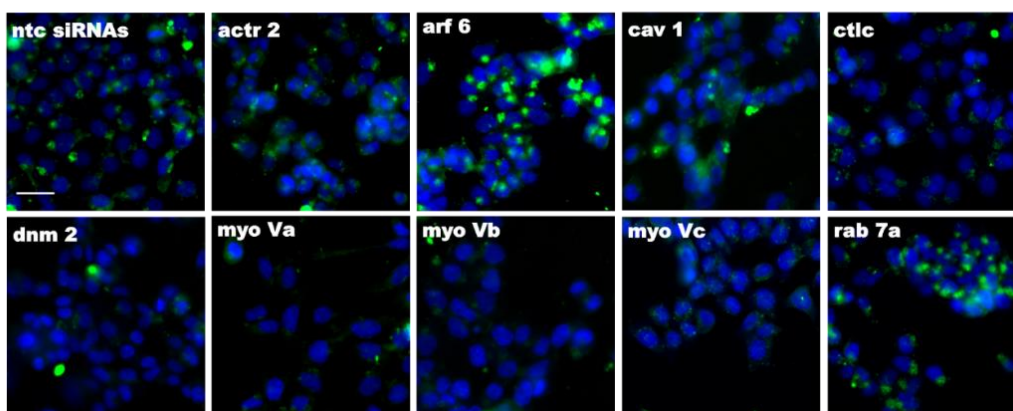


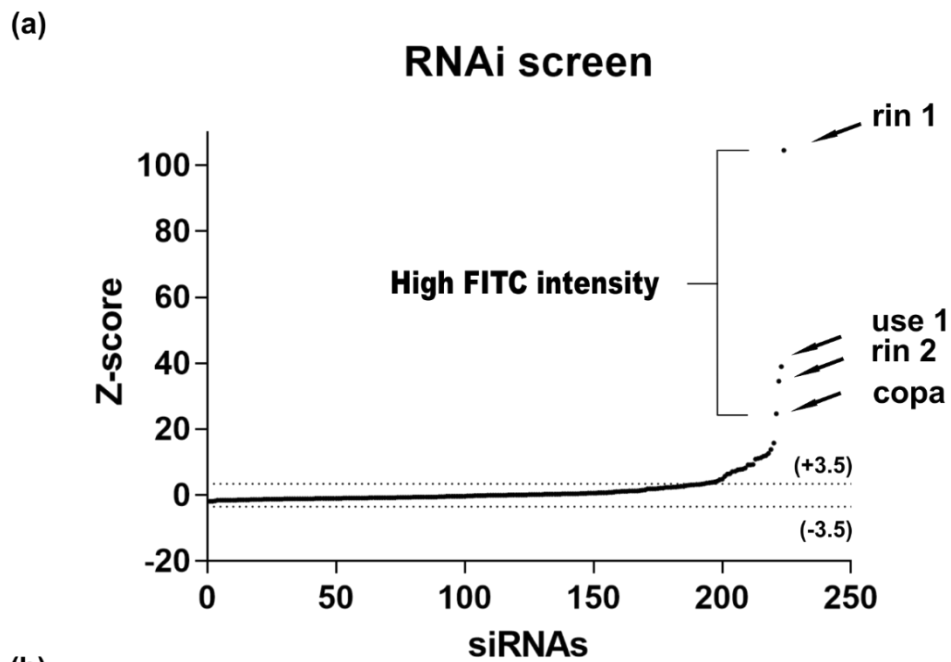
Figure 77. Variation in the fluorescence intensity evaluated with high-content microscopy in HCT-116 cancer cells after RNAi and FITC-G(IKK)₃I-NH₂ exposure. Cells were transfected with siRNAs for three days, exposed to the peptide for another extra day then fixed in formaldehyde. A quantitative analysis of the green FITC fluorescence (a) was performed. The results are expressed as a percentage of FITC Integrated Intensity and normalised to the negative control (mean of the 4 non-targeting siRNAs). The values obtained are averages of independent experiments \pm standard error mean (\pm SEM). Statistically significant differences between non-targeting and targeting siRNA transfections were determined by Student's t-test (* p <0.05; ** p <0.01). In (b) images showing the distinct levels of FITC intensity related to the different genes knock down. Hoechst 33342 (2 μ g/ml) (blue) was used as nuclear staining. Bar = 25 μ m. All the images are scaled at the same size.

6.2 High-content genome screen on FITC-G(IKK)₃I-NH₂

For the high content screen on the fluorescent peptide FITC-G(IKK)₃I-NH₂ a designed library called Traffic-ome was used (genes selected by Prof Elizabeth Smythe and Dr. Andrew Peden); a plate with more than 200 siRNAs targeting the gene expression of genes involved in endocytic pathways. See Table 7 at the end of this chapter for the complete list of genes. The experimental procedure was the same adopted for the assay development and explained in the previous section.

Once fixed, the cell number was counted and the FITC fluorescence intensity quantified using MetaXpress®. The data were subsequently normalized using the robust z-score method ($Z = (X_i - \text{median}) / \text{MAD}$) which uses median and median absolute deviation (MAD) instead of mean and standard deviation. The median absolute deviation is defined as $\text{MAD} = \text{median} (|X_i - \text{median} (X_{i \dots n})|)$ and corresponds to the median of the absolute deviation from the median of the data points X_i to X_n . It is less sensitive to outliers than the standard deviation therefore more preferable to use in RNAi screens^{294, 295}. The possible “hits” were identified in the outliers scoring $\geq - 3.5$ or $+ 3.5$ z-scores.

The identified hits were 31; Rin 1, Use 1, Rin 2 and Copa knock downs gave Z-scores very high compared to the rest of the distribution (Figure 78 a). Images of the correspondent cells (Figure 78 b) show how the fluorescence intensity of the peptide is much higher compared to the negative control cells (transfected with non-targeting siRNAs); especially in the case of Rin1, where the peptide completely saturated the cell cytoplasm. The predictive interactions between them could be observed in Figure 79 The representation was built using STRING 10.5 database (<https://string-db.org/>).



(b)

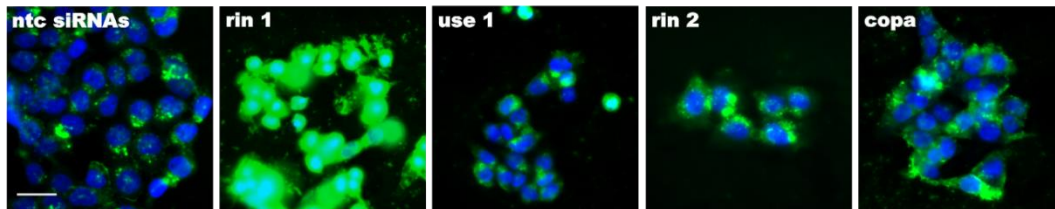


Figure 78. Z-scores distribution and string map of putative hits genes. The robust Z-score method was used to normalise the data obtained from independent replicates. In (a) there is the graphical representation of the RNAi screen output with the distribution of Z-scores across the whole library. In (b) there are images of cells in which Rin 1, Use 1, Rin 2 and Copa were knocked down. The level of green FITC fluorescence intensity were much higher compared to the control (non-targeting siRNAs). Hoechst 33342 (2 $\mu\text{g/ml}$) (blue) was used as nuclear staining. Bar = 25 μm . All the images are scaled at the same size.

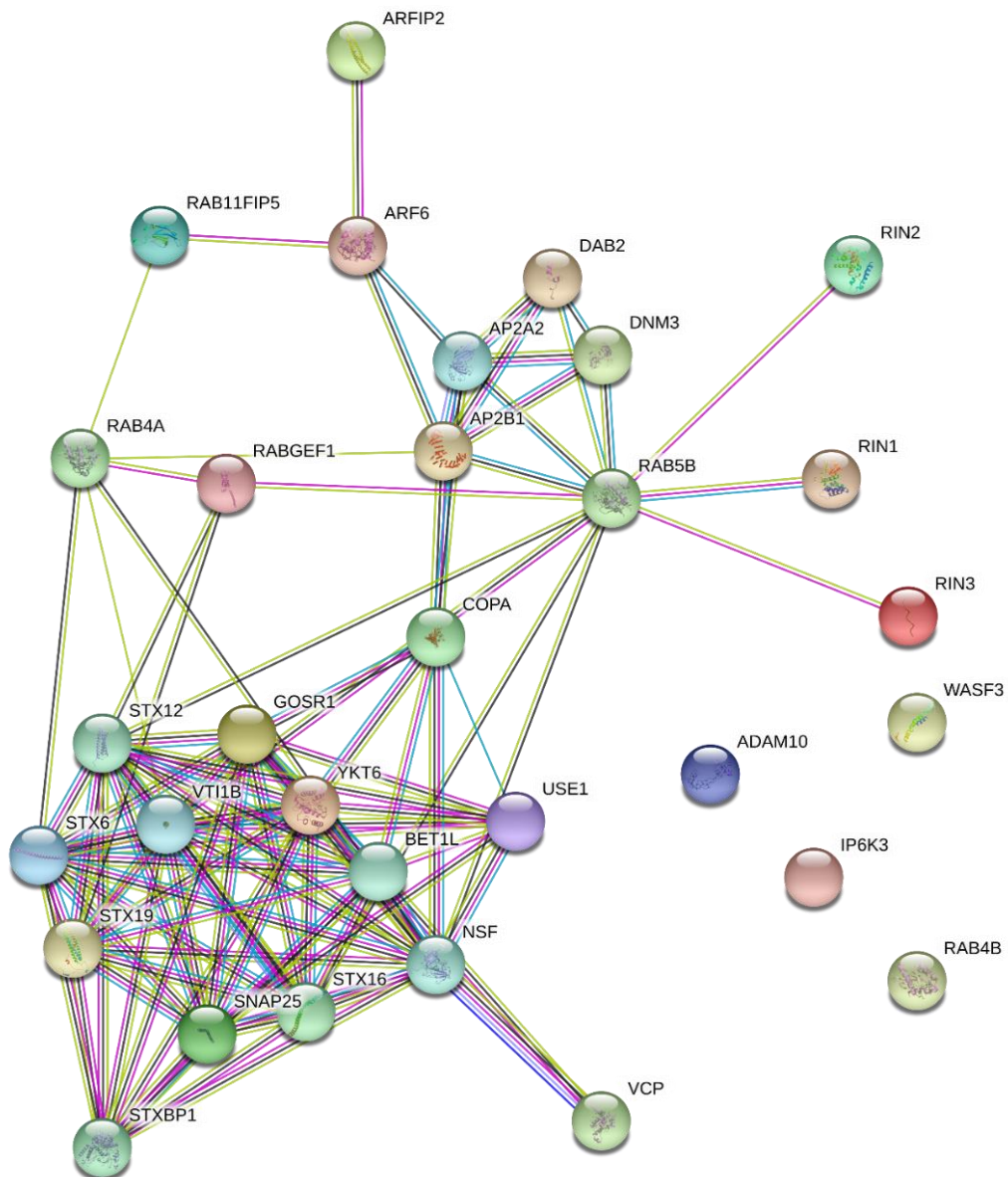


Figure 79. Schematic representation interactions between the hits found in the screen. String 10.5 was used to create the hit interaction map. The majority of the genes found as hits are interconnected with each other forming an intricate net which could be divided in two main clusters; one related to the vesicles trafficking to and from the Golgi network and one associated with the early endosome and vesicles recycling. The lines were created according to text mining (yellow), experiment results (pink) or online databases (blue).

The hits can be divided in two big interconnected clusters; one related with endocytic recycling pathways and the other regarding vesicles transport between secretory compartments but mainly associated with the Golgi network. Excluded from these groups there are only three genes; IP6K3 which encodes for the Inositol hexaphosphate kinase 3, a protein that regulates inositol phosphate-stimulated vesicle formation and trafficking ²⁹⁶; ADAM10 that encodes for a sheddase, metallopeptidase which cleaves membrane proteins at the cellular surface ²⁹⁷ and WASF3 that encodes for Wiskott-Aldrich syndrome protein family member 3, a protein that plays a crucial role in actin polymerization through the activation of the actin-related protein (Arp) 2/3 complex and it is required for filopodia formation and cell motility ²⁹⁸.

Associated with the recycling pathways cluster there are Rin 1, Rin 2, and Rin 3 which have all been found with high z-scores. These proteins are Guanine Nucleotide Exchange Factors (GEFs) for Rab proteins and are involved in many biological functions including cell growth, differentiation and endocytosis receptor mediated ²⁹⁹. Several components of the Rab family, the largest group of Ras superfamily of monomeric G proteins generally involved in vesicle trafficking were found as hits: Rab 5b, Rab GEF1, Rab 4a, Rab 4b and Rab 11FIP5 specifically involved in the kinetics of membrane trafficking in the early endocytic pathway, and in the regulation of both rapid and slow endocytic recycling ³⁰⁰⁻³⁰³. Interestingly, Arf 6, involved in many biological functions including membrane trafficking and endosomal recycling, was already identified as a hit from the pilot screen, performed prior to the main one. ARFIP2 a gene that encodes for ADP Ribosylation factor interacting protein 2 (or Arfapti-2) involved in mediating cross-talk between Rac (a member of the Rho family) and Arf 1 or Arf 6 was found with a positive z-score as well ¹⁵⁹.

The majority of hits fell in another big cluster which contains proteins more generally involved in vesicular trafficking, especially to and from the Golgi Network. The hits Bet 1-like, Gosr 1, Snap 25, Syntaxins 6, 12, 16 and 19, Use 1, Vtib and Ykt 6 are all Soluble N-ethylmaleimide-sensitive factor attachment protein (SNAP) receptors (SNAREs), involved in targeting and fusion of Golgi-ER derived anterograde, retrograde and and intra-Golgi vesicles transport ³⁰⁴⁻³¹¹. The Syntaxin binding protein (or Munc 18-1) encoded by STXBPI gene was considered a hit; this protein is an essential exocytotic vesicle trafficking protein which strongly interacts with Syntaxins.

In the same cluster there is also the N-ethylmaleimide-sensitive factor (NSF), homo-hexameric ATPase indispensable for numerous intracellular fusion processes ³¹², and Coatamer subunit α , part of a cytosolic protein complex (coatamer) required for membrane trafficking of coated vesicles in the Golgi-ER (ER) retrograde transport ³¹³.

Other few hits genes were related to the clathrin-dependent endocytosis, including AP2A2, AP2B1, DAB2 and DNM3. The presence of these hits gave positive confirmation that the RNAi screen effectively worked. Adaptor related protein complex 2 subunit alpha 2 and adaptor related protein complex 2 subunit beta are components of the adaptor protein complex 2, involved in cargo selection ¹⁵⁶. Disabled homolog 2 is an endocytic adaptor protein implicated in clathrin-mediated endocytosis and cargo trafficking in eukaryotes ³¹⁴ while Dynamin 3 is a large GTP-ase associated with microtubules and involved in membrane fission events mainly associated with clathrin-mediated endocytosis ³¹⁵.

Valosin-containing protein (VCP), instead, also known as ATPases associated with diverse cellular activities (AAA+) or ATPase p97, performs various biological functions; included protein degradation, DNA repair, DNA replication, cell cycle regulation, membrane fusion and biogenesis of ER, Golgi and lysosomes and regulation of the Endoplasmic reticulum-associated degradation (ERAD) pathway ³¹⁶. The ERAD allow the retrotranslocation of failed folded proteins from the ER into the cytosol to be further degraded by the proteasome ³¹⁷.

6.3 RNAi mini-screen with FITC-A₉K

To establish whether there are differences between the two peptides used in this thesis FITC-A₉K was screened investigating FITC-A₉K internalisation pathway. Selected genes were knocked down using RNAi and cells were exposed to a fixed concentration of peptide according to the procedure previously explained. Adaptor related protein complex 2 subunit alpha 2 (AP2A2), adaptor related protein complex 2 subunit beta (AP2B1), actin related protein 2/3 complex subunit 1 B (ARPC1B), clathrin light chain a (CLTA), clathrin light chain b (CLTB) and clathrin heavy chain (CLTC) siRNAs were selected to knock down the corresponding gene expression. The siRNAs were from SiGenome collection of design siRNAs from Dharmacon (see Table 5 for information regarding the genes IDs and functions). All these genes, with the exclusion of ARPC1B, are strictly related with the clathrin-dependent endocytic pathway.

Table 5. List of the genes for which siRNAs were selected in the mini-screen for FITC-A₉K peptide. Gene name, NCBI's database gene ID and gene function are provided.

Gene	ID	Function
AP2A2	161	Components of the adaptor protein complex 2, which is involved in cargo selection in the clathrin-dependent endocytosis ¹⁵⁶
AP2B1	163	
ARPC1B	10095	Subunit of the human Arp2/3 protein complex which is involved in the regulation of actin polymerization ¹⁵⁷
CLTA	1211	Clathrin light and heavy chain proteins components of a polyhedral structure of coated pits and vesicles which entraps specific molecules during receptor-mediated endocytosis ¹⁵⁸
CLTB	1212	
CLTC	1213	

Clathrin is a protein involved in coating vesicles, which are then endocytosed from the plasma membrane into endosomes. Clathrin is composed of three heavy chains and three light chains that rearrange in a typical triskelion shape. Humans possess two isoforms of clathrin heavy chain, Chc17 and Chc22, but only Chc17 is involved in membrane trafficking. Chc22 is expressed in skeletal muscle and has been reported to have a role in membrane organisation. Chc17 and Chc22 are encoded by CLTC and CLTD genes that share 85% of amino acid similarity. Moreover, CLTA and CLTB genes encode the only two clathrin light chains found in humans (a and b) which are

both involved in endocytosis and have 60% amino acid identity. When clathrin triskelion nucleate they form a polyhedral lattice (hexagonal or pentagonal) that surrounds vesicles and allows their transportation into the cell ¹⁵⁸.

The clathrin cages alone are not able to bind the membranes but they need specific adaptor protein complexes to do so. There are 5 different adaptor protein complexes (AP-1/5) which mediate intracellular endocytic membrane trafficking and secretory transport pathways but only AP-1, AP-2 and AP-3 are associated with clathrin. Each complex is composed by two large subunits (one each of $\gamma/\alpha/\delta/\epsilon/\zeta$ and β 1-5, respectively), one medium-sized subunit (μ 1-5) and one small-sized subunit (σ 1-5) ³¹⁸. AP-2 contains α -, β 2-, μ 2-, and σ 2-subunits and localises on the plasma membrane. It is involved in the clathrin-dependent endocytosis of many molecules included receptors, adhesion molecules. The large α - subunit binds to PIP₂ (phosphatidylinositol (4,5)-bisphosphate), positioning AP-2 on the membrane, while the other large subunit β 2- binds to the terminal domain of Chc17 promoting the lattice assembly. The cargo proteins are recognised and bound by the medium μ 2- subunit. The small subunit σ 2- instead seems to have more a structural role ¹⁵⁶. ARPC1B encodes for one of the seven subunits Arp2/3 complex, which is involved in the regulation of the actin filaments polymerisation. Arp2/3 complex is crucial for a variety of the eukaryotic cellular processes related with the actin cytoskeleton; including cell migration, endocytosis, vesicles trafficking and cytokinesis ¹⁵⁷.

To investigate whether the endocytic genes are involved in the peptide uptake, an siRNA knock down mini-screening experiment was done. Red fluorescent siGLO (Dharmacon) was selected as positive control for the transfection efficiency while 5 non-targeting siRNAs (On-TARGET plus non-targeting control #1, #2, #3, #4 and Non-targeting pooled - all 4 siRNAs) were selected as negative controls.

Procedures for knock down and the assay are as before and once the cells were fixed and stained using the standard fixation protocol, a cell count analysis was performed to evaluate the cells health and ensure that the transfection with non-targeting siRNAs (negative controls) did not cause a decrease in cell viability. Cells were counted using the MetaXpress® Software 5.0.0.20 that recognizes the Hoechst stained nuclei. The results are shown in Figure 80. Panel (a) shows data from the negative control siRNAs. None of the non-targeting siRNAs gave cellular toxicity. Figure 80 (b) shows the cell

counts from the functional siRNAs. None of the chosen siRNAs induced a significant decrease in cell growth. Transfection using the red fluorescent siGLO did not decrease cell viability with a value of 92% compared to the negative control (data not shown).

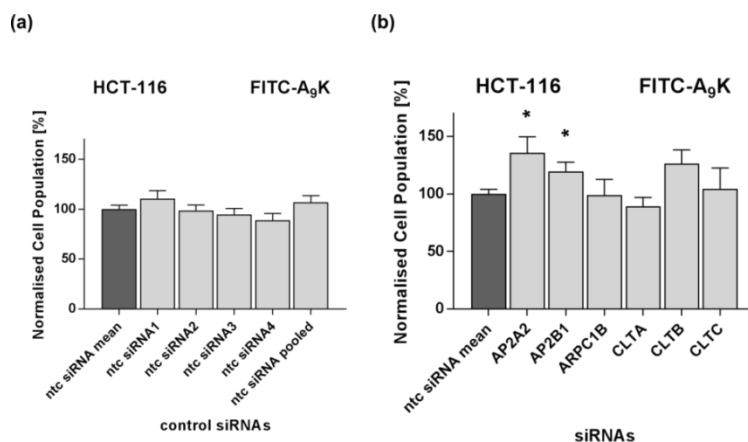


Figure 80. HCT-116 cell number evaluated with high-content microscopy after RNAi and FITC-A₉K exposure. Cells were transfected with (a) non-targeting siRNAs; (b) endocytosis-related siRNAs for three days, exposed to the peptide for another day then fixed in formaldehyde and stain with Hoechst 33342 (2 µg/ml) to reveal the nuclei. Images were acquired using ImageXpress® Micro microscope and cell number was counted using the Multi Wavelength Scoring algorithm within the MetaXpress® software. The results are expressed as a percentage of number of cells normalized to the negative control (mean of the 5 non-targeting siRNAs). The values obtained are averages of independent experiments ± standard error mean (±SEM). Statistically significant differences from the negative control were determined by Student's t-test (*p<0.05).

Once established that the siRNAs were not toxic, the integrated intensity of the peptide fluorophore, FITC, was measured using High Content Microscopy. If endocytosis is involved in the peptide uptake, the RNAi knock down of the selected target mRNA will cause a significant reduction in peptide FITC signal inside the cells. The results of the quantitative analysis of the total FITC fluorescence intensity per cell are graphically expressed in Figure 81 (a) and represented as a percentage compared to the negative controls of total FITC fluorescence. It is possible to observe, when the cells were transfected with the functional siRNAs the amount of peptide internalised drastically

dropped by 70% or more, suggesting that endocytosis and possibly the clathrin-mediated one plays a crucial role in the A₉K internalisation. Images of the cells following siRNA transfection and peptide exposure (Figure 81 b) confirmed poor A₉K uptake, especially compared to cells transfected with non-targeting siRNAs.

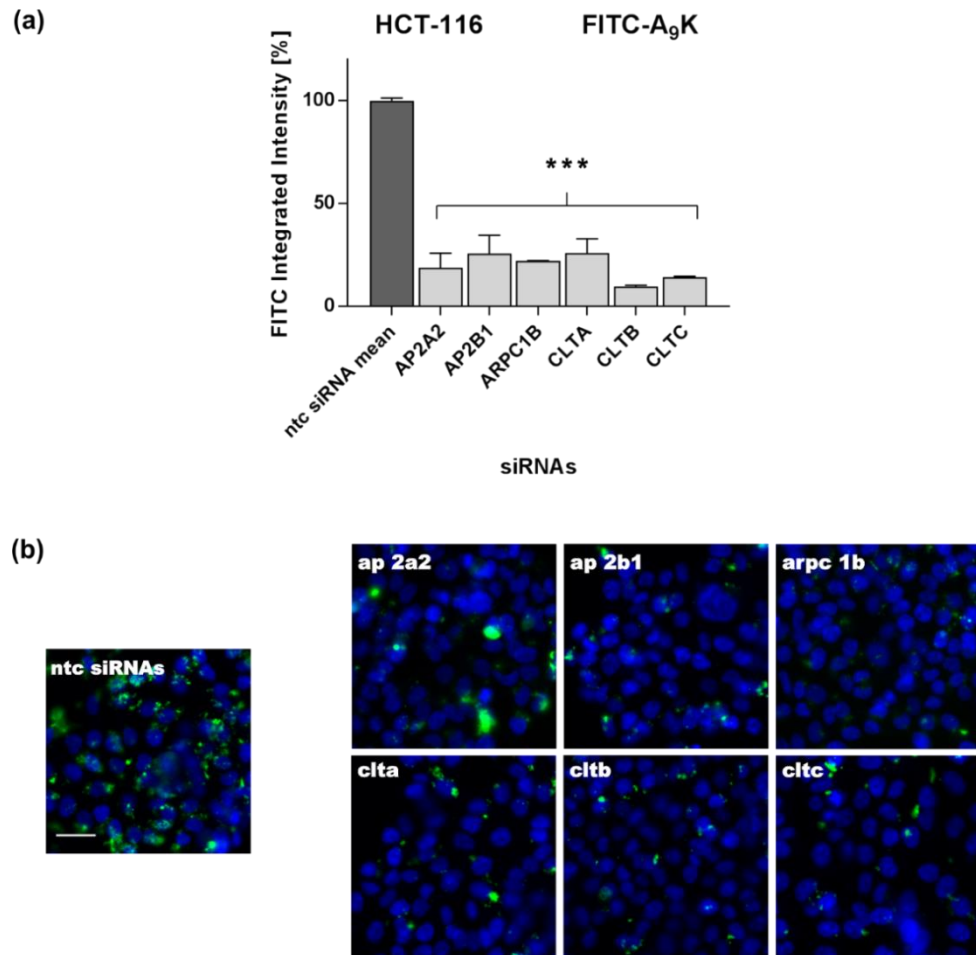


Figure 81. Variation in the fluorescence intensity evaluated with high-content microscopy in HCT-116 cancer cells after RNAi and FITC-A₉K exposure. Cells were transfected with siRNAs for three days, exposed to the peptide for another day then fixed in formaldehyde. A quantitative analysis of the green FITC fluorescence (a) was performed, the results expressed as a percentage of FITC Integrated Intensity and normalised to the negative control (mean of the 5 non-targeting siRNAs). The values obtained are averages of independent experiments \pm standard error mean (\pm SEM). Statistically significant differences between non-targeting and targeting siRNA transfections were determined by Student's t-test (** $p < 0.001$). In (b) images showing the distinct levels of FITC intensity related to the different genes knocked down. Hoechst 33342 (2 μ g/ml) (blue) was used as nuclear staining. Bar = 25 μ m. All the images are scaled at the same size.

Table 6. List of genes in ASD2 siRNA library. Gene names and IDs provided.

Gene	ID	Gene	ID	Gene	ID	Gene	ID
ACTR2	10097	CSNK1G1	53944	MYO5A	4644	PRKG1	5592
ADP-GK	83440	DGKB	1607	MYO5B	4645	PSKH1	5681
AK1	203	DNM2	1785	MYO5C	55930	PTK9	5756
AK7	122481	DYRK4	8798	NAGK	55577	RAB7A	7879
ALS2CR7	65061	EEF2K	29904	NEK11	79858	RIOK1	83732
ANKK1	255239	EPHA10	284656	NEK4	6787	RIOK2	55781
ARF6	382	EPHA5	2044	NME5	8382	RIPK2	8767
AURKC	6795	ERK8	225689	NPR2	4882	RPS6KA4	8986
BMP2K	55589	ETNK1	55500	PAPSS2	9060	RPS6KB2	6199
CALM1	801	FGFR3	2261	PCTK3	5129	SGK2	10110
CAV1	857	FLJ32685	152110	PDGFRL	5157	SNF1LK	150094
CAMK2G	818	FRAP1	2475	PDK2	5164	SNRK	56861
CAMKIINALPHA	55450	GOLGA5	9950	PFKP	5214	SRC	6714
CAMKK2	10645	GUCY2D	3000	PFTK1	5218	STK17B	9262
CDC7	8317	HCK	3055	PHKB	5257	STK24	8428
CKMT1B	1159	IRAK1	2654	PIK3CA	5290	STK25	10494
CKS1B	1159	IRAK4	51135	PIK3CG	5294	TNNI3K	51086
CKSC1B	1163	ITPKC	80271	PRKAA1	5562	TRIO	7204
CLK1	1195	KIAA1361	57551	PRKCE	5581	TRPM6	140803
CLTC	1213	KIAA1639	57729	PRKCL1	5585	URKL1	54963

Table 7. List of genes in the Traffic-ome siRNA library. Gene names and IDs provided. In bold the hits found with the RNAi screen.

Gene	ID	Gene	ID	Gene	ID	Gene	ID	Gene	ID	Gene	ID	Gene	ID
ACTR2	10097	ARPC1B	10095	CBLC	23624	EPN1	29924	ITSN2	50618	PIK4CA	5297	RAB7B	338382
ACTR3	10096	ARPC2	10109	CDC42	998	EPN2	22905	LIMK1	3984	PIP5K1A	8394	RAB7L1	8934
ADAM10	102	ARPC3	10094	CFL1	1072	EPN3	55040	MAP1LC3A	84557	PSCD3	9265	RAB8A	4218
ALS2	57679	ARPC4	10093	CIB1	10519	EPS15	2060	MAP4K2	5871	RAB11A	8766	RAB8B	51762
AMPH	273	ARPC5	10092	CIB2	10518	EPS15L1	58513	MAPK8IP1	9479	RAB11B	9230	RABEP1	9135
ANKFY1	51479	ARRB1	408	CIB3	117286	EXOC6	54536	MAPK8IP2	23542	RAB1A	5861	RABGEF1	27342
AP1B1	162	ARRB2	409	CLTA	1211	EXOC7	23265	MAPK8IP3	23162	RAB2	5862	RAC1	5879
AP1M1	8907	ATG12	9140	CLTB	1212	FLOT1	10211	MICAL1	64780	RAB21	23011	RAPH1	65059
AP1M2	10053	ATM	472	CLTC	1213	FYN	2534	MYO5A	4644	RAB22A	57403	RBSN	64145
AP2A1	160	ATP6V0A1	535	CLTCL1	8218	GAF1	26056	MYOVB	4645	RAB31	11031	RHOA	387
AP2A2	161	BECN1	8678	COPA	1314	GAPVD1	26130	MYO5C	55930	RAB3A	5864	RIN1	9610
AP2B1	163	BET1	10282	DAB2	1601	GIT1	28964	NEDD4	4734	RAB3B	5865	RIN2	54453
AP2M1	1173	BET1L	51272	DDEF2	8853	GOPC	57120	NEDD4L	23327	RAB3C	115827	RIN3	79890
AP3D1	8943	BIN1	274	DIAPH1	1729	GORASP1	64689	NSF	4905	RAB3D	9545	ROCK1	6093
AP4E1	23431	BNIP1	662	DNM1	1759	GOSR1	9527	OCRL	4952	RAB4A	5867	ROCK2	9475
APPL1	26060	C13ORF9	51028	DNM2	1785	GOSR2	9570	PACSIN1	29993	RAB4B	53916	SARA1	56681
APPL2	55198	CAMK1	8536	DNM3	26052	GRB2	2885	PACSIN3	29763	RAB5A	5868	SCFD1	23256
ARF1	375	CAV1	857	EEA1	8411	HGS	9146	PAK1	5058	RAB5B	5869	SEC13L1	6396
ARF6	382	CAV2	858	EFS	10278	HIP1	3092	PDCD6IP	10015	RAB5C	5878	SEC22A	26984
ARFIP2	23647	CAV3	859	EHD1	10938	HIP1R	9026	PICALM	8301	RAB6A	5870	SEC22B	9554
ARHGAP26	23092	CBL	867	ELKS	23085	IP6K3	117283	PIK3C2G	5288	RAB6B	51560	SEC22C	9117
ARHGDI A	396	CBLB	868	ENTH	9685	ITSN1	6453	PIK3CG	5294	RAB7A	7879	SH3GL2	6456

Gene	ID	Gene	ID	Gene	ID	Gene	ID	Gene	ID	Gene	ID	Gene	ID
SH3GLB1	51100	SNX9	5148	STX8	9482	STXBP2	6813	TSG101	7251	VAPA	9218	VTI1A	143187
SH3GLB2	56904	STAU	6780	STX10	8677	STXBP3	6814	USE1	55850	VAPB	9217	VTI1B	10490
SNAP23	8773	STX1A	6804	STX11	8676	STXBP5L	9515	VAMP1	6843	VAV2	7410	WAS	7454
SNAP25	6616	STX2	2054	STX12	23673	STXBP6	29091	VAMP2	6844	VCP	7415	WASF1	8936
SNAP29	9342	STX3	6809	STX16	8675	SYNJ1	8867	VAMP3	9341	VIL2	7430	WASF2	10163
SNAP47	116841	STX4	6810	STX17	55014	SYNJ2	8871	VAMP4	8674	VPS33A	65082	WASF3	10810
SNAP91	9892	STX5	6811	STX18	53407	SYT1	6857	VAMP5	10791	VPS33B	26276	YKT6	10652
SNX1	6642	STX6	10228	STX19	415117	SYT2	127833	VAMP7	6845	VPS45	11311		
SNX2	6643	STX7	8417	STXBP1	6812	TNIK	23043	VAMP8	8673	VPS4A	27183		

7 DISCUSSION AND CONCLUSIONS

7.1. Introductory background

Cancer is one of the leading causes of death worldwide and, according to the World Health Organisation (WHO), in 2015 it was responsible for almost 9 million deaths, second only to ischaemic heart diseases and strokes, which together caused the death of nearly 15 million people (<http://www.who.int/topics/cancer/en/>). The National Cancer Institute, one of the eleven agencies of the U.S. Department of Health and Human Services, in its annual report predicted that in 2017 there will be almost 2 million new diagnosed cases and 600'000 deaths in the US alone ³¹⁹.

With these numbers, it is not a surprise to read that in the last decades many efforts have been made to find a successful approach to cure cancer. The standard strategies, especially when surgery is not an option, are chemotherapy and radiotherapy. Unluckily, these procedures are often ineffective and give severe short- and long-term side effects due to the lack of cell-selectivity ³²⁰.

Novel cancer therapies have been proposed with the aim of improving the selectivity towards the malignant cells and, at the same time, to minimise the side effects. Targets of these new approaches are the so called “hallmarks of cancer”; specific characteristics that favour the tumour development, growth and metastasising. These include sustained proliferative signalling, evasion of growth suppressors, induced angiogenesis, genomic instability and evasion of immune detection and destruction ³²¹.

Examples are the immunotherapies such as antibodies or personalised cancer vaccines which in the recent years, have been object of intensive study ³²². The main purpose of these therapies is to boost the immune system’s ability to target and destroy cancer cells. Cancer vaccines are designed to stimulate T-cells to target antigens normally overexpressed in cancer cells called tumour-associated antigens (TAAs). Sipuleucel-T was the first therapeutic cancer vaccine to treat prostatic tumours to be approved by the U.S. Food and Drug Administration (FDA) in 2011. It consists of autologous dendritic

cells activated in culture and presenting the human protein PAP–GM-CSF; a recombinant fusion protein of prostatic acid phosphatase (PAP) (antigen expressed in 95% of prostate cancer) and granulocyte–macrophage colony-stimulating factor (GM-CSF), an immune cell activator ³²³. Despite a few isolated successes, cancer vaccines still remain expensive treatments that rarely produce robust therapeutic benefits, mainly due to weak immunogenicity response combined with a lack of adequate infiltration to the tumour site ³²⁴. For this reason, the use of synthetic peptides was introduced. Peptide vaccines incorporate amino acid sequences of tumour antigens; they are cheaper to manufacture, easier to synthesise and safer to handle. However, current peptide vaccines have little success in promoting tumour regression, despite producing a good grade of T-cells stimulation. Susceptibility of peptidases degradation, poor bioavailability, high elimination rate and unspecific binding to non-professional antigen-presenting cells (APC) that cause tolerances and anergy effects, are all major problems that currently are limiting the use of peptide vaccines in cancer immunotherapy ³²⁵.

The use of peptides as anticancer treatment, however, is not limited to vaccines. Indeed, many other peptide types have been studied and employed. First of all, the so called anticancer peptides (ACPs); natural or synthetic small cationic amphiphilic peptides discovered or designed for their antimicrobial effects but that also display strong anticancer properties ^{105, 115}. Peptides that exhibit both anticancer and antimicrobial effects can be divided into two categories, depending on their behaviour towards normal mammalian cells; some are indiscriminately toxic towards any type of cells (e.g. Mellitin, Defensins and human LL-37) while some others are selectively harmful only against bacteria and cancer cells (e.g. Cecropins, Magainins) ^{107, 111}.

The cancer cells specificity displayed by ACPs is not completely understood yet. Evidence suggest that the differences in composition of cancer and non-cancer cells' plasma membranes are the main reason of this behaviour; cancer cells' membranes are slightly negatively charged with more fluid due to reduced levels of cholesterol, while the normal cells' membranes are zwitterionic and enriched in cholesterol which protects them from the insertion of lytic peptides ^{105, 106, 108}.

ACPs show several modes of action to target and kill cancer cells; direct ways include plasma and mitochondrial membranes lysis or DNA and protein synthesis inhibition. ACPs can also indirectly target cancer cells via recruitment and stimulation of the innate immune response, similarly to what happens with peptide vaccines^{107, 115}. Ultimately, ACPs can also be conjugated with a variety of cargoes and, exploiting their penetration abilities, to selectively deliver in cancer cells drugs, DNA or RNA molecules to inhibit the cellular growth^{122, 326}.

Unfortunately, despite many promising studies that have been published regarding ACPs, there is still a remarkable absence of success when translated into clinical trials. The difficulties in accomplishing outstanding preclinical results may be linked to the complexity of the biological system involved, together with the partial lack of information concerning the interaction between peptides and eukaryotic cells. Further studies are necessary to elucidate what is still unclear and to improve the development of more efficient peptide-based anticancer systems.

7.2. Achievements of the project

This project was initiated with the aim of studying the effects on cancer cells of three synthetic peptides, initially designed to specifically target and kill bacteria but then found to have anticancer cell selectivity: A₆K and A₉K, two self-assembled β -sheet peptides and G(IKK)₃I-NH₂, a monomeric α -helical peptide. FITC- fluorescently labelled versions of A₉K and G(IKK)₃I-NH₂ were also included in the experimental plan.

A₆K and A₉K were part of a series of short and simple amino acid sequences composed by consecutive alanine residues, which together form the hydrophobic tail, and a positively charged lysine representing the hydrophilic head. Thanks to the interactions between the hydrophobic tails, the electrostatic repulsion between charged head and the hydrogen bonding between peptide backbones, these peptides self-assemble in aqueous solutions adopting bigger, more defined β -sheet nanostructures. A₆K forms long

nanofibers with lengths of 1 μm or more and diameter of 8 nm, while A₉K forms stable nanorods with diameters of 3 nm and lengths that do not exceed 100 nm ¹⁷⁵.

G(IKKK)₃I-NH₂ instead was part of G(IKKK)_nI-NH₂ (n=1-4), a short cationic peptide amphiphiles series containing the IKKK repeat. These peptides have the characteristic of maintain random coil conformation in aqueous solution but with the ability of adopting an amphipathic α -helical structure when interacting with negatively charged membranes. In the series, G(IKKK)₃I-NH₂ had the best antimicrobial effect and cancer cell selectivity and was therefore selected for further studies ¹¹⁷.

7.2.1 What was previously known

All the peptides used in this thesis were previously tested against strains of both Gram-positive and Gram-negative bacteria and the obtained results are summarised in Table 8. The peptide that gave the best results was G(IKKK)₃I-NH₂, followed by A₉K. A₆K by contrast had only a mild effect ^{117, 126}. The results are expressed as MIC₅₀, the lowest concentration of peptides at which 50% of the bacteria were inhibited from growing.

Table 8. Bactericidal effect of A₆K, A₉K and G(IKKK)₃I-NH₂ expressed as minimum inhibitory concentration (MIC₅₀). These peptides were the best of their groups and amongst them G(IKKK)₃I-NH₂ was the one that showed the greater antimicrobial effect. MIC₅₀ = the lowest peptide concentration at which 50% of the bacteria were inhibited.

Peptides	MIC ₅₀ (μM)			References
	<i>E. coli</i>	<i>B. subtilis</i>	<i>S. aureus</i>	
A ₆ K	320	-	160	Chen et al., ¹²⁶
A ₉ K	20	-	60	Chen et al., ¹²⁶
G(IKKK) ₃ I-NH ₂	8	2	7.5	Hu et al., ¹¹⁷

A₉K and G(IKKK)₃I-NH₂ were further selected to be tested against cancer, non-cancer cell lines and human erythrocytes. The toxicity towards eukaryotic cells was assessed with the MTT assay and the results are showed in Table 9 and Table 10. G(IKKK)₃I-NH₂ was the peptide that once again gave the best results in targeting and inhibiting the

growth of cancer cells but A₉K resulted in less toxicity against normal mammalian cells or erythrocytes^{116-118, 126, 327}.

The results in both tables are expressed as inhibitory concentration (IC₅₀) or erythrocytes lysis (EC₅₀) for cells and erythrocytes, respectively, which correspond to the peptides concentration needed to induce the 50% of cellular growth inhibition or 50% erythrocytes lysis.

Table 9. Inhibitory effect of A₉K and G(IKKK)₃I-NH₂ on different human cancer cell lines expressed as inhibitory concentration (IC₅₀). G(IKKK)₃I-NH₂ gives the higher toxicity against cancer cells. IC₅₀ = inhibitory concentration corresponding to the peptide concentration needed to induce cellular growth inhibition of 50%.

Peptides	IC ₅₀ (μM)			References
	<i>HeLa</i>	<i>HL60</i>	<i>HepG2</i>	
A₉K	60	100	-	Chen et al., ¹²⁶ Xu et al., ¹¹⁶
G(IKKK)₃I-NH₂	15	25	25	Hu et al., ¹¹⁷ Chen et al., ^{118, 327}

Table 10. Inhibitory effect of A₉K and G(IKKK)₃I-NH₂ on different normal mammalian cell lines expressed as inhibitory concentration (IC₅₀) or erythrocytes lysis (EC₅₀). A₉K's results showed it to be the safer peptide. IC₅₀ = inhibitory concentration corresponding to the peptide concentration needed to induce cellular growth inhibition of 50%. EC₅₀ = haemolytic activity of human erythrocytes expressed as EC₅₀ and corresponding to the peptide concentration needed to cause the lysis of 50% of erythrocytes.

Peptides	IC ₅₀ (μM)			EC ₅₀ (μM)	References
	<i>NIH 3T3</i>	<i>Cos 7</i>	<i>HDFa</i>		
A₉K	> 240	> 240	-	600	Chen et al., ¹²⁶ Xu et al., ¹¹⁶
G(IKKK)₃I-NH₂	-	-	>100	256	Hu et al., ¹¹⁷ Chen et al., ^{118, 327}

7.2.2 The peptides and their impact on the cells' metabolism and proliferation

This PhD project started with the idea of focusing in more detail on the interactions between the peptides and cancer cells; A₆K, which had not previously tested was included as well. The results obtained have been explained in detail in the previous chapters but will be briefly summarised here. The effect of the peptides on different cell lines, cancer and non-cancer was evaluated. A₆K and A₉K were tested on A431, epithelial human cancer cells and HDFs, human dermal fibroblasts using the MTT assay. A concentration range between 6.25 and 100 µM was chosen while 24, 48 or 72 hrs were selected as exposure times. Table 11 shows the IC₅₀ calculated at each experimental time-point. A₆K peptide, with an average IC₅₀ of 50 µM showed more consistence in inhibiting the metabolism of A431 compared to A₉K, which, for the first two time-points did not induce any toxic effect. A₉K induced a significant decrease in MTT reduction after 72 hrs exposure and the IC₅₀ calculated was 28 µM. Both peptides showed no harm towards the fibroblasts, and for the tested concentrations it was not possible to extrapolate an IC₅₀.

Table 11. Metabolic inhibitory effect of A₆K and A₉K evaluated in A431 epithelial cancer cells and HDFs human fibroblasts. A₆K was the peptide that gave the best results against cancer cells. Both peptides were found to be non-toxic towards fibroblasts. The graphs showing all the results can be find in Chapter 3, section “3.2.1 MTT assay”. IC₅₀ = inhibitory concentration corresponding to the peptide concentration needed to induce cellular growth inhibition of 50%.

Peptides	IC ₅₀ (µM)					
	A431			HDFs		
	24 hrs	48 hrs	72 hrs	24 hrs	48 hrs	72 hrs
A ₆ K	40	52	45	>100	>100	>100
A ₉ K	>100	>100	28	>100	>100	>100

Normally it is possible to estimate the cellular viability via comparison of the MTT assay absorbance values with the number of cells present in a plate. However, for the experiments just described, no visible changes in the cell number between the different

experimental conditions were observed. For this reason, a more precise quantification of the cell number was done; the experiment was repeated without adding the MTT in the final step but instead cells were fixed in formaldehyde and stained with Hoechst. A cell count was performed using high content microscopy and an algorithm written to recognise nuclear stain (Figure 23). The results confirmed what was anticipated; the cell number did not significantly vary when the A431 were exposed to different concentrations of peptides. Consequently, no IC_{50} was calculated. Later, when FITC-A₉K was used, the fluorescent version of A₉K, a similar cell count experiment was performed, and the results obtained were consistent with the ones of the standard peptide (Figure 23).

The selectivity of G(IKKK)₃I-NH₂ towards cancer cells was tested using HCT-116 colon cancer cells while the HDFs fibroblasts were chosen once again as a non-cancer model. The concentration range and the exposure times were the same used for the previous peptides, but a cell count was directly performed this time. For the fluorescently labelled FITC-G(IKKK)₃I-NH₂, 24 hrs only were chosen as the exposure time. The relative IC_{50} were calculated and are summarised in Table 12. G(IKKK)₃I-NH₂ significantly decreased the cell number of HCT-116 cells at all time-points and an average IC_{50} of 50 μ M per time was calculated. No evident decrease in cell number was observed against the fibroblasts. Interestingly, FITC-G(IKKK)₃I-NH₂ results showed more sensitivity towards fibroblasts and an IC_{50} of 86 μ M was found. Against the cancer cells it maintained a similar level of sensitivity and the corresponding IC_{50} was 60 μ M.

Table 12. Effects on cell viability of G(IKK)₃I-NH₂ and FITC-G(IKK)₃I-NH₂ evaluated in HCT-116 colon cancer cells and HDFs human fibroblasts. Both G(IKK)₃I-NH₂ and its fluorescently labelled version had an effect on cancer cells and significantly decreased the cell number. Against fibroblasts, only FITC-G(IKK)₃I-NH₂ had a slight toxic effect. The graphs showing all the results can be find in Chapter 4, section “4.2.1 Cell counting assay as evaluation of peptide toxic effect”. IC₅₀ = inhibitory concentration corresponding to the peptide concentration needed to induce cellular growth inhibition of 50%.

Peptides	IC ₅₀ (μM)					
	HCT-116			HDFs		
	24 hrs	48 hrs	72 hrs	24 hrs	48 hrs	72 hrs
G(IKK) ₃ I-NH ₂	56	50	43	>100	>100	>100
FITC-G(IKK) ₃ I-NH ₂	60			86		

After the results obtained with A₆K and A₉K peptides, it was clear that both peptides were interfering with the A431 cellular metabolism but without inducing cell death.

The MTT tetrazolium salt reduction occurs intracellularly, mainly by mitochondrial enzymes and in small part also in endosomal and lysosomal vesicles^{140, 141, 208, 211}. It was hypothesised that the peptides were interacting with the mitochondria preventing them from functioning correctly. For this reason, two different fluorescent dyes were used to stain live mitochondria; MitoTracker® Red CMXRos and JC-1 (Thermo Fisher Scientific)^{143, 212}. A431 cells were exposed to three different concentrations of peptides (6.25, 25 and 100 μM) and stained with MitoTracker® Red CMXRos after 72 hrs exposure or with JC-1 after 24-48 hrs exposure (from Figure 26 to Figure 31). MitoTracker® Red CMXRos gives information about the mitochondria morphology while JC-1, since it fluoresces differently depending on the fluctuations of the mitochondrial membrane potential ($\Delta\psi_m$), gives useful information regarding the mitochondrial health²¹⁵. The data collected from both staining showed that mitochondria changed their morphology from large interconnected networks to fragments circularly shaped and their $\Delta\psi_m$ was less negative, causing the membranes' depolarisation. These two phenomena can be associated with unhealthy mitochondria and damaged cells³²⁸. MitoTracker® Red CMXRos staining was performed as well on

HCT-116 colon cancer cells exposed to 6.25, 12 or 25 μM of FITC-A₉K for 48 hrs and gave results comparable to its standard version.

7.2.3 Could the peptides have a role as delivery vectors of nucleic acids molecules?

Due to their cationicity A₆K, A₉K and G(IKKK)₃I-NH₂ could, at least on paper, all be able to bind negatively charged molecules. Therefore, their complexing ability with DNA or RNA molecules was examined to evaluate a possible usage as transfection vectors. Initially complexes at different cationic/anionic charge ratios (0.5/1; 1/1; 2/1; 3/1 and 5/1) of A₆K and A₉K were made with FAM-labelled oligonucleotides (ODNs) and visualised using the gel electrophoresis technique (Figure 1). The results showed that A₆K surprisingly did not bind the DNA molecules, while A₉K was bound to the DNA in a dose-dependent manner (Figure 82).

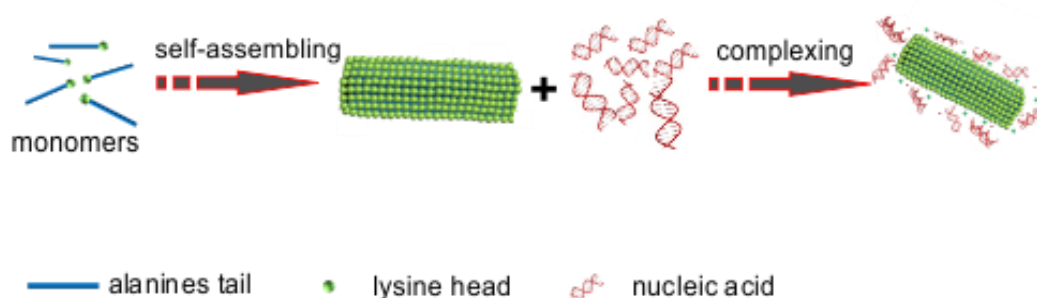


Figure 82. Schematic representation of A₉K self-assembling and interacting with nucleic acid molecules. (redrawn from data published by Chen et al.,¹²⁶). The positive hydrophilic lysine representing the peptide head is shown in green while the tail, composed by consecutives hydrophobic alanines, is shown in blue. Due to their hydrophilic nature, the lysines are exposed on the molecule surface and allow the interaction with the negatively charges phosphate groups of the nucleic acids. The alanines due to their hydrophobicity are buried instead in the core of the molecule.

A₉K and G(IKKK)₃I-NH₂ abilities in transfecting cancer and non-cancer cell lines were evaluated using high content microscopy. 0.05 $\mu\text{g}/\text{ml}$ of FAM-labelled ODNs were initially chosen to be transfected in A431 and HDFs cells. Charge ratios between 0.1/1

and 3/1 were selected while transfection with Oligofectamine (Life Technologies) was added as positive control. The results showed a clear selectivity of both A₉K (Figure 2) and G(IKKK)₃I-NH₂ (Figure 32) for cancer cells where many fluorescent puncta could be observed correctly internalised in the cytoplasm. In the fibroblasts, the transfection efficiency was in contrast quite poor (Figure 5 and Figure 33). Moreover, when high concentrations of A₉K were used (2/1 and above), the peptide/nucleic acids complexes were visible as big agglomerates, mainly localised externally of the cellular membranes. On the other hand, with G(IKKK)₃I-NH₂, no matter which concentration was selected, the fluorescent ODNs always appeared as small distinct puncta. Subsequently, A₉K and G(IKKK)₃I-NH₂ were complexed with 75 nM of fluorescently labelled siRNA molecules (red siGLO, Dharmacon) and transfected in A431, HCT-116 cancer cells or HDFs. Charge ratios between 0.1/1 and 3/1 were selected while transfection with DharmaFECT1 (DF1, Dharmacon) was added as a positive control. As happened with the ODNs, both peptides showed selectivity for the cancer cells and many red puncta were internally localised in the cells (Figure 6, Figure 34 and Figure 35). In fibroblasts, the transfection efficiency stayed poor, especially when compared to DF1 (Figure 9 and Figure 35). Fluorescently labelled FITC-A₉K and -G(IKKK)₃I-NH₂ complexing and transfection abilities were tested as well using the red siGLO and the HCT-116 colon cancer cells. The results showed good transfection efficiency of both peptides and, depending on the concentration used, yellow puncta were observed as consequence of the red and green fluorescent signals overlapping, indicating the co-localisation in the same cellular compartment of siRNA molecules and fluorescent peptides (Figure 14 and Figure 38).

A₉K and G(IKKK)₃I-NH₂ were employed as well in transfecting 3D spheroids cancer cellular models. A431 were originally selected and transfected with 75 nM of red fluorescent siGLO and 2/1 or 5/1 peptides ratios. However, due to the frailty and irregular morphology of the A431 spheroids, HCT-116 were selected and used afterwards. Spheroids generated from the colon cancer cells were compact solid spherical masses with an average diameter of 600-800 µm. DF1 was once again used as positive transfection reagent. The spheroids were imaged using wide-field fluorescent and light-sheet fluorescence microscopes. Light-sheet microscopy is more ideal for bigger samples like spheroids and, moreover, allows the collection of multiple stacks to generate 3D images ¹⁹⁴. The light-sheet images revealed that both peptides could

transfect the spheroids deeper than DF1, reaching the core of the masses. DF1 instead, was able to give only a superficial transfection showing the red siGLO puncta localised exclusively on the outer surface (Figure 12, Figure 13 and Figure 40).

With G(IKKK)₃I-NH₂, a co-culture experiment was performed as well to prove its selectivity for cancer cells; HCT-116 and HDFs fibroblasts were seeded together in a plate. Transfection of 50 nM of red siGLO was performed using the peptide at different charge ratios (from 0.5/1 to 3/1) or with DF1 as positive control. The results illustrated in Figure 37 showed how, when the peptide was used as delivery vector, the red fluorescent siGLO was prevalently localised in the cancer cells while with DF1 both cell types had equally amounts of siRNA.

Following these promising results, it was decided to test the ability of A₉K, G(IKKK)₃I-NH₂ and their fluorescently labelled versions to transfect functional siRNAs in both A431 and HCT-116 cancer cell lines. 30 nM of ECT2 (Epithelial Cell Transforming 2 Oncogene) or Polo-Like Kinase 1 (PLK1) were therefore transfected using different ratios of peptides (between 0.5/1 and 10/1). The commercial reagent DF1 was employed as a positive control. ECT2 and PLK1 are two genes encoding for proteins involved in several cellular functions regarding the cell cycle progression and the mitotic phase^{195, 197}. These genes are often overexpressed in cancers and their depletion causes a dramatic inhibition in the cellular proliferation and induces cell apoptosis^{136-138, 198-202}. The transfections of either ECT2 or PLK1 siRNAs, performed with A₉K or FITC-A₉K did not allow a successful knock down at any of the used ratios (Figure 15 and Figure 16) and the number of cells did not vary from the control. The transfection using DF1 by contrast regularly worked. On the other hand, when G(IKKK)₃I-NH₂ and FITC-G(IKKK)₃I-NH₂ were used as delivery vectors, a good level of knock down was assessed for both ECT2 and PLK1 siRNAs and the cell population decreased accordingly (Figure 41 and Figure 42). For PLK1, the peptide's transfection efficiency resulted even better than with the commercial DF1. The reasons of such a different behaviour between A₉K and G(IKKK)₃I-NH₂ peptides in modulate gene expression are probably related to their secondary structure and ability in self-assemble or not; A₉K is a β -sheet peptide which self assembles in nanorods of several nanometres length while G(IKKK)₃I-NH₂ stays in monomeric form and adopts an alpha helical structure only in presence of a negatively charged molecules (or membranes).

7.2.4 Exploiting the peptides fluorescence to explore the interactions with the cells

Due to the interesting results achieved with G(IKKK)₃I-NH₂ and FITC-G(IKKK)₃I-NH₂, it was decided to perform further experiments to study the interactions between these peptides and cancer cells and unravel some of the unanswered questions regarding their cell specificity. FITC-G(IKKK)₃I-NH₂, due to its fluorescence and easy ability to be tracked was the preferred choice.

Electron microscopy was used to acquire high resolution images of HCT-116 cells after exposure to FITC-G(IKKK)₃I-NH₂. Scanning electron microscopy (SEM) was performed to obtain detailed images of the cell membranes while transmission electron microscopy (TEM) was used to localise the peptide once internalised in the cells. For SEM three peptides concentrations were selected (0.3, 6.25 and 100 µM) and images up to 20000X magnification acquired (Figure 48 and Figure 49) Interestingly, cells exposed to the highest peptide concentration had a drastic change in their membranes morphology showing the complete loss of filopodia and lamellipodia, thin protrusions made of actin filaments essential for cell migration, adhesion, morphogenesis, endocytosis and phagocytosis ³²⁹.

For the TEM, a single concentration of FITC-G(IKKK)₃I-NH₂ was selected (6.25 µM) and complexed with an antibody anti-FITC conjugated with 10 nm gold nanoparticles. The antibody was used to localise the peptide under the microscope; indeed, due to their high electron density, gold nanoparticles can be easily recognised as dark spheres. Cells were exposed to the peptide for 3 or 24 hrs then fixed, embedded in resin and cut in ultrathin sections (85 nm). Untreated cells, or cells exposed to a solution of antibody only were considered as negative controls. The images illustrated in Figure 50 and Figure 51 show the presence of many gold nanoparticles (and therefore FITC-G(IKKK)₃I-NH₂) internalised in endosomal vesicular compartments. The anti-FITC antibody except where complexed with the peptide was not found in the cells. The presence of the peptide in vesicles suggested the possibility that an active mechanism, such as endocytosis, was involved in its internalisation. For this reason, more experiments were undertaken to decide whether or not an energy-dependent process was responsible for the peptide uptake.

The cellular speed in internalising FITC-G(IKK)₃I-NH₂ complexed with siGLO or on its own was assessed in both HCT-116 and HDFs cell lines. For the transfection, DF1 was included as well as a positive control. Different time-points were selected, between 15 minutes and 24 hrs. The results showed a diverse internalisation speed between colon cancer cells and fibroblasts, with the second ones much slower in taking up the fluorescent peptide; while for the colon cancer cells 30 minutes were enough to see fluorescent puncta internally localised and for the fibroblasts nothing was visible until 24 hrs of exposure time. The complexes peptide/siRNA, unless a high ratio was used, required at least an hour in both cell types to be observed, while with DF1 few red dots were already visible after 15 minutes (Figure 52 and Figure 54). A wider range of FITC-G(IKK)₃I-NH₂ concentrations was used (from 6.25 to 100 µM) on HCT-116 and HDFs for 24 hrs (Figure 53 and Figure 55). The fluorescent intensity of the peptide in both the cell lines increased proportionally, with the concentration used.

The peptide uptake by HCT-116 was live imaged over a 24 hrs time period, acquiring a picture every 30 minutes and mounting a video with the image stacks. Two different concentrations of FITC-G(IKK)₃I-NH₂ were used; 6.25 to 100 µM while untreated cells corresponded to the negative control. In 24 hrs, a normal healthy cell population proliferate and migrate along the well surface and this is what was observed in the unexposed cells. However, cells treated with the peptide behaved differently; in the video of cells exposed to 6.25 µM it was possible to see the peptide uptake which made the cells brighter and brighter. The brightest cells adopted a rounded-up morphology and stopped moving, remaining still for hours. Nevertheless, this behaviour was not homogenous in the population and only a few cells presented this phenotype. Cells exposed to 100 µM were crammed almost instantaneously with peptide and the microscope green fluorescent channel got saturated. The behaviour adopted by these cells was the same already observed for 6.25 µM; cells were motionless. Interestingly, no apoptotic cells were observed (Figure 59).

The live videos and SEM images showed that FITC-G(IKK)₃I-NH₂ has probably a more cytostatic effect than a cytotoxic effect and at high concentration is able to partially destroy the membrane features and block the cells ability to move. To evaluate the impact of peptide on the cellular functions, the following experiment was performed; cells were exposed to 100 µM of fluorescent peptide for 30 minutes (enough time to completely be saturated by the peptide) or overnight. In the first case, the

medium containing the peptide was replaced with new complete medium. The next day, cells were fixed, imaged under the fluorescent microscope and the cell population counted (Figure 61). Surprisingly, cells left overnight in normal medium were able to recover from the peptide uptake, pump it out from the cytoplasm and start proliferating again.

The peptide uptake by cancer cells was evaluated also in cold conditions when all the cellular energy-dependent processes are blocked, included endocytosis, which is strictly reliant on the cell temperature. Indeed, if the temperature goes down to 4 °C, the internalisation of molecules via endocytic pathways becomes strongly inhibited^{152, 153, 238}. HCT-116 were left in ice and exposed to a cold solution of FITC-G(IKK)₃I-NH₂ (12.5 μM) for 30 minutes. After that, cells were rapidly fixed and the fluorescence in the cells quantified. Some HCT-116 instead of being fixed were switched back to 37 °C for 3 hours. This helped to evaluate the cellular efficiency in regaining the ability of internalising FITC-G(IKK)₃I-NH₂ when moved to a more suitable environment. Medium containing the peptide was removed and substituted with complete culture medium prior to the 3 hours incubation at 37 °C. In this way, the ability of the peptide in binding the cell membranes, even if not internalised, was analysed. Control plates of cells exposed to the peptide and left for 30 minutes or 3 hours at 37 °C were added as well. Since cells have a certain level of green auto-fluorescence, a plate of HCT-116 not exposed to the peptide was added as additional control. The background green fluorescence was then measured and subtracted from the other quantification data. The analyses revealed that in cold conditions, cells were unable to uptake the peptide but when moved back to 37 °C, they could restore their endocytic functions and fluorescence was again observed in the cells. If the medium containing FITC-G(IKK)₃I-NH₂ was discharged before the switch to warm conditions, very little peptide was observed in the cells afterwards, suggesting that an energy-dependent mechanism could also be necessary for the initial interaction with the cellular membrane (Figure 56).

To analyse the effective amount of FITC-G(IKK)₃I-NH₂ internalised in cells and to distinguish differences between cancer and noncancer cells, an acid stripping was applied to cells (both colon cancer and fibroblasts) exposed to a various range of FITC-G(IKK)₃I-NH₂ concentrations (between 6.25 and 50 μM) but prior to fixation. This was

because, the fixation procedure formaldehyde mediated, can permeabilize the membranes, allowing the translocation inside the cells of materials attached on the outer surface¹⁵⁴.

The acid washes remove from the membranes anything not covalently bound and therefore could detach all the peptide molecules attached on the extracellular membranous surface. The quantitative analyses of FITC fluorescence intensities of washed and unwashed cells revealed that the acid stripping was able to remove the peptide that was just attached on the outside of the membranes. Significant differences between washed and unwashed cells were obtained especially with fibroblasts, which confirmed their poor ability in taking up the fluorescent peptide (Figure 57.). The cells were also stained with Cell Mask Orange (Thermo Fisher) to better visualise and define the cellular borders. In doing so, an interesting phenomenon was observed: cells in mitosis were not internalising the peptide (Figure 58). This was also spotted when cells were stained with Alexa Fluor® 568 Phalloidin (Thermo Fisher), another dye used to enhance the cellular boundaries (Figure 46). This new evidence supports once more the idea of an endocytic mechanism being involved in the internalisation process since it is generally believed that the endocytosis is strongly inhibited during the early mitotic phases²²⁶.

7.2.5 RNAi screens to elucidate the endocytic pathway involved in the peptide uptake

Exploiting the fluorescence of FITC-A₉K and FITC-G(IKK)₃I-NH₂, a mini-screen and a high-content screen were performed on HCT-116 cells with the goal of isolating the endocytic genes responsible for peptides internalisation and identifying, if possible, the pathway(s) involved. Before executing the high content screen, an assay development screen was prepared and several experimental parameters were simultaneously checked in order to find the perfect conditions to successfully perform the screen afterwards. More importantly, few genes were selected to be tested as possible “hits” if knocked down using RNAi.

The assay development screen for FITC-G(IKK)₃I-NH₂ was composed by a siRNA library called assay development plate 2 (ASD2), specifically designed for genome-

wide RNAi screens. The library was mainly composed by a selection of siRNAs which knock down kinases, enzymes that catalyse the phosphorylation between high-energy and specific substrates and regulate many cellular functions³³⁰. Some of the siRNAs were related with endocytic pathways and therefore chosen as possible “hits”; Actin Related Protein 2 Homolog (ACTR2), ADP-ribosylation factor 6 (ARF6), Caveolin 1 (CAV1), Clathrin heavy chain (CLTC), Dynamin 2 (DNM2), Myosin Va (MYO5A), Myosin Vb (MYO5B), Myosin Vc (MYO5C) and Ras-related protein 7a (RAB7A).

CLTC and CAV1 are specific of the clathrin-dependent and caveolin-dependent endocytic pathways while the others have a more generic role in endocytosis: ACTR2 encodes for a component of actin related protein 2/3 complex which is involved in the regulation of the actin filaments polymerisation; Arf 6 is GTP-binding that regulates endocytic recycling and cytoskeleton remodelling; Dynamin 2 is another GTP-binding protein associated with microtubules and implicated in endocytosis and cell motility; the Myosin V are motor proteins involved in the endocytic vesicular trafficking and endosomes recycling in neuronal and epithelial cells while Rab 7a is key regulator in endo-lysosomal trafficking and in the early-to-late endosomal maturation¹⁵⁷⁻¹⁶⁴. Four non-targeting siRNAs were included in the assay as negative controls.

Clathrin light chain a (CLTA), Clathrin light chain b (CLTB), Clathrin heavy chain (CLTC), Adaptor related protein complex 2 subunit alpha 2 (AP2A2), Adaptor related protein complex 2 subunit beta (AP2B1) and Actin related protein 2/3 complex subunit 1 B (ARPC1B) siRNAs were selected to knock down the correspondent genes in the FITC-A₉K mini-screen. All the siRNAs were picked from the SiGenome collection of design siRNAs from Dharmacon.

With the exclusion of ARPC1B which encodes for one of the seven subunits of the already cited Arp2/3 complex, all the other genes are related with the clathrin-dependent endocytic pathway¹⁵⁶⁻¹⁵⁸. Red fluorescent siGLO was selected as the positive control for the transfection efficiency while 5 non-targeting siRNAs were selected as negative controls.

In both experiments, a cell count analysis was performed to evaluate the cellular viability after siRNA transfection and RNAi. The averages of the non-targeting siRNAs

viabilities were considered as negative controls and all the other cell counts were normalised to this. In the assay development with FITC-G(IKK)₃I-NH₂ ACTR2, CAV1, MYO5A and MYO5B siRNAs significantly decreased the cellular viability (Figure 75) while in the mini-screen with FITC-A₉K none of the siRNAs employed decreased the cell viability (Figure 80). The green fluorescence associated within the cells was quantitatively analysed as well and compared to the negative controls in order to evaluate possible phenotypic changes in the peptides internalisation following RNAi. In the FITC-G(IKK)₃I-NH₂ development assay CAV1, CLTC, DNMT2, MYO5A, MYO5B and MYO5C siRNAs knock down caused a significant reduction in the peptide uptake. On the contrary, ARF6 had the opposite effect and it significantly increased the amount of peptide found in the cells. No effects were observed instead for ACTR2 and RAB7A (Figure 77). In the mini-screen with FITC-A₉K, all the selected siRNAs significantly decreased the peptide uptake (Figure 81).

The cell count analysis was performed in all the ASD2 plate and, as expected, the knock down of kinases had a severe impact on the cellular viability. The bottom 5% (95% of cells dead) was plotted in a graph (Figure 76) and it is represented by FRAP1, RIOK2, PDJ2, KIAA1804, IRAK1, PFTK1 and NAGK. All genes that encode for kinases play a pivotal role in cellular growth, differentiation, cell cycle and apoptosis and are often overexpressed in tumours, especially in colon cancer³³¹⁻³⁴².

For the focused high-content screen on cells exposed to FITC-G(IKK)₃I-NH₂, a designed library of Traffic-ome targeting siRNAs was used. Following transfection and exposure to the peptide, cells were fixed and any phenotypic change in the fluorescence intensity distribution of the peptide quantified. The data obtained were subsequently normalized using the robust z-score method which is less sensitive to outliers than the standard z- score and preferable for use in RNAi screens^{294, 295}. The possible “hits” were 31, identified in the outliers scoring $\leq - 3.5$ or $\geq + 3.5$ (Figure 78). The biological functions of the hits are illustrated in Figure 83; the majority of these genes can be divided into two main clusters; one related to vesicles recycling to the cell surface and the other related to vesicle trafficking within different organelles but mainly associated with the Trans-Golgi network. Three genes were excluded from the clusters; ADAM 10 which encodes for a cell membrane metalloproteinase, IP6K3 which encodes for a protein that regulates inositol phosphate-stimulated vesicle formation and trafficking and WASF3 that encodes for a protein involved in the actin polymerization through the

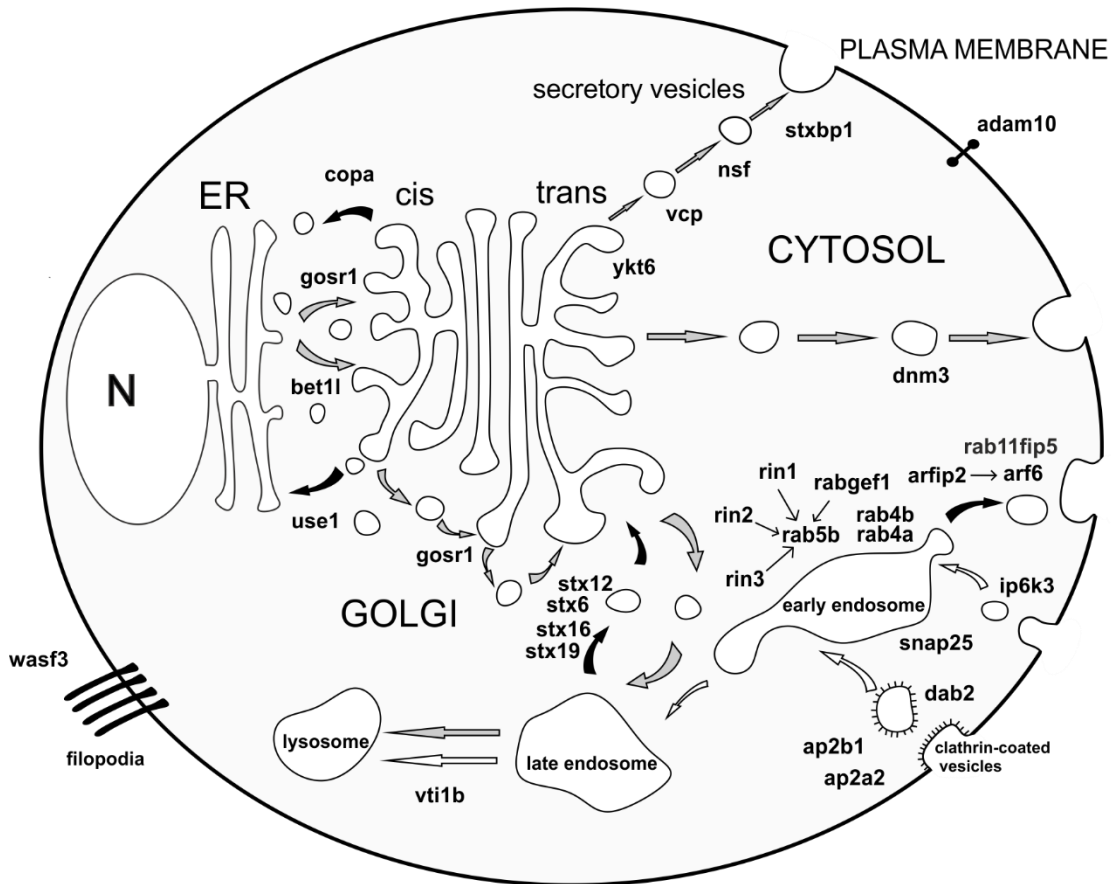


Figure 83. Schematic representation of the hits main functions in the cell endocytosis. The hits could be divided into two main clusters, one related to the vesicles trafficking to and from the Golgi network and one associated with the early endosome and vesicles recycling. Adam 10, metalloproteinase (cleaves the extracellular domain of transmembrane proteins), Wasf3 (involved in filopodia formation and motility) and Ip6k3 (regulator of inositol phosphate-stimulated vesicle formation and trafficking) instead do not fall in any category. Legend: N = nucleus; ER = endoplasmic reticulum.

7.2.6 In vivo toxicity and bio distribution in *Danio rerio* embryos

Microinjections in one cell stage zebrafish embryos (*Danio rerio*) were performed to evaluate the toxicity of A₉K and FITC-G(IKKK)₃I-NH₂ using a wide range of concentrations (from 6.25 pg to 4 ng per embryo). A₉K induced only a mild toxicity in the embryos and exclusively at high peptide concentrations (from 1 to 4 ng per embryo). On the other hand, FITC-G(IKKK)₃I-NH₂ caused severe toxicity even at very low concentrations (6.25 pg). The LC₅₀ calculated for A₉K were 1.7 and 1.4 ng in 1 or 3 days post fertilisation embryos (dpf) corresponding respectively to 2 and 1.7 mM. LC₅₀ calculated for FITC-G(IKKK)₃I-NH₂ were instead 7 and 2 pg in 1 or 3 dpf embryos, corresponding respectively to 3,5 and 1 μM (Table 13).

Table 13. In vivo toxicity of A₉K and FITC-G(IKKK)₃I-NH₂ on zebrafish embryos.

FITC-G(IKKK)₃I-NH₂ gave the strongest toxic effect and even a few pg of it were enough to kill most of the embryos. The complete results can be find in Chapter 5, sections “5.4 Microinjections of A₉K peptide in zebrafish embryos” and “5.5 Microinjections of FITC-G(IKKK)₃I-NH₂ peptide in zebrafish embryos”. LC₅₀ = lethal concentration which corresponds to peptides concentration needed to kill 50% of embryos.

Peptides	LC ₅₀ (pg)	
	1 dpf	3 dpf
A ₉ K	1700	1400
FITC-G(IKKK) ₃ I-NH ₂	7	2

FITC-G(IKKK)₃I-NH₂ was so toxic that even at the first check-point (5 hours post-fertilisation), with the exclusion of 6.25 pg, in all the other concentrations the surviving rate was already below 50% (Figure 65) To evaluate if FITC-G(IKKK)₃I-NH₂ would decrease its toxicity if injected in an embryo when complexed with negatively charged molecules, another injection experiment was performed; the peptide was complexed with siGLO red at two charge ratios (1/1 or 4/1). To decide which amount of siGLO it was appropriate to use, a dose-curve experiment was initially performed with the fluorescent siRNA, testing siGLO concentrations between 20 and 80 pg per embryos. The LC₅₀ calculated for siGLO were 76, 73 and pg in 5 hpf, 1 or 3 dpf embryos,

respectively (Table 14). 20 pg was therefore selected as safe concentration to use in the complexation with FITC-G(IKKK)₃I-NH₂.

Table 14. In vivo toxicity of siGLO red on zebrafish embryos. The siRNA is toxic to zebrafish embryos only at concentrations above 60 pg, therefore 20 pg was selected as concentration to be used complexed with FITC-G(IKKK)₃I-NH₂. The results can be found in Chapter 5, section “5.6.1 Microinjections of siGLO to estimate the siRNA toxic threshold”. LC₅₀ = lethal concentration which corresponds to peptides concentration needed to kill 50% of embryos.

siRNA	LC ₅₀ (pg)		
	5 hpf	1 dpf	3 dpf
siGLO	76	73	56

When the complexes peptide/siRNA were injected in 1 cell stage embryos and the viability checked it was found that the peptide overall toxicity decreased and more than 50% of embryos were still alive even after 3 days at both charge ratios (1/1 and 4/1 corresponding to 20 and 80 pg of FITC-G(IKKK)₃I-NH₂) (Figure 71).

Ultimately, the bio distribution of FITC-G(IKKK)₃I-NH₂ in the blood circulation of 4 dpf larvae was assessed. The peptide together with FITC fluorophore used as a negative control were injected in the larvae at the concentration of 25 pg/nl. To be able to visualise the blood vessels under the fluorescent microscope the transgenic zebrafish line, TG(*kdrl:HRAS-mCherry*), was used¹⁴⁷. Larvae were injected in a caudal vein and then mounted in a solution of agarose and Tricaine (anaesthetic) to be visualised under the light-sheet microscope. Unfortunately, both peptide and fluorophore leaked out from the fish system too quickly, preventing the correct development of the planned experiment (Figure 73 and Figure 74).

7.3. Discussion

7.3.1 Membranolytic or mitochondrial target?

The strategies adopted by the so-defined anticancer peptides (ACPs) to target and kill cancer cells are believed to be similar to the ones used by the antimicrobial peptides (AMPs) when targeting bacteria, which can be generalised into two main mechanisms: membrane permeabilization and membrane translocation to hit intracellular targets^{106, 343}. The cationic amphiphilic peptides discussed in this thesis exert their antimicrobial effects destroying the bacterial membranes and are believed to display membranolytic activity also towards mammalian cancer cells^{117, 126}. Moreover, previous published studies on A₉K and G(IKKK)₃I-NH₂ suggested that these peptides can also target intracellular organelles such as mitochondria and induce apoptosis^{116, 118}.

However, the results obtained in this study and previously described, tell a slightly different story. For example, when the MTT assay was performed on A431 cancer cells exposed to A₆K and A₉K peptides, a significant decrease in the MTT salt reduction was observed, but a direct sign of growth inhibition was only weakly detected, at least at the tested concentrations. The cell counting experiments afterwards showed absence of cell death induced by the peptides, which might exclude membrane permeabilization as mechanism of targeting cancer cells.

The staining using Mitotracker and JC-1 dyes subsequently showed that mitochondria dramatically changed in morphology and had more depolarised membrane potential ($\Delta\Psi_m$) in cells exposed to the peptides. Mitochondria are dynamic organelles and their shape and morphology can change rapidly in response to the cellular environment or to stressful conditions³⁴⁴. Because of their critical role in the energy production and also in the regulation of other various pathways, including cell apoptosis, Ca²⁺ signalling and redox homeostasis, mitochondria have the ability to remodel their architecture and undergo a series of balanced membrane fusion and fission events within the cytoplasm. Normally a shift toward fusion creates large interconnected mitochondria networks associated with healthy and metabolic active cells while a shift towards fission produces instead many mitochondrial fragments with the shape of small spheres or short rods and is generally associated with quiescent or damaged cells³²⁸. Mitochondrial fusion and

fission are clearly antagonistic process and the rates of fusion and fission must be precisely controlled to keep the right balance required for the maintenance of mitochondrial morphology during changes of the physiological conditions. Perturbations or failures in the maintenance of this delicate equilibrium are signs of defective cells and normally lead to the triggering of mitophagy (autophagy of mitochondria) or apoptosis signalling²¹³.

The presence of altered mitochondria could suggest that both the β -sheet peptides have a more cytostatic effect than cytotoxic. ACPs often affect the mitochondria of cancer cells and a few examples can be cited from literature: the bovine antimicrobial peptide BMAP-28 which induced the mitochondrial membrane depolarisation in the U937 (promonocytic) cells²¹⁴; Lactoferricin B, another bovine antimicrobial peptide which depolarised $\Delta\psi_m$ and also induced the activation of caspase-6, -7 and -9 in neuroblastoma cell lines³⁴⁵; Mastoparan obtained from the *Vespula lewisii* venom that induced apoptosis in a the murine melanoma cell line B16F10 via permeabilization of the mitochondrial membrane³⁴⁶ and hCAP18 that induced mitochondrial depolarization and apoptosis in SAS-H1, high invasive cells derived from the human squamous cell line SAS³⁴⁷.

The JC1, Mitotracker and MTT data combined together suggest that something critical happens to the cells and, specifically, to the mitochondria when exposed to A₆K and A₉K. However, it is still not clear if the observed effects are related to a direct interaction between the peptides and the mitochondrial membranes or if it is just a secondary effect.

The cell counting on G(IKK)₃I-NH₂ showed a decrease in HCT-116 cell number depending on the peptide concentration and exposure time. The maximum effect was observed with 100 μ M at which, on average, 90% of cell reduction was observed at each time point. It is not clear from the initial results whether this α -helical peptide is cytotoxic and membranolytic. However, further evidence showed that the peptide interacts very differently with the cells. Moreover, thanks to the opportunity of using the FITC-labelled fluorescent version it was possible to directly observe how this peptide was interacting with cells.

7.3.2 Endocytosis as mechanism of cellular internalisation

The first clues that a different mechanism was involved in the peptide internalisation came when Alexa Fluor® 568 Phalloidin and CellMask Orange were used to stain the F-actin filaments and the plasma membrane, respectively. Thanks to these stainings it was possible to visualise the cellular boundaries and better localise FITC-G(IKK)₃I-NH₂ in the cells. It was noticed that if a cancer cell was in a clear mitotic phase, the fluorescent peptide was not able to become internalised, but it was mainly bound to the external leaflet of the cell membrane. A possible explanation would be that the peptide could be internalised via endocytosis, which is believed to be inhibited during mitosis³⁴⁸. For example, a recent study published by Fielding et al., showed that a fluorescent CD8 chimera system, normally used to study sorting signals of transmembrane proteins³⁴⁹ and fluorescent transferrin molecules were both not internalised in early mitotic stages suggesting that clathrin-mediated endocytosis was temporarily switched off²²⁶.

After this first indication that the peptide might have an alternative way to get inside the cells, more experiments were conducted to evaluate if an energy-dependent mechanism was actually involved. From the literature, it is well known that all the energy-dependent biological functions are strictly reliant on the temperature, and if 4 °C is reached, all the active process in the cell are inhibited, endocytosis included^{152, 153, 238}. When the FITC-G(IKK)₃I-NH₂ uptake was evaluated in HCT-116 cells in cold conditions, it was shown that at 4 °C cells were unable to internalise the peptide, suggesting that endocytosis-dependent pathways could be the major uptake mechanisms. Moreover, TEM images also showed that the peptide molecules were localised in big vesicular compartments, indicating endocytosis as a plausible mode of entry. In the literature, many studies are published regarding the mechanisms of entry of cationic peptides in cancer cells showing how differently these small molecules can behave, depending on multiple environmental factors. For example, Wang et al., recently published an interesting study on L-K6 (IKKILSKIKKLLK-NH₂), a synthetic lysine/leucine-rich cationic antimicrobial peptide with anticancer activity, analogue of the natural temporin-1CEb, isolated from the skin secretions of the Chinese brown frog (*Rana chesinensis*). Their results showed that the peptide exerted cancer cell selectivity and induced cytotoxicity on different cancer cell lines (especially MCF-7) in dose-,

time- and energy- dependent ways. If the temperature was dropped down to 4 °C or if the ATP pool was depleted by pre-incubating the cells with sodium azide (NaN₃), the cytotoxic effect of the peptide diminished. They also showed how L-K6 induced permeabilization and morphological changes in the cancer cells membranes but without causing the membranes disruption. Methyl-β-cyclodextrin (Mβ-CD), cytochalasin D (CyD) and chlorpromazine (CPZ) inhibitors were used to selectively block caveolae-mediated endocytosis, macropinocytosis and clathrin-mediated endocytosis, respectively. The results showed a partial blocking of FITC-labelled L-K6 internalisation when caveolae-mediated endocytosis was inhibited and a more significant block with macropinocytosis inhibition but no effect with the clathrin-mediated endocytosis inhibitor, suggesting that macropinocytosis was majorly involved in the internalization of L-K6 by cancer cells ³⁵⁰.

Lim et al., instead studied the toxicity and the internalisation pathways of BH2, a novel cancer specific peptide derived from the synthetic buforin IIb, analogue of the natural antimicrobial peptide buforin and extract from stomach tissues of the Asian toad *Bufo bufo* which displays membrane penetrating activity in bacteria. BH2 was tested against various cancer (HeLa, HCT-116 and mouse melanoma B16/F10) and non-cancer (NIH 3T3, HaCat and human fibroblast BJ) cell lines, showing selectivity for the cancer cells but no cytotoxicity for the normal mammalian cells. To further understand the peptide uptake, the effects of temperature (cells kept at 4 °C) and metabolic inhibitors (pre-treatment with NaN₃) were investigated in HeLa cells using a FITC-labelled version of BH2. Moreover, the role of endocytosis was examined by pre-treating cells with amiloride, nocodazole and methyl-β-cyclodextrin (MβCD), endocytic inhibitors which block macropinocytosis, clathrin-mediated pathway and lipid raft-mediated macropinocytosis (which produces larger vesicles that do not fuse with early endosomes), respectively. The results showed that both temperature and ATP depletion caused a reduction of peptide uptake and the lipid raft-mediated macropinocytosis was the major internalisation pathway ³⁵¹.

In another study the synthetic lytic-peptide K8L9 designed by Ohara and co-workers showed to enter human glioma U251 via clathrin-mediated endocytosis, macropinocytosis but also with direct penetration and the pre-treatment of the cancer

cells with endocytosis inhibitors (Cytochalasin D, chlorpromazine and 5-(N-ethyl-N-isopropyl) amiloride (EIPA) decreased the peptide internalisation ³⁵².

There are several factors that could affect the cellular uptake of a selected peptide, including aminoacidic composition, peptide amphiphaticity, temperature, cell surface components, cell culture medium composition and peptide concentration ^{73, 74}. Thus, a peptide could enter in a cell using both direct penetration or endocytosis and sometimes this can even occur simultaneously.

For example, the internalisation of fluorescent oligoarginines (R_n) peptides (where n = 4, 8, 12, 16) was investigated in HeLa and CHO cells by Kosuge et al., The presence of serum in the culture medium, the temperature and the peptides concentrations were determinant factors in the internalisation pathways adopted by the cells. Results showed that in absence of serum, higher amounts of R12 and R16 were retrieved in the cells incubated at 37 °C. The peptides were mainly internalised via an energy-independent non-endocytic mechanism which however, did not cause the membrane disruption. Minimal variations in cellular uptake were observed instead for R4 and R8. The temperature played an important role as well and if the cells were incubated in complete culture medium at 37 °C the peptides were internalised via endocytosis while, when the cells were kept at 4 °C and without serum, peptides entered the cells by direct translocation. Wild-type CHO-K1 line, and its mutant variant, A-745 defective in proteoglycans biosynthesis were also incubated with increasing concentrations of fluorescent R12 peptide in medium lacking serum. Proteoglycans are essential for a rapid interaction with arginine-rich peptides and considered the first step for internalisation. At low concentrations, no differences were observed between the cell lines but with the increase of the peptide concentration the mutant cell line generally accumulated less peptide. Moreover, the distribution of R12 in the cells changed depending on the peptide concentration; fluorescent puncta were predominantly observed at low concentrations suggesting endocytic uptake, while with higher concentrations, the peptide diffused in the cytosol indicating a direct membrane translocation. For the wild type cell line, the cytosolic diffusion was observed even at relatively low concentrations while for the mutant cell line a higher peptide concentration was needed, suggesting that the lack of membrane-associated proteoglycans was responsible for the decrease in R12 peptide translocation ⁷⁵.

The SEM images of HCT-116 exposed to different concentrations of FITC-G(IKK)₃I-NH₂ showed how the cellular membranes were affected by the peptide. At lower (0,3 μM) and medium concentrations (6.25 μM), no visible differences were observed when compared to an untreated sample, but when the cells were exposed to 100 μM, the membranes drastically changed morphology, showing a complete loss of filopodia, the thin protrusion made of actin filaments essential to probe the nearby environment ³²⁹. Filopodia are particularly active in cancer cells, where they promote invasion through 3D micro-environments and are essential for driving cancer cell metastasis and helping survival and proliferation ³⁵³. Clinical data revealed that several filopodia proteins, such as fascin, are upregulated in many human cancers and are essential for cancer cell invasion *in vitro* ³⁵⁴.

This particular phenotype observed in cells after exposure to 100 μM of peptide could suggest that a direct translocation occurred and caused intensive membrane disruption. However, cells exposed to the same concentration for 30 minutes and then kept overnight with fresh replaced medium showed the ability to recover from their damaged status, expelling the peptide from their cytoplasm and proliferating again. This may suggest that even at extremely high concentrations, the peptide is internalised by the cells via endocytosis and has a more cytostatic effect, but under favourable conditions cells can still pump the peptide out. The secretory methods used by cells to expel nanomaterials have only just started to be studied and there is still little information available ²⁴¹.

Missirlis et al., recently conducted some studies on Peptide Amphiphiles (PAs), a class of amphiphilic molecules that self-assemble in organised nanostructures similarly to A₆K and A₉K. It was shown how the peptides internalisation and trafficking inside the cells was dependent on the composition of their hydrophobic tail. For example, diC₁₆p53 PA used the clathrin-mediated endocytosis to enter SJS-1 human osteosarcoma cells ³⁵⁵, while RPARPAR PAs mostly used a clathrin-independent uptake (lipid raft-mediated macropinocytosis) to enter in PPC-1 humane prostate cancer cells. Moreover, the fate of the peptides after the uptake was investigated and it was found that after 24 hrs while some peptides molecules were still associated with the plasma membrane while the majority of them were co-localised either in endocytic vesicles Rab 4-; Rab 11- positive, which are markers for 'short loop' or long-loop' recycling

endosomes, or with the late-endosomal marker Rab 7, suggesting that they were directed towards lysosomes³⁵⁶. The “short loop” is a fast recycling pathway regulated by Rab 4, and is characterised by cargoes that rapidly exit the early endosome to recycle to the plasma membrane, while the ‘long-loop’ is slow and is regulated by Rab 11 and the cargoes are recycled from recycling endosomes³⁵⁷.

A few studies are also found about exocytosis of nanoparticles, for example Panyam et al., studied endocytosis, exocytosis and intracellular retention of biodegradable poly (D,Llactide-co-glycolide) nanoparticles on human arterial vascular smooth muscle cells (VSMCs). The results showed that both uptake and secretion of nanoparticles were energy dependent processes and fluid-phase pinocytosis and nonspecific receptor-mediated endocytosis were the internalisation pathways. The uptake was time and dose-dependent but, when higher concentrations were used, the internalisation speed was reduced probably due to the cell saturation. Endocytosis and exocytosis were proceeding simultaneously but secretion started to be effective only when the nanoparticles were removed from the external media²³⁹.

Thanks to the time-lapse videos it was possible to observe the internalisation of the fluorescent FITC-G(IKK)₃I-NH₂ occurring live. The results so obtained are extremely important because they added valuable information about the cell physiology and morphology in presence of the peptide which were not possible to acquire with just standard fixed fluorescent pictures. For example, with 100 µM, cells became rapidly saturated, stopped moving and dividing but did not appear apoptotic. Over a period of 24 hrs they did not decrease in number suggesting that the peptide has a cytostatic effect but without inducing the lysis of the plasma membranes.

7.3.3 RNAi screen reveals the importance of having functional recycling and vesicle trafficking systems

With the mini-screen involving FITC-A₉K, it was suggested that clathrin-dependent endocytosis was responsible for the peptide internalisation since the fluorescence intensity quantified in the cells with knock down of CLTA, CLTB, CLTC, AP2A2, AP2B1 or ARPC1B was drastically reduced compared to the cells transfected with non-

functional siRNAs. However, the results obtained for the screen development assay performed on cells exposed to FITC-G(IKK)₃I-NH₂ showed that probably more than one pathway could be involved, since both CAV1 and CLTC loss of expression induced a decrease in the peptide internalisation compared to the controls. The decrease in fluorescence intensity observed in DNM2, MYO5A, MYO5B and MYO5C knocked down cells confirmed the role of energy dependent pathways in the peptide uptake. Moreover, the increased fluorescence intensity in cells ARF6 knocked down anticipated the importance of vesicle recycling for the intracellular movements of the peptide.

With the more focused high-content screen, many endocytic proteins levels were altered and despite observing an effective decrease in the peptide internalisation, no obvious phenotypes could be distinguished, probably due to gene or pathway redundancies ²⁸⁶.

Interestingly, the knocking down of genes involved in the recycling of more general vesicular trafficking between secretory compartments induced drastic changes in the cellular phenotypes. The cellular uptake of cationic amphipathic peptides with cell penetrating properties is fairly well characterised. However, what happens next is still poorly understood and the internal trafficking is still relatively unknown ³⁵⁸.

Once internalised, a cargo is sent to the early endosomes where it will be sorted to its final destination. From there, it could go to late endosomes and then lysosomes to be degraded; to the trans-Golgi network (TGN) or to recycling endosomes, which bring the cargo back to the plasma membrane. Indeed, the internalisation of extracellular material, proteins, lipids or ligands via endocytosis is normally followed by endosomal recycling pathways that bring it back to the cell surface most of the molecules that belong to the plasma membrane; the composition of the membrane is maintained by this delicate equilibrium which supports many biological functions, such as nutrient uptake, signal transduction, cell adhesion, cell migration and cytokinesis ³⁵⁹. Misfolded proteins, activated growing factors or anything that has to be degraded go the late endosomes via Multivesicular bodies (MVBs); a specialised type of endosomes transporting intraluminal vesicles (ILVs). ILVs and their content are degraded, via fusion with lysosomes, or released externally, via fusion with the plasma membrane ³⁶⁰. The specific transport of a cargo that exits the endosomes and reaches biosynthetic or secretory compartments (TGN, Golgi membranes, or ER) is defined as retrograde and can happen in different parts of the endocytic pathway. Pathogens or pathogenic

products such as viruses and bacteria toxins can use this route as well to promote their infectious mechanisms³⁶¹.

Several studies showed that Cell Penetrating Peptides (CPPs) can escape endosomes and be transported through the Golgi network and the ER via retrograde trafficking; for example, the uptake and intracellular trafficking of fluorescently labelled Penetratin, R9, and Tat peptides were investigated on adherent MC57 mouse fibrosarcoma cells and HeLa cells by Fischer et al., Initially, Wortmannin, which affects early endosome fusion, bafilomycin A1 and chloroquine, which instead bind protons and inhibit vacuolar H⁺-ATPases, were used to inhibit endocytosis and endosomal acidification in MC5-7 cells, respectively. R9 and Penetratin uptake was reduced with the three inhibitors, while with Tat only a small effect and even an increased intracellular concentration were observed. This outcome was further analysed with pulse/chase experiments and MALDI MS analysis showing that Tat peptide is highly susceptible to intracellular proteases which generate fragments that could easily exit the cells. The peptides uptake was evaluated as well in HeLa cells showing that this cell line can internalize 3 times more peptides than MC5-7 cells but when the treatment with bafilomycin A1 occurred, a similar reduction in intracellular fluorescence was still observed. Subsequently, the involvement of the Golgi complex in the intracellular trafficking was better evaluated. MC5-7 cells were incubated with the three peptides with or without the presence of brefeldin A and Nordihydroguaiaretic acid (NDGA), two drugs that interfere with the integrity of the Golgi apparatus. For both compounds the cellular fluorescence of R9 and Penetratin was reduced while Tat fluorescence was reduced only by brefeldin A and enhanced instead by NDGA. NDGA blocks protein transport from the ER to the Golgi complex and induces the redistribution of Golgi proteins into the ER until both organelles are not functional anymore. For this reason, NDGA can be used as Golgi-disrupting drug or as an inducer of retrograde transport. The ability of NDGA in affecting the subcellular localisation of Tat was further evaluated in HeLa cells following a pulse/chase experiment. If incubated with medium alone, cells showed only vesicular fluorescence, but when incubated with NDGA-containing medium a cytoplasmic fluorescence was instead visible. Finally, both cell lines were exposed to the peptides and incubated with a cell-permeable Golgi tracer (Bodipy ceramide) or an acidic compartment-specific probe (LysoTracker) for lysosomes; the images showed partially co-localisation of the peptides with the Golgi

complex but little or no co-localisation with the lysosomes. Altogether, the data collected in this paper supported the hypothesis that CPPs can escape the endocytic compartments, retrograde transported to the Golgi and then enter the cytosol ³⁶².

Missirlis et al., in the previously discussed paper, showed how amphiphilic peptides can also be recycled to the membrane following both rapid (Rab 4 mediated) or slow (Rab 11 mediated) recycling pathways ³⁵⁷.

To date, this was the first time that an RNAi screen was performed on an amphiphilic cationic peptide showing that even with no evident cell penetrating abilities, it could enter cells via endocytosis, exit the endosomal compartments, possibly be retrograde transported to TGN and recycled back to the plasma membrane.

7.3.4 Cancer cell selectivity is maintained

Consistent with the previously published data, all the peptides resulted in no harm to HDFs, human dermal fibroblasts, the mammalian cell line chosen as non-cancer model. Interestingly, the cancer cell selectivity of the fluorescently labelled FITC-G(IKKK)₃I-NH₂ diminished compared to the non-fluorescent version and when it was tested on fibroblasts it caused a decrease in cell number at the highest used concentration (100 μM). The presence of the fluorophore could have modified the physicochemical properties of the peptide reducing its selectivity for cancer cells. Indeed, studies have showed that depending on the modifications, the translocation efficacy and the activity of a peptide could be drastically altered ^{363, 364}.

The standard formaldehyde fixation could cause the membrane permeabilization allowing the translocation inside the cells of any molecules attached to the outer surface ¹⁵⁴. To avoid this, an acid stripping was performed. The procedure allows the removal of anything not covalently bound from the membranes and gives the possibility of quantifying the amount of peptide properly internalised by the cells. Results showed that, especially for the fibroblasts, after acid washes, significantly less amount of fluorescent peptide was observed in the cells consolidating the selectivity of FITC-G(IKKK)₃I-NH₂ for cancer cells.

7.3.5 Antibodies binding as a possible new strategy to kill cancer cells

The complexation of FITC-G(IKK)₃I-NH₂ with anti-FITC monoclonal antibodies labelled with gold nanoparticles not only allowed the localisation of the peptide inside cellular vesicles, thus implanting the idea of an active process as a mechanism of internalisation, but also it proved that FITC-G(IKK)₃I-NH₂ is able to bind to antibodies and more importantly it could transport them inside the cells. In the recent years, there has been an increased interest in what are called therapeutic monoclonal antibodies (TMAs) which can be used to recognize and kill cancer cells. Moreover, antibodies that can be conjugated with drugs (antibodies-drug conjugated ADCs) have been developed to deliver anti-cancer drugs directly into cancerous cells, reducing in this way the side effects of normal chemotherapy³⁶⁵. Due to its cancer cell selectivity, FITC-G(IKK)₃I-NH₂ could potentially be used to complex ADCs and deliver them in targeted cancer cells, consequently increasing the antibodies specificity and opening the doors to a new totally functionality for this peptide.

For example, in the already discussed paper by Lim et al., the BR2 penetrating peptide was also fused with a single-chain variable fragment (scFv) antibody against mutated K-ras and tested on HCT-116 colon cancer cells. The results showed that the peptide fused with the antibody was quickly internalised by the cells and inhibited the cell proliferation of Ras-mutated cells promoting apoptosis³⁵¹.

Cell penetrating peptides can also be used together with radiolabelled antibodies to enhance tumour uptake and retention. Jain et al., co-administered Penetratin in LS174T colon carcinoma xenograft-bearing mice with ¹²⁵I-labeled, divalent [sc(Fv)₂] antibody derived from the anti-tumor-associated glycoprotein 72 monoclonal antibody (mAb) CC49. The results showed that co-injection of peptide with the radiolabelled antibody fragment improved the retention and homogenous distribution of sc(Fv)₂ in the tumour without alterations of pharmacokinetics and uptake in non-target tissues. The increased penetration was probably due to electrostatic interaction through linker regions between the positively charged Penetratin and the negative sc(Fv)₂ molecules³⁶⁶.

7.3.6 The ability of efficiently deliver nucleic acid molecules in cancer cells

A big part of this project was the focus on studying the ability of A₆K, A₉K and G(IKK)₃I-NH₂ in binding negative molecules such as DNA or RNA and to investigate their possible usage as delivery vectors to specifically target cancer cells.

A₆K was unable to bind ODNs or siRNA molecules while A₉K, despite transfecting both types of molecules in cancer cells, was unable to release the siRNAs which prevented their gene silencing activity. Only G(IKK)₃I-NH₂ (and its fluorescent version) were successful in binding, transfecting and releasing nucleic acids, especially siRNA molecules. An endosomal escape by this peptide was already proposed following the results obtained with high-content RNAi screen. With the discovery of RNAi (interference), the biological process which mediates the knock down of targeted mRNA transcripts, a new field of therapeutics delivery was born: small interfering RNA (siRNAs) could be introduced in the cells to precisely modulate gene expression³⁶⁷. Naked siRNA molecules cannot trespass the plasma membrane due to their size and overall negative nature, therefore they need carriers. Over the years, a long series of carriers were introduced to be used with siRNAs, including viral and non-viral vectors such as polymers, lipids, nanoparticles and of course peptides³⁶⁸⁻³⁷⁰. Host cells toxicity, immunogenicity, RNA degradation, poor cell selectivity and distribution, endosomal escape are just few of the several barriers which preclude the use of siRNAs as therapeutics^{187, 371}.

For example, MPG-8, a 21-residue amphipathic peptide was able to deliver siRNA molecules in cultured mammalian cells and *in vivo* on mice upon injection. This short peptide is an improved variant of the amphipathic peptide MPG derived from the fusion sequence of the hydrophobic HIV protein gp41, the hydrophilic nuclear localization sequence of SV40 large T antigen and a short linker that separates these domains. In the study conducted by Crombez et al., Cyc-B1 siRNA targeting cyclin B1, a non-redundant mitotic partner of cyclin-dependent kinase 1 (cdk1) a regulatory protein involved in mitosis, was complexed with MPG-8 forming stable non-covalently bound nanoparticles. The complexes were transfected in Adherent HS68 fibroblasts, HeLa,

PC3 (prostate cancer), MCF-7 (breast cancer) and SCK3-Her2 (breast cancer) cell lines or intravenously and intra-tumoural injected in athymic female nude mice previously subcutaneously inoculated with PC3 or SCK3-Her2 cells. The peptide efficiently delivered the siRNA into cells inducing G2 arrest with downregulation of both cyclin B1 protein and mRNA levels. The effect was remarkably significant in cancer cells but only moderate on fibroblasts because the knock down of proteins required for the G2/M transition, has normally only a limited effect on non-cancer cells with an active G2/M checkpoint machinery. Also *in vivo*, both topic and systemic injections blocked the tumour growth making MPG-8 a promising candidate for clinical trials ³⁷².

Another example is given by PepFect14 (PF14), an amphipathic peptide designed to improve the nucleic acid delivery and whose structure is based on that of transportan-10 (TP10), a 21-residue peptide derived from Mastoparan, of the wasp *Vespa lewisii* venom. PF14 was complexed with two siRNAs targeting firefly luciferase and hypoxanthine phosphoribosyl transferase (HPRT1), an enzyme involved in the purines recycling, important process for the production of DNA and RNA. Luciferase-expressing BHK21 (baby hamster kidney), HepG2 (human hepatocellular carcinoma) and HEK293 (embryonic kidney) cell lines were used for the luciferase knockdown while HUH 7 (human hepatocellular carcinoma) and Jurkat (acute T cell leukaemia) cell lines were used for assessing HPRT1 endogenous gene knockdown. PF14/siRNA complexes were successful in mediating the RNAi knock down of both, luciferase and HPRT1 and the transfection efficiency of the peptide was even higher than the standard transfection reagents (Lipofectamine 2000 and Lipofectamine RNAimax®). Moreover, the stability of the complexes peptide/siRNA was tested to evaluate a possible usage for oral administration. Prior transfection in HEK293 cells, the nanocomplexes were left in the simulated gastric fluid (SGF), a highly acidic solution with or without pepsin. Results showed that the complexes gave good knock down efficiency when left up to 2 hrs in the SCF but in presence of pepsin the limit was set to 30 minutes ³⁷³.

Interestingly, both A₉K and G(IKK)₃I-NH₂ were able to deeply transfect 3D spheroids model of colon cancer cells, unlike the commercial lipid transfection reagent. Tumour penetration is a crucial quality that an anticancer treatment should have to be effective. If a therapy is unable to reach all the cells in a tumour that have regenerating properties, then its efficacy is highly reduced ¹⁸⁹. Cells in the centre of a solid tumour are hypoxic

and much evidence suggest that this type of cell is not only resistant to radiation treatment, but it is also able to regenerate the tumour after intense chemotherapy²¹⁷. A good way to study tumour penetration and develop better anticancer therapies is to work with 3D models of immortalized established cancer cells lines. 3D cultures have many of the real tumours characteristics, such as cell-cell interactions, drug penetration resistance, hypoxia and production of extracellular matrix. *In vitro* 3D cultures could potentially be a good intermediate between the standard *in vitro* 2D monolayer cultures and in *in vivo* animal models¹³⁴.

To date this was the first time that amphiphilic cationic peptides without clear cell penetrating sequences were able to selectively transfected 2D and 3D cancer models with siRNA molecules and in some extensions also modulate gene expression

7.3.6 *In vivo* toxicity

The results obtained with the *in vivo* microinjections in zebrafish embryos showed how β -sheet and α -helical peptides can behave differently in a living complex organism. The extreme toxicity of FITC-G(IKKK)₃I-NH₂ when compared to A₉K gives rise to a few questions regarding the mechanism of interaction of these peptides with zebrafish embryos. Their different structures (α -helical and single monomer the first or β -sheet and self-assembled in long nanorods the latter) might play a crucial role in the way they behave, once injected. From the transfection experiments described in Chapter 3 and Chapter 4, it had already emerged how, despite both peptides being able to correctly transfect small nucleic acids molecules inside human cancer cells, only FITC-G(IKKK)₃I-NH₂ was releasing its “cargo” and modulated gene expression.

Zebrafish embryos are often used as a model for assessing the toxicity of chemical compounds, nanomaterials and drugs due to their rapid development, a physiology, compatible with the human one, relative cheap maintenance and optic clear embryogenesis that allows one to easily score phenotypical changes^{242, 374, 375}.

Normally, the material which needs to be tested is directly dissolved in the embryos' medium and any changes from the standard embryonic development are carefully

recorded. However, in some cases microinjections in one cell stage embryos could be performed instead ^{253, 254}. Microinjections could be a suitable alternative for the environmental toxicity testing of compounds of large size or a net charge, like A₉K and FITC-G(IKKK)₃I-NH₂, which might not be able otherwise to cross the chorion, a thick acellular envelope that naturally protects the embryos ³⁷⁶. Moreover, if microinjected, the concentration to be tested could be much higher than when simply dissolved in medium, allowing the exploration of the effect of wider ranges. For example, for A₉K and FITC-G(IKKK)₃I-NH₂ concentrations up to 5 mM and 2 mM respectively have been tested.

Schubert et al., used the microinjection technique on one-cell stage zebrafish embryos to evaluate the effects of four vehicle substances which are normally used as solvents in bioassays; autoclaved tap water, dimethyl sulfoxide (DMSO), methanol, and triolein. The survival rate of injected embryos was recorded after 24 or 96 hrs and varied depending on the substance or the injected volume (0.5 and 4.2 nl). Between the two time points there were no significant differences while larger injected volumes caused more mortality (for some substances the difference in survival rate was 20% or more). This is because high injected volumes (≥ 4.2 nL) could cause swelling of the yolk sac with consequent leakage of its content through the injection pierce. Overall, methanol and DMSO caused higher mortalities than triolein and water with the survival rates decreased up to 60% when higher volumes were injected. This study confirmed the possibility of using the microinjection technique to administer substances into newly fertilized fish eggs and test their toxicity. In this way, any type of compound can be easily administered, overcoming all the embryos' natural barriers ²⁵⁶.

Cationic amphipathic peptides have been tested on zebrafish embryos and their acute toxicity evaluated. For example, in the previously cited paper by Wang et al., several rhodamine B-conjugated peptides derived from viperacidin (pit viper venom) hypervariable C-terminal regions were tested in 3 dpf larvae in a range of 1-100 μ M. Rhodamine B-conjugated EVP50 was the most toxic, exhibiting an LD₅₀ of 6 μ M and therefore selected for further studies. The distribution of RhoB-EVP50 was assessed in 3dpf larvae which were incubated with 10 μ M of peptide for 24 hrs and the fluorophore accumulation and emission observed under the fluorescent microscope. Free rhodamine B was used as negative control. The images showed that, while the free fluorophore

accumulated only in the yolk sac, the peptide was distributed in the cardiovascular system, especially in the posterior cardinal vein, in the intersegmental vessels and in the cardiomyocytes of the heart. Experiments on breast cancer cells (MCF-7 and MDA-MB-231) showed that this peptide is toxic to both cancer cell lines in a dose-dependent manner and can uniformly accumulate in the cells damaging the membranes and causing their lysis within few minutes ³⁶³.

Crotamine, another cationic peptide derived from snake venom (rattlesnake) was conjugated with the fluorophore Rhodamine-B and tested on 3dpf zebrafish larvae. Chan and collaborators assessed the survival rate of zebrafish embryos exposed to different concentrations of the peptide (0-16 μM) at several time points (10 min, 30 min, 3 hrs and 24 hrs). The results showed that the peptide at concentrations higher than 4 μM induced death in all the individuals after only 10 minutes. Moreover, the distribution of the peptide was evaluated using a fluorescent microscope and the images showed that, when the embryos were exposed for 24 hrs to 1 μM of RhoB-crotamine, the peptide being mainly localised in the yolk sac and intestine ³⁷⁷.

Since A_9K and FITC-G(IKKK)₃I-NH₂ were injected directly inside zebrafish oocytes, they could potentially have directly or indirectly damaged the DNA, inducing genotoxicity and causing, depending on the concentration, apoptosis. The images taken with the stereomicroscope of embryos at 1 or 3 dpf injected with A_9K showed that, at low doses (150-500 pg), the peptide did not alter the fish development and the phenotype of the injected embryos was comparable with the relative controls. At higher concentrations (1000-4000 pg) however, the embryogenesis was affected, and malformations or tissue degradation were observed. However, these effects could be not peptide-specific but associated with increased volumes introduced in the embryos ²⁵⁶. For example, morpholino-modified antisense oligonucleotides (MOs) have a threshold of 3-4 ng per embryo and higher amounts (> 5 ng) cause non-specific toxic effects, such as cell death (often in the brain) or general developmental delays via activation of p53 ³⁷⁸⁻³⁸⁰. A normal 1 dpf embryo should display several somites, rudimental organs, budded tail, primordial neuronal system and a principle of eyes ¹⁴⁶. However, embryos injected with 1000-4000 pg of A_9K (Figure 63) showed tissue darkening compatible with widespread necrosis or apoptosis and progressive growth retardation. Stronger phenotypes showed an almost complete suppression of head and tail structures. These

effects could be associated with an induction of p53 signalling³⁸¹. 3 dpf embryos should display complete blood circulation, advanced neuronal system, most of the organs morphologically defined and developed eyes¹⁴⁶. The embryos injected with higher volumes of peptide (Figure 64) kept presenting major defects; pericardial and yolk sac oedemas were the most prominent followed by spine malformation and severe brain development retardation. Oedemas are accumulations of organic fluids due to swelling and persistent inflammation. In zebrafish, the pericardial oedema is a common phenotype of a defective cardiovascular system. It is caused by the absence of structural development contractility or electrophysiological coordination due to defects in the specification or differentiation of cardiac progenitor cells, failures during the heart tube, cardiac chambers or vasculature morphogenesis^{382, 383}. Exposure in early developmental stages to chemical compounds such as 2,3,7,8-Tetrachlorodibenzo-p-dioxin (TCDD) or nanomaterials such as fullerenes can induce cardiac malformations and hemodynamic alterations with consequent pericardial or yolk swelling^{384, 385}.

FITC-G(IKKK)₃I-NH₂ clearly had a more devastating effect, especially considering the amount of eggs found with coagulation signs already after only 5 hpf. To evaluate if the peptide toxicity could decrease if unable to interact with DNA or RNA, FITC-G(IKKK)₃I-NH₂ was complexed with siGLO and injected in the embryos. The new set of data showed indeed that FITC-G(IKKK)₃I-NH₂ reduced its toxicity. Evidently, FITC-G(IKKK)₃I-NH₂ is a quite active molecule and when injected on its own could interact with the cellular material inside the embryo, causing extreme toxicity even in the first few hours following fertilisation. But once mixed with siGLO the overall toxicity decreased by a significant 50% showing that in its complexed form it could be less prone to kill the embryos. It would not be the first case that a cationic peptide with anticancer properties damages the embryos' DNA. Morash et al., conducted a study on 26 natural variants of Pleurocidins, a family of positively charged α -helical antimicrobial peptides secreted by the mucosal surfaces of flatfish. Their cytotoxicity and anti-cancer activities were assessed *in vitro* on HL60 human leukaemia cells and *in vivo* on zebrafish embryos at different developmental stages (4 hpf, 28 hpf and 52 hpf). 14 peptides were not toxic against the cancer cells while 12 caused more than 50% of cell death for concentrations of ≤ 32 μ g/ml. Four peptides were not toxic against the embryos even at the highest tested concentration (25 μ M) while one peptide was found to be extremely toxic and killed immediately with 1 μ M all the 4 hpf embryos. Another

four peptides induced toxicity at the same concentration but only after 24 hrs exposure while most of the peptides caused mortality at one or more developmental stages at concentrations of $\geq 5 \mu\text{M}$ after 24 hrs exposure. One of the highly toxic peptides, NRC-03, was further studied and its impact on 48 hpf embryos analysed with different fluorescent stainings. Superoxide-sensitive dye dihydroethidium (DHE) assay demonstrated the production of reactive oxygen species (ROS) as a sign of damaged mitochondria; the TUNEL-staining of nicked DNA ends, together with the phalloidin staining showed that the peptide caused DNA fragmentation in association with actin condensation while the Vybrant apoptosis assay indicated that cells death was caused by membrane permeabilization ³⁸⁶.

When the embryos, injected with the peptide/siGLO complexes were observed under the fluorescent microscope, it appeared that while in 1 dpf embryos the fluorescence of both siRNA and peptide was uniformly distributed across the embryo's body, in 3 dpf embryos, the fluorescence was instead mainly concentrated in the yolk. A possible explanation of this phenomenon is that in the yolk the fluorescent molecules might be more stable and less prone to be degraded compared to other tissues. Moreover, the yolk, the embryo's main food source, shrinks more and more during the developmental stages while the cells of the rest of the body undergo several divisions increasing in number and augmenting in embryo's volume. This means that, in the yolk the amount of initial siRNA and peptide was progressively concentrated in a smaller area resulting in a more intense fluorescence, while in the rest of the body, they were instead distributed in a bigger volume of cells and as a consequence the fluorescence started fading. The retention of the fluorescent peptide in the yolk sac could also indicate potential liver toxicity. Indeed, several chemical compounds known to be hepatotoxic have been found to firstly accumulate in the yolk sac, then reduce the liver size and induce morphological abnormalities ³⁸⁷.

7.3.7 Caudal injections of FITC-G(IKKK)₃I-NH₂ in 4 dpf larvae leaked out

The assessment of FITC-G(IKKK)₃I-NH₂ distribution in the vascular system of zebrafish larvae was important to evaluate its efficacy in targeting tumours or as possible vector for systemic therapies. Unfortunately, the outcome of the experiment was unsuccessful and both peptide and the negative control, FITC, leaked out almost immediately from the fish system. However, it is unclear why the leakage was only concentrated in two exit points (gills and choroid plexus) while the rest of the larvae's bodies did not show any traces of fluorescence. A possible explanation could be that the endothelium of the gills between the 4th and 5th days under goes an extensively remodelling process with many integrity changes to increase the surface area for respiration ¹⁴⁶. At the same time, brain pericytes, important regulators of vascular integrity and permeability have just started actively proliferating and being recruited to the brain area ³⁸⁸. Even the blood-brain barrier (BBB) and its tight-junction proteins, which would have easily retained the compounds, are not completely formed yet ³⁸⁹. At this stage of embryonic development, it was not possible to determine whether, FITC-G(IKKK)₃I-NH₂ would be retained in the vascular system and eventually be used as delivery vector for systemic drugs or to selectively target cancer cells. Fish at a later embryonic developmental stage (> 5 dpf) should have been employed for this type of experiment but the licence in possession at the time did not allow for maintaining the embryos alive for so long.

7.4. Conclusions, future works and perspectives

The data collected and explained in this thesis helped give a better understanding of the interactions of three amphipathic small cationic peptides with mammalian (cancer and non-cancer) cells. The mode of action towards cancer cells, initially hypothesised to be mainly membranolytic had been found to be more complex than expected. The peptides did not show lysing abilities but instead accumulate in the cytoplasm in a dose-dependent manner.

An energy-dependent endocytic pathway seems to be responsible for the peptides uptake and low temperatures (4 °C) drastically inhibits their internalisation. According to the RNAi mini-screen performed on HCT-116 cells exposed to FITC-A₉K, the clathrin-dependent endocytic pathways could be involved in the cellular uptake, however with the high-content screen performed on the cells exposed to FITC-G(IKK)₃I-NH₂, an exact pathway could not be identified due to redundancy effects. For many knocked down genes a general decrease in the internalisation of the fluorescent peptide was observed. Combinatorial RNAi screens, in which two genes are simultaneously silenced could be used to overcome this problem. The robust Z-score was calculated identifying several 31 outliers and possible hits. A careful analysis revealed that recycling to the cell surface and vesicle transport trafficking within secreting organelles were the processes generally associated with the outliers. This discovery suggests that FITC-G(IKK)₃I-NH₂ can escape the endosomes and retrograde transport to the Trans Golgi Network (TGF), eventually being recycled on the cell surface, but when the vesicular trafficking is disrupted the peptide accumulates instead in endosomal compartments. To date this was the first time that the intracellular trafficking of a cationic amphiphilic peptide was investigated and the results discussed in this thesis could be the starting point to better understanding of the cellular mechanisms between this class of peptides and mammalian cells. A₉K and G(IKK)₃I-NH₂ but not A₆K were able to bind DNA and RNA molecules and transfect them selectively in 2D and 3D cancer models without decreasing the cell viability. However, only the α -helical peptide could escape the endosomes and correctly release the siRNA to allow the gene knock down via the RNAi machinery. The toxicity of A₉K and G(IKK)₃I-NH₂ was assessed as well in *Danio rerio* embryos *in vivo* models. In

literature, it is possible to find studies where zebrafish embryos are used to assess the acute and chronic toxicity of cationic amphiphilic peptides, but normally the peptide solution is dissolved into the medium of embryos between 4 hpf and 3 dpf old which are consequently exposed to it. To our knowledge, this was the first time that the microinjection procedure was applied to evaluate the toxicity of amphiphilic cationic peptides. The results generated good dose-response curves, confirming that this method could be successfully applied for *in vivo* toxicity assessments. A₉K was less toxic compared to FITC-G(IKKK)₃I-NH₂. However, if the α -helical peptide was complexed with negative molecules prior to injection, the overall toxicity massively decreased. This suggests that the peptide could still potentially be used as systemic drug vector upon carefully investigation of its toxic thresholds.

These promising results lay the foundation for an interesting novel approach in cancer therapy where, cationic amphiphilic peptides such as G(IKKK)₃I-NH₂ could potentially be used as carriers for siRNA, drugs or antibody to selectively target cancer cells and induce their death. Further investigations should be done to evaluate the ability of this peptide to inhibit the cell growth of 3D spheroidal tumours or to identify the pathway(s) of internalisation as a method to increase their cancer cell specificity.

8 REFERENCES

1. Zamyatnin AA, Borchikov AS, Vladimirov MG, Voronina OL. The EROP-Moscow oligopeptide database. *Nucleic Acids Research*. 2006;34(Database issue):D261-D266.
2. Wang Y, Wang M, Yin S, Jang R, Wang J, Xue Z, Xu T. NeuroPep: a comprehensive resource of neuropeptides. *Database: The Journal of Biological Databases and Curation*. 2015;2015:bav038.
3. Waghugh FH, Gopi L, Barai RS, Ramteke P, Nizami B, Idicula-Thomas S. CAMP: Collection of sequences and structures of antimicrobial peptides. *Nucleic Acids Research*. 2014;42(Database issue):D1154-D1158.
4. Wang G, Li X, Wang Z. APD3: the antimicrobial peptide database as a tool for research and education. *Nucleic Acids Research*. 2016;44(D1):D1087-D1093.
5. Tyagi A, Tuknait A, Anand P, Gupta S, Sharma M, Mathur D, Joshi A, Singh S, Gautam A, Raghava GPS. CancerPPD: a database of anticancer peptides and proteins. *Nucleic Acids Research*. 2015;43(D1):D837-D843.
6. Hallen HE, Luo H, Scott-Craig JS, Walton JD. Gene family encoding the major toxins of lethal *Amanita* mushrooms. *Proceedings of the National Academy of Sciences of the United States of America*. 2007;104(48):19097-19101.
7. Hill C, Yee J, Selsted M, Eisenberg D. Crystal structure of defensin HNP-3, an amphiphilic dimer: mechanisms of membrane permeabilization. *Science*. 1991;251(5000):1481-1485.
8. Basso N, Terragno NA. History About the Discovery of the Renin-Angiotensin System. *Hypertension*. 2001;38(6):1246-1249.
9. Dalayeyun JF, Nores JM, Bergal S. Physiology of beta-endorphins. A close-up view and a review of the literature. *Biomed Pharmacother*. 1993;47(8):311-320.
10. Nicastro G, Franzoni L, de Chiara C, Mancin AC, Giglio JR, Spisni A. Solution structure of crotamine, a Na⁺ channel affecting toxin from *Crotalus durissus terrificus* venom. *European Journal of Biochemistry*. 2003;270(9):1969-1979.
11. Dockray GJ. Gastrin and gastric epithelial physiology. *The Journal of Physiology*. 1999;518(Pt 2):315-324.
12. Jiang G, Zhang BB. Glucagon and regulation of glucose metabolism. *American Journal of Physiology - Endocrinology And Metabolism*. 2003;284(4):E671-E678.
13. Dürr UHN, Sudheendra US, Ramamoorthy A. LL-37, the only human member of the cathelicidin family of antimicrobial peptides. *Biochimica et Biophysica Acta (BBA) - Biomembranes*. 2006;1758(9):1408-1425.
14. Zasloff M. Magainins, a class of antimicrobial peptides from *Xenopus* skin: isolation, characterization of two active forms, and partial cDNA sequence of a precursor. *Proceedings of the National Academy of Sciences of the United States of America*. 1987;84(15):5449-5453.
15. Raghuraman H, Chattopadhyay A. Melittin: a Membrane-active Peptide with Diverse Functions. *Bioscience Reports*. 2007;27(4-5):189-223.
16. Ross HE, Young LJ. Oxytocin and the neural mechanisms regulating social cognition and affiliative behavior. *Frontiers in Neuroendocrinology*. 2009;30(4):534-547.
17. Harrison S, Geppetti P. Substance P. *The International Journal of Biochemistry & Cell Biology*. 2001;33(6):555-576.

18. Burbach JPH. What Are Neuropeptides? In: Merighi A, ed. *Neuropeptides: Methods and Protocols*. Totowa, NJ: Humana Press; 2011:1-36.
19. Esplugues JV. NO as a signalling molecule in the nervous system. *British Journal of Pharmacology*. 2002;135(5):1079-1095.
20. Zhang X, Bao L, Ma G-Q. Sorting of neuropeptides and neuropeptide receptors into secretory pathways. *Progress in Neurobiology*. 2010;90(2):276-283.
21. Millington GW. The role of proopiomelanocortin (POMC) neurones in feeding behaviour. *Nutrition & Metabolism*. 2007;4(1):18.
22. Veening JG, Barendregt HP. The effects of Beta-Endorphin: state change modification. *Fluids and Barriers of the CNS*. 2015;12:3.
23. Hegadoren KM, O'Donnell T, Lanius R, Coupland NJ, Lacaze-Masmonteil N. The role of beta-endorphin in the pathophysiology of major depression. *Neuropeptides*. 2009;43(5):341-353.
24. De Wied D, Sigling HO. Neuropeptides involved in the pathophysiology of schizophrenia and major depression. *Neurotoxicity Research*. 2002;4(5):453-468.
25. Charbogne P, Kieffer BL, Befort K. 15 years of genetic approaches in vivo for addiction research: Opioid receptor and peptide gene knockout in mouse models of drug abuse. *Neuropharmacology*. 2014;76:204-217.
26. Racz I, Schurmann B, Karpushova A, Reuter M, Cichon S, Montag C, Furst R, Schutz C, Franke PE, Strohmaier J, Wienker TF, Terenius L, Osby U, Gunnar A, Maier W, Bilkei-Gorzo A, Nothen M, Zimmer A. The opioid peptides enkephalin and beta-endorphin in alcohol dependence. *Biol Psychiatry*. 2008;64(11):989-997.
27. Waldum HL, Sagatun L, Mjønes P. Gastrin and Gastric Cancer. *Frontiers in Endocrinology*. 2017;8(1).
28. Li XC, Zhang J, Zhuo JL. The vasoprotective axes of the renin-angiotensin system: Physiological relevance and therapeutic implications in cardiovascular, hypertensive and kidney diseases. *Pharmacological Research*.
29. Daugherty A, Manning MW, Cassis LA. Angiotensin II promotes atherosclerotic lesions and aneurysms in apolipoprotein E-deficient mice. *Journal of Clinical Investigation*. 2000;105(11):1605-1612.
30. Daugherty A, Rateri DL, Cassis LA. Role of the Renin - Angiotensin System in the Development of Abdominal Aortic Aneurysms in Animals and Humans. *Annals of the New York Academy of Sciences*. 2006;1085(1):82-91.
31. Wang F, Herrington M, Larsson J, Permert J. The relationship between diabetes and pancreatic cancer. *Molecular Cancer*. 2003;2(1):4.
32. Brown RJ, Sinaii N, Rother KI. Too Much Glucagon, Too Little Insulin: Time course of pancreatic islet dysfunction in new-onset type 1 diabetes. *Diabetes Care*. 2008;31(7):1403-1404.
33. John AM, Schwartz RA. Glucagonoma syndrome: a review and update on treatment. *Journal of the European Academy of Dermatology and Venereology*. 2016;30(12):2016-2022.
34. Cryer PE. Minireview: Glucagon in the Pathogenesis of Hypoglycemia and Hyperglycemia in Diabetes. *Endocrinology*. 2012;153(3):1039-1048.
35. Garcia J, Costa VM, Carvalho A, Baptista P, de Pinho PG, de Lourdes Bastos M, Carvalho F. Amanita phalloides poisoning: Mechanisms of toxicity and treatment. *Food and Chemical Toxicology*. 2015;86:41-55.
36. Capani F, Deerinck TJ, Ellisman MH, Bushong E, Bobik M, Martone ME. Phalloidin-Eosin Followed by Photo-oxidation. *Journal of Histochemistry & Cytochemistry*. 2001;49(11):1351-1361.

37. Huang Z, Haugland RP, You W, Haugland RP. Phallotoxin and actin binding assay by fluorescence enhancement. *Analytical Biochemistry*. 1992;200(1):199-204.
38. Vetter J. Toxins of *Amanita phalloides*. *Toxicon*. 1998;36(1):13-24.
39. Oguiura N, Boni-Mitake M, Rádis-Baptista G. New view on crotamine, a small basic polypeptide myotoxin from South American rattlesnake venom. *Toxicon*. 2005;46(4):363-370.
40. Mancin AC, Soares AM, Andrião-Escarso SH, Faça VM, Greene LJ, Zuccolotto S, Pelá IR, Giglio JR. The analgesic activity of crotamine, a neurotoxin from *Crotalus durissus terrificus* (South American rattlesnake) venom: A biochemical and pharmacological study. *Toxicon*. 1998;36(12):1927-1937.
41. Kerkis I, Hayashi MAF, Prieto da Silva ARB, Pereira A, De Sá Júnior PL, Zaharenko AJ, Rádis-Baptista G, Kerkis A, Yamane T. State of the Art in the Studies on Crotamine, a Cell Penetrating Peptide from South American Rattlesnake. *BioMed Research International*. 2014;2014:675985.
42. Bulet P, Stöcklin R, Menin L. Anti-microbial peptides: from invertebrates to vertebrates. *Immunological Reviews*. 2004;198(1):169-184.
43. Brogden KA. Antimicrobial peptides: pore formers or metabolic inhibitors in bacteria? *Nat Rev Micro*. 2005;3(3):238-250.
44. Shah P, Hsiao FSH, Ho YH, Chen CS. The proteome targets of intracellular targeting antimicrobial peptides. *PROTEOMICS*. 2016;16(8):1225-1237.
45. Hancock REW, Sahl H-G. Antimicrobial and host-defense peptides as new anti-infective therapeutic strategies. *Nat Biotech*. 2006;24(12):1551-1557.
46. Steiner H, Hultmark D, Engstrom A, Bennich H, Boman HG. Sequence and specificity of two antibacterial proteins involved in insect immunity. *Nature*. 1981;292(5820):246-248.
47. Ganz T, Selsted ME, Lehrer RI. Defensins. *European Journal of Haematology*. 1990;44(1):1-8.
48. Nguyen LT, Haney EF, Vogel HJ. The expanding scope of antimicrobial peptide structures and their modes of action. *Trends in Biotechnology*. 2009;29(9):464-472.
49. Powers JP, Hancock RE. The relationship between peptide structure and antibacterial activity. *Peptides*. 2003;24(11):1681-1691.
50. Takahashi D, Shukla SK, Prakash O, Zhang G. Structural determinants of host defense peptides for antimicrobial activity and target cell selectivity. *Biochimie*. 2010;92(9):1236-1241.
51. Pasupuleti M, Schmidtchen A, Malmsten M. Antimicrobial peptides: key components of the innate immune system. *Critical Reviews in Biotechnology*. 2012;32(2):143-171.
52. Schitteck B, Hipfel R, Sauer B, Bauer J, Kalbacher H, Stevanovic S, Schirle M, Schroeder K, Blin N, Meier F, Rassner G, Garbe C. Dermcidin: a novel human antibiotic peptide secreted by sweat glands. *Nat Immunol*. 2001;2(12):1133-1137.
53. Jenssen H, Hamill P, Hancock REW. Peptide Antimicrobial Agents. *Clinical Microbiology Reviews*. 2006;19(3):491-511.
54. Burian M, Schitteck B. The secrets of dermcidin action. *International Journal of Medical Microbiology*. 2015;305(2):283-286.

55. Czaplewski L, Bax R, Clokie M, Dawson M, Fairhead H, Fischetti VA, Foster S, Gilmore BF, Hancock REW, Harper D, Henderson IR, Hilpert K, Jones BV, Kadioglu A, Knowles D, Ólafsdóttir S, Payne D, Projan S, Shaunak S, Silverman J, Thomas CM, Trust TJ, Warn P, Rex JH. Alternatives to antibiotics—a pipeline portfolio review. *The Lancet Infectious Diseases*. 2016;16(2):239-251.
56. Mahlapuu M, Håkansson J, Ringstad L, Björn C. Antimicrobial Peptides: An Emerging Category of Therapeutic Agents. *Frontiers in Cellular and Infection Microbiology*. 2016;6:194.
57. Pieta P, Mirza J, Lipkowski J. Direct visualization of the alamethicin pore formed in a planar phospholipid matrix. *Proceedings of the National Academy of Sciences*. 2012;109(52):21223-21227.
58. Sengupta D, Leontiadou H, Mark AE, Marrink S-J. Toroidal pores formed by antimicrobial peptides show significant disorder. *Biochimica et Biophysica Acta (BBA) - Biomembranes*. 2008;1778(10):2308-2317.
59. Lee M-T, Sun T-L, Hung W-C, Huang HW. Process of inducing pores in membranes by melittin. *Proceedings of the National Academy of Sciences*. 2013;110(35):14243-14248.
60. Pino-Angeles A, Leveritt JM, III, Lazaridis T. Pore Structure and Synergy in Antimicrobial Peptides of the Magainin Family. *PLOS Computational Biology*. 2016;12(1):e1004570.
61. Sato H, Feix JB. Peptide–membrane interactions and mechanisms of membrane destruction by amphipathic α -helical antimicrobial peptides. *Biochimica et Biophysica Acta (BBA) - Biomembranes*. 2006;1758(9):1245-1256.
62. Cho JH, Sung BH, Kim SC. Buforins: Histone H2A-derived antimicrobial peptides from toad stomach. *Biochimica et Biophysica Acta (BBA) - Biomembranes*. 2009;1788(8):1564-1569.
63. Conibear AC, Craik DJ. The Chemistry and Biology of Theta Defensins. *Angewandte Chemie International Edition*. 2014;53(40):10612-10623.
64. Ganz T. Defensins: antimicrobial peptides of innate immunity. *Nat Rev Immunol*. 2003;3(9):710-720.
65. Hong J, Guan W, Jin G, Zhao H, Jiang X, Dai J. Mechanism of tachyplesin I injury to bacterial membranes and intracellular enzymes, determined by laser confocal scanning microscopy and flow cytometry. *Microbiological Research*. 2015;170:69-77.
66. Paredes-Gamero EJ, Martins MNC, Cappabianco FAM, Ide JS, Miranda A. Characterization of dual effects induced by antimicrobial peptides: Regulated cell death or membrane disruption. *Biochimica et Biophysica Acta (BBA) - General Subjects*. 2012;1820(7):1062-1072.
67. Haukland HH, Ulvatne H, Sandvik K, Vorland LH. The antimicrobial peptides lactoferricin B and magainin 2 cross over the bacterial cytoplasmic membrane and reside in the cytoplasm. *FEBS Letters*. 2001;508(3):389-393.
68. Tu Y-H, Ho Y-H, Chuang Y-C, Chen P-C, Chen C-S. Identification of Lactoferricin B Intracellular Targets Using an Escherichia coli Proteome Chip. *PLOS ONE*. 2011;6(12):e28197.
69. Ghosh A, Kar RK, Jana J, Saha A, Jana B, Krishnamoorthy J, Kumar D, Ghosh S, Chatterjee S, Bhunia A. Indolicidin Targets Duplex DNA: Structural and Mechanistic Insight through a Combination of Spectroscopy and Microscopy. *ChemMedChem*. 2014;9(9):2052-2058.

70. Fehlbaum P, Bulet P, Chernysh S, Briand JP, Roussel JP, Letellier L, Hetru C, Hoffmann JA. Structure-activity analysis of thanatin, a 21-residue inducible insect defense peptide with sequence homology to frog skin antimicrobial peptides. *Proceedings of the National Academy of Sciences of the United States of America*. 1996;93(3):1221-1225.
71. Guidotti G, Brambilla L, Rossi D. Cell-Penetrating Peptides: From Basic Research to Clinics. *Trends in Pharmacological Sciences*. 38(4):406-424.
72. Koren E, Torchilin VP. Cell-penetrating peptides: breaking through to the other side. *Trends in Molecular Medicine*. 2012;18(7):385-393.
73. Jiao C-Y, Delaroché D, Burlina F, Alves ID, Chassaing G, Sagan S. Translocation and Endocytosis for Cell-penetrating Peptide Internalization. *Journal of Biological Chemistry*. 2009;284(49):33957-33965.
74. Madani F, Lindberg S, Langel, #220, Ito, Futaki S, Gr, #228, Slund A. Mechanisms of Cellular Uptake of Cell-Penetrating Peptides. *Journal of Biophysics*. 2011;2011.
75. Kosuge M, Takeuchi T, Nakase I, Jones AT, Futaki S. Cellular Internalization and Distribution of Arginine-Rich Peptides as a Function of Extracellular Peptide Concentration, Serum, and Plasma Membrane Associated Proteoglycans. *Bioconjugate Chemistry*. 2008;19(3):656-664.
76. Fretz Marjan M, Penning Neal A, Al-Taei S, Futaki S, Takeuchi T, Nakase I, Storm G, Jones Arwyn T. Temperature-, concentration- and cholesterol-dependent translocation of L- and D-octa-arginine across the plasma and nuclear membrane of CD34+ leukaemia cells. *Biochemical Journal*. 2007;403(2):335-342.
77. Frankel AD, Pabo CO. Cellular uptake of the tat protein from human immunodeficiency virus. *Cell*. 1988;55(6):1189-1193.
78. Joliot A, Pernelle C, Deagostini-Bazin H, Prochiantz A. Antennapedia homeobox peptide regulates neural morphogenesis. *Proceedings of the National Academy of Sciences*. 1991;88(5):1864-1868.
79. Copolovici DM, Langel K, Eriste E, Langel Ü. Cell-Penetrating Peptides: Design, Synthesis, and Applications. *ACS Nano*. 2014;8(3):1972-1994.
80. Nascimento FD, Hayashi MAF, Kerkis A, Oliveira V, Oliveira EB, Rádiz-Baptista G, Nader HB, Yamane T, dos Santos Tersariol IL, Kerkis I. Crotonamine Mediates Gene Delivery into Cells through the Binding to Heparan Sulfate Proteoglycans. *Journal of Biological Chemistry*. 2007;282(29):21349-21360.
81. Chen P-C, Hayashi MAF, Oliveira EB, Karpel RL. DNA-Interactive Properties of Crotonamine, a Cell-Penetrating Polypeptide and a Potential Drug Carrier. *PLOS ONE*. 2012;7(11):e48913.
82. Peschel A, Sahl H-G. The co-evolution of host cationic antimicrobial peptides and microbial resistance. *Nat Rev Micro*. 2006;4(7):529-536.
83. Andersson DI, Hughes D, Kubicek-Sutherland JZ. Mechanisms and consequences of bacterial resistance to antimicrobial peptides. *Drug Resistance Updates*. 2016;26:43-57.
84. Li M, Cha DJ, Lai Y, Villaruz AE, Sturdevant DE, Otto M. The antimicrobial peptide-sensing system *aps* of *Staphylococcus aureus*. *Molecular Microbiology*. 2007;66(5):1136-1147.
85. Shafer WM, Veal WL, Lee EH, Zarantonelli L, Balthazar JT, Rouquette C. Genetic organization and regulation of antimicrobial efflux systems possessed by *Neisseria gonorrhoeae* and *Neisseria meningitidis*. *J Mol Microbiol Biotechnol*. 2001;3(2):219-224.

86. Bader MW, Navarre WW, Shiau W, Nikaido H, Frye JG, McClelland M, Fang FC, Miller SI. Regulation of *Salmonella typhimurium* virulence gene expression by cationic antimicrobial peptides. *Molecular Microbiology*. 2003;50(1):219-230.
87. Sieprawska-Lupa M, Mydel P, Krawczyk K, Wójcik K, Puklo M, Lupa B, Suder P, Silberring J, Reed M, Pohl J, Shafer W, McAleese F, Foster T, Travis J, Potempa J. Degradation of Human Antimicrobial Peptide LL-37 by *Staphylococcus aureus*-Derived Proteinases. *Antimicrobial Agents and Chemotherapy*. 2004;48(12):4673-4679.
88. Guina T, Yi EC, Wang H, Hackett M, Miller SI. A PhoP-Regulated Outer Membrane Protease of *Salmonella enterica* Serovar Typhimurium Promotes Resistance to Alpha-Helical Antimicrobial Peptides. *Journal of Bacteriology*. 2000;182(14):4077-4086.
89. Fjell CD, Hiss JA, Hancock REW, Schneider G. Designing antimicrobial peptides: form follows function. *Nat Rev Drug Discov*. 2012;11(1):37-51.
90. Bacalum M, Radu M. Cationic Antimicrobial Peptides Cytotoxicity on Mammalian Cells: An Analysis Using Therapeutic Index Integrative Concept. *International Journal of Peptide Research and Therapeutics*. 2015;21(1):47-55.
91. Chen Y, Mant CT, Farmer SW, Hancock RE, Vasil ML, Hodges RS. Rational design of alpha-helical antimicrobial peptides with enhanced activities and specificity/therapeutic index. *J Biol Chem*. 2005;280(13):12316-12329.
92. Matsuzaki K. Control of cell selectivity of antimicrobial peptides. *Biochimica et Biophysica Acta (BBA) - Biomembranes*. 2009;1788(8):1687-1692.
93. Flamm RK, Rhomberg PR, Simpson KM, Farrell DJ, Sader HS, Jones RN. In Vitro Spectrum of Pexiganan Activity When Tested against Pathogens from Diabetic Foot Infections and with Selected Resistance Mechanisms. *Antimicrobial Agents and Chemotherapy*. 2015;59(3):1751-1754.
94. Khandelia H, Kaznessis YN. Molecular dynamics simulations of helical antimicrobial peptides in SDS micelles: what do point mutations achieve? *Peptides*. 2005;26(11):2037-2049.
95. Kavanagh K, Dowd S. Histatins: antimicrobial peptides with therapeutic potential. *Journal of Pharmacy and Pharmacology*. 2004;56(3):285-289.
96. Oudhoff MJ, Bolscher JGM, Nazmi K, Kalay H, van 't Hof W, Amerongen AVN, Veerman ECI. Histatins are the major wound-closure stimulating factors in human saliva as identified in a cell culture assay. *The FASEB Journal*. 2008;22(11):3805-3812.
97. Rivas L, Luque-Ortega JR, Andreu D. Amphibian antimicrobial peptides and Protozoa: Lessons from parasites. *Biochimica et Biophysica Acta (BBA) - Biomembranes*. 2009;1788(8):1570-1581.
98. Klotman ME, Chang TL. Defensins in innate antiviral immunity. *Nat Rev Immunol*. 2006;6(6):447-456.
99. Hazrati E, Galen B, Lu W, Wang W, Ouyang Y, Keller MJ, Lehrer RI, Herold BC. Human α - and β -Defensins Block Multiple Steps in Herpes Simplex Virus Infection. *The Journal of Immunology*. 2006;177(12):8658-8666.
100. Hsieh I-N, Hartshorn K. The Role of Antimicrobial Peptides in Influenza Virus Infection and Their Potential as Antiviral and Immunomodulatory Therapy. *Pharmaceuticals*. 2016;9(3):53.
101. Pachón-Ibáñez ME, Smani Y, Pachón J, Sánchez-Céspedes J. Perspectives for clinical use of engineered human host defense antimicrobial peptides. *FEMS Microbiology Reviews*. 2017;41(3):323-342.

102. Currie SM, Findlay EG, McHugh BJ, Mackellar A, Man T, Macmillan D, Wang H, Fitch PM, Schwarze J, Davidson DJ. The Human Cathelicidin LL-37 Has Antiviral Activity against Respiratory Syncytial Virus. *PLOS ONE*. 2013;8(8):e73659.
103. Currie SM, Gwyer Findlay E, McFarlane AJ, Fitch PM, Böttcher B, Colegrave N, Paras A, Jozwik A, Chiu C, Schwarze J, Davidson DJ. Cathelicidins Have Direct Antiviral Activity against Respiratory Syncytial Virus In Vitro and Protective Function In Vivo in Mice and Humans. *The Journal of Immunology*. 2016;196(6):2699-2710.
104. Doss M, Ruchala P, Tecele T, Gantz D, Verma A, Hartshorn A, Crouch EC, Luong H, Micewicz ED, Lehrer RI, Hartshorn KL. Hapivirins and Diprovirins: Novel θ -Defensin Analogs with Potent Activity against Influenza A Virus. *The Journal of Immunology*. 2012;188(6):2759-2768.
105. Gaspar D, Veiga AS, Castanho MARB. From antimicrobial to anticancer peptides. A review. *Frontiers in Microbiology*. 2013;4:294.
106. Schweizer F. Cationic amphiphilic peptides with cancer-selective toxicity. *European Journal of Pharmacology*. 2009;625(1-3):190-194.
107. Papo N, Shai Y. Host defense peptides as new weapons in cancer treatment. *Cellular and Molecular Life Sciences CMLS*. 2005;62(7-8):784-790.
108. Mulder K, Lima LA, Miranda V, Dias S, Franco O. Current scenario of peptide-based drugs: the key roles of cationic antitumor and antiviral peptides. *Frontiers in Microbiology*. 2013;4(321).
109. Bhutia SK, Maiti TK. Targeting tumors with peptides from natural sources. *Trends in Biotechnology*. 2008;26(4):210-217.
110. Chernysh S, Kim SI, Bekker G, Pleskach VA, Filatova NA, Anikin VB, Platonov VG, Bulet P. Antiviral and antitumor peptides from insects. *Proceedings of the National Academy of Sciences of the United States of America*. 2002;99(20):12628-12632.
111. Hoskin DW, Ramamoorthy A. Studies on anticancer activities of antimicrobial peptides. *Biochimica et Biophysica Acta (BBA) - Biomembranes*. 2008;1778(2):357-375.
112. Suttman H, Retz M, Paulsen F, Harder J, Zwergel U, Kamradt J, Wullich B, Unteregger G, Stöckle M, Lehmann J. Antimicrobial peptides of the Cecropin-family show potent antitumor activity against bladder cancer cells. *BMC Urology*. 2008;8(1):5.
113. Lehmann J, Retz M, Sidhu SS, Suttman H, Sell M, Paulsen F, Harder J, Unteregger G, Stöckle M. Antitumor Activity of the Antimicrobial Peptide Magainin II against Bladder Cancer Cell Lines. *European Urology*. 2006;50(1):141-147.
114. Yang D, Zou R, Zhu Y, Liu B, Yao D, Jiang J, Wu J, Tian H. Magainin II modified polydiacetylene micelles for cancer therapy. *Nanoscale*. 2014;6(24):14772-14783.
115. Felício MR, Silva ON, Gonçalves S, Santos NC, Franco OL. Peptides with Dual Antimicrobial and Anticancer Activities. *Frontiers in Chemistry*. 2017;5(5).
116. Xu H, Chen CX, Hu J, Zhou P, Zeng P, Cao CH, Lu JR. Dual modes of antitumor action of an amphiphilic peptide A9K. *Biomaterials*. 2013;34(11):2731-2737.
117. Hu J, Chen C, Zhang S, Zhao X, Xu H, Zhao X, Lu JR. Designed Antimicrobial and Antitumor Peptides with High Selectivity. *Biomacromolecules*. 2011;12(11):3839-3843.

118. Chen C, Hu J, Zeng P, Pan F, Yaseen M, Xu H, Lu JR. Molecular mechanisms of anticancer action and cell selectivity of short α -helical peptides. *Biomaterials*. 2014;35(5):1552-1561.
119. Lee CH, Patino H, Stevens C, Rege S, Chesnel L, Louie T, Mullane KM. Surotomylin versus vancomycin for *Clostridium difficile* infection: Phase 2, randomized, controlled, double-blind, non-inferiority, multicentre trial. *Journal of Antimicrobial Chemotherapy*. 2016;71(10):2964-2971.
120. Fujimaki T, Itoh K, Terasaki M, Narita Y, Arakawa Y, Sugiyama K, Nishikawa R, Aoki T, Kumabe T, Nagane M. P07.02 Trials of a personalized peptide vaccine (ITK-1) for patients with recurrent or progressive glioblastoma (GBM). *Neuro-Oncology*. 2017;19(suppl_3):iii52-iii52.
121. Dissanayake S, Denny WA, Gamage S, Sarojini V. Recent developments in anticancer drug delivery using cell penetrating and tumor targeting peptides. *Journal of Controlled Release*. 2017;250:62-76.
122. Roveri M, Bernasconi M, Leroux J-C, Luciani P. Peptides for tumor-specific drug targeting: state of the art and beyond. *Journal of Materials Chemistry B*. 2017;5(23):4348-4364.
123. Régina A, Demeule M, Ché C, Lavallée I, Poirier J, Gabathuler R, Béliveau R, Castaigne JP. Antitumour activity of ANG1005, a conjugate between paclitaxel and the new brain delivery vector Angiopep-2. *British Journal of Pharmacology*. 2008;155(2):185-197.
124. Regina A, Demeule M, Tripathy S, Lord-Dufour S, Currie J-C, Iddir M, Annabi B, Castaigne J-P, Lachowicz JE. ANG4043, a Novel Brain-Penetrant Peptide–mAb Conjugate, Is Efficacious against HER2-Positive Intracranial Tumors in Mice. *Molecular Cancer Therapeutics*. 2015;14(1):129-140.
125. Zelezetsky I, Tossi A. Alpha-helical antimicrobial peptides—Using a sequence template to guide structure–activity relationship studies. *Biochimica et Biophysica Acta (BBA) - Biomembranes*. 2006;1758(9):1436-1449.
126. Chen C, Pan F, Zhang S, Hu J, Cao M, Wang J, Xu H, Zhao X, Lu JR. Antibacterial Activities of Short Designer Peptides: a Link between Propensity for Nanostructuring and Capacity for Membrane Destabilization. *Biomacromolecules*. 2010;11(2):402-411.
127. Jullian M, Hernandez A, Maurras A, Puget K, Amblard M, Martinez J, Subra G. N-terminus FITC labeling of peptides on solid support: the truth behind the spacer. *Tetrahedron Letters*. 2009;50(3):260-263.
128. Giard DJ, Aaronson SA, Todaro GJ, Arnstein P, Kersey JH, Dosik H, Parks WP. In Vitro Cultivation of Human Tumors: Establishment of Cell Lines Derived From a Series of Solid Tumors. *Journal of the National Cancer Institute*. 1973;51(5):1417-1423.
129. Akan P, Alexeyenko A, Costea P, Hedberg L, Solnestam B, Lundin S, Hallman J, Lundberg E, Uhlen M, Lundeborg J. Comprehensive analysis of the genome transcriptome and proteome landscapes of three tumor cell lines. *Genome Medicine*. 2012;4(11):86.
130. Brattain MG, Fine WD, Khaled FM, Thompson J, Brattain DE. Heterogeneity of Malignant Cells from a Human Colonic Carcinoma. *Cancer Research*. 1981;41(5):1751-1756.
131. Schroy PC, Brown-Shimer, S., Kim, K., Johnson, K. A., Murnane, M. J., Yang, S., O'brein, M. J., Carney, W. P. and Kupchik, H. Z. . Detection of p21ras mutations in colorectal adenomas and carcinomas by enzyme-linked immunosorbent assay. *Cancer*. 1995;76(2).

132. Lügering N KT, Gockel H, Sorg C, Stoll R, Domschke W. . Human intestinal epithelial cells down-regulate IL-8 expression in human intestinal microvascular endothelial cells; role of transforming growth factor-beta 1 (TGF-b1). *Clinical and Experimental Immunology*. 1998;114(3).
133. Sharma S, Rao A. RNAi screening: tips and techniques. *Nature immunology*. 2009;10(8):799-804.
134. Zanoni M, Piccinini F, Arienti C, Zamagni A, Santi S, Polico R, Bevilacqua A, Tesei A. 3D tumor spheroid models for in vitro therapeutic screening: a systematic approach to enhance the biological relevance of data obtained. *Scientific Reports*. 2016;6:19103.
135. Fennema E, Rivron N, Rouwkema J, van Blitterswijk C, de Boer J. Spheroid culture as a tool for creating 3D complex tissues. *Trends in Biotechnology*. 2013;31(2):108-115.
136. Xie JIE, Lei P, Hu Y. Small interfering RNA-induced inhibition of epithelial cell transforming sequence 2 suppresses the proliferation, migration and invasion of osteosarcoma cells. *Experimental and Therapeutic Medicine*. 2015;9(5):1881-1886.
137. Spänkuch-Schmitt B, Bereiter-Hahn J, Kaufmann M, Strebhardt K. Effect of RNA Silencing of Polo-Like Kinase-1 (PLK1) on Apoptosis and Spindle Formation in Human Cancer Cells. *Journal of the National Cancer Institute*. 2002;94(24):1863-1877.
138. Liu X, Lei M, Erikson RL. Normal Cells, but Not Cancer Cells, Survive Severe Plk1 Depletion. *Molecular and Cellular Biology*. 2006;26(6):2093-2108.
139. Ivatt RM, Sanchez-Martinez A, Godena VK, Brown S, Ziviani E, Whitworth AJ. Genome-wide RNAi screen identifies the Parkinson disease GWAS risk locus SREBF1 as a regulator of mitophagy. *Proceedings of the National Academy of Sciences*. 2014;111(23):8494-8499.
140. van de Loosdrecht AA, Beelen RHJ, Ossenkoppele GJ, Broekhoven MG, Langenhuijsen MMAC. A tetrazolium-based colorimetric MTT assay to quantitate human monocyte mediated cytotoxicity against leukemic cells from cell lines and patients with acute myeloid leukemia. *Journal of Immunological Methods*. 1994;174(1-2):311-320.
141. Mosmann T. Rapid colorimetric assay for cellular growth and survival: Application to proliferation and cytotoxicity assays. *Journal of Immunological Methods*. 1983;65(1-2):55-63.
142. Slater TF, Sawyer B, Sträuli U. Studies on succinate-tetrazolium reductase systems: III. Points of coupling of four different tetrazolium salts III. Points of coupling of four different tetrazolium salts. *Biochimica et Biophysica Acta*. 1963;77(0):383-393.
143. Perelman A, Wachtel C, Cohen M, Haupt S, Shapiro H, Tzur A. JC-1: alternative excitation wavelengths facilitate mitochondrial membrane potential cytometry. *Cell Death Dis*. 2012;3:e430.
144. Goldberg MW, Fiserova J. Immunogold Labelling for Scanning Electron Microscopy. In: Schwartzbach SD, Osafune T, eds. *Immunolectron Microscopy: Methods and Protocols*. Totowa, NJ: Humana Press; 2010:297-313.
145. Sirerol-Piquer MS, Cebrián-Silla A, Alfaro-Cervelló C, Gomez-Pinedo U, Soriano-Navarro M, Verdugo J-MG. GFP immunogold staining, from light to electron microscopy, in mammalian cells. *Micron*. 2012;43(5):589-599.

146. Kimmel CB, Ballard WW, Kimmel SR, Ullmann B, Schilling TF. Stages of embryonic development of the zebrafish. *Developmental Dynamics*. 1995;203(3):253-310.
147. Hogan BM, Bos FL, Bussmann J, Witte M, Chi NC, Duckers HJ, Schulte-Merker S. *cobel* is required for embryonic lymphangiogenesis and venous sprouting. *Nat Genet*. 2009;41(4):396-398.
148. Xu Q. Microinjection into Zebrafish Embryos. In: Guille M, ed. *Molecular Methods in Developmental Biology: Xenopus and Zebrafish*. Totowa, NJ: Humana Press; 1999:125-132.
149. Rosen JN, Sweeney MF, Mably JD. Microinjection of Zebrafish Embryos to Analyze Gene Function. 2009(25):e1115.
150. Benard EL, van der Sar AM, Ellett F, Lieschke GJ, Spaink HP, Meijer AH. Infection of Zebrafish Embryos with Intracellular Bacterial Pathogens. *Journal of Visualized Experiments : JoVE*. 2012(61):3781.
151. Icha J, Schmied C, Sidhaye J, Tomancak P, Preibisch S, Norden C. Using Light Sheet Fluorescence Microscopy to Image Zebrafish Eye Development. 2016(110):e53966.
152. Hong G, Wu JZ, Robinson JT, Wang H, Zhang B, Dai H. Three-dimensional imaging of single nanotube molecule endocytosis on plasmonic substrates. *Nature Communications*. 2012;3:700.
153. Tomoda H, Kishimoto Y, Lee YC. Temperature effect on endocytosis and exocytosis by rabbit alveolar macrophages. *Journal of Biological Chemistry*. 1989;264(26):15445-15450.
154. Jamur MC, Oliver C. Permeabilization of Cell Membranes. In: Oliver C, Jamur MC, eds. *Immunocytochemical Methods and Protocols*. Totowa, NJ: Humana Press; 2010:63-66.
155. Semerdjieva S, Shortt B, Maxwell E, Singh S, Fonarev P, Hansen J, Schiavo G, Grant BD, Smythe E. Coordinated regulation of AP2 uncoating from clathrin-coated vesicles by rab5 and hRME-6. *The Journal of Cell Biology*. 2008;183(3):499-511.
156. Traub LM. Sorting it out: AP-2 and alternate clathrin adaptors in endocytic cargo selection. *The Journal of Cell Biology*. 2003;163(2):203-208.
157. Goley ED, Welch MD. The ARP2/3 complex: an actin nucleator comes of age. *Nat Rev Mol Cell Biol*. 2006;7(10):713-726.
158. Royle SJ. The cellular functions of clathrin. *Cellular and molecular life sciences : CMLS*. 2006;63(16):1823-1832.
159. Donaldson JG. Multiple Roles for Arf6: Sorting, Structuring, and Signaling at the Plasma Membrane. *Journal of Biological Chemistry*. 2003;278(43):41573-41576.
160. Liu P, Rudick M, Anderson RGW. Multiple Functions of Caveolin-1. *Journal of Biological Chemistry*. 2002;277(44):41295-41298.
161. Ferguson SM, De Camilli P. Dynamin, a membrane-remodelling GTPase. *Nat Rev Mol Cell Biol*. 2012;13(2):75-88.
162. Trybus KM. Myosin V from head to tail. *Cellular and molecular life sciences : CMLS*. 2008;65(9):1378-1389.
163. Lapierre LA, Kumar R, Hales CM, Navarre J, Bhartur SG, Burnette JO, Provance DW, Mercer JA, Bähler M, Goldenring JR. Myosin Vb Is Associated with Plasma Membrane Recycling Systems. *Molecular Biology of the Cell*. 2001;12(6):1843-1857.
164. Zhang M, Chen L, Wang S, Wang T. Rab7: roles in membrane trafficking and disease. *Bioscience Reports*. 2009;29(3):193-209.

165. Zhang L, Rozek A, Hancock REW. Interaction of Cationic Antimicrobial Peptides with Model Membranes. *Journal of Biological Chemistry*. 2001;276(38):35714-35722.
166. Shai Y. Mode of action of membrane active antimicrobial peptides. *Peptide Science*. 2002;66(4):236-248.
167. Silhavy TJ, Kahne D, Walker S. The Bacterial Cell Envelope. *Cold Spring Harbor Perspectives in Biology*. 2010;2(5):a000414.
168. Giangaspero A, Sandri L, Tossi A. Amphipathic α helical antimicrobial peptides. *European Journal of Biochemistry*. 2001;268(21):5589-5600.
169. Jiang Z, Vasil AI, Hale JD, Hancock REW, Vasil ML, Hodges RS. Effects of Net Charge and the Number of Positively Charged Residues on the Biological Activity of Amphipathic α -Helical Cationic Antimicrobial Peptides. *Biopolymers*. 2008;90(3):369-383.
170. Tang C, Qiu F, Zhao X. Molecular Design and Applications of Self-Assembling Surfactant-Like Peptides. *Journal of Nanomaterials*. 2013;2013:9.
171. von Maltzahn G, Vauthey S, Santoso S, Zhang S. Positively Charged Surfactant-like Peptides Self-assemble into Nanostructures. *Langmuir*. 2003;19(10):4332-4337.
172. Dehsorkhi A, Castelletto V, Hamley IW. Self-assembling amphiphilic peptides. *Journal of Peptide Science*. 2014;20(7):453-467.
173. Colherinhas G, Fileti E. Molecular Dynamics Study of Surfactant-Like Peptide Based Nanostructures. *The Journal of Physical Chemistry B*. 2014;118(42):12215-12222.
174. Wang J, Han S, Meng G, Xu H, Xia D, Zhao X, Schweins R, Lu JR. Dynamic self-assembly of surfactant-like peptides A6K and A9K. *Soft Matter*. 2009;5(20):3870-3878.
175. Xu H, Wang J, Han S, Wang J, Yu D, Zhang H, Xia D, Zhao X, Waigh TA, Lu JR. Hydrophobic-Region-Induced Transitions in Self-Assembled Peptide Nanostructures. *Langmuir*. 2009;25(7):4115-4123.
176. Han S, Cao S, Wang Y, Wang J, Xia D, Xu H, Zhao X, Lu JR. Self-Assembly of Short Peptide Amphiphiles: The Cooperative Effect of Hydrophobic Interaction and Hydrogen Bonding. *Chemistry – A European Journal*. 2011;17(46):13095-13102.
177. Chen C, Hu J, Zhang S, Zhou P, Zhao X, Xu H, Zhao X, Yaseen M, Lu JR. Molecular mechanisms of antibacterial and antitumor actions of designed surfactant-like peptides. *Biomaterials*. 2012;33(2):592-603.
178. Yin LM, Edwards MA, Li J, Yip CM, Deber CM. Roles of Hydrophobicity and Charge Distribution of Cationic Antimicrobial Peptides in Peptide-Membrane Interactions. *Journal of Biological Chemistry*. 2012;287(10):7738-7745.
179. Chen J-X, Xu X-D, Yang S, Yang J, Zhuo R-X, Zhang X-Z. Self-Assembled BOLA-like Amphiphilic Peptides as Viral-Mimetic Gene Vectors for Cancer Cell Targeted Gene Delivery. *Macromolecular Bioscience*. 2013;13(1):84-92.
180. Damen M, Aarbiou J, van Dongen SFM, Buijs-Offerman RM, Spijkers PP, van den Heuvel M, Kvashnina K, Nolte RJM, Scholte BJ, Feiters MC. Delivery of DNA and siRNA by novel gemini-like amphiphilic peptides. *Journal of Controlled Release*. 2010;145(1):33-39.
181. Fominaya J, Gasset M, García R, Roncal F, Pablo Albar J, Bernad A. An optimized amphiphilic cationic peptide as an efficient non-viral gene delivery vector. *The Journal of Gene Medicine*. 2000;2(6):455-464.

182. Koloskova OO, Nikonova AA, Budanova UA, Shilovskiy IP, Kofiadi IA, Ivanov AV, Smirnova OA, Zverev VV, Sebaykin YL, Andreev SM, Khaitov MR. Synthesis and evaluation of novel lipopeptide as a vehicle for efficient gene delivery and gene silencing. *European Journal of Pharmaceutics and Biopharmaceutics*. 2016;102:159-167.
183. Luan L, Meng Q, Xu L, Meng Z, Yan H, Liu K. Peptide amphiphiles with multifunctional fragments promoting cellular uptake and endosomal escape as efficient gene vectors. *Journal of Materials Chemistry B*. 2015;3(6):1068-1078.
184. Zhu Y, Sheng R, Luo T, Li H, Sun W, Li Y, Cao A. Amphiphilic Cationic [Dendritic poly(L-lysine)]-block-poly(L-lactide)-block-[dendritic poly(L-lysine)]s in Aqueous Solution: Self-Aggregation and Interaction with DNA as Gene Delivery Carriers. *Macromolecular Bioscience*. 2011;11(2):174-186.
185. Agrawal N, Dasaradhi PVN, Mohammed A, Malhotra P, Bhatnagar RK, Mukherjee SK. RNA Interference: Biology, Mechanism, and Applications. *Microbiology and Molecular Biology Reviews*. 2003;67(4):657-685.
186. Zuckerman JE, Davis ME. Clinical experiences with systemically administered siRNA-based therapeutics in cancer. *Nat Rev Drug Discov*. 2015;14(12):843-856.
187. Whitehead KA, Langer R, Anderson DG. Knocking down barriers: advances in siRNA delivery. *Nat Rev Drug Discov*. 2009;8(2):129-138.
188. Wittrup A, Lieberman J. Knocking down disease: a progress report on siRNA therapeutics. *Nat Rev Genet*. 2015;16(9):543-552.
189. Minchinton AI, Tannock IF. Drug penetration in solid tumours. *Nat Rev Cancer*. 2006;6(8):583-592.
190. Weiswald L-B, Bellet D, Dangles-Marie V. Spherical Cancer Models in Tumor Biology. *Neoplasia*. 2015;17(1):1-15.
191. Tung Y-C, Hsiao AY, Allen SG, Torisawa Y-s, Ho M, Takayama S. High-throughput 3D spheroid culture and drug testing using a 384 hanging drop array. *Analyst*. 2011;136(3):473-478.
192. Karlsson H, Fryknäs M, Larsson R, Nygren P. Loss of cancer drug activity in colon cancer HCT-116 cells during spheroid formation in a new 3-D spheroid cell culture system. *Experimental Cell Research*. 2012;318(13):1577-1585.
193. Wei B, Han X-Y, Qi C-L, Zhang S, Zheng Z-H, Huang Y, Chen T-F, Wei H-B. Coaction of Spheroid-Derived Stem-Like Cells and Endothelial Progenitor Cells Promotes Development of Colon Cancer. *PLoS ONE*. 2012;7(6):e39069.
194. Pampaloni F, Ansari N, Stelzer EHK. High-resolution deep imaging of live cellular spheroids with light-sheet-based fluorescence microscopy. *Cell and Tissue Research*. 2013;352(1):161-177.
195. Huff LP, DeCristo MJ, Trembath D, Kuan PF, Yim M, Liu J, Cook DR, Miller CR, Der CJ, Cox AD. The Role of Ect2 Nuclear RhoGEF Activity in Ovarian Cancer Cell Transformation. *Genes & Cancer*. 2013;4(11-12):460-475.
196. He D, Xiang J, Li B, Liu H. The dynamic behavior of Ect2 in response to DNA damage. *Scientific Reports*. 2016;6:24504.
197. van Vugt MATM, Medema RH. Getting in and out of mitosis with Polo-like kinase-1. *Oncotarget*. 2016;7(17):2844-2859.
198. Murata Y, Minami Y, Iwakawa R, Yokota J, Usui S, Tsuta K, Shiraishi K, Sakashita S, Satomi K, Iijima T, Noguchi M. ECT2 amplification and overexpression as a new prognostic biomarker for early-stage lung adenocarcinoma. *Cancer Science*. 2014;105(4):490-497.

199. Luo Y, Qin S-L, Mu Y-F, Wang Z-S, Zhong M, Bian Z-Q. Elevated expression of ECT2 predicts unfavorable prognosis in patients with colorectal cancer. *Biomedicine & Pharmacotherapy*. 2015;73:135-139.
200. Jin Y, Yu Y, Shao Q, Ma Y, Zhang R, Yao H, Xu Y. Up-regulation of ECT2 is associated with poor prognosis gastric cancer patients. *International Journal of Clinical and Experimental Pathology*. 2014;7(12):8724-8731.
201. Weng Ng WT, Shin J-S, Roberts TL, Wang B, Lee CS. Molecular interactions of polo-like kinase 1 in human cancers. *Journal of Clinical Pathology*. 2016;69(7):557-562.
202. Tut TG, Lim SHS, Dissanayake IU, Descallar J, Chua W, Ng W, de Souza P, Shin JS, Lee CS. Upregulated Polo-Like Kinase 1 Expression Correlates with Inferior Survival Outcomes in Rectal Cancer. *PLOS ONE*. 2015;10(6):e0129313.
203. Takahashi T, Sano B, Nagata T, Kato H, Sugiyama Y, Kunieda K, Kimura M, Okano Y, Saji S. Polo-like kinase 1 (PLK1) is overexpressed in primary colorectal cancers. *Cancer Science*. 2003;94(2):148-152.
204. Han D-p, Zhu Q-l, Cui J-t, Wang P-x, Qu S, Cao Q-f, Zong Y-p, Feng B, Zheng M-h, Lu A-g. Polo-like kinase 1 is overexpressed in colorectal cancer and participates in the migration and invasion of colorectal cancer cells. *Medical Science Monitor : International Medical Journal of Experimental and Clinical Research*. 2012;18(6):BR237-BR246.
205. Zhang W, Li J, Liu L-W, Wang K-R, Song J-J, Yan J-X, Li Z-Y, Zhang B-Z, Wang R. A novel analog of antimicrobial peptide Polybia-MPI, with thioamide bond substitution, exhibits increased therapeutic efficacy against cancer and diminished toxicity in mice. *Peptides*. 2010;31(10):1832-1838.
206. Hilchie A, Doucette C, Pinto D, Patrzykat A, Douglas S, Hoskin D. Pleurocidin-family cationic antimicrobial peptides are cytolytic for breast carcinoma cells and prevent growth of tumor xenografts. *Breast Cancer Research*. 2011;13(5):R102.
207. Sinthuvanich C, Veiga AS, Gupta K, Gaspar D, Blumenthal R, Schneider JP. Anticancer beta-hairpin peptides: membrane-induced folding triggers activity. *J Am Chem Soc*. 2012;134(14):6210-6217.
208. Berridge MV, Herst PM, Tan AS. Tetrazolium dyes as tools in cell biology: New insights into their cellular reduction. In: El-Gewely MR, ed. *Biotechnology Annual Review*. Vol Volume 11: Elsevier; 2005:127-152.
209. Wise SS, Holmes AL, Wise Sr JP. Particulate and soluble hexavalent chromium are cytotoxic and genotoxic to human lung epithelial cells. *Mutation Research/Genetic Toxicology and Environmental Mutagenesis*. 2006;610(1-2):2-7.
210. Nijs M, Kirsch-Volders M. Induction of spindle inhibition and abnormal mitotic figures by Cr(II), Cr(III) and Cr(VI) ions. *Mutagenesis*. 1986;1(4):247-252.
211. Liu Y, Peterson DA, Kimura H, Schubert D. Mechanism of Cellular 3-(4,5-Dimethylthiazol-2-yl)-2,5-Diphenyltetrazolium Bromide (MTT) Reduction. *Journal of Neurochemistry*. 1997;69(2):581-593.
212. Kholmukhamedov A, Schwartz JM, Lemasters JJ. MitoTracker Probes and Mitochondrial Membrane Potential. *Shock (Augusta, Ga.)*. 2013;39(6):543-543.
213. Karbowski M, Youle RJ. Dynamics of mitochondrial morphology in healthy cells and during apoptosis. *Cell Death Differ*. 0000;10(8):870-880.

214. Risso A, Braidot E, Sordano MC, Vianello A, Macrì F, Skerlavaj B, Zanetti M, Gennaro R, Bernardi P. BMAP-28, an Antibiotic Peptide of Innate Immunity, Induces Cell Death through Opening of the Mitochondrial Permeability Transition Pore. *Molecular and Cellular Biology*. 2002;22(6):1926-1935.
215. Perry SW, Norman JP, Barbieri J, Brown EB, Gelbard HA. Mitochondrial membrane potential probes and the proton gradient: a practical usage guide. *BioTechniques*. 2011;50(2):98-115.
216. Li X, Shen B, Chen Q, Zhang X, Ye Y, Wang F, Zhang X. Antitumor effects of cecropin B-LHRH' on drug-resistant ovarian and endometrial cancer cells. *BMC Cancer*. 2016;16:251.
217. Brown JM, Wilson WR. Exploiting tumour hypoxia in cancer treatment. *Nat Rev Cancer*. 2004;4(6):437-447.
218. Cook DR, Rossman KL, Der CJ. Rho guanine nucleotide exchange factors: regulators of Rho GTPase activity in development and disease. *Oncogene*. 2014;33(31):4021-4035.
219. Fields AP, Justilien V. The guanine nucleotide exchange factor (GEF) Ect2 is an oncogene in human cancer. *Advances in Enzyme Regulation*. 2010;50(1):190-200.
220. Iyoda M, Kasamatsu A, Ishigami T, Nakashima D, Endo-Sakamoto Y, Ogawara K, Shiiba M, Tanzawa H, Uzawa K. Epithelial Cell Transforming Sequence 2 in Human Oral Cancer. *PLOS ONE*. 2010;5(11):e14082.
221. Zitouni S, Nabais C, Jana SC, Guerrero A, Bettencourt-Dias M. Polo-like kinases: structural variations lead to multiple functions. *Nat Rev Mol Cell Biol*. 2014;15(7):433-452.
222. Lu L-Y, Yu X. The balance of Polo-like kinase 1 in tumorigenesis. *Cell Division*. 2009;4(1):4.
223. Gjertsen BT, Schoffski P. Discovery and development of the Polo-like kinase inhibitor volasertib in cancer therapy. *Leukemia*. 2015;29(1):11-19.
224. Wieland T, de Vries JX, Schäfer A, Faulstich H. Spectroscopic evidence for the interaction of phalloidin with actin. *FEBS Letters*. 1975;54(1):73-75.
225. Wieland T, Govindan VM. Phallotoxins bind to actins. *FEBS Letters*. 1974;46(1-2):351-353.
226. Fielding AB, Willox AK, Okeke E, Royle SJ. Clathrin-mediated endocytosis is inhibited during mitosis. *Proceedings of the National Academy of Sciences*. 2012;109(17):6572-6577.
227. Cummings BS, Wills LP, Schnellmann RG. Measurement of Cell Death in Mammalian Cells. *Current protocols in pharmacology*. 2004;0 12:10.1002/0471141755.ph0471141208s0471141725.
228. Hällbrink M, Oehlke J, Papsdorf G, Bienert M. Uptake of cell-penetrating peptides is dependent on peptide-to-cell ratio rather than on peptide concentration. *Biochimica et Biophysica Acta (BBA) - Biomembranes*. 2004;1667(2):222-228.
229. McMullan D. Scanning electron microscopy 1928–1965. *Scanning*. 1995;17(3):175-185.
230. Vernon-Parry KD. Scanning electron microscopy: an introduction. *III-Vs Review*. 2000;13(4):40-44.
231. Winey M, Meehl JB, O'Toole ET, Giddings TH. Conventional transmission electron microscopy. *Molecular Biology of the Cell*. 2014;25(3):319-323.
232. Gold nanoparticles delivery in mammalian live cells: a critical review. *Nano Reviews*. 2010;1(1):4889.

233. Cai W, Gao T, Hong H, Sun J. Applications of gold nanoparticles in cancer nanotechnology. *Nanotechnology, science and applications*. 2008;2008(1):10.2147/NSA.S3788.
234. Dykman L, Khlebtsov N. Gold nanoparticles in biomedical applications: recent advances and perspectives. *Chemical Society Reviews*. 2012;41(6):2256-2282.
235. Mechanisms of Endocytosis. *Annual Review of Biochemistry*. 2009;78(1):857-902.
236. Kumari S, Mg S, Mayor S. Endocytosis unplugged: multiple ways to enter the cell. *Cell Res*. 2010;20(3):256-275.
237. Mayor S, Pagano RE. Pathways of clathrin-independent endocytosis. *Nat Rev Mol Cell Biol*. 2007;8(8):603-612.
238. Perumal OP, Inapagolla R, Kannan S, Kannan RM. The effect of surface functionality on cellular trafficking of dendrimers. *Biomaterials*. 2008;29(24):3469-3476.
239. Panyam J, Labhasetwar V. Dynamics of Endocytosis and Exocytosis of Poly(D,L-Lactide-co-Glycolide) Nanoparticles in Vascular Smooth Muscle Cells. *Pharmaceutical Research*. 2003;20(2):212-220.
240. Christophe Youta D, Maya K, Rima Z, Regis M, Didier B. Characterization of endocytosis and exocytosis of cationic nanoparticles in airway epithelium cells. *Nanotechnology*. 2010;21(35):355102.
241. Oh N, Park J-H. Endocytosis and exocytosis of nanoparticles in mammalian cells. *International Journal of Nanomedicine*. 2014;9(Suppl 1):51-63.
242. MacRae CA, Peterson RT. Zebrafish as tools for drug discovery. *Nat Rev Drug Discov*. 2015;14(10):721-731.
243. Streisinger G, Walker C, Dower N, Knauber D, Singer F. Production of clones of homozygous diploid zebra fish (*Brachydanio rerio*). *Nature*. 1981;291(5813):293-296.
244. Ribas L, Piferrer F. The zebrafish (*Danio rerio*) as a model organism, with emphasis on applications for finfish aquaculture research. *Reviews in Aquaculture*. 2014;6(4):209-240.
245. Nasiadka A, Clark MD. Zebrafish Breeding in the Laboratory Environment. *ILAR Journal*. 2012;53(2):161-168.
246. Novodvorsky P, Watson O, Gray C, Wilkinson RN, Reeve S, Smythe C, Beniston R, Plant K, Maguire R, M. K. Rothman A, Elworthy S, van Eeden FJM, Chico TJA. klf2ash317 Mutant Zebrafish Do Not Recapitulate Morpholino-Induced Vascular and Haematopoietic Phenotypes. *PLOS ONE*. 2015;10(10):e0141611.
247. Wilkinson RN, van Eeden FJM. Chapter Five - The Zebrafish as a Model of Vascular Development and Disease. In: Timothy JAC, ed. *Progress in Molecular Biology and Translational Science*. Vol Volume 124: Academic Press; 2014:93-122.
248. Wilkinson RN, Jopling C, van Eeden FJM. Chapter Four - Zebrafish as a Model of Cardiac Disease. In: Timothy JAC, ed. *Progress in Molecular Biology and Translational Science*. Vol Volume 124: Academic Press; 2014:65-91.
249. Dooley K, Zon LI. Zebrafish: a model system for the study of human disease. *Current Opinion in Genetics & Development*. 2000;10(3):252-256.
250. Sipes NS, Padilla S, Knudsen TB. Zebrafish—As an integrative model for twenty-first century toxicity testing. *Birth Defects Research Part C: Embryo Today: Reviews*. 2011;93(3):256-267.

251. He J-H, Gao J-M, Huang C-J, Li C-Q. Zebrafish models for assessing developmental and reproductive toxicity. *Neurotoxicology and Teratology*. 2014;42:35-42.
252. OECD. *Test No. 203: Fish, Acute Toxicity Test*: OECD Publishing.
253. OECD. *Test No. 236: Fish Embryo Acute Toxicity Test*: OECD Publishing.
254. Klüver N, König M, Ortmann J, Massei R, Paschke A, Kühne R, Scholz S. Fish Embryo Toxicity Test: Identification of Compounds with Weak Toxicity and Analysis of Behavioral Effects To Improve Prediction of Acute Toxicity for Neurotoxic Compounds. *Environmental Science & Technology*. 2015;49(11):7002-7011.
255. Kais B, Schneider KE, Keiter S, Henn K, Ackermann C, Braunbeck T. DMSO modifies the permeability of the zebrafish (*Danio rerio*) chorion-Implications for the fish embryo test (FET). *Aquatic Toxicology*. 2013;140–141:229-238.
256. Schubert S, Keddig N, Hanel R, Kammann U. Microinjection into zebrafish embryos (*Danio rerio*) - a useful tool in aquatic toxicity testing? *Environmental Sciences Europe*. 2014;26(1):32.
257. Chen S, Kimelman D. The role of the yolk syncytial layer in germ layer patterning in zebrafish. *Development*. 2000;127(21):4681-4689.
258. Westerfield M. *The zebrafish book. A guide for the laboratory use of zebrafish (Danio rerio)*. 4th ed; 2000.
259. Rohde LA, Heisenberg CP. Zebrafish Gastrulation: Cell Movements, Signals, and Mechanisms. *International Review of Cytology*. Vol Volume 261: Academic Press; 2007:159-192.
260. Kimmel CB, Warga RM, Schilling TF. Origin and organization of the zebrafish fate map. *Development*. 1990;108(4):581-594.
261. Ng ANY, de Jong-Curtain TA, Mawdsley DJ, White SJ, Shin J, Appel B, Dong PDS, Stainier DYR, Heath JK. Formation of the digestive system in zebrafish: III. Intestinal epithelium morphogenesis. *Developmental Biology*. 2005;286(1):114-135.
262. Wallace KN, Pack M. Unique and conserved aspects of gut development in zebrafish. *Developmental Biology*. 2003;255(1):12-29.
263. Liu W-Y, Wang Y, Sun Y-H, Wang Y, Wang Y-P, Chen S-P, Zhu Z-Y. Efficient RNA interference in zebrafish embryos using siRNA synthesized with SP6 RNA polymerase. *Development, Growth & Differentiation*. 2005;47(5):323-331.
264. Dodd A, Chambers SP, Love DR. Short interfering RNA-mediated gene targeting in the zebrafish. *FEBS Letters*. 2004;561(1–3):89-93.
265. Oates AC, Bruce AEE, Ho RK. Too Much Interference: Injection of Double-Stranded RNA Has Nonspecific Effects in the Zebrafish Embryo. *Developmental Biology*. 2000;224(1):20-28.
266. Wang L, Zhou J-y, Yao J-h, Lu D-r, Qiao X-j, Jia W. U6 promoter-driven siRNA injection has nonspecific effects in zebrafish. *Biochemical and Biophysical Research Communications*. 2010;391(3):1363-1368.
267. Zhao X-F, Fjose A, Larsen N, Helvik JV, Drivenes Ø. Treatment with small interfering RNA affects the microRNA pathway and causes unspecific defects in zebrafish embryos. *FEBS Journal*. 2008;275(9):2177-2184.
268. Nasevicius A, Ekker SC. Effective targeted gene 'knockdown' in zebrafish. *Nat Genet*. 2000;26(2):216-220.
269. Bill BR, Petzold AM, Clark KJ, Schimmenti LA, Ekker SC. A Primer for Morpholino Use in Zebrafish. *Zebrafish*. 2009;6(1):69-77.

270. Takaki K, Davis JM, Winglee K, Ramakrishnan L. Evaluation of the pathogenesis and treatment of Mycobacterium marinum infection in zebrafish. *Nature protocols*. 2013;8(6):1114-1124.
271. Lim J, Lee HK, Yu W, Ahmed S. Light sheet fluorescence microscopy (LSFM): past, present and future. *Analyst*. 2014;139(19):4758-4768.
272. Keller PJ. In vivo imaging of zebrafish embryogenesis. *Methods (San Diego, Calif.)*. 2013;62(3):268-278.
273. Arbiser JL. Zebrafish lead the way in control of vascular permeability. *Blood*. 2012;120(11):2162-2164.
274. Detrich Iii HW, Westerfield M, Zon LI. The Zebrafish: Cellular and Developmental Biology, Part 1. In: H. William Detrich MW, Leonard IZ, eds. *Methods in Cell Biology*. Vol Volume 100: Academic Press; 2010:xiii.
275. Jeong J-Y, Kwon H-B, Ahn J-C, Kang D, Kwon S-H, Park JA, Kim K-W. Functional and developmental analysis of the blood-brain barrier in zebrafish. *Brain Research Bulletin*. 2008;75(5):619-628.
276. Xie J, Farage E, Sugimoto M, Anand-Apte B. A novel transgenic zebrafish model for blood-brain and blood-retinal barrier development. *BMC Developmental Biology*. 2010;10(1):76.
277. Henson HE, Parupalli C, Ju B, Taylor MR. Functional and genetic analysis of choroid plexus development in zebrafish. *Frontiers in Neuroscience*. 2014;8:364.
278. Lee RC, Feinbaum RL, Ambros V. The *C. elegans* heterochronic gene *lin-4* encodes small RNAs with antisense complementarity to *lin-14*. *Cell*. 1993;75(5):843-854.
279. Kim VN, Han J, Siomi MC. Biogenesis of small RNAs in animals. *Nat Rev Mol Cell Biol*. 2009;10(2):126-139.
280. Carthew RW, Sontheimer EJ. Origins and Mechanisms of miRNAs and siRNAs. *Cell*. 2009;136(4):642-655.
281. Snead NM, Rossi JJ. Biogenesis and function of endogenous and exogenous siRNAs. *Wiley Interdisciplinary Reviews - RNA*. 2010;1(1):117-131.
282. Grimm D. Small silencing RNAs: State-of-the-art. *Advanced Drug Delivery Reviews*. 2009;61(9):672-703.
283. Cullen LM, Arndt GM. Genome-wide screening for gene function using RNAi in mammalian cells. *Immunol Cell Biol*. 2005;83(3):217-223.
284. Simpson JC, Joggerst B, Laketa V, Verissimo F, Cetin C, Erfle H, Bexiga MG, Singan VR, Heriche J-K, Neumann B, Mateos A, Blake J, Bechtel S, Benes V, Wiemann S, Ellenberg J, Pepperkok R. Genome-wide RNAi screening identifies human proteins with a regulatory function in the early secretory pathway. *Nat Cell Biol*. 2012;14(7):764-774.
285. Boutros M, Ahringer J. The art and design of genetic screens: RNA interference. *Nat Rev Genet*. 2008;9(7):554-566.
286. Mohr SE, Smith JA, Shamu CE, Neumuller RA, Perrimon N. RNAi screening comes of age: improved techniques and complementary approaches. *Nat Rev Mol Cell Biol*. 2014;15(9):591-600.
287. Mohr SE, Perrimon N. RNAi screening: new approaches, understandings, and organisms. *Wiley Interdisciplinary Reviews: RNA*. 2012;3(2):145-158.
288. Mohr S, Bakal C, Perrimon N. Genomic screening with RNAi: results and challenges. *Annu Rev Biochem*. 2010;79:37-64.
289. Zanella F, Lorens JB, Link W. High content screening: seeing is believing. *Trends in Biotechnology*. 2010;28(5):237-245.

290. Shatz M, Liscovitch M. Caveolin-1: A tumor-promoting role in human cancer. *International Journal of Radiation Biology*. 2008;84(3):177-189.
291. Ha T-K, Her N-G, Lee M-G, Ryu B-K, Lee J-H, Han J, Jeong S-I, Kang M-J, Kim N-H, Kim H-J, Chi S-G. Caveolin-1 Increases Aerobic Glycolysis in Colorectal Cancers by Stimulating HMGA1-Mediated *GLUT3* Transcription. *Cancer Research*. 2012;72(16):4097-4109.
292. Patlolla JM, Swamy MV, Raju J, Rao CV. Overexpression of caveolin-1 in experimental colon adenocarcinomas and human colon cancer cell lines. *Oncol Rep*. 2004;11(5):957-963.
293. Progida C, Cogli L, Piro F, De Luca A, Bakke O, Bucci C. Rab7b controls trafficking from endosomes to the TGN. *Journal of Cell Science*. 2010;123(9):1480-1491.
294. Birmingham A, Selfors LM, Forster T, Wrobel D, Kennedy CJ, Shanks E, Santoyo-Lopez J, Dunican DJ, Long A, Kelleher D, Smith Q, Beijersbergen RL, Ghazal P, Shamu CE. Statistical methods for analysis of high-throughput RNA interference screens. *Nat Meth*. 2009;6(8):569-575.
295. Fisher KH, Wright VM, Taylor A, Zeidler MP, Brown S. Advances in genome-wide RNAi cellular screens: a case study using the *Drosophila* JAK/STAT pathway. *BMC Genomics*. 2012;13:506-506.
296. Saiardi A, Sciambi C, McCaffery JM, Wendland B, Snyder SH. Inositol pyrophosphates regulate endocytic trafficking. *Proceedings of the National Academy of Sciences of the United States of America*. 2002;99(22):14206-14211.
297. Miller MA, Sullivan RJ, Lauffenburger DA. Molecular Pathways: Receptor Ectodomain Shedding in Treatment, Resistance, and Monitoring of Cancer. *Clinical Cancer Research*. 2017;23(3):623-629.
298. Sossey-Alaoui K, Ranalli TA, Li X, Bakin AV, Cowell JK. WAVE3 promotes cell motility and invasion through the regulation of MMP-1, MMP-3, and MMP-9 expression. *Experimental Cell Research*. 2005;308(1):135-145.
299. Woller B, Luiskandl S, Popovic M, Prieler BEM, Ikonge G, Mutzl M, Rehmann H, Herbst R. Rin-like, a novel regulator of endocytosis, acts as guanine nucleotide exchange factor for Rab5a and Rab22. *Biochimica et Biophysica Acta (BBA) - Molecular Cell Research*. 2011;1813(6):1198-1210.
300. Bucci C, Parton RG, Mather IH, Stunnenberg H, Simons K, Hoflack B, Zerial M. The small GTPase rab5 functions as a regulatory factor in the early endocytic pathway. *Cell*. 1992;70(5):715-728.
301. Yudowski GA, Puthenveedu MA, Henry AG, von Zastrow M. Cargo-Mediated Regulation of a Rapid Rab4-Dependent Recycling Pathway. *Molecular Biology of the Cell*. 2009;20(11):2774-2784.
302. Perrin L, Lacas-Gervais S, Gilleron J, Ceppo F, Prodon F, Benmerah A, Tanti J-F, Cormont M. Rab4b controls an early endosome sorting event by interacting with the γ -subunit of the clathrin adaptor complex 1. *Journal of Cell Science*. 2013;126(21):4950-4962.
303. Schonteich E, Wilson GM, Burden J, Hopkins CR, Anderson K, Goldenring JR, Prekeris R. The Rip11/Rab11-FIP5 and kinesin II complex regulates endocytic protein recycling. *Journal of Cell Science*. 2008;121(22):3824-3833.
304. Aoki T, Ichimura S, Itoh A, Kuramoto M, Shinkawa T, Isobe T, Tagaya M. Identification of the Neuroblastoma-amplified Gene Product as a Component of the Syntaxin 18 Complex Implicated in Golgi-to-Endoplasmic Reticulum Retrograde Transport. *Molecular Biology of the Cell*. 2009;20(11):2639-2649.

305. Tai G, Lu L, Wang TL, Tang BL, Goud B, Johannes L, Hong W. Participation of the Syntaxin 5/Ykt6/GS28/GS15 SNARE Complex in Transport from the Early/Recycling Endosome to the Trans-Golgi Network. *Molecular Biology of the Cell*. 2004;15(9):4011-4022.
306. Fusella A, Micaroni M, Di Giandomenico D, Mironov AA, Beznoussenko GV. Segregation of the Qb-SNAREs GS27 and GS28 into Golgi Vesicles Regulates Intra-Golgi Transport. *Traffic*. 2013;14(5):568-584.
307. Pooley RD, Reddy S, Soukoulis V, Roland JT, Goldenring JR, Bader DM. CytLEK1 Is a Regulator of Plasma Membrane Recycling through Its Interaction with SNAP-25. *Molecular Biology of the Cell*. 2006;17(7):3176-3186.
308. Jung J-J, Inamdar Shivangi M, Tiwari A, Choudhury A. Regulation of intracellular membrane trafficking and cell dynamics by syntaxin-6. *Bioscience Reports*. 2012;32(4):383-391.
309. Chen Y, Gan BQ, Tang BL. Syntaxin 16: Unraveling cellular physiology through a ubiquitous SNARE molecule. *Journal of Cellular Physiology*. 2010;225(2):326-332.
310. Gordon DE, Bond LM, Sahlender DA, Peden AA. A Targeted siRNA Screen to Identify SNAREs Required for Constitutive Secretion in Mammalian Cells. *Traffic*. 2010;11(9):1191-1204.
311. Pryor PR, Mullock BM, Bright NA, Lindsay MR, Gray SR, Richardson SCW, Stewart A, James DE, Piper RC, Luzio JP. Combinatorial SNARE complexes with VAMP7 or VAMP8 define different late endocytic fusion events. *EMBO reports*. 2004;5(6):590-595.
312. Fan J, Zhou X, Wang Y, Kuang C, Sun Y, Liu X, Toomre D, Xu Y. Differential requirement for N-ethylmaleimide-sensitive factor in endosomal trafficking of transferrin receptor from anterograde trafficking of vesicular stomatitis virus glycoprotein G. *FEBS Letters*. 2017;591(2):273-281.
313. Watkin LB, Jessen B, Wiszniewski W, Vece TJ, Jan M, Sha Y, Thamsen M, Santos-Cortez RLP, Lee K, Gambin T, Forbes LR, Law CS, Stray-Pedersen A, Cheng MH, Mace EM, Anderson MS, Liu D, Tang LF, Nicholas SK, Nahmod K, Makedonas G, Canter DL, Kwok P-Y, Hicks J, Jones KD, Penney S, Jhangiani SN, Rosenblum MD, Dell SD, Waterfield MR, Papa FR, Muzny DM, Zaitlen N, Leal SM, Gonzaga-Jauregui C, Baylor-Hopkins Center for Mendelian G, Boerwinkle E, Eissa NT, Gibbs RA, Lupski JR, Orange JS, Shum AK. COPA mutations impair ER-Golgi transport and cause hereditary autoimmune-mediated lung disease and arthritis. *Nat Genet*. 2015;47(6):654-660.
314. Finkielstein CV, Capelluto DGS. Disabled-2: A modular scaffold protein with multifaceted functions in signaling. *BioEssays*. 2016;38:S45-S55.
315. Wu Y, O'Toole ET, Girard M, Ritter B, Messa M, Liu X, McPherson PS, Ferguson SM, De Camilli P. A dynamin 1-, dynamin 3- and clathrin-independent pathway of synaptic vesicle recycling mediated by bulk endocytosis. *eLife*. 2014;3:e01621.
316. Stach L, Freemont PS. The AAA+ ATPase p97, a cellular multitool. *Biochemical Journal*. 2017;474(17):2953-2976.
317. Stein A, Ruggiano A, Carvalho P, Rapoport Tom A. Key Steps in ERAD of Luminal ER Proteins Reconstituted with Purified Components. *Cell*. 2014;158(6):1375-1388.
318. Park Sang Y, Guo X. Adaptor protein complexes and intracellular transport. *Bioscience Reports*. 2014;34(4):e00123.
319. Society AC. Cancer Facts and Figures 2017. *Atlanta, Ga: American Cancer Society*. 2017;2017.

320. Bentzen SM. Preventing or reducing late side effects of radiation therapy: radiobiology meets molecular pathology. *Nat Rev Cancer*. 2006;6(9):702-713.
321. Hanahan D, Weinberg Robert A. Hallmarks of Cancer: The Next Generation. *Cell*. 2011;144(5):646-674.
322. Sasada T, Noguchi M, Yamada A, Itoh K. Personalized peptide vaccination: A novel immunotherapeutic approach for advanced cancer. *Human Vaccines & Immunotherapeutics*. 2012;8(9):1309-1313.
323. Cheever MA, Higano CS. PROVENGE (Sipuleucel-T) in Prostate Cancer: The First FDA-Approved Therapeutic Cancer Vaccine. *Clinical Cancer Research*. 2011;17(11):3520-3526.
324. Kumai T, Fan A, Harabuchi Y, Celis E. Cancer immunotherapy: moving forward with peptide T cell vaccines. *Current Opinion in Immunology*. 2017;47:57-63.
325. Slingluff CL. The Present and Future of Peptide Vaccines for Cancer: Single or Multiple, Long or Short, Alone or in Combination? *Cancer journal (Sudbury, Mass.)*. 2011;17(5):343-350.
326. Bolhassani A. Potential efficacy of cell-penetrating peptides for nucleic acid and drug delivery in cancer. *Biochimica et Biophysica Acta (BBA) - Reviews on Cancer*. 2011;1816(2):232-246.
327. Chen C, Chen Y, Yang C, Zeng P, Xu H, Pan F, Lu JR. High Selective Performance of Designed Antibacterial and Anticancer Peptide Amphiphiles. *ACS Applied Materials & Interfaces*. 2015;7(31):17346-17355.
328. Westermann B. Mitochondrial fusion and fission in cell life and death. *Nat Rev Mol Cell Biol*. 2010;11(12):872-884.
329. Mattila PK, Lappalainen P. Filopodia: molecular architecture and cellular functions. *Nat Rev Mol Cell Biol*. 2008;9(6):446-454.
330. Manning G, Whyte DB, Martinez R, Hunter T, Sudarsanam S. The Protein Kinase Complement of the Human Genome. *Science*. 2002;298(5600):1912-1934.
331. Maiese K, Chong ZZ, Shang YC, Wang S. mTOR: On Target For Novel Therapeutic Strategies In The Nervous System. *Trends in molecular medicine*. 2013;19(1):51-60.
332. Easton JB, Houghton PJ. mTOR and cancer therapy. *Oncogene*. 2006;25(48):6436-6446.
333. Read RD, Fenton TR, Gomez GG, Wykosky J, Vandenberg SR, Babic I, Iwanami A, Yang H, Cavenee WK, Mischel PS, Furnari FB, Thomas JB. A Kinome-Wide RNAi Screen in Drosophila Glia Reveals That the RIO Kinases Mediate Cell Proliferation and Survival through TORC2-Akt Signaling in Glioblastoma. *PLOS Genetics*. 2013;9(2):e1003253.
334. Liu K, Chen H-L, Wang S, Gu M-M, Chen X-M, Zhang S-L, Yu K-J, You Q-S. High Expression of RIOK2 and NOB1 Predict Human Non-small Cell Lung Cancer Outcomes. *Scientific Reports*. 2016;6:28666.
335. Bonnet S, Archer SL, Allalunis-Turner J, Haromy A, Beaulieu C, Thompson R, Lee CT, Lopaschuk GD, Puttagunta L, Bonnet S, Harry G, Hashimoto K, Porter CJ, Andrade MA, Thebaud B, Michelakis ED. A Mitochondria-K⁺ Channel Axis Is Suppressed in Cancer and Its Normalization Promotes Apoptosis and Inhibits Cancer Growth. *Cancer Cell*. 2007;11(1):37-51.
336. Contractor T, Harris CR. p53 Negatively Regulates Transcription of the Pyruvate Dehydrogenase Kinase Pdk2. *Cancer Research*. 2012;72(2):560-567.

337. Martini M, Russo M, Lamba S, Vitiello E, Crowley EH, Sassi F, Romanelli D, Frattini M, Marchetti A, Bardelli A. Mixed Lineage Kinase MLK4 Is Activated in Colorectal Cancers Where It Synergistically Cooperates with Activated RAS Signaling in Driving Tumorigenesis. *Cancer Research*. 2013;73(6):1912-1921.
338. Rhyasen GW, Starczynowski DT. IRAK signalling in cancer. *Br J Cancer*. 2015;112(2):232-237.
339. Li N, Jiang J, Fu J, Yu T, Wang B, Qin W, Xu A, Wu M, Chen Y, Wang H. Targeting interleukin-1 receptor-associated kinase 1 for human hepatocellular carcinoma. *Journal of Experimental & Clinical Cancer Research : CR*. 2016;35(1):140.
340. Shu F, Lv S, Qin Y, Ma X, Wang X, Peng X, Luo Y, Xu B-e, Sun X, Wu J. Functional characterization of human PFTK1 as a cyclin-dependent kinase. *Proceedings of the National Academy of Sciences of the United States of America*. 2007;104(22):9248-9253.
341. Zhu J, Liu C, Liu F, Wang Y, Zhu M. Knockdown of PFTK1 Protein Kinase 1 (PFTK1) Inhibits Proliferation, Invasion, and EMT in Colon Cancer Cells. *Oncol Res*. 2016;24(3):137-144.
342. Weihofen WA, Berger M, Chen H, Saenger W, Hinderlich S. Structures of Human N-Acetylglucosamine Kinase in Two Complexes with N-Acetylglucosamine and with ADP/Glucose: Insights into Substrate Specificity and Regulation. *Journal of Molecular Biology*. 2006;364(3):388-399.
343. Baxter AA, Lay FT, Poon IKH, Kvensakul M, Hulett MD. Tumor cell membrane-targeting cationic antimicrobial peptides: novel insights into mechanisms of action and therapeutic prospects. *Cellular and Molecular Life Sciences*. 2017.
344. Picard M, Shirihai OS, Gentil BJ, Burelle Y. Mitochondrial morphology transitions and functions: implications for retrograde signaling? *American Journal of Physiology - Regulatory, Integrative and Comparative Physiology*. 2013;304(6):R393-R406.
345. Eliassen LT, Berge G, Leknessund A, Wikman M, Lindin I, Løkke C, Ponthan F, Johnsen JI, Sveinbjørnsson B, Kogner P, Flægstad T, Rekdal Ø. The antimicrobial peptide, lactoferricin B, is cytotoxic to neuroblastoma cells in vitro and inhibits xenograft growth in vivo. *International Journal of Cancer*. 2006;119(3):493-500.
346. de Azevedo RA, Figueiredo CR, Ferreira AK, Matsuo AL, Massaoka MH, Girola N, Auada AVV, Farias CF, Pasqualoto KFM, Rodrigues CP, Barbuto JA, Levy D, Bydlowski SP, de Sá-Junior PL, Travassos LR, Lebrun I. Mastoparan induces apoptosis in B16F10-Nex2 melanoma cells via the intrinsic mitochondrial pathway and displays antitumor activity in vivo. *Peptides*. 2015;68:113-119.
347. Okumura K, Itoh A, Isogai E, Hirose K, Hosokawa Y, Abiko Y, Shibata T, Hirata M, Isogai H. C-terminal domain of human CAP18 antimicrobial peptide induces apoptosis in oral squamous cell carcinoma SAS-H1 cells. *Cancer Letters*. 2004;212(2):185-194.
348. Fielding AB, Royle SJ. Mitotic inhibition of clathrin-mediated endocytosis. *Cellular and molecular life sciences : CMLS*. 2013;70(18):3423-3433.
349. Kozik P, Francis RW, Seaman MNJ, Robinson MS. A Screen for Endocytic Motifs. *Traffic (Copenhagen, Denmark)*. 2010;11(6):843-855.

350. Wang C, Dong S, Zhang L, Zhao Y, Huang L, Gong X, Wang H, Shang D. Cell surface binding, uptake and anticancer activity of L-K6, a lysine/leucine-rich peptide, on human breast cancer MCF-7 cells. *Scientific Reports*. 2017;7(1):8293.
351. Lim KJ, Sung BH, Shin JR, Lee YW, Kim DJ, Yang KS, Kim SC. A Cancer Specific Cell-Penetrating Peptide, BR2, for the Efficient Delivery of an scFv into Cancer Cells. *PLOS ONE*. 2013;8(6):e66084.
352. Ohara K, Kohno M, Hamada T, Kawakami K. Entry of a cationic lytic-type peptide into the cytoplasm via endocytosis-dependent and -independent pathways in human glioma U251 cells. *Peptides*. 2013;50:28-35.
353. Jacquemet G, Hamidi H, Ivaska J. Filopodia in cell adhesion, 3D migration and cancer cell invasion. *Current Opinion in Cell Biology*. 2015;36:23-31.
354. Machesky LM, Li A. Fascin: Invasive filopodia promoting metastasis. *Communicative & Integrative Biology*. 2010;3(3):263-270.
355. Missirlis D, Krogstad DV, Tirrell M. Internalization of p53(14–29) peptide amphiphiles and subsequent endosomal disruption results in SJSA-1 cell death. *Molecular pharmaceutics*. 2010;7(6):2173-2184.
356. Missirlis D, Teesalu T, Black M, Tirrell M. The Non-Peptidic Part Determines the Internalization Mechanism and Intracellular Trafficking of Peptide Amphiphiles. *PLOS ONE*. 2013;8(1):e54611.
357. Stenmark H. Rab GTPases as coordinators of vesicle traffic. *Nat Rev Mol Cell Biol*. 2009;10(8):513-525.
358. Heitz F, Morris MC, Divita G. Twenty years of cell-penetrating peptides: from molecular mechanisms to therapeutics. *British Journal of Pharmacology*. 2009;157(2):195-206.
359. Grant BD, Donaldson JG. Pathways and mechanisms of endocytic recycling. *Nature reviews. Molecular cell biology*. 2009;10(9):597-608.
360. Gruenberg J, Stenmark H. The biogenesis of multivesicular endosomes. *Nat Rev Mol Cell Biol*. 2004;5(4):317-323.
361. Johannes L, Popoff V. Tracing the Retrograde Route in Protein Trafficking. *Cell*. 2008;135(7):1175-1187.
362. Fischer R, Köhler K, Fotin-Mleczek M, Brock R. A Stepwise Dissection of the Intracellular Fate of Cationic Cell-penetrating Peptides. *Journal of Biological Chemistry*. 2004;279(13):12625-12635.
363. Wang L, Chan JYW, Rêgo JV, Chong C-M, Ai N, Falcão CB, Rádis-Baptista G, Lee SMY. Rhodamine B-conjugated encrypted viperidin nonapeptide is a potent toxin to zebrafish and associated with in vitro cytotoxicity. *Biochimica et Biophysica Acta (BBA) - General Subjects*. 2015;1850(6):1253-1260.
364. El-Andaloussi S, Järver P, Johansson Henrik J, Langel Ü. Cargo-dependent cytotoxicity and delivery efficacy of cell-penetrating peptides: a comparative study. *Biochemical Journal*. 2007;407(2):285-292.
365. Scott AM, Wolchok JD, Old LJ. Antibody therapy of cancer. *Nat Rev Cancer*. 2012;12(4):278-287.
366. Jain M, Chauhan SC, Singh AP, Venkatraman G, Colcher D, Batra SK. Penetratin Improves Tumor Retention of Single-Chain Antibodies: A Novel Step toward Optimization of Radioimmunotherapy of Solid Tumors. *Cancer Research*. 2005;65(17):7840-7846.
367. Elbashir SM, Harborth J, Lendeckel W, Yalcin A, Weber K, Tuschl T. Duplexes of 21-nucleotide RNAs mediate RNA interference in cultured mammalian cells. *Nature*. 2001;411(6836):494-498.

368. Tomar RS, Matta H, Chaudhary PM. Use of adeno-associated viral vector for delivery of small interfering RNA. *Oncogene*. 2003;22(36):5712-5715.
369. Gao K, Huang L. Non-viral Methods for siRNA Delivery. *Molecular pharmaceuticals*. 2009;6(3):651-658.
370. Meade BR, Dowdy SF. Exogenous siRNA delivery using peptide transduction domains/cell penetrating peptides. *Advanced Drug Delivery Reviews*. 2007;59(2):134-140.
371. Wang J, Lu Z, Wientjes MG, Au JLS. Delivery of siRNA Therapeutics: Barriers and Carriers. *The AAPS Journal*. 2010;12(4):492-503.
372. Crombez L, Morris MC, Dufort S, Aldrian-Herrada G, Nguyen Q, Mc Master G, Coll J-L, Heitz F, Divita G. Targeting cyclin B1 through peptide-based delivery of siRNA prevents tumour growth. *Nucleic Acids Research*. 2009;37(14):4559-4569.
373. Ezzat K, Zaghoul EM, El Andaloussi S, Lehto T, El-Sayed R, Magdy T, Smith CIE, Langel Ü. Solid formulation of cell-penetrating peptide nanocomplexes with siRNA and their stability in simulated gastric conditions. *Journal of Controlled Release*. 2012;162(1):1-8.
374. George S, Xia T, Rallo R, Zhao Y, Ji Z, Lin S, Wang X, Zhang H, France B, Schoenfeld D, Damoiseaux R, Liu R, Lin S, Bradley KA, Cohen Y, Nel AE. Use of a High-Throughput Screening Approach Coupled with In Vivo Zebrafish Embryo Screening To Develop Hazard Ranking for Engineered Nanomaterials. *ACS Nano*. 2011;5(3):1805-1817.
375. Chakraborty C, Sharma AR, Sharma G, Lee S-S. Zebrafish: A complete animal model to enumerate the nanoparticle toxicity. *Journal of Nanobiotechnology*. 2016;14(1):65.
376. Rawson DM, Zhang T, Kalicharan D, Jongebloed WL. Field emission scanning electron microscopy and transmission electron microscopy studies of the chorion, plasma membrane and syncytial layers of the gastrula-stage embryo of the zebrafish *Brachydanio rerio*: a consideration of the structural and functional relationships with respect to cryoprotectant penetration. *Aquaculture Research*. 2000;31(3):325-336.
377. Chan JY-W, Zhou H, Kwan YW, Chan SW, Radis-Baptista G, Lee SM-Y. Evaluation in zebrafish model of the toxicity of rhodamine B-conjugated crotamine, a peptide potentially useful for diagnostics and therapeutics. *Journal of Biochemical and Molecular Toxicology*. e21964-n/a.
378. Robu ME, Larson JD, Nasevicius A, Beiraghi S, Brenner C, Farber SA, Ekker SC. p53 Activation by Knockdown Technologies. *PLOS Genetics*. 2007;3(5):e78.
379. Gerety SS, Wilkinson DG. Morpholino artifacts provide pitfalls and reveal a novel role for pro-apoptotic genes in hindbrain boundary development. *Developmental Biology*. 2011;350(2):279-289.
380. Bedell VM, Westcot SE, Ekker SC. Lessons from morpholino-based screening in zebrafish. *Briefings in Functional Genomics*. 2011;10(4):181-188.
381. Langheinrich U, Hennen E, Stott G, Vacun G. Zebrafish as a Model Organism for the Identification and Characterization of Drugs and Genes Affecting p53 Signaling. *Current Biology*. 2002;12(23):2023-2028.
382. Miura GI, Yelon D. A Guide to Analysis of Cardiac Phenotypes in the Zebrafish Embryo. *Methods in Cell Biology*. 2011;101:161-180.

383. Stainier DY, Fouquet B, Chen JN, Warren KS, Weinstein BM, Meiler SE, Mohideen MA, Neuhauss SC, Solnica-Krezel L, Schier AF, Zwartkruis F, Stemple DL, Malicki J, Driever W, Fishman MC. Mutations affecting the formation and function of the cardiovascular system in the zebrafish embryo. *Development*. 1996;123(1):285-292.
384. Antkiewicz DS, Burns CG, Carney SA, Peterson RE, Heideman W. Heart Malformation Is an Early Response to TCDD in Embryonic Zebrafish. *Toxicological Sciences*. 2005;84(2):368-377.
385. Usenko CY, Harper SL, Tanguay RL. In vivo evaluation of carbon fullerene toxicity using embryonic zebrafish. *Carbon*. 2007;45(9):1891-1898.
386. Morash MG, Douglas SE, Robotham A, Ridley CM, Gallant JW, Soanes KH. The zebrafish embryo as a tool for screening and characterizing pleurocidin host-defense peptides as anti-cancer agents. *Disease Models & Mechanisms*. 2011;4(5):622-633.
387. Vliegenthart ADB, Tucker CS, Del Pozo J, Dear JW. Zebrafish as model organisms for studying drug-induced liver injury. *British Journal of Clinical Pharmacology*. 2014;78(6):1217-1227.
388. Wang Y, Pan L, Moens CB, Appel B. Notch3 establishes brain vascular integrity by regulating pericyte number. *Development (Cambridge, England)*. 2014;141(2):307-317.
389. Fleming A, Diekmann H, Goldsmith P. Functional Characterisation of the Maturation of the Blood-Brain Barrier in Larval Zebrafish. *PLOS ONE*. 2013;8(10):e77548.

